LUND UNIVERSITY

Renormalization in Effective Field Theory and Hidden Radiation

Carloni, Lisa

2011

Total number of authors:
1

Renormalization in Effective Field Theory and Hidden Radiation

Lisa Carloni

Department of Theoretical Physics
Lund University

ii

Organization **LUND UNIVERSITY** Department of Astronomy and Theoretical Physics Sölvegatan 14A SE–223 62 LUND Sweden	Document name **DOCTORAL DISSERTATION**
	Date of issue February 2011
	Sponsoring organization
Author(s) Lisa Carloni	

Title and subtitle Renormalization in Effective Field Theory and Hidden Radiation

Abstract

This thesis deals with the field of high-energy particle physics. It is mainly concerned with two issues: the "renormalization of effective field theories" and the "detection of hidden sectors". The first two papers are dedicated to the renormalization issue while the second two deal with the hidden sectors. Renormalization is crucial when one calculates physical observables to a high degree of precision in quantum field theory using perturbative expansions. The field has lately seen many new developments, a recent one is the Weinberg-Büchler-Colangelo algorithm for calculating so-called Leading Logarithms (LL). These terms appear at each refinement of the calculation of a physical observable, i.e. at higher-orders in the perturbative expansion. They can be used to give a rough estimate of the size of each higher-order correction (refinement), to verify that each new calculation will yield a small correction to the previous estimate. This way, once the desired precision is reached, one can be sure that ulterior (often lengthy) calculations will not be necessary.

In paper I we apply the algorithm to the calculation of the mass, in a particularly simple model called $O(N+1)/O(N)$ non-linear massive sigma model. Though the model has a simple structure, it has the interesting feature that for $N = 3$ it describes two-flavour ChPT (chiral perturbation theory), the theory for low energy particle interactions, like $\pi - \pi$ scattering. In paper II we apply the algorithm to the decay constant, the vacuum expectation value, the scattering amplitude, the pion scalar and vector form factors. We perform the calculation to very high precision (the first four or five LLs, depending on the observable), and show in which cases it is preferable to express the logs in terms of the physical observables and in which cases in terms of the model parameters. We also solve (part of) the long-standing problem of summing the contributions of infinite refinements, for all these observables. We do this in the large number of fields N limit approximation. We prove this to be a poor approximation of the generic N expressions for most observables.

The second topic deals with the detection of new hypothetical light mass particle sectors, hidden from ordinary matter by an energy barrier. We exploit the high energies reached by particle colliders to breach the barrier and observe the deviations from standard particle distributions induced by the hidden sector. We consider both hadron colliders like LHC in CERN, where protons collide, and the case of lepton colliders, where electron and positron collide. We develop models and tools to simulate the effects of these new particles. The tools are inserted in a full scale random Monte Carlo event generator called PYTHIA 8. This is used to simulate particle collisions, so that one can connect the probabilities calculated from the theory with the particle distributions observed in the detectors. In paper III we explore the idea of discovering a new hidden sector charge through the effects of its radiation on the standard particle kinematics. In paper IV we seek to determine the structure of said charges, through differences between the induced radiation and hadronization patterns and the subsequent effects on standard distributions.

Key words: Renormalization, Effective theories, Phenomenological Models, Hidden Sectors

Classification system and/or index terms (if any):

Supplementary bibliographical information:	Language English

ISSN and key title:	ISBN 978-91-7473-075-3

Recipient's notes	Number of pages 190	Price
	Security classification	

Distributor

Lisa Carloni

Department of Theoretical Physics, Sölvegatan 14A, SE–223 62 Lund, Sweden

Signature _____   Date 2011-02-13

DOKUMENTDATABLAD enl SIS 61 41 21

Sammanfattning

Denna avhandling handlar om modeller inom partikelfysik, vilka beskriver naturens minsta beståndsdelar. För att studera dessa små grundläggande byggstenar behöver man hög energi. Desto större energi ju mindre avstånd kan man studera. Med höga energier kan man se atomerna, och med ännu högre energier kan man se kärnan och elektronerna, som atomerna består av. Sedan 60-talet har vi sett att även protonerna och neutronerna som kärnan består av, består av ännu mindre partiklar som kallas kvarkar. Partikelacceleratorexperiment, som LEP (Large Electron Proton collider), där subatomära partiklar kolliderar med mycket hög energi, avslöjar detaljer om dessa små partiklar. De partiklar som produceras vid kollisionen studeras och kan användas för att dra slutsatser om strukturen hos de partiklar som skapats vid kollisionen.

Experimenten inom partikelfysik är mycket dyra att bygga och därför finns det endast ett fåtal i världen. LHC vid CERN, som är det största experimentet hittills, startade 2009. Snart kommer vi att få se nya resultat och testa våra teorier om vad som förenar de olika partiklar vi observerar.

När fysiker upptäcker nya partiklar, kategoriserar de dem och försöker hitta mönster som avslöjar hur de grundläggande byggstenarna i universum växelverkar. Fysiker har utvecklat en teori som kallas Standardmodellen som förklarar hur de här partiklarna växelverkar genom den starka kraften (som håller ihop atomkärnor), den svaga kraften (som ger energi till stjärnorna) och elektromagnetism. Det är en omfattande teori som förklarar alla de hundratals partiklar som observerats och hur de växelverkar med endast 6 kvarkar, 6 leptoner (som elektronen) och kraftbärande partiklar, som fotonen och gluonen. Standardmodellen formulerades på 1970-talet och har sedan dess utsatts för många tester. De allra flesta delarna av teorin är bekräftade och teorin beskriver nästan all mätningar som gjorts på ett tillfredsställande sätt. Den enda partikeln som finns i standardmodellen som inte upptäckts än är Higgs-partikeln, vilken ger de andra partiklarna deras massa.

Men Standardmodellen har brister, både teoretiskt och experimentellt. Det finns ingen förklaring till att det inte finns lika många partiklar som anti-partiklar. Neutrinomassan inkluderas inte. Det finns ingen förklaring till varför partikelmassor bör vara vad de är. I själva verket beskriver Standardmodellen bara 4% av materien i universum. Den har ingen förklaring till all mörk materia och mörk energi som står för de resterande 96% av energin i universum. En annan viktig fråga är att standardmodellen inte inkluderar gravitation. Vid de små avstånd vi observerar i partikelacceleratorer, är gravitationen försumbar, men det betyder fortfarande att teorin är ofullständig.

Det finns också ett annat problem med Standardmodellen, som är ett beräkningsproblem snarare än att teoretisk problem. Även om vi vet att det

är den korrekta beskrivningen av alla partiklarna som hittills undersökts och deras växelverkan, kan den inte alltid användas för att göra förutsägelser vid låga energier, där den starka kraften blir starkare. Växelverkan mellan partiklar med låg massa, som η-mesoner, pioner och kaoner till exempel, kan inte beskrivas i termer av kvarkar och gluoner. Istället måste man använda effektiva teorier i detta fall, som till exempel Kiral Störningsteori.

Den första delen av denna avhandling handlar om effektiva teorier. Frågan vi tar itu med är hur man kan göra mer exakta förutsägelser baserade på dessa effektiva teorier och hur viktigt det är att införa förbättringar i beräkningarna.

Den andra delen handlar om utökningar av Standardmodellen. Det finns många teorier för detta, beroende på vilken av Standardmodellens brister de vill ta itu med. Många modeller innehåller nya partiklar och nya växelverkningar. Vi vill ta itu med frågan "Om det finns en ny växelverkan, och nya partiklar med laddning, som vi inte har observerat tidigare, skulle vi kunna mäta strålningen som kommer från den laddningen i framtida experiment?". "Och vad kan man säga om denna ny laddning? Vad kan man förstå om den nya växelverkans struktur genom att observera strålningen?". För att besvara denna fråga simulerar vi effekterna av den nya strålningen på de standardmodell partiklar som kan detecteras vid LHC. Just nu producerar LHC första data, så vi kommer snart att kunna jämföra våra simuleringar med data och att testa de nya teorierna.

To my aunt Flavia

This thesis is based on the following publications:

I **Leading Logarithms in the Massive O(N) Nonlinear Sigma Model**
Johan Bijnens, Lisa Carloni
Nuclear Physics B 827:237-255,2010
e-Print: arXiv:0909.5086 [hep-ph]

II **The Massive O(N) Non-linear Sigma Model at High Orders**
Johan Bijnens, Lisa Carloni
Nuclear Physics B 843:55-83,2011
e-Print: arXiv:1008.3499 [hep-ph]

III **Visible Effects of Invisible Hidden Valley Radiation**
Lisa Carloni, Torbjörn Sjöstrand
Journal of High Energy Physics 1009:105,2010
e-Print: arXiv:1006.2911 [hep-ph]

IV **Discerning secluded sector gauge structures**
Lisa Carloni, Johan Rathsman, Torbjörn Sjöstrand
LU TP 11-09
MCnet 11-06
e-Print: arXiv:1102.3795 [hep-ph]

Contents

i

Introduction

We shall not cease from exploration,
and the end of all our exploring will be
to arrive where we started,
and know the place for the first time.
T. S. Eliot

As many others before me, I have not worked on one single subject during my four years as a PhD student, but rather on several different topics. As a consequence, this thesis contains publications dealing with very different aspects of particle physics. One half revolves around the idea of "Renormalization in Effective Field Theories", while the other half is dedicated to New Physics and in particular to the "Detection of Hidden Radiation". The first one is essentially an analytical work, while the second one is rather a phenomenological study of the New Physics models using Monte Carlo simulations. As such, it is rather difficult to put all this work into one common framework. In the following, I will try to explain a bit of the common ground physics behind the papers, and then go on to discuss the specific background of the first two and of the last two. The introduction to the general background was brutally cut short to to make space for the introduction to the papers and of course it has its limitations, so I recommend reading [1–3], for a deeper understanding.

i.1   Common ground

i.1.1   High-energy particle physics

The picture of high-energy physics today is quite varied. As new particle accelerators are built and we are able to explore higher-and higher energies, the usual electrons, protons and neutrons from which common matter is made, are seen to be accompanied by a plethora of new heavier particles (see Fig. *i*.1), $\mu, \nu_\mu, \tau, \nu_\tau, \eta, \pi, K, \rho, \Lambda, \Delta$, just to mention some. Fortunately most of these particles and their interactions fit a theory, known as the Standard Model (SM), in
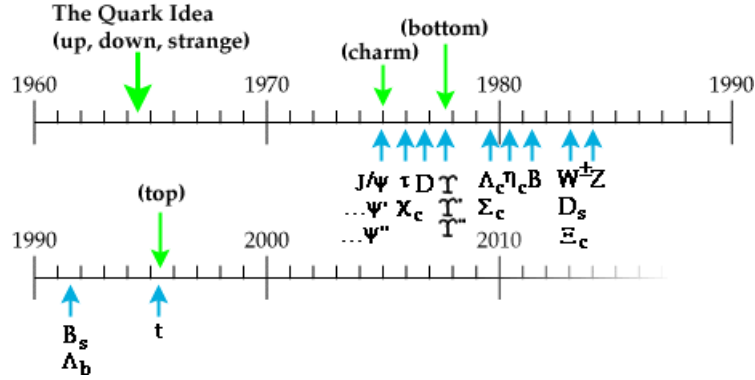
Figure *i*.1: The new particles discovered since 1964 at SLAC (Stanford Linear Accelerator), CERN (Conseil Européen pour la récherche Nucléaire), DESY (Deutches Elektronen-Syncrotron), LEP (Large Electron-Positron) collider, BNL (Brookhaven National Laboratories) and Tevatron.

Figure *i*.2: Tracks drawn by particles in a detector called bubble chamber. On the r.h.s. is a close-up of the central region, where a particle and antiparticle spiral in opposite directions.

which all particles can be classified according to their mass, spin and quantum charges.

The first distinction one makes is between particles and anti-particles. Each particle has an anti-particle partner, that is a particle with the same mass and the same spin, but with opposite charges, for instance the positron e^+ is the antiparticle of the electron e^-, though sometimes anti-particle and particle coincide, as in the photon γ case. In Fig. *i*.2 one the r.h.s. you can see the particles curving to the left, due to their interaction with the magnetic field, and the anti-particles curving to the right. One of the yet unsolved mysteries of physics is why the universe should be filled with particles and have so few anti-particles. For our existence it is quite fortunate, because if particles and
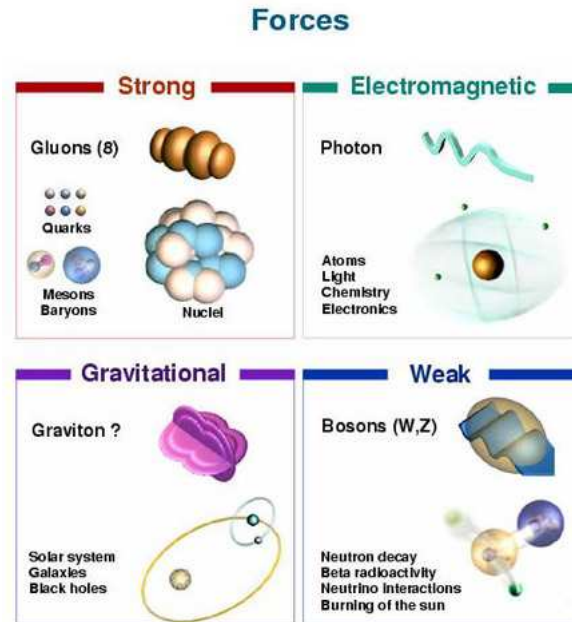
Forces

The particle drawings are simple artistic representations

Figure *i*.3: All known interactions up to this day. For each force one can find the gauge boson, that is the carrier of the force, and the phenomena they govern.

anti-particles were present in equal quantities, they would annihilate and only radiation would be left, but it is nonetheless a puzzling question.

Particles with half-integer spin $(1/2, 3/2, ...)$ are called fermions and particles with integer spin $(0, 1, 2, ...)$ are called bosons. The spin dictates their behaviour in the presence of magnetic fields and their statistics, that is whether they can clump together in one point in space or repel each other instead.

Particles are also classified according to other quantum numbers, internal quantum numbers, which decide each particle's interactions, whether they have strong interactions, weak interactions or electromagnetic interactions and how strong these interactions are. All particles carrying an electric charge have electromagnetic interactions. Particles with a weak charge, called *flavor*, can have weak interactions and finally particles carrying strong charges, called *color* charges, can have strong interactions. Particles like $\pi, K, \rho, p, n, \Delta$ (collectively called hadrons) can have strong, weak or electromagnetic interactions, while leptons $e^-, \nu_e, \mu^-, \nu_\mu, \tau^-, \nu_\tau$ only have weak or electromagnetic interactions (if they are electrically charged). The force carriers, called gauge

Figure *i*.4: The figure shows the classification of fermionic particles into *leptons*, *quarks* and *gauge bosons*. Leptons can only have electro-weak interactions, while quarks can have both strong and electro-weak interactions, since they also carry a strong quantum number. Each group comes in three generations, so-called flavors,i.e. three replicas of the same two-particle structure (e^-, ν_e), (μ^-, ν_μ), (τ^-, ν_τ) for the leptons and (u, d), (s, c) and (b, t) for the quarks. The quanta of the electromagnetic, strong and weak interactions, the gauge bosons $\gamma, g, Z^0, W^\pm$, are in the last column.

bosons, can be charged themselves. The gluon g for instance, the carrier of the strong interactions, has strong charges, so it can exchange strong interactions with other gluons. Similarly for the $Z^0, W^\pm$ gauge bosons, the carriers of the weak interactions. The photon γ instead is not electrically charged so it cannot exchange electromagnetic interactions with other photons. Fig. *i*.3 depicts the different forces and the corresponding force carriers, i.e. the gauge bosons, and the phenomena they are responsible for.

The electromagnetic interactions are perhaps the ones we have a better understanding of, because they also take place at a macroscopic scale. At a quantum level though, they consist in the exchanges of photons γs (the force carries of the electromagnetic field), and are described by Quantum Electro Dynamics (QED). The weak interactions are less familiar, but they are responsible for, among others, the β decays, which are crucial for the heating of the sun and of the other stars. These interactions are considered weak as compared to the electromagnetic ones, because they only happen a million times slower than the electromagnetic ones. The strong interactions on the other hand happen at a much faster rate than the electromagnetic ones, about one million times

faster. Their range though is much shorter than the electromagnetic interaction, they do not extend much beyond the proton size (10^{-15} m). So strong is this interaction however that the residual force outside the proton is what keeps the nucleons bound together in the nucleus of the atom. The strong interactions though are not just the interactions of nucleons, they are actually interactions of quarks and gluons, the hadron constituents. These quarks are never observed as free particles, but only confined to hadrons. The current description of these strong interactions, called Quantum Chromo Dynamics[1] (QCD) cannot explain why it is that these quarks are confined into hadrons, see Section *i*.1.2. Note that I have not mentioned the fourth fundamental interaction of nature, gravity. That is because as of today there is still no way of combining it with the other three forces into one consistent unified quantum description. Since gravity is very weak at the scales we are talking about, one may easily neglect its effects.

In Fig. *i*.4 one can see how leptons and quarks come in three families, each with different masses. Why it is so, is still not known. The interactions however (disregarding mass differences) are the same for every generation. There are many other unsolved questions in the Standard Model and I will return to (some of) them in section *i*.1.4.

One particle I have still not mentioned is the Higgs boson H, the particle that according to the SM is responsible for giving mass to all the other particles. It has as yet not been observed, though it was originally expected to have a mass well within the discovery reach of the LEP collider first, then of Tevatron collider. It is currently the single most sought after particle at the newly built Large Hadron Collider (LHC).

The electroweak and strong interactions of all these particles may be encoded into the mathematical formalism of a Lagrangian. This Lagrangian contains the kinetic energy, the potential of each particle (including the part due to the mass) and all the possible particle interactions written in terms of the field operators associated the particles. For instance a neutral boson particle is associated with a field ϕ and a fermion with a field ψ. The form of the Lagrangian is determined by the symmetries of the system, which encode the interactions of the system. For the Standard Model Lagrangian these symmetries are

$$SU(3)_c \times SU(2)_w \times U(1)_Y. \qquad (i.1)$$

The first symmetry group $SU(3)_c$, is called the color group (*chromo=color*), and reflects the fact that quarks come in three colors, red, blue, green. The second symmetry group is the weak interaction group $SU(2)_w$, and the third one is the hypercharge group $U(1)_Y$. These two groups together describe all the electromagnetic and weak interactions, brought about by γs and $Z^0, W^{\pm}$. The

---

[1]From the Greek word *chromo* for color.

$SU(2)_w \times U(1)_Y$ symmetry is therefore said to unify electromagnetic and weak interactions into one electroweak interaction.

The Lagrangian describing all these particle interactions consists of the QCD Lagrangian, the Electro-Weak one and the Higgs Lagrangian.

$$\mathcal{L} = \mathcal{L}_{\text{QCD}} + \mathcal{L}_{\text{EW}} + \mathcal{L}_{\text{Higgs}}. \qquad (i.2)$$

From this one can extract all physical quantities. The complication is that, as mentioned above, while QCD is formulated in terms of qs and gs, the physically observables states are hadrons, so in order to calculate the observables such as the mass or the scattering amplitude, one must resort to using approximate, effective models in which it is the hadrons that interact instead of the quarks and the gluons.

Effective theories are a very powerful tool for describing interactions, for calculating observables and thus for making predictions. Indeed they are such an important topic that they are the subject matter of the next section. For a better description see [4, 5].

i.1.2 Effective Field Theories

To understand what I mean by Effective Theory, consider the problem of describing a physical system. Typically, one would like to isolate the relevant features of the system and disregard the other details. "The crucial point is to make an appropriate choice of variables, able to capture the physics which is most important for the problem at hand" [6]. An effective field theory is precisely a theory which is capable of reproducing the key features of the system.

In particle physics, usually one deals with problems involving very different energy scales, from 100 MeV (corresponding to the π mass) to tens of TeV (the New Physics Frontier) to the Planck scale 10^{19} GeV, and one generally uses the expression "Effective Theory" as a synonym for low-energy theory. What this low-energy limit is depends upon the context. For instance both projects I have dealt with, the renormalization project and the hidden sector one, deal with effective field theories, but the energy range, and thus the physics they describe, are very different. To understand where these two projects lie on this energy scale, consider an axis going from the electron mass [2] to the Planck scale depicted in Figure *i*.5.

In the first case, that is for the renormalization project, a typical example of effective field theory the we (my supervisor and I) often refer to in the text is Chiral Perturbation Theory (ChPT), the theory of π, K, η mesons. See [2] for an introduction.

---

[2] In the following we will always use the convention $c = 1$, for which energy and mass have the same dimensions.
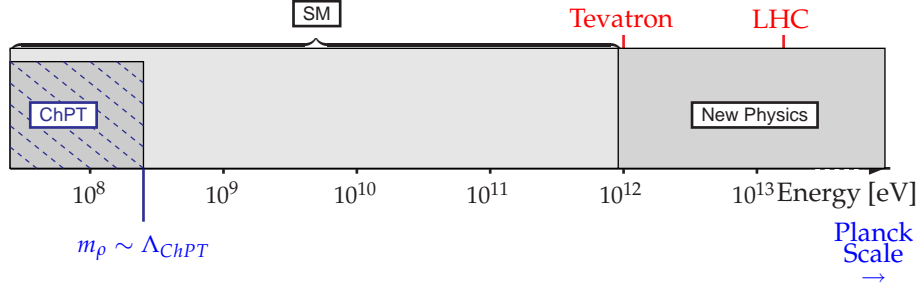
Figure *i*.5: Typical energy scales in Particle Physics. In particular note that ChPT, the low energy effective theory of QCD, lies below the ρ meson mass scale and below 1 GeV, the scale at which QCD interactions become strong. The Standard model extends up to the scales thus far explored at the Tevatron accelerator, i.e. up to 1.2 TeV. New Physics as an extension of the Standard Model is expected somewhere above this scale. If it occurs at a scale below 14 TeV it might be detected by the Large Hadron Collider (LHC).

ChPT is an effective description of these light states of QCD, in the low energy regime $p^2 \ll M_\rho^2 \sim (700)^2$ MeV^2. The reasons why it is preferable to use ChPT rather than QCD to describe their properties (symmetries, masses, decay constants) are twofold.

First, as mentioned above, QCD is formulated in terms of quarks (q) and gluons (g), the meson constituents, and not in terms of the physically observable π, K, η mesons themselves. As of today, the exact link between the QCD quarks and gluons, and the mesons is not fully understood. QCD does not explain why one does not observe quarks as free particles at low energies. The are many hints[3] indicating that if quarks are separated in space, the strong force between them grows stronger, binding quarks together. However, the mathematical formulation for hadronization, the mechanism confining quarks and gluons into the hadrons, has yet to be written.

Second, in particle physics one cannot usually calculate a physical observable outright, but must rely on a systematic approximation procedure. The result is called a perturbation series of the observable, because the underlying assumption is that the system is well described by the first term and that each new correction is just a small perturbation to the result. In QCD this procedure leads to expressing the observables O as power expansions of the quark-gluon coupling α_s.

$$O = O_0 + \alpha_s O_1 + \alpha_s^2 O_2 + \alpha_s^3 O_3 + \cdots \qquad (i.3)$$

Each new refinement of the calculation, i.e. each new term in the series above, is expected to be a small correction to the previous estimate. This strategy

---

[3]For example coming from lattice QCD calculations.

gives extraordinary results[4] when applied to QCD in the high energy regime $p^2 \gg 1$ GeV^2, where $\alpha_s < 1$. However, in the low energy regime $p^2 \ll 1$ GeV^2, which is the region of interest if we want to describe mesons, there is no hierarchy between the size of the terms. This makes it impossible to decide beforehand when to truncate the perturbative series, i.e. to determine whether or not the first n terms of the perturbative series are sufficient to describe the observable with the desired degree of precision. The reason is that the QCD coupling α_s grows as the momentum transferred[5] becomes smaller and in this energy regime it is larger than 1. It is preferable then to use an approximate theory which uses hadrons as fundamental particles and which allows for a systematic perturbation theory approach. That this can be done is proven by a theorem [6–8] which can loosely be stated as

Theorem 1 *For a given set of asymptotic states, perturbation theory with the most general Lagrangian containing all the terms allowed by the assumed symmetries will yield the most general S-matrix elements consistent with analyticity, perturbative unitarity cluster decomposition and the assumed symmetries.*

This means that regardless of the underlying theory, once one identifies which fundamental states and which symmetries are relevant at the energy scale at hand, the effective Lagrangian built with these fundamental fields and symmetries will encode the same physics of the underlying theory.

If one can also identify a small parameter in the effective theory, such as the ratio $r = p/\Lambda$ between the scale of the process and the cut-off scale for the theory, one can then perform a meaningful perturbative expansion in powers of r.

i.1.3   Building an effective field theory

In the following I will introduce those principles of effective field theory building that I deem necessary for the understanding of the mechanics of renormalization.

Once one has identified the fundamental fields of the theory, the two ingredients one needs to construct a workable effective theory are

- an ordering criterion for the various terms in the perturbative expansion,
- an understanding of the symmetries of the system, so one can write the most general Lagrangian compatible with the symmetries. The Lagrangian and the matrix elements (which yield the physical observables)

---

[4]Examples are scaling violation in Deep Inelastic Scattering experiments confirmed by SLAC, the running of the QCD coupling constant confirmed by the three-jet distributions observed by PETRA, the jet cross sections at colliders, the event shape observables at LEP, the heavy-quark production at colliders.

[5]If a particle changes its momentum by emitting a gauge boson, the momentum of the gauge boson is called transferred momentum.

built upon these symmetries encode all the physics of the system. Note that the symmetries and renormalization procedure are intimately connected, I will discuss this issue in section *i*.2.

To build an effective Lagrangian for a process happening at a scale $p \ll \Lambda$ one can use an expansion in powers of p/Λ, where Λ is the cut-off scale of the model[6]. One may then organize the Lagrangian in terms of series of growing powers of momenta, i.e. of derivatives.

$$\mathcal{L} = \mathcal{L}_2 + \mathcal{L}_4 + \cdots + \mathcal{L}_{2n} \qquad (i.4)$$

where the subscript indicates the number of derivatives. Once the Lagrangian has been ordered this way, one may use Weinberg's [7] power counting to determine which Feynman diagrams, that is which terms in the perturbative expansion of an observable, are to be taken into account. Feynman diagrams are pictorial representations of the terms, which make the physical meaning of the mathematical expression more apparent. For instance consider the diagram on the left hand side of Fig. *i*.6. Time flows from left to right. An arrow going from left to right represents a fermion, while one going from right to left an anti-fermion. The wiggly line represents a gauge boson (in this cases a W or a Z) propagating from one place to the other of space time. To each of these elements is associated a function, so that the diagram has a one to one correspondence with the mathematical expression of the probability amplitude of that process taking place. Weinberg's power counting states the first and most important diagrams one should consider come from the lowest order Lagrangian $\mathcal{L}_2$, and are to be *tree* level diagrams, that is without loops. The contribution coming from $\mathcal{L}_2$ loop diagrams are suppressed compared with the tree level ones, but are roughly of the same size (of the same order) as the first order Lagrangian $\mathcal{L}_4$

$$\mathcal{L}^{\text{tree}} = \overbrace{\mathcal{L}_2^{\text{tree}}}^{0^{\text{th}}\ \text{order}} + \overbrace{\mathcal{L}_2^{\text{1loop}} + \mathcal{L}_4^{\text{tree}}}^{1^{\text{st}}\ \text{order}} + \cdots \qquad (i.5)$$

Generalizing, each loop adds one suppression factor p^2/Λ^2, so that an n-loop diagram is suppressed like a term in the $\mathcal{L}_{2n}$ Lagrangian.

The second issue, that is the determination of which symmetries appear or disappear when one takes the low energy limit $p/\Lambda \to 0$ of a theory, depends on the terms in the Lagrangian and on how these scale with p/Λ. Some operators present in the high-energy underlying theory may disappear in the low-energy limit. For instance nowadays we know that in electroweak interactions fermions interact by exchanging W, Z bosons, as shown by the Feynman

---

[6]In some cases several cut-off scales Λ_i may be involved, then the understanding of the hierarchy between the various terms of the perturbative expansion in powers of the different p/Λ_i may be more complicated. I will not discuss this case here.

diagram on the l.h.s. of Fig. *i*.6. In Fermi's time though, in the 30's, accelerators did not have enough energy to resolve the W, Z particles propagating from x to y, and the weak interactions $f\bar{f} \rightarrow f\bar{f}$ appeared as the local four-fermion interaction on the r.h.s. of Fig. *i*.6. In this effective theory the ffZ coupling disappeared, so the similarities between a Z exchange and a photon exchange (essentially the same as that in Fig. *i*.6 but with a photon in the place of the Z, W), were lost and weak and electromagnetic interactions appeared to be different. The symmetry linking the weak and electromagnetic into one electroweak interaction is lost in the low-energy effective theory.

To determine which interaction terms remain relevant in the limit $p/\Lambda \rightarrow 0$, one must look at each term in the Lagrangian and consider the dimension of each of the operators. The Lagrangian is given by

$$\mathcal{L} = \sum_i c_i O_i, \tag{i.6}$$

where the O_i are the different operators O_i and the c_i the operator coefficients. These operators are functions of the ϕ, ψ fields associated to the particles, such as the kinetic energy operator $\partial_\mu \phi \partial^\mu \phi$ or the ϕ^2 operator in the mass term $m^2 \phi^2$. Depending upon the energy dimension of each operator, they can be *relevant* ($d_i < 4$), *marginal* ($d_i = 4$) or *irrelevant* ($d_i > 4$). The effects of irrelevant operators are suppressed by powers of p/Λ, so they disappear in the limit $p/\Lambda \rightarrow 0$. These operators are usually the remnants of the underlying higher energy theory, as in the case of the effective four-fermion coupling in Fermi's theory of weak interactions. Typical examples of relevant operators are instead given by
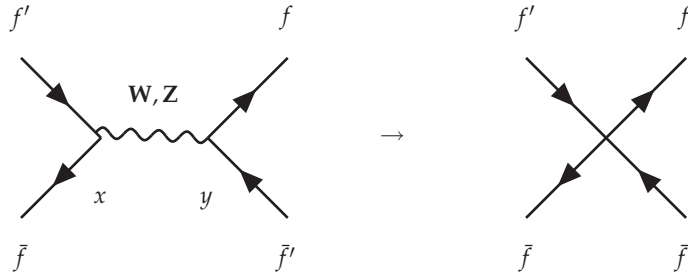
Figure *i*.6: Electroweak interactions between fermions. Fermions f and $\bar{f}$ produce a Z, W bosons which propagates and then decays into another $f\bar{f}$. At lower energy resolutions this interaction appears as Fermi's effective local four-fermion interaction. The corresponding operator in the effective Lagrangian $\bar{\psi}_f \psi_{f'} \bar{\psi}^{f'} \psi^f$ has energy dimension 4 and is thus irrelevant.

mass terms $-m^2 \phi^2$ and $m\bar{\psi}\psi$. These operators are dominant in the low-energy

limit. Finally kinetic terms $\partial_\mu \phi^\dagger \partial^\mu \phi$ are typical examples of marginal operators and are in first approximation equally important at all momentum scales[7].

When one takes the low energy limit of a theory, irrelevant terms disappear and the symmetries of the system are given by the remaining terms.

I will not discuss these issues further here. I will come back to relevant/irrelevant operators and discuss their connection with *renormalization* in section *i*.2.

i.1.4   The Standard Model as an effective theory

Returning to the issue of the effective field theories, theorem 1 above also implies that the argument may be reversed: one can use the symmetries and phenomenology[8] of the effective low energy theory to understand what the underlying higher energy theory should be. This bottom-up approach is used by New Physics models builders, to constrain Standard Model extensions.

As of today, the SM, the theory that describes the strong and electroweak interactions of all the known particles, quarks, leptons and gauge bosons, has shown only one unequivocal discrepancy with data, the lack of neutrino masses. In Figure *i*.5 one may see the impressive energy range of applicability of the SM, which extends over 12 orders of magnitude and describes phenomena that are as different as jet[9] distributions at colliders, neutron decays or photon exchanges. *It is however a fact that it is just an effective theory, since it does not include gravity*.

There are other experimental results hinting at physics beyond the Standard one, as suggested in section *i*.1.1: nothing in the SM can explain the matter-antimatter asymmetry or the presence of dark matter (DM), which alone accounts for 23% of the matter in the universe, as depicted in Fig. *i*.7 and described in [9].

There are also very strong indications for New physics coming from theoretical arguments, such as the "naturalness argument". This argument is connected to the mass of Higgs boson, the only fundamental scalar particle

---

[7]The symmetries of the theory are in first approximation, that is at a tree level, those given by the Lagrangian in which one neglects all irrelevant operators. Quantum loop corrections can however greatly complicate the picture. First of all, loop corrections can break the classical symmetries thus affecting the renormalization procedure. Second, they can give rise to anomalous dimensions which tilt the behaviour of marginal operators. Finally, loops involving irrelevant operators are in principle not suppressed, since p/Λ is integrated over all energy scales.

[8]The collection of all the Particle physics phenomenology is the part of theoretical particle physics that deals with the application of theory to high energy particle physics experiments. Within the Standard Model, phenomenology is the calculating of detailed predictions for experiments, usually at high precision. Phenomenology may in some sense be regarded as forming a bridge between the highly mathematical world of theoretical quantum field theories and experimental particle physics.

[9]Highly boosted particle sprays.
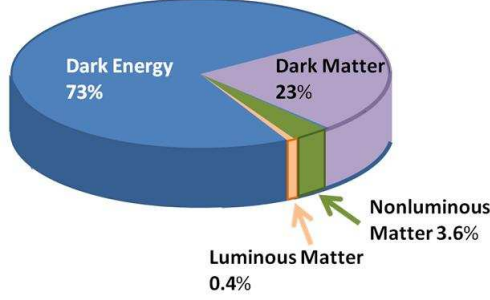
Figure *i*.7: Pie chart of the relative abundances of dark energy (73%), dark matter (23%) and matter (4%) in the universe.
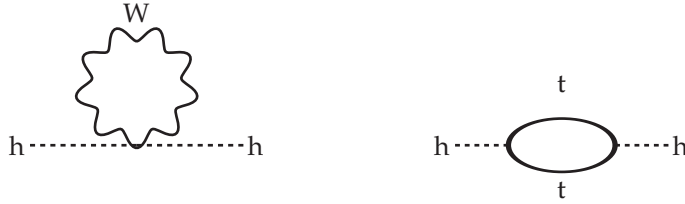
Figure *i*.8: Some one-loop diagrams contributing to the quadratic divergence of the mass of the Higgs boson.

present in the SM[10]. Since it is a scalar, the perturbative expansion of its physical mass squared has a characteristic Λ_{SM}^2 dependence on the cut-off scale of the theory:

$$m_{\text{phys}}^2 = m_0^2 + \alpha \Lambda_{\text{SM}}^2 \qquad (i.7)$$

where m_0^2 represents the classical, tree level contribution and $\alpha\Lambda_{\text{SM}}^2$ contains all the quantum corrections arising from one-loop diagrams[11]. Some of these diagrams are in Fig. *i*.8. The naturalness argument can loosely be stated as *"if the Standard Model were correct up to the Planck scale (the scale at which it must be abandoned in flavor of a theory including quantum gravity effects) the SM cut-off scale in Eq. i.7 would be $\Lambda_{\text{SM}} \simeq O(10^{19})$ GeV; in order to give the Higgs boson the expected mass of $O(100\text{GeV})$, one should have a very unnatural cancellation between*

---

[10]Disregarding bound states of the fundamental fields, such as the π of ChPT.

[11]The quantum corrections add up to

$$\frac{6}{\sqrt{2}}\frac{G_F}{\pi^2}\left(m_t^2 - \frac{m_W^2}{2} - \frac{m_Z^2}{4} - \frac{m_H^2}{4}\right)\Lambda_{SM}^2 \qquad (i.8)$$

where G_F is the Fermi constant, m_t, m_Z, m_W, m_H are the masses of the top quark, and of the Z, W, H bosons respectively.
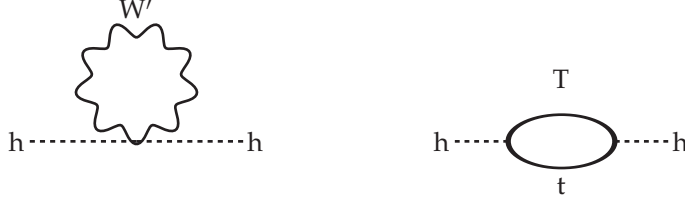
Figure *i*.9: Examples of new diagrams causing the partial cancellation of the quadratic divergence due to the introduction of new particles, in this case in Little Higgs models. T and W' are the new particles whose loops cancel the greater part of the quantum corrections in Fig. *i*.8.

the two terms on the r.h.s. of Eq. (i.7). For this cut-off Λ_{Planck} *the two completely un-correlated numbers should differ (in absolute value) only by one part in* 10^{32}*"*. In SM extensions one assumes that this cancellation is not accidental, but rather the result of some new symmetry which is only manifest at energies $E \gtrsim \Lambda_{\text{SM}} \sim 1$ TeV (the energy frontier explored by the Tevatron accelerator). Beyond the cut-off scale the SM must be extended to include the new symmetries and new particles. Typically, the new symmetries ensure that the quantum corrections induced by the new particles naturally cancel[12] the large SM quantum corrections in Eq. *i*.7. For example in Little Higgs SM extensions, the large contributions coming from the diagrams in Fig. *i*.8 are canceled by the new W' and T particle loops described in Fig. *i*.9. Another very popular SM extension is SuperSymmetry (SUSY). See ref. [10] for an introduction. In SUSY each fermion has a boson superpartner and each boson has a fermion superpartner with the same charges. The large quantum contribution in Eq. *i*.7 is then cancelled by the superpartner.

The new particles are usually given masses above the TeV scale, because the larger the mass, the lower the impact on the dynamics of the lower energy ones[13]. This way one can avoid large modifications of the SM phenomenology[14] [11]. Note however that not all new particles necessarily have to be this

---

[12]Or very nearly cancel.

[13]This is due to the decoupling theorem.

[14]Typical SM physical observables affected by the presence of new articles are scattering amplitudes, production cross sections, unitarity triangle relations, S, T, U parameters. The scattering amplitude, the probability amplitude that two particles α and β collide and the same two α and β emerge, can be modified in many ways by new physics, by modifying the couplings, or by introducing new quantum corrections similar to the ones described for the Higgs mass. The production cross-section (proportional to the probability to produce the particle) can be affected the same way. The unitarity triangle relations are relations due to the fact that there are exactly three generations in the SM, these would be dramatically affected by the introduction of a fourth generation. The S, T, U parameters encode the quantum corrections to the way a Z boson propagates and are very sensitive to new particle quantum loops.

heavy. In section *i*.3 I will for instance describe new physics scenarios in which the new sector is light.

i.2   Renormalization in effective field theories

In the previous section *i*.1 I often touched upon the subject of quantum corrections and the precise determination of the value of an observable, such as the mass of the Higgs. For instance, in Eq. *i*.7 I pointed out how the quantum correction grew as Λ_{SM}^2. If the SM theory were correct up to infinitely high Λ_{SM} scales, the quantum correction would grow very rapidly to be infinite, making the whole idea of a quantum correction as a small perturbation of the result somewhat problematic.

One solution, suggested by Eq. *i*.7, is to assume that the physical mass on the l.h.s. of the equation is the *measured* one, and that the sum of tree level result and of the quantum loop corrections on the r.h.s. is just the expression of the mass in terms of parameters. Since it is the *sum* that must be finite, we can assume the tree-level term to be infinite too so it can cancel the loop quantum divergence.

We need to find a systematic way to handle the infinite quantum corrections to extract meaningful results though, and this procedure is called *renormalization*.

i.2.1   The concept of renormalization

The problem arises, as I said, when one considers the perturbative expansion of a physical observable in terms of the couplings in the Lagrangian. Very often the quantum fluctuations, i.e. the quantum loops, are ultra violet[15] (UV) and/or infra-red[16] (IR) divergent. The physical observables expressed in terms of the Lagrangian parameters thus turn out to be infinite.

The key point to realize though, is that what is infinite is just the relationship between the physical observable and the parameters in the Lagrangian, as in Eq. *i*.7 between m_{phys} and m_0. The physical relations between physical observables, between mass m_{phys} and charge e_{phys}, will still be finite.

Consider two observables A and B, each expressed in terms of the Lagrangian parameters a and b. The relationship between A and a, b may be infinite, as may be the relation between B and a, b, however the relationship between the two physical A and B is finite and that is what is physically meaningful and measurable. *Renormalization consist in writing the observable in terms of other physical observables rather than in terms of Lagrangian parameters.*

---

[15]I.e. in the high energy region $p \rightarrow \infty$, or more physically p much larger than the typical scale of the process at hand.

[16]I.e. at scales much smaller than the typical scale of the process.
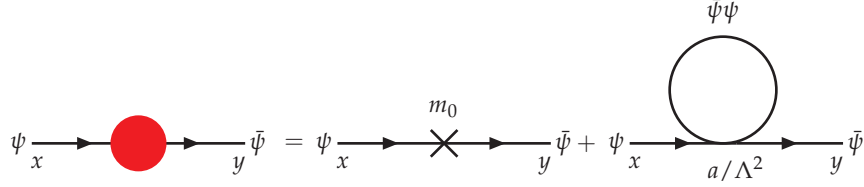
Figure *i*.10: First quantum corrections to the mass of a fermion induced by $a/\Lambda^2(\bar\psi\psi)^2$ terms in the Lagrangian. The loop on the r.h.s. leads to a divergent contribution.

If the theory contains two parameters a and b, consider two observables and calculate their expression in terms of the parameters, $A = A(a,b)$ and $B = (a,b)$, up to the desired precision. These relationships can be inverted, $a = a(A,B)$ and $b = b(A,B)$. Any other quantity can now be expressed in terms of $a = a(A,B)$ and $b = b(A,B)$, so in terms of the physical A and B.

The renormalization procedure can be carried out in a systematic way. Thus, assuming a sufficient number of physical observables is measured to fix the parameters, one can make predictions on the size of new physical observables.

A theory which only contains relevant and marginal operators is called a *renormalizable* theory, because one only needs a finite number of physical observables to fix all the parameters and make predictions to any degree of precision in perturbation theory, whatever the energy. Ideally, given the algorithm generating all the terms in the perturbative expansion, one could resum them and predict the size of any physical observable to infinite precision[17].

A theory with irrelevant operators is instead *non-renormalizable*, in the sense that at each order in the perturbative expansion one needs to fix new parameters, which requires the measurement of new observables. If the scope were to predict the size of a physical observable F with an infinite degree of precision at any energy scale, then a non-renormalizable theory would be useless. Usually however, we are content with calculating the size of F up to a certain degree of accuracy ϵ. In this case the main features of the system can sometimes be described more efficiently by the first few terms of the p/Λ expansion of a non-renormalizable effective theory, especially in the case of a large difference in scales between p and Λ.

i.2.2 Mechanics of renormalization

Consider for example the one-loop quantum corrections to the mass of a fermion depicted in Fig. *i*.10. On the l.h.s. a fermion propagates from x to

---

[17]Experimental errors on the measurements aside.

y with a given kinetic energy and a given physical mass *m*, represented by the red blob in the picture. The physical mass can be extracted from this propagation. On the r.h.s. is the expression of the propagation in terms of Lagrangian parameters, calculated with one quantum-loop correction precision. The first term represents the classical mass term $m_0 \psi \bar{\psi}$, while the second one the quantum correction induced by the irrelevant[18] interaction $a/\Lambda^2 (\bar{\psi}\psi)^2$. The loop correction affects the way the fermion propagates and thus the determination of the physical mass. The size of this correction is given by a/Λ^2 times the integral

$$ m_0 \int \frac{d^4 k}{(2\pi)^4} \frac{1}{k^2 - m_0^2}, \qquad\qquad (i.9) $$

where m_0 is the fermion mass parameter appearing in the Lagrangian. This integral is quadratically divergent as one sends *k* momentum cut-off $\Lambda \to \infty$. The physical mass though can be finite if the contribution from the first diagram cancels the infinity coming from the second one.

Another example is given by Quantum Electro Dynamics (QED). I will consider the electric charge *e* renormalization, or rather the renormalization of $\alpha = e^2/4\pi$ and show how another observable, the scattering amplitude[19] $T_{e^+ e^- \to e^+ e^-}$, can be calculated with one-loop precision and yield sensible finite results once it is expressed in terms of the renormalized α.

The physical scattering amplitude $T_{e^+ e^- \to e^+ e^-}$ is given at one loop order by the sum of the diagrams in Fig. *i*.11, plus a few more that we shall neglect for the sake of the argument. The first diagram describes the $e^+ e^-$ entering on the l.h.s. and coupling to a photon with Lagrangian coupling e_0. The photon propagates and then produces a new $e^+ e^-$ pair. The diagram contains two e_0 parameters, so it is proportional to α. The second diagram describes the same interaction, but this time with a quantum loop correction to the propagator[20] of the photon. This correction is called a vacuum polarization correction, and indicated with $\Pi^{\mu\nu}$.

The integral associated to the loop diverges like $\int d^4 k (1/k^2)$. One way to handle this divergence is to make the integral finite, by integrating only up to a momentum cut-off Λ. This procedure is called *regularization*. Applying a cut-off is not the only way to make the integral finite. The integral can be regularized by dimensional regularization[21], that is performing the calculation in

---

[18]This operator has energy dimension six.

[19]This amplitude squared and summed over phase al possible final particle momenta (and spin) gives the probability that the process $e^+ e^- \to e^+ e^-$ takes place.

[20]The function associated to it's propagation.

[21]The physical predictions are independent of the regularization or renormalization scheme chosen. Dimensional regularization, together with mass-independent renormalization schemes such as minimal subtraction (MS) or $\overline{MS}$, ensures that the regularization does not introduce an artificial breaking of the symmetries of the system. This way, the limit $m \ll \Lambda$ loop corrections are suppressed, while with the cut-off regularization in order to obtain the same results one must
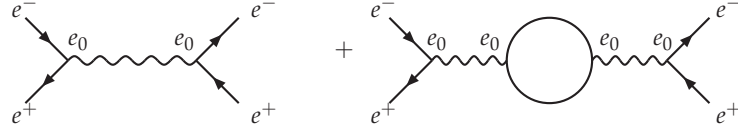
Figure *i*.11: The $e^+e^- \to e^+e^-$ scattering amplitude calculation up to the first quantum corrections, in diagrammatic form. Only one quantum correction diagram is shown

$D = 4 + 2\epsilon$ dimensions. This makes the integral convergent. After all observables are expressed in terms of other physical observables one can get rid of the regularization by sending $\epsilon \to 0$ ($\Lambda \to \infty$).

The vacuum polarization for a photon propagating with momentum q then becomes

$$\Pi^{\mu\nu}(q) = (-q^2 g^{\mu\nu} + q^\mu q^\nu)\Pi(q^2) \qquad (i.10)$$

where

$$\Pi(q^2) = -\frac{4}{3}\frac{\alpha}{4\pi}\mu^{2\epsilon}\left\{\frac{1}{\hat{\epsilon}} + \log\left(\frac{-q^2}{\mu^2}\right) - \frac{5}{3} + O(\epsilon)\right\} \qquad (i.11)$$

and $\frac{1}{\hat{\epsilon}} = \frac{1}{\epsilon} + \gamma_E - \log(4\pi)$ and μ is an arbitrary mass scale. This expression shows two characteristic features of quantum corrections: first, the divergence is given by a simple pole for $\epsilon \to 0$, second the dependence on the scale q^2 is logarithmic. The first implies that one could cancel the divergences by adding to the Lagrangian operators with $\sim \frac{1}{\hat{\epsilon}}$ coefficients[22], i.e *counterterms*. The procedure is not unique, that is, one may decide to not only cancel the divergent part of the quantum contributions but also finite but large ones, which make the convergence of the perturbative expansion slow. Since the splitting of the Lagrangian into an infinite part and a counterterm part is completely arbitrary and non-physical, the result is renormalization procedure independent.

Once $\Pi(q^2)$ has been split into a diverging and a finite piece we

$$\Pi(q^2) = \Pi_\epsilon^{\text{div}}(\mu^2) + \Pi(q^2/\mu^2), \qquad (i.12)$$

calculate the physically observable scattering amplitude $T_{e^+e^- \to e^+e^-}$ drawn in Fig. *i*.11, up to precision one-loop. Its expression in terms of Lagrangian parameters is given by

$$T_{e^+e^- \to e^+e^-}(q^2) = -J^\mu J_\mu \frac{4\pi\alpha_{\text{bare}}}{q^2}\{1 - \Pi(q^2)\}, \qquad (i.13)$$

---

sum over an infinite number of contributions at each order $1/\Lambda$. For this reason one prefers to use the dimensional regularization.

[22]For higher orders one will need $\sim 1/\epsilon^n$ counterterms.

where J^μ is the electromagnetic current. This can however be re-interpreted in terms of a renormalized α. The factor $\alpha_{\mathrm{bare}}\{1 - \Pi(q^2) + \cdots\}$ in Eq. *i*.13 can be split off into a renormalized coupling $\alpha_R(\mu^2)$ and a finite scattering renormalization factor

$$\alpha_{\mathrm{bare}} \left\{ 1 - \Pi_\epsilon^{\mathrm{div}}(\mu^2) - \Pi(q^2/\mu^2) \right\} = \alpha_{\mathrm{R}}(\mu^2) \left\{ 1 - \Pi_{\mathrm{R}}(q^2/\mu^2) \right\} \qquad (i.14)$$

where

$$\alpha_R(\mu^2) = \alpha_{\mathrm{bare}} \left\{ 1 + \frac{\alpha_{\mathrm{bare}}}{3\pi} \mu^{2\epsilon} \left[\frac{1}{\epsilon} + \mathrm{const} + \cdots \right] \right\} \qquad (i.15)$$

and where the constant depends upon the scheme. Once the α is re-defined this way, the scattering amplitude

$$T_{e^+e^- \rightarrow e^+e^-}(q^2) = -J^\mu J_\mu \frac{4\pi\alpha_R(\mu)}{q^2} \{1 - \Pi(q^2/\mu^2)\}, \qquad (i.16)$$

is manifestly finite.

Complications for effective field theories

In the case of a generic effective field theory the situation is complicated by the fact that going to higher orders[23] in the perturbative expansion in powers of p^2/Λ^2, we can have new operators in the Lagrangian and new coupling constants. For instance in ChPT [2, 12], the lowest order (lowest precision) Lagrangian describing the interactions of the pion fields (all collected into the field U) is given by

$$\mathcal{L}_2 = \frac{F^2}{4} Tr[D_\mu U^\dagger D^\mu U] + \frac{F^2}{4} 2B_0 Tr[M^\dagger U + U^\dagger M], \qquad (i.17)$$

with just two operators and two coupling constants[24], F and B_0. Already the first order Lagrangian $\mathcal{L}_4$ [13] contains ten new operators (not considering the last two operators connected to the external fields) and ten new coupling constants $L_1, ..., L_{10}$:

$$
\begin{aligned}
\mathcal{L}_4 =\ & L_1 Tr[D_\mu U^\dagger D^\mu U] + L_2 Tr[D_\mu U^\dagger D^\nu U] Tr[D_\mu U^\dagger D^\nu U] \\
& + L_3 Tr[D_\mu U^\dagger D^\mu U D_\nu U^\dagger D^\nu U] + L_4 Tr[D_\mu U^\dagger D^\nu U] Tr[M^\dagger U + U^\dagger M] \\
& + L_5 Tr[D_\mu U^\dagger D^\mu U (M^\dagger U + U^\dagger M)] + L_6 Tr[M^\dagger U + U^\dagger M]^2 \\
& + L_7 Tr[M^\dagger U + U^\dagger M]^2 + L_8 Tr[M^\dagger U M^\dagger U + U^\dagger M U^\dagger M] \\
& - iL_9 Tr[F_R^{\mu\nu} D_\mu U D_\nu U^\dagger + F_L^{\mu\nu} D_\mu U D_\nu U^\dagger] + L_{10} Tr[U^\dagger F_R^{\mu\nu} U F_{L,\mu\nu}] \\
& + H_1 Tr[F_R^{\mu\nu} F_{R,\mu\nu} + F_L^{\mu\nu} F_{L,\mu\nu} + H_2 Tr[M^\dagger M].
\end{aligned}
\qquad (i.18)
$$

---

[23]Higher precision.

[24]In first approximation F corresponds to the pion decay constant and B_0 gives the size of the chiral symmetry breaking.

For details about the meaning of this Lagrangian see [2, 13].

When we calculate an observable, the new Lagrangians, with their new coupling constants enter the expression according to Weinberg's power counting. For instance at one-loop order, we should consider the tree level diagrams coming from the lowest order Lagrangian $\mathcal{L}_2$ (leading order), then the one-loop diagrams coming from the lowest order Lagrangian and the tree level diagrams coming from the first order Lagrangian

$$\mathcal{L}_2^{\text{tree}} + \mathcal{L}_2^{\text{loop}} + \mathcal{L}_4^{\text{tree}}. \tag{i.19}$$

The $\mathcal{L}_2$ loop diagrams will be divergent and will have to be renormalized by the same-order counterterms, i.e. by the couplings in the $\mathcal{L}_4$ $L_1, ..., L_{10}$.

The situation becomes very rapidly rather involved as one goes to higher orders: when calculating an observable up to second order in the perturbative expansion, corresponding to a two-loop expansion, the power counting states that one should take

- tree level diagrams from the lowest order Lagrangian, $\mathcal{L}_2$,
- one-loop diagrams from the $\mathcal{L}_2$ and tree level diagram from the $\mathcal{L}_4$,
- two-loop diagrams from the $\mathcal{L}_2$, one-loop diagrams from the $\mathcal{L}_4$ and tree level diagrams from the $\mathcal{L}_6$.

With so many contributions coming from the various operators in the different Lagrangians it is not trivial to understand how quickly does the perturbative expansion converge. Some indications can come from the series of the leading logarithms,

$$O_0 + (O_1^1 L + O_2^2 L^2 + O_3^3 L^3 + \cdots), \tag{i.20}$$

where L^n stands for $(\log)^n$. As discussed above, these logarithms arise when one calculates higher order corrections to an observable and describe the scale dependence of the higher order correction. The leading logarithm at order n in the perturbative expansion is $(\log)^n$.

The reason why one concentrates on the leading logarithmic series is that the coefficients of the series are constrained by renormalization group equations (RGE) to be a function of the lowest order Lagrangian parameters only [7, 14], that is, they do not depend upon the higher order Lagrangian coupling constants. The leading logarithmic series are the focus of the first two papers in this thesis.

i.3   Hidden Valley: a new light sector

Rom: The kemocite! If we vent plasma from the warp core into the cargo hold,
we may be able to start a cascade reaction in the kemocite. Then we can modulate
the reaction to create an inversion wave in the warp field and force the ship back
into normal space. If I time it just right, I should be able to get us close enough to
Earth to make an emergency landing.
Quark: Rom! You're a genius!
Rom:: Think so?
Quark: How should I know? I have no idea what you're talking about.

"Star Trek: Deep Space Nine" (1995)

In Section *i*.1 I discussed some of the unsolved issues with the Standard Model and suggested that it may need to be extended. No one knows what this extension should be. The slide in Fig. *i*.12 is taken from a recent conference talk[25] and shows a small part of the Standard Model extensions concerning the Higgs boson.

As pointed out in the same section though, new physics models are severely constrained by SM phenomenology, masses in particular. For example for new charged leptons the PDG[26] gives a lower bound $m_{L^{\pm}} < 100.8$ GeV. For the leptoquarks predicted by quark-lepton unification theories it gives a lower bound of $m_{LQ} < 136$ GeV for the scalar leptoquarks and of $m_{LQ} > 200$ GeV for the vector ones [15]. The bound on top partners, such as the ones depicted in Fig. *i*.9, are even more stringent, it is usually assumed that they have masses around 1-5 TeV [16].

These constraints can be evaded though if the effective coupling of the new particles to the Standard Model ones is suppressed for some reason, for instance because of an energy barrier or because Standard Model and new particles only communicate via a very large mass particle, via a very small gauge boson coupling or via quantum loop suppressed interactions. This is what happens the Hidden Valley models [17]. In these models the SM sector and a new secluded sector are both light, in the sense that they both contain $O(1\text{GeV})$ mass particles. Ordinarily, that is for energies well below the SM cut-off scale $p \ll \Lambda_{SM} \sim$ TeV, the two sectors hardly have any interactions. However, as SM colliders gain access to higher energies, they may be able reach the threshold for producing new massive "communicator" particles, particles which can interact with both SM and hidden sector. Figure *i*.13 shows a cartoon of hidden valley models. The two valleys representing the Standard Model sector and the new secluded sector are separated by an energy barrier, represented by the

---

[25]Courtesy of C. Grojean.
[26]Particle Data Group [11].
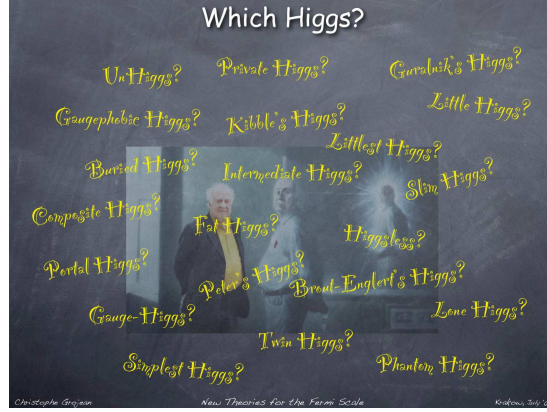
Figure *i*.12: A slide presented at a recent talk. Some of Standard Model extensions proposed to solve the Higgs mass problem.

crest. An accelerator like LEP (Large Electron-Proton collider) would not have had enough energy to go over the barrier, but LHC, with its 14 TeV, could have enough energy to do so. The barrier in the picture could for instance represent the communicator's heavy mass. A typical example of communicator is the Z' in the electron- positron annihilation process $e^+e^- \rightarrow Z' \rightarrow q_v\bar{q}_v$, in which SM particles annihilate to produce the Z', which then decays into new light particles called valley-quarks. This is the communicator used in the first hidden valley scenario that was studied [17]. Another example of communicator is given by new Higgs-like scalars.

Similar hidden valley models are compatible with many Beyond Standard Model (BSM) theories, unparticle scenarios [18], Super Symmetric models [19], just to mention some. The reason why so different SM extensions can all display Hidden Valley features is that the Hidden Valley, being a light sector, is itself the low energy limit of the underlying higher energy theory. The dynamics at these low energies does not depend upon the details of the dynamics at high energies.

In the original paper by Strassler and Zurek [17], the valley quarks are subject to a strong force similar to QCD, which ensures the confinement of the q_vs into v-hadrons, with masses around the confinement scale Λ_v [27]. Heavier v-hadrons can decay down to the lowest lying states at the bottom of the valley. Some of these low energy states may be stable v-pions (making for good DM candidates[28]), while others may decay/tunnel back into the visible SM sector

---

[27] Just as in the QCD case, in this case Λ_v indicates a lower boundary on the theory, below which perturbation theory is no longer valid.

[28] A requisite of a good DM candidate is that it should be stable and only interact ultraweakly
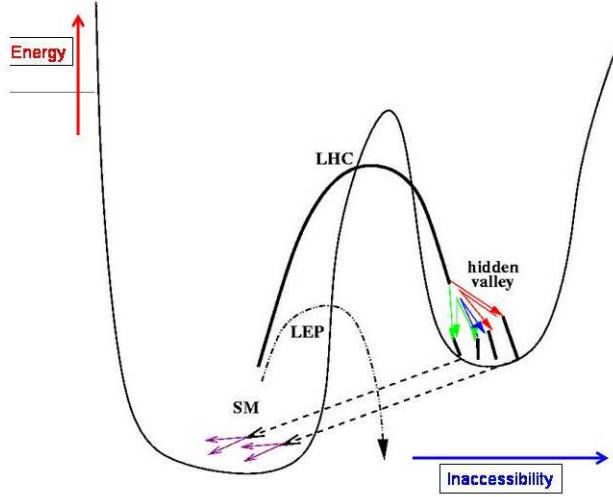
Figure *i*.13: Cartoon for Hidden Valley models. One valley corresponds to the SM particles and is separated from the adjoining valley representing the hidden sector by a barrier (a crest). At ordinary energies, i.e. below TeV scales, the standard sector and the hidden one are secluded. There are hardly any interactions between SM particles and Valley ones. This was the situation observed by LEP for instance. LHC however might have a large enough center of mass energy to reach the threshold and produce a communicator particle, that is to go over the crest, and gain access to the hidden valley. The communicator would then eventually cascade down into the bottom of the hidden valley producing large number of valley particles, some of which could tunnel back to the Standard valley.

and affect SM particle distributions.

In papers III and IV we have analyzed these spectra in hopes of

- detecting hidden valley radiation,
- distinguishing different valley sector symmetry structures.

Hidden valleys are an ideal terrain to address the question of detecting a new source of radiation, because of the large mass disparity between the communicator and the lowest lying v-states. The large mass difference implies that when a communicator decays into a hidden valley quark, q_v has a large kinetic energy, which can lead to the radiation of numerous hidden sector gauge bosons. On the other hand, hidden valleys are not necessarily the ideal models to distinguish different gauge symmetry structures, because, as remarked above, many different higher energy structures may appear to have

---

with Standard particles.

the same low energy phenomenology.

In order to study the effects of the hidden radiation onto the SM particle distributions, Torbjörn Sjöstrand and I have implemented some new tools in a Monte Carlo event generator PYTHIA 8 [20].

i.3.1   Monte Carlo event generators for Hidden Valley models
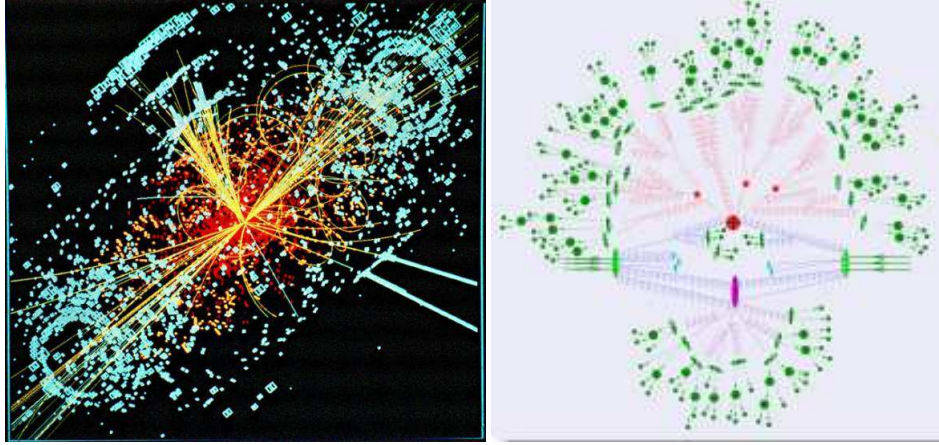
Figure *i*.14: Events are very chaotic environments, on the left is a picture of an event in the CMS (Compact Muon Solenoid) detector in LHC. On the right is a cartoon of the outcome of a simulation of a *pp* collision with an event generator.

The reason why we need to use a random event generator to study hidden valley phenomenology is that the particle colliders where we look for hidden valley signals are very chaotic environments. The QCD interactions especially generate large amounts of soft (low energy) particles, see Fig. *i*.14. In such a busy environment it is crucial to be able to separate the signal from the background noise. Event generators are essential tools for the understanding of both the background and the signal, as shown in Fig. *i*.15.

They connect matrix elements calculated from the Lagrangian, to the particle distributions observed in detectors, such as angular distributions of the particles, momentum distributions. They are particularly useful to connect the high-energy quarks, which the perturbative calculation is based upon, to the low-energy hadrons.
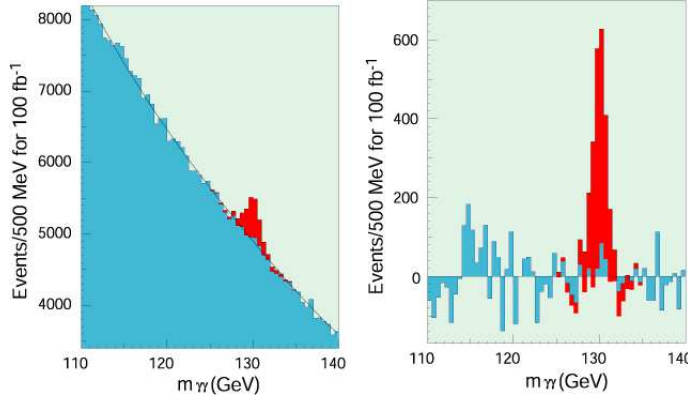
Figure *i*.15: An example of the importance of background subtraction. Distribution of the two photon invariant mass after the accumulation of a 100 fb^{-1} of data. The red histogram corresponds to the Higgs signal (Higgs mass of 130 GeV is assumed) and the blue histogram represents all the backgrounds. Left and Right plots represent before and after background subtraction.

Event simulation

PYTHIA is an event[29] generator used to simulate events at e^+e^-, pp and $p\bar{p}$ colliders, like CLIC[30], LHC and Tevatron. The scope of the program is to connect the high energy interactions[31] with the lower energy hadronic jet distributions observed in the detectors.

In these simulations each event can be in first approximation decomposed into steps, as described in the cartoon in Fig. *i*.16.

- Two elementary particles are selected from the colliding beams, e^+e^- in the case described in Fig. *i*.16, or two partons (quarks or gluons), in the pp collision case in Fig. *i*.17. In this latter case each parton only carries a fraction x of the overall momentum of the proton it comes from.

- Each particle can emit radiation, called *initial state radiation* (ISR). Electrons will emit photons, while quarks will emit gluons. In the process the particle loses energy and momentum. Each radiated photon or gluon can emit two quarks or two leptons if it has enough kinetic energy. These can in turn emit new radiation. The whole process rapidly gives rise to a shower of particles.

---

[29]At a collider the term event indicates everything that happens after the collision of two particles, down to the final distributions observed in the detectors.

[30]Compact Linear Collider, currently under design at CERN.

[31]More precisely the matrix elements (ME) one would like to reconstruct.
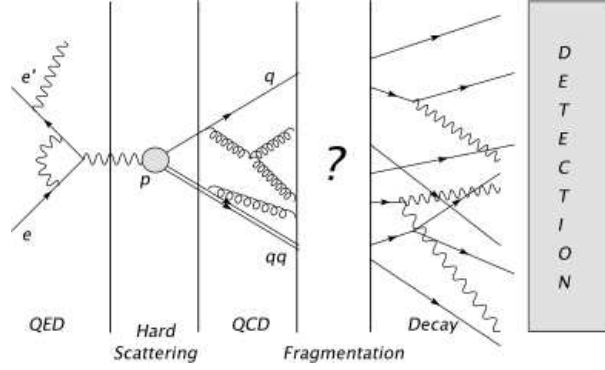
Figure *i*.16: Cartoon of the various stages of the simulation of a collision, collectively called event: from the production from e^+e^- colliding, possibly radiating a photon before they collide, and annihilating into $\gamma^\star/z'$, pair producing particles (hard interaction), through QCD final state radiation, fragmentation/hadronization, decay and detection.

- The two particles interact. This part is called *hard interaction*[32].
- Each interaction product can subsequently emit *final state radiation* (FSR).
- All color-charged particles *hadronize* and can produce jets.
- Unstable particles decay into lower mass ones.

The key underlying assumption, that allows us to follow this time sequence in the Monte Carlo simulation, is that the hard interaction happens at a scale close to the collider center of mass energy $\sqrt{s}$, while the hadronization happens at a scale $\Lambda \lesssim 1$ GeV, the energy scale at which the QCD coupling α_s becomes strong. From $\Delta E \Delta t \geq 1$, we then know that there is a high probability that the hard interaction takes place at time-scale $\sim 1/\sqrt{s}$, while the hadronization takes place at a much later time scale $\sim 1/\Lambda$. In between the hard interaction energy[33] scale Q^2 and the hadronization scale Λ, one can use perturbation theory to calculate the probability that a gluon emission takes place using QCD Feynman diagrams. This probability diverges for soft and/or collinear emissions. After quantum corrections are taken into account, the divergences are cancelled, but the probability in still enhanced compared with harder and/or non-collinear emissions[34]. This implies that, if particles are radiated, they most likely will be soft and/or nearly parallel to the emitter. Each radiated g/γ only causes a small change in the energy and momentum of the emitter. Neither is the flavor of a particle changed by an emission. Thus

---

[32]The expressions hard and soft are synonyms for high and low energy.
[33]More properly, virtuality scale.
[34]This remains true for QED photon emissions.
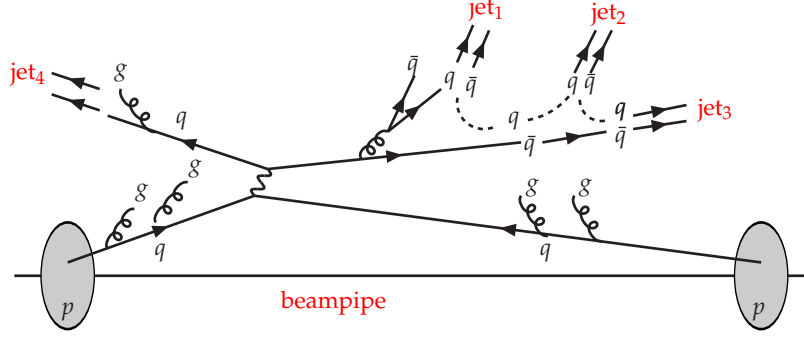
Figure *i*.17: The collision of two protons, from which two partons are extracted, each with momentum fractions x_1 and x_2. The partons each radiate ISR, then at the scale $Q^2_{\max}$ they have the hard interaction, from which two new particles emerge. The new particles emit FSR. As the particles reach the scale Λ hadronization starts. New $Q\bar{Q}$ pairs are produced from the vacuum and give rise to $q\bar{Q}$ mesons and/or qqQ barions. These boosted sprays of hadrons called jets are finally observed in the detectors.

the structure of the hard interaction products is approximately conserved even after the emission of the radiation. If the hard interaction was described by a $2 \rightarrow 2$ body interaction, most probably the outgoing particle distributions will appear pencil-like in the detector, with the two jets nearly back-to-back along the direction of the original two particles coming out of the hard interaction. A much smaller fraction of events will have three and four jets. In this way we can reconstruct the hard interaction starting from the jet distribution.

Of course when the instable particles decay, the decay products can be boosted in the same direction of the instable particle and be clustered in the same jet, but they can also decay isotropically (especially if they have low kinetic energy) around the direction of the mother particle.

The picture is also much complicated by multiple parton-parton interactions in the same pp collision, initial and final state radiation interacting, color-charged particles interacting with the beam remnants.

Monte Carlo

As described above, the parton shower consists of a particle successively emitting radiation. The parton repeatedly loses energy and momentum and evolves from a maximum kinetic energy and momentum, fixed by the hard interaction, down to lower energy and momentum [35]. This iterative process

---

[35]For clarity I only discuss the time-like shower (FSR), similar arguments apply for the space-like shower (ESR).

of a particle branching into a particle plus radiation is very well suited for computer implementation. The process is however not deterministic, in the sense that we do not know if/when a given parton will radiate, we can only calculate the probability that it will. To introduce this probabilistic component into the simulation we use a Monte Carlo method. We have the computer select a random number R between 0 and 1, and then compare the number with the probability of having an emission at scale Q_1 and then evolving from scale Q_1^2 to scale Q_2^2 without any emission. This way one can extract the scale of the next emission with the correct probability distribution.

One key ingredient is the calculation of the emission probability. In general the probability of a single emission will be proportional to the strong coupling $\alpha_s < 1$. Two emissions will be suppressed by a factor α_s^2, and in general the probability of having multiple emissions will be small. In the case of soft and collinear emissions though, the probability is enhanced compared with the hard and/or large angle emission case. If one sums up many contributions from this kinematic region the overall probability can turn out to be substantial. The final state parton shower program then takes into account all the possible emissions of partons from this soft and collinear region. The calculation is greatly simplified by taking into account only the leading contributions to the probability surviving in the limit $E, \theta \to 0$, where E is the energy of the radiated particle and θ the angle between the radiator and radiated momenta.

For example, the QCD probability for $e^+ e^- \to q\bar{q}g$ calculated with Feynman diagrams is proportional to

$$\frac{\alpha_s}{2\pi} \frac{x_1^2 + x_2^2}{(1 - x_1)(1 - x_2)}, \tag{i.21}$$

where $x_i = 2E_i / \sqrt{s}$ are the energy fractions of the outgoing quarks. As one may see, it is divergent when either of the $x_i \to 0$. In the approximate approach described above, the gluon emission can be interpreted as a two step process, $e^+ e^- \to q\bar{q}$ followed by $q \to qg$. If the q takes a fraction z of the energy and g takes $(1 - z)$, the probability that at the scale Q^2 the parton emits a gluon with energy fraction $(1 - z)$ is given by

$$dP = \frac{dQ^2}{Q^2} C_F \frac{\alpha_s}{2\pi} \frac{1 + z^2}{1 - z} dz, \tag{i.22}$$

where C_F is the Casimir factor[36] In order to obtain the probability that at the scale Q^2 one has a first emission, this probability should be multiplied by the probability that there was no prior emission, the so-called Sudakov factor.

Starting from these elements one can implement a cascade evolution. Each q and $\bar{q}$ emerging from the hard interaction, is individually evolved down-

---

[36]Dependent on the number N_c of quark colors, for QCD $N_c = 3$.

wards from some initial Q_1^2 to the scale Q_2^2 of the next branching, where the mother parton is replaced by its daughter partons and the process is repeated.

Hidden Valley showers
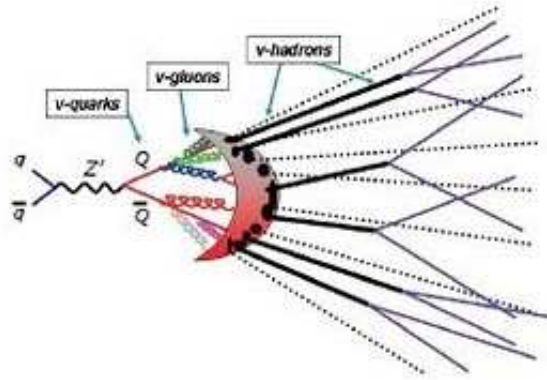
Figure *i*.18: Carton of the hidden dynamics. The new valley-quarks shower v-gluons until the hadronization scale is reached. The hadronization (represented by the shield in the picture, turns the partons into valley-pions, v-Ks and into v-hadrons in general.(Courtesy of M. Strassler)

If instead of standard model partons the hard interaction produces pairs of valley-quarks, the parton showers ought to be modified, so that the different types of gauge bosons can be emitted (as depicted in Fig. *i*.18). The probability to radiate must be adjusted to take into account the fact that the gauge boson may be massive and has different Casimir factors[37]. If the matter sector in the hidden valley contains both heavy and light v-quarks, the matrix elements[38] for the radiation must also be modified to take into account the mass difference.

A second modification of the shower algorithm accounts for the fact that in some models the communicator is charged under both the SM and the valley gauge group, so it can simultaneously emit SM and new gauge bosons, during a common shower evolution.

Finally, if the new sector is confining then one must also modify the hadronization routines, so that the valley quarks hadronize into π_v, K_v and more massive v-hadrons, as depicted in Fig. *i*.18.

---

[37]Which depends upon the number of v-colors.
[38]Proportional to the probability.

Hidden Valley particle decays

Many hidden valley models involve a mechanism allowing v-particles to decay back into SM particles. The mechanisms are model dependent, however one may divide them in three classes. Those in which the hidden radiation couples directly to the standard one, those in which first v-pions are formed and then the pions decay back into the standard model sector, those in which the some v-quarks decay directly into the SM, before the v-hadronization.

All these possibilities require an *ad-hoc* implementation in the event generator.

i.3.2   Hidden valley event analysis

With these tools at hand one can generate valley events and study the collider phenomenology.

One of the greatest advantages of an analysis of simulated events compared with a real analysis of experimental data, is that in the simulation one can isolate the different effects and determine the cause of a certain behaviour of the distribution. One can also tune the model parameters so as to give more relevance to certain features rather than others.

Depending upon the collider and detector resolution, the first distributions one could study when looking for hidden particles are missing energy and momentum, angular distribution, event shapes, transverse momentum p_T distributions. Any significant deviation from the expected SM distributions will be a signal for beyond Standard Model physics. The issue, once one such signal is found, will be to understand *which* standard model extension causes the deviation.

i.4   Introduction to papers

i.4.1   Paper I

In paper I we exploit the Büchler-Colangelo algorithm [14] to calculate the Leading Logarithmic corrections to the pion mass, in the massive $O(N + 1)/O(N)$ non-linear sigma model. We calculate the corrections up to order five loops for the generic number of flavors N, and use the results to study how each higher order correction scales with energy and to estimate the convergence of the perturbative expansion. The results are particularly interesting in the $N = 3$ flavor case, which corresponds to 2-flavor Chiral Perturbation Theory. We calculate the mass to such a high degree of precision in hopes to find a pattern in the Leading Logarithm coefficients, in order to resum the series. We do not recognize the pattern in the generic N coefficients, however, we manage to solve the problem of resumming the whole series of perturbative corrections to the mass in the large N case.

i.4.2   Paper II

Paper II is an extension of the analysis performed for paper I. We apply the same principles to scattering amplitude, decay constant, vacuum expectation value, scalar and vector form factors. For each of these observables we derive the finite number of flavor N expressions for the Leading Log coefficients and the all loop order resummed expressions for the large N limit. We study how the higher-order corrections scale with energy, and how the series converge as a function of the physical mass and decay constant, or as a function of the Lagrangian parameters.

i.4.3   Paper III

Paper III is a first attempt to determine the collider signatures of hidden valley radiation. We construct a toy model based on a valley $SU(N)$ color group, with fermions charged under both standard and valley interactions, and we implement it in PYTHIA 8 to generate valley events. We concentrate our study of the phenomenology on the impact of the $SU(N)$ hidden radiation on the standard model particle kinematic distributions. The analysis is a comprehensive parton-level study of these signatures at e^+e^-, LHC at 7 TeV and LHC 14 TeV.

i.4.4   Paper IV

Paper IV addresses the issue of distinguishing between different secluded sector gauge symmetry structures. The tools implemented for our prior study

are extended to comprehend different setups, so as to make the results of phenomenological analysis as model independent as possible. In particular the new set-ups comprehend a broken $\not{U}(1)$ and a confining $SU(N)$. New tools include hidden sector fragmentation and hadronization and effective decays of hidden sector particles to Standard Model particles through kinetic mixing. The analysis we perform is limited to e^+e^- collider phenomenology, because it is easier to isolate the features connected to the gauge structures. We illustrate the the differences between abelian and non abelian distributions through the study of six different setups. We find that a number of distributions give very different results. Even if we tune the paramters in such a way as to have the same number of secluded sector particles decaying back into the standard model, we find a very sizable difference in the jet angular distributions.

i.4.5 List of contributions

- **Paper I:** The ideas in this paper came from my supervisor. In order to actually perform the calculation we also had to rely heavily on the previously developed FORM programs. I reproduced independently all the results. The paper was written together by my supervisor and myself.
- **Paper II:** This is a follow up to the previous paper. Again, my supervisor and I performed the calculations separately and compared the results. The paper was written together by my supervisor and myself.
- **Paper III:** The idea for the paper was developed by myself and Peter Skands. The model implementation was done by Törbjorn Sjöstrand, while the analysis was performed together. I also contributed with some insight on theoretical tools for the analysis. The paper was written together by Törbjorn Sjöstrand and myself.
- **Paper IV:** This paper expands some of the ideas that had emerged during the previous study. In this case I had a more active part in the calculations required by the PYTHIA 8 implementation, some of the new tools however still required Torbjörn Sjöstrand's expertise. I had a large part in the decision making about the models to be studied and in their analysis. The paper was a joint effort. I had constant feedback from both Torbjörn Sjöstrand and Johan Rathsman on the calculations, analysis, the theoretical issues associated with the models and writing.

i.4.6 Copyright information

- Fig. *i*.2 and Fig. *i*.2 © CERN / Science & Society
- Fig.*i*.14 and Fig. *i*.15 © CERN 2008-2011 - CMS Outreach

Acknowledgments

i References

[1] G. L. Kane, *Modern Elementary Particle Physics*. Westview Press, 1993.

[2] J. F. Donoghue, E. Golowich, and H. B. R., *Dynamics of the Standard Model*. Cambridge Monographs on Particle Physics, Nuclear Physics and Cosmology. Cambridge University Press, 1994.

[3] M. E. Peskin and D. V. Schroeder, *An Introduction To Quantum Field Theory*. Westview Press, 1995.

[4] D. B. Kaplan, "Effective field theories," `arXiv:nucl-th/9506035`.

[5] A. V. Manohar, "Effective field theories," `arXiv:hep-ph/9606222`.

[6] A. Pich, "Effective field theory," `arXiv:hep-ph/9806303`.

[7] S. Weinberg, "Phenomenological Lagrangians," *Physica* **A96** (1979) 327.

[8] H. Leutwyler, "On the foundations of chiral perturbation theory," *Ann. Phys.* **235** (1994) 165–203, `arXiv:hep-ph/9311274`.

[9] J. Gribbon, "Dark matter and the universe," *Science* **March** (1994) .

[10] S. P. Martin, "A Supersymmetry Primer," `arXiv:hep-ph/9709356`.

[11] **Particle Data Group** Collaboration, K. Nakamura *et al.*, "Review of particle physics," *J. Phys.* **G37** (2010) 075021.

[12] G. Ecker, "Chiral perturbation theory," *Prog. Part. Nucl. Phys.* **35** (1995) 1–80, `arXiv:hep-ph/9501357`.

[13] J. Gasser and H. Leutwyler, "Chiral Perturbation Theory to One Loop," *Ann. Phys.* **158** (1984) 142.

[14] M. Buchler and G. Colangelo, "Renormalization group equations for effective field theories," *Eur. Phys. J.* **C32** (2003) 427–442, `arXiv:hep-ph/0309049`.

[15] **D0** Collaboration, V. M. Abazov *et al.*, "Measurement of the ratios of the Z/G* + ≥ n jet production cross sections to the total inclusive Z/G* cross section in ppbar collisions at sqrt(s) = 1.96 TeV," *Phys. Lett.* **B658** (2008) 112–119, `arXiv:hep-ex/0608052`.

[16] N. Arkani-Hamed, A. G. Cohen, E. Katz, and A. E. Nelson, "The littlest Higgs," *JHEP* **07** (2002) 034, `arXiv:hep-ph/0206021`.

[17] M. J. Strassler and K. M. Zurek, "Echoes of a hidden valley at hadron colliders," *Phys. Lett.* **B651** (2007) 374–379, `arXiv:hep-ph/0604261`.

[18] M. J. Strassler, "Why Unparticle Models with Mass Gaps are Examples of Hidden Valleys," `arXiv:0801.0629 [hep-ph]`.

[19] M. J. Strassler, "Possible effects of a hidden valley on supersymmetric phenomenology," `arXiv:hep-ph/0607160`.

[20] T. Sjostrand, S. Mrenna, and P. Z. Skands, "A Brief Introduction to PYTHIA 8.1," *Comput. Phys. Commun.* **178** (2008) 852–867, `arXiv:0710.3820 [hep-ph]`.

i

I

Leading Logarithms in the Massive $O(N)$ Nonlinear Sigma Model

Johan Bijnens and Lisa Carloni

Department of Theoretical Physics, Lund University,
Sölvegatan 14A, SE 223-62 Lund, Sweden

I

We review Büchler and Colangelo's result that leading divergences at any loop order can be calculated using only one-loop calculations and we provide an alternative proof. We then use this method to calculate the leading divergences of and thus the leading logarithmic corrections to the meson mass in the massive $O(N)$ nonlinear sigma model to five-loop order. We also calculate the all-loop result to leading order in the large N expansion by showing that only cactus diagrams contribute and by summing these via a generalized gap equation.

I.1   Introduction

In a renormalizable theory the use of Renormalization Group Equations (RGE) is common practice. RGEs have not yet received the same attention in non renormalizable effective theories. This is partially due to the fact that one does not normally have the problem of evolving coupling constants through a large energy range, and partially to the fact that RGEs in non renormalizable theories get more complicated as one goes to higher orders. Loop corrections however can be significant [1–3] and need to be dealt with.

Consider for example the scattering length a_0^0 in $\pi\pi$ S-wave, $I = 0$ scattering in ChPT. Close to threshold, this amplitude may be expressed in terms of the expansion parameter $(M_\pi/4\pi F_\pi)^2 \sim 0.01$. Despite the smallness of the expansion parameter, the one loop contributions cause a 28% corrections to the tree level prediction [4]. The reason for this is that beyond tree level the expressions for observables contain non-analytic functions [5] such as $M^2 \log M^2$ which may be large if M^2 is small, even near threshold. It is only natural then to wonder about the size of higher order n contributions like $(M^2 \log M^2)^n$, the so called leading logarithms, and about the size of their coefficients.

In a renormalizable theory these coefficients are fully determined by a one-loop calculation. This is a consequence of the RGEs The difference between a renormalizable and a non-renormalizable theory is that in the first case the counterterms needed at any given order have the same form, while in the latter case new ones are needed at every order. Nevertheless, one can still make predictions on the leading logarithms. This fact was first pointed out by Weinberg [1] in the context of Chiral Perturbation Theory (ChPT). He showed that at two loops the coefficient of leading logarithm $(M^2 \log M^2)^2$ can be determined simply by performing a one-loop calculation.

This method has since been used in ChPT [1–3] to two loop order in $\pi\pi$ scattering [6] and in general [7]. It is no longer much used in the purely mesonic sector, since most processes are actually fully known at two-loop order as reviewed in e.g. [8].

In the last few years though, Weinberg's argument has received new attention [9–13], especially since Büchler and Colangelo were able to generalize the result to all orders [9]. They showed explicitly that one can obtain the (coefficient of the) leading logarithm at any order by simply performing one-loop calculations and that this coefficient is just a function of the lowest order coupling constants. The relevant part of their paper [9] and their algorithm to find the coefficients is described in Sect. I.2.

In Section I.2.3 we provide an alternative proof of their results which does not rely explicitly on β-functions but follows directly from the fact that all non-local divergences must cancel. This version of the proof has the benefit that it shows immediately that one only needs to calculate the divergent part

without worrying about classifying higher order Lagrangians and that there is a direct link between divergences and leading logarithms.

We then apply this method to the case of a *massive $O(N)$* non-linear sigma model and calculate the corrections to the meson mass up to five loops. Sect. I.5 contains a detailed explanation of our calculation. Similar calculations have been performed by [12,13] who showed how to obtain the leading logarithms in the massless case by deriving a recursion relation for all possible vertices with up to four mesons. Since in the massless limit the tadpoles vanish, this allows obtain the leading logarithms in a straightforward fashion.

The authors of [10] instead calculated the two-point function up to five loops in ChPT in the chiral limit using dispersive methods[1]. Once the first five leading logarithms where known, the next step was finding an algorithm that would allow them to calculate the n-th order one and eventually to resum the series. In paper [11] they considered a *linear sigma* model and compared the correlator leading logarithms they found with those from ChPT, both in the chiral limit. They showed that it is not possible to simply use RGEs in the linear sigma model to resum the chiral logarithm series. The two scales present in the linear sigma model both generate logarithms that cannot be disentangled.

We are however able to calculate the the five-loop meson mass in the *massive non-linear* case. What allows us to obtain these results is the observation that while one needs a *complete* Lagrangian to any order, this does not have to be *minimal* (see Sect. I.2.2), nor does one need its explicit form in terms of chirally invariant operators. This, combined with the power of FORM [14], allows us to calculate the relevant parts to five-loop order for the meson mass.

A calculation of this magnitude needs as many checks as possible to ensure that no mistakes are made. We use two main checks. We perform the calculations in different parametrizations of the $O(N)$ nonlinear sigma model. Since different parametrizations distribute contributions very differently over the the various Feynman diagrams, the agreement provides a rather stringent check. Another check is that the leading term in N agrees with the result of the large N expansion of the model.

To the best of our knowledge, this is the first time a study of the massive $O(N)$ is performed in this limit, whereas there is a vast literature on large N in the massless case, especially for the linear sigma model, see [15] and papers citing it.

We solve the mass in the $O(N)$ model in a fashion similar to that often used in the Nambu-Jona-Lasinio model, see [16] and references therein. We first proof that only "cactus" diagrams contribute and that they can all be recursively generated by an equation for the exact propagator, a generalization of

---

[1]In the same paper the authors also calculate the dispersive part of the three-loop pion form factor.

the usual gap equation. Finally, we are able to find a compact implicit expression for the all-loop physical mass. A thorough explanation of the study can be found in Section I.4.

This paper is organized as follows. In Sect. I.2 we discuss the results of [9] (Sect. I.2.1) and use their proof to show that one does not need a minimal nor a fully symmetrically formulated Lagrangian at higher orders (Sect. I.2.2). Sect. I.2.3 provides an alternative proof of the results of [9]. Sect. I.3 defines the $O(N)$ nonlinear sigma model and the different parametrizations that we use. Section I.4 discusses the large N case to all orders. The calculation of the leading divergences for the mass to five-loop order in the general case is described in Sect. I.5, there we also give the result of the calculation. Sect. I.6 summarizes our main results. The way we perform the integrals is described in App. I.7.

I.2 Renormalization group arguments

I.2.1 The equations for the divergences

This subsection recapitulates the parts of [9] we will use. We use dimensional regularization with $d = 4 - w$. The Lagrangians can be ordered in an expansion in $\hbar$. We denote the lowest order Lagrangian with $\mathcal{L}_0$.

$$
\begin{aligned}
\mathcal{L}^{\text{bare}} &= \sum_{n \geq 0} \hbar^n \mathcal{L}_n^{\text{bare}}, \\
\mathcal{L}_n^{\text{bare}} &= \frac{1}{\mu^{nw}} \left(\mathcal{L}_n + \mathcal{L}_n^{\text{div}} \right).
\end{aligned}
\tag{I.1}
$$

The divergent part contains the inverse powers of w needed for the subtraction of the loop divergences at order n [2].

We now expand each term into a set of N_n operators $\mathcal{O}_i^{(n)}$:

$$
\begin{aligned}
\mathcal{L}_n &= \sum_{i=1}^{N_n} c_i^{(n)} \mathcal{O}_i^{(n)}, \\
\mathcal{L}_n^{\text{div}} &= \sum_{i=1}^{N_n} \left(\sum_{k=1}^{n} \frac{\mathcal{A}_{ki}^{(n)}}{w^k} \right) \mathcal{O}_i^{(n)}.
\end{aligned}
\tag{I.2}
$$

One key difference between a renormalizable Lagrangian and these is that here the minimal basis of operators $\mathcal{O}_i^{(n)}$ grows with n. In the remainder, we will assume that all one particle irreducible diagrams (1PI) are made finite

---

[2]When comparing with ChPT one should remember that our order $\hbar^n$ corresponds to the order p^{2n+2} in ChPT.

separately. This simplifies the calculations and arguments. That this can always be done is discussed in [9]. We have already used here, in the expression of $\mathcal{L}_n^{\mathrm{div}}$, the fact that all divergences are local. The $c_i^{(n)}$ are usually referred to as Low-Energy-Constants (LECs).

The bare Lagrangian is μ independent. This leads to the equations

$$
\begin{aligned}
0 &= \mu \frac{d}{d\mu} \mathcal{L}_n^{\mathrm{bare}} \\
&= \frac{1}{\mu^{nw}} \sum_{i=1}^{N_n} \mathcal{O}_i \left[-nwc_i^{(n)} + \mu \frac{d}{d\mu} c_i^{(n)} + \sum_{k=1}^{n} \left(-nw + \mu \frac{d}{d\mu} \right) \frac{\mathcal{A}_{ki}^{(n)}}{w^k} \right].
\end{aligned}
\tag{I.3}
$$

These must be fulfilled separately for each n, i and inverse power of w. We define the β functions via

$$
\mu \frac{d}{d\mu} c_i^{(n)} = \beta_i^{(n)} + nwc_i^{(n)}.
\tag{I.4}
$$

The RGEs of (I.3) thus become

$$
\beta_i^{(n)} + \sum_{k=1}^{n} \left(-nw + \mu \frac{d}{d\mu} \right) \frac{\mathcal{A}_{ki}^{(n)}}{w^k} = 0.
\tag{I.5}
$$

The $\mathcal{A}_{ki}^{(n)}$ do not depend explicitely on the μ. They do, however, depend upon the $c_i^{(n)}$, since they must cancel the divergences stemming from the loops of the lower order Lagrangians. We can thus simplify (I.5) to

$$
\beta_i^{(n)} + \sum_{k=1}^{n} \left[-nw + \sum_{m,j} \left(mwc_j^{(m)} + \beta_j^{(m)} \right) \frac{\partial}{\partial c_j^{(m)}} \right] \frac{\mathcal{A}_{ki}^{(n)}}{w^k} = 0.
\tag{I.6}
$$

The loop contributions must be polynomials in the coupling constants $c_i^{(m)}$. It follows that $\mathcal{A}_{ki}^{(n)}/w^k$ must also be a polynomial. This means that we can split (I.6) further into separate equations. It must be true for each power in w, but also for each $c_i^{(n)}$ monomial, since these are independent parameters and can, in principle, be varied freely. The coefficient of each separate monomial in the $c_i^{(n)}$ in (I.6) then must vanish separately. It is this extra information that allows us to obtain all the leading divergences from one-loop calculations [1, 9].

The powers of $\hbar$ in any diagram come from two places, a factor $\hbar^l$ comes from the number of loops l and the remainder from the $\hbar^n c_i^{(n)}$ present in the diagrams when vertices with $\mathcal{O}_i^{(n)}$ occur. This shows that each monomial in the $c_i^{(n)}$ will also come from a well specified loop level.

I

Let us write out the various equations for the first few orders. To order $\hbar$, we only get the equations

$$\beta_i^{(1)} - \mathcal{A}_{1i}^{(1)} = 0 \,. \tag{I.7}$$

There is no dependence on any of the higher order LECs. We now introduce a notation for the LEC dependence. For both $\beta_i^{(n)}$ and $\mathcal{A}_{ki}^{(n)}$ we add a subscript l indicating the loop level it came from and an argument indicating its polynomial dependence on the $c_j^{(m)}$. In order to simplify notation in the following we shall omit the i index, so that now $\beta_i^{(n)}$ and $\mathcal{A}_{ki}^{(n)}(j)$ become $\beta_l^{(n)}(j)$ and $\mathcal{A}_{lk}^{(n)}$, but one should remember throughout the calculation that we are always speaking about the component β_i^n or $\mathcal{A}_{lki}^{(n)}$. At one loop this only adds a subscript 1

$$
\begin{aligned}
\beta^{(1)} &\rightarrow \beta_1^{(1)} \\
\mathcal{A}_1^{(1)} &\rightarrow \mathcal{A}_{11}^{(1)} \,.
\end{aligned}
\tag{I.8}
$$

At order $\hbar^2$ the $\beta_1^{(2)}$ function and $\mathcal{A}_{11}^{(2)}$ can have a first order dependence on $c_{j_1}^{(1)}$, we make this explicit

$$
\begin{aligned}
\beta^{(2)} &\rightarrow \beta_2^{(2)} + c_{j_1}^{(1)} \beta_1^{(2)}(j_1) \,, \\
\mathcal{A}_2^{(2)} &\rightarrow \mathcal{A}_{22}^{(2)} \,, \\
\mathcal{A}_1^{(2)} &\rightarrow \mathcal{A}_{21}^{(2)} + c_{j_1}^{(1)} \mathcal{A}_{11}^{(2)}(j_1) \,.
\end{aligned}
\tag{I.9}
$$

A sum over j_1 is implied. The j_1 indicates that one should consider the minimal set of operators available at order 1. Putting (I.9) in (I.6) gives three conditions on the various coefficients of the monomials in the $c_i^{(n)}$:

$$
\begin{aligned}
\beta_2^{(2)} &= 2\mathcal{A}_{21}^{(2)} \,, \\
\beta_1^{(2)}(j_1) &= \mathcal{A}_{11}^{(2)}(j_1) \,, \\
2\mathcal{A}_{22}^{(2)} &= \beta_1^{(1)}(j_1) \mathcal{A}_{11}^{(2)}(j_1) \,.
\end{aligned}
\tag{I.10}
$$

At order $\hbar^3$ the polynomial dependence gets more complicated

$$
\begin{aligned}
\beta^{(3)} &\rightarrow \beta_3^{(3)} + c_{j_1}^{(1)} \beta_2^{(3)}(j_1) + c_{j_2}^{(2)} \beta_1^{(3)}(j_2) + c_{j_1}^{(1)} c_{k_1}^{(1)} \beta_1^{(3)}(j_1 k_1) \,, \\
\mathcal{A}_3^{(3)} &\rightarrow \mathcal{A}_{33}^{(3)} \,, \\
\mathcal{A}_2^{(3)} &\rightarrow \mathcal{A}_{32}^{(3)} + c_{j_1}^{(1)} \mathcal{A}_{21}^{(3)}(j_1) \,, \\
\mathcal{A}_1^{(3)} &\rightarrow \mathcal{A}_{31}^{(3)} + c_{j_1}^{(1)} \mathcal{A}_{21}^{(3)}(j_1) + c_{j_1}^{(2)} \mathcal{A}_{11}^{(3)}(2j) + c_{j_1}^{(1)} c_{k_1}^{(1)} \mathcal{A}_{11}^{(3)}(j_1 k_1) \,.
\end{aligned}
\tag{I.11}
$$

Which terms can show up at which level follows from the $\hbar$ counting and the fact that l loops can at most diverge like $1/w^l$. Putting (I.11) in (I.6) gives the

relations from the $\mathcal{O}(w^0)$ in (I.6)

$$
\begin{aligned}
\beta_3^{(3)} &= 3\mathcal{A}_{31}^{(3)}, \\
\beta_2^{(3)}(j_1) &= 2\mathcal{A}_{21}^{(3)}(j_1), \\
\beta_1^{(3)}(j_2) &= \mathcal{A}_{11}^{(3)}(j_2), \\
\beta_1^{(3)}(j_1 k_1) &= \mathcal{A}_{11}^{(3)}(j_1 k_1).
\end{aligned}
\tag{I.12}
$$

The $-nw$ and $\sum_{m,j} mw c_j^{(m)} \partial / \partial c_j^{(m)}$ terms in (I.6) always combine to give exactly the loop level back, see [9] for the general proof. This gives the first equation in (I.17).

The w^{-1} part gives

$$
\begin{aligned}
3\mathcal{A}_{2i}^{(3)} &= \beta_{1j_1}^{(1)} \mathcal{A}_{21i}^{(3)}(j_1) + \beta_{2j_2}^{(2)} \mathcal{A}_{11i}^{(3)}(j_2), \\
2\mathcal{A}_{22i}^{(3)}(j_1) &= 2\beta_{1k_1}^{(1)} \mathcal{A}_{11i}^{(3)}(j_1 k_1) + \beta_{1k_2}^{(2)}(j_1)\mathcal{A}_{11i}^{(3)}(k_2).
\end{aligned}
\tag{I.13}
$$

Here we have written out the operator $\mathcal{O}_i^{(n)}$ subscripts (i, j_2, k_1, k_2). That is to stress the fact that there is a sum over a *different* index $j_1 \neq i$. We will omit it in the following. In deriving the second equation we have used that $\mathcal{A}_{11i}^{(3)}(j_1 k_1)$ is symmetric in $j_1 k_1$ and relabeled some indices. The final equation comes from the w^{-2} part and reads

$$
3\mathcal{A}_{33}^{(3)} = \beta_{1j_1}^{(1)} \mathcal{A}_{22}^{(3)}(j_1).
\tag{I.14}
$$

The set of equations gives

$$
6\mathcal{A}_{33}^{(3)} = \beta_{1j_1}^{(1)} \left[2\beta_{1k_1}^{(1)} \mathcal{A}_{11}^{(3)}(j_1 k_1) + \beta_{1k_1}^{(2)}(j_1)\mathcal{A}_{11}^{(3)}(k_2) \right].
\tag{I.15}
$$

As one can see, the leading divergence $\mathcal{A}_{33}^{(3)}$ can be calculated with purely one-loop calculations.

The argument above can be generalized to all orders, see [9], here we only quote the results. We introduce the notation

$$
\nabla_l = \sum_{m=l}^{\infty} \sum_j \beta_j^{(m)} \frac{\partial}{\partial c_j^{(m)}}
\tag{I.16}
$$

The general set of equations thus reads

$$
\begin{aligned}
\beta_l^{(n)} &= l\mathcal{A}_{l1}^{(n)}, &\qquad l &= 1,\dots,n, \\
l\mathcal{A}_{lk}^{(n)} &= \sum_{l'=1}^{l-k+1} \nabla_{l'} \mathcal{A}_{l-l',k-1}^{(n)}, &\qquad l &= k,\dots,n; \ k = 2,\dots,n.
\end{aligned}
\tag{I.17}
$$

For the leading divergence $\mathcal{A}_{nn}^{(n)}$ this equation reads

$$
\begin{aligned}
n! \mathcal{A}_{nn}^{(n)} &= \nabla_1^{n-1} \beta_1^{(n)}, \\
\beta_1^{(n)} &= \mathcal{A}_{11}^{(n)}.
\end{aligned}
\tag{I.18}
$$

which is a generalization of (I.7), (I.10) and (I.15). This is the main result of [9] we will be using. This is a recursive relation. The order $n = 1$ counterterm $\mathcal{A}_{11}^{(1)} \mathcal{O}^{(1)}$ is fixed by the requirement that it should cancel the $\mathcal{L}_0$ one loop $1/w$ pole. This is now the order $n = 1$ coupling in the Lagrangian. The order $n = 2$ coupling $\mathcal{A}_{22}^{(2)}$ is fixed by the requirement that it cancels the one loop $1/w^2$ pole coming form the $\mathcal{L}_1$ with the $\mathcal{A}_{11}^{(1)}$ coupling we fixed in the previous step. And so on, the n-th order $\mathcal{A}_{nn}^{(n)}$ is fixed by the requirement that it cancels the $1/w^n$ divergences. These can be calculated by considering all one loop diagrams generated by the $\mathcal{A}_{n-1,n-1}^{(n-1)} \mathcal{O}^{(n-1)}$,..., $\mathcal{A}_{11}^{(1)} \mathcal{O}^{(1)}$ and $\mathcal{L}_0$ vertices that can contribute to order n.

The renormalized coupling $c^{(1)}$ now contains a $\log \mu$. This exactly cancels the $\log \mu$ dependence that comes from the $\mathcal{L}_0$ loop integral, which has the same coefficient as the divergence. Analogously, when an observable is calculated up to order n its expression contains a $(\log \mu)^n$ term whose coefficient is given by the $\mathcal{A}_{nn}^{(n)}$. So (I.18) gives a recursive expression for the coefficients of the leading logarithms.

I.2.2 Nonminimal sets of operators

In Section I.2.1 we shortly went through the arguments of [9] to derive the leading divergence at any order from only one-loop calculations. In practical applications of the formulas above one needs a classification of the terms $\mathcal{O}_i^{(n)}$ needed at each order n. Determining the complete and minimal set is in general rather complicated, see e.g. [17] for $\mathcal{L}_2$ in ChPT. Luckily we do not have to have a minimal and complete Lagrangian in general.

It is sufficient to have a Lagrangian that is complete for the particular process at hand and lower order Lagrangians that are complete enough so that all needed $\beta_i^{(n)}(1)$ can be obtained. The Lagrangian does not need to be minimal since the arguments in Section I.2.1 relied on the fact that all $c_i^{(n)}$ can be varied independently. If we add an irrelevant term, e.g. one that vanishes via partial integration or other identities, its coefficient can definitely be freely varied and will not show up in any actual higher order calculations. This also means that the β function of this irrelevant term can be chosen freely since it will never appear in any expressions.

If we now have two related terms $c_1^{(n)} \mathcal{O}_1^{(n)}$ and $c_2^{(n)} \mathcal{O}_2^{(n)}$, we can always write them as an irrelevant one $c_{irr}^{(n)} \mathcal{O}_{irr}^{(n)}$ and a relevant one $c_{rel}^{(n)} \mathcal{O}_{rel}^{(n)}$. Since the irrel-

evant combination will never appear and its $\beta_{\text{irr}}^{(n)}$ function is free, we can just as well leave both terms $c_1^{(n)} \mathcal{O}_1^{(n)}$ $c_2^{(n)} \mathcal{O}_2^{(n)}$ in the Lagrangian and leave the $\beta_{\text{rel}}^{(n)}$ spread over the original two terms $\beta_1^{(n)}$ and $\beta_2^{(n)}$. How it is split between the two terms depends upon the choice of $\beta_{\text{irr}}^{(n)}$, which is free.

In practice, it is sufficient to calculate the divergences and to express them in some complete set of operators $\mathcal{O}_i^{(n)}$. As long as the set is complete for the given application we will obtain the correct result.

When constructing a Lagrangian one normally takes into account all terms that have the correct symmetry at the required order and then one removes the so called equation of motion terms, see [17] App. A, for a discussion. In this case, however, we will use neither constraint. We will keep the equation of motion terms, since then we can make all 1PI diagrams finite, see the discussion in [9]. We will also use a standard Feynman diagram calculation to obtain the infinities and not a more sophisticated method such as e.g. the heat kernel expansion that was used in [18].

The reason is that this way we can use standard Feynman integral techniques and we do not have to evaluate all the divergent combinations of propagators that can appear, see [18, 19], which is rather difficult at higher orders. The drawback is that this procedure breaks the symmetries of the Lagrangian in individual parts of the calculation even though the final result will respect all symmetry properties when we use dimensional regularization. However, as we saw in the previous section, we only use the divergent parts of these terms and these must obey the symmetries since they are recursively determined by a symmetric lowest order Lagrangian.

The answer for the divergences for a given process will thus be correct even without explicitly fixing counterterms with Ward identities. The correct combinations must show up in our procedure.

The conclusion from this section is that we simply calculate all one-loop diagrams and rewrite them as terms in the Lagrangians, without bothering to check if we have a minimal Lagrangian.

We also do not need to have a complete Lagrangian, an operator $\mathcal{O}_i^{(n)}$ will only be relevant if it has a nonzero β function. We thus let the calculation itself produce all terms that have a divergence, give them a coefficient $c_i^{(n)}$, and use those in the equations derived in Section I.2.1.

For the subleading divergence, the same type of argument shows that it is sufficient to have the lowest and first order Lagrangian in a symmetric form to get the subleading divergence at all orders and the obvious generalization to the further divergences.

I.2.3   An alternative proof

A more direct proof of the results of Büchler and Colangelo is also possible.

We have presented their method as well since the arguments in Sect. I.2.2 made use of their formulation of the proof in [9].

We rely here on using only 1PI diagrams and assume they are made fully finite, as was shown to be possible in [9] . In this section we obtain the same relations in a more transparent fashion. We first rewrite (I.1) and (I.2) as

$$\mathcal{L}^{\text{bare}} = \sum_{n \geq 0} \hbar^n \mu^{-nw} \sum_i \left(\sum_{k=0}^{n} c_{ki}^{(n)} w^{-k} \right) \mathcal{O}_i^{(n)} . \tag{I.19}$$

We introduce the notation $\{c\}_l^n$ to indicate all possible combinations $c_{k_1 j_1}^{(m_1)} c_{k_2 j_2}^{(m_2)} \ldots c_{k_r j_r}^{(m_r)}$ with $m_i \geq 1$, such that $\sum_{i=1,r} m_i = n$ and $\sum_{i=1,r} k_i = l$. The $c_{ki}^{(n)}$ with $k \geq 1$ have no direct μ dependence. They only depend on μ through their dependence on lower order parameters. The $c_{0i}^{(n)}$ do depend directly on μ. Note that since we consider only 1PI diagrams we have that $\{c\}_n^n = \{c_{ni}^{(n)}\}$.

We denote the contribution from all l-loop diagrams at order $\hbar^n$ as L_l^n and we expand this as

$$L_l^n = \sum_{k=0}^{l} L_{lk}^n w^{-k} . \tag{I.20}$$

This only includes the divergences coming from the loop integrations, not those from the coefficients in the Lagrangian.

A main observation [9] is that a given loop level at a given order $\hbar^n$ always comes with the same power of μ because of the way the powercounting works.

We can now study the contributions at the different orders in $\hbar$ and $1/w$. For clarity we add here as well which combinations of couplings of order $n \geq 1$ the results depend on.

At order $\hbar^0$ we have only L_0^0. At order $\hbar^1$ we have

$$\frac{1}{w} \left(\mu^{-w} L_{00}^1(\{c\}_1^1) + L_{11}^1 \right) + \mu^{-w} L_{00}^1(\{c\}_0^1) + L_{10}^1 . \tag{I.21}$$

The divergence must cancel so to get the divergent combinations we have that

$$L_{00}^1(\{c\}_1^1) = -L_{11}^1 . \tag{I.22}$$

This allows to determine the divergences that need to be subtracted from a one-loop calculation and it shows that by expanding μ^{-w} and taking $w \to 0$ the explicit $\log \mu$ dependence of any process is

$$- \log \mu \, L_{00}^1(\{c\}_1^1) = \log \mu \, L_{11}^1 . \tag{I.23}$$

At order $\hbar^2$ the full contribution is

$$\frac{1}{w^2} \left(\mu^{-2w} L_{00}^2(\{c\}_2^2) + \mu^{-w} L_{11}^2(\{c\}_1^1) + L_{22}^2 \right)$$
$$+ \frac{1}{w} \left(\mu^{-2w} L_{00}^2(\{c\}_1^2) + \mu^{-w} L_{11}^2(\{c\}_0^1) + \mu^{-w} L_{10}^2(\{c\}_1^1) + L_{21}^2 \right)$$
$$+ \left(\mu^{-2w} L_{00}^2(\{c\}_0^2) + \mu^{-w} L_{10}^2(\{c\}_0^1) + L_{20}^2 \right) . \tag{I.24}$$

All divergences must cancel, also those with powers of $\log \mu$. If we only look at the parts with $1/w^2$ and $\log \mu / w$ we obtain two equations

$$L_{00}^2(\{c\}_2^2) + L_{11}^2(\{c\}_1^1) + L_{22}^2 = 0 ,$$
$$2L_{00}^2(\{c\}_2^2) + L_{11}^2(\{c\}_1^1) = 0 \tag{I.25}$$

The difference in the coefficients from the first to the second equation comes from the expansion of the different powers of μ^{-w}. These equations have the solution

$$\begin{aligned} L_{00}^2(\{c\}_2^2) &= L_{22}^2 , \\ L_{11}^2(\{c\}_1^1) &= -2L_{22}^2 . \end{aligned} \tag{I.26}$$

The leading logarithm can be obtained by expanding μ^{-w} in (I.24) and using (I.26):

$$\frac{1}{2} \log^2 \mu \left(4L_{00}^2(\{c\}_2^2)L^2 + L_{11}^2(\{c\}_1^1) \right) = \log^2 \mu \; L_{22}^2 . \tag{I.27}$$

So here we reproduce the known result and that it can be obtained from a one-loop calculation. The calculation for the next two orders follows the same lines. A clear pattern emerges.

At order $\hbar^n$, the leading part is given by

$$\frac{1}{w^n} \left(\mu^{-nw} L_{00}^n(\{c\}_n^n) + \mu^{-(n-1)w} L_{11}^n(\{c\}_{n-1}^{n-1}) + \cdots + \mu^{-w} L_{n-1\,n-1}^n(\{c\}_1^1) + L_{nn}^n \right) . \tag{I.28}$$

This part is the one that contributes to the $1/w^n, \log \mu / w^{n-1}, \ldots, \log^{n-1} \mu / w$ divergences leading to the set of equations:

$$\sum_{i=0}^{n} i^j L_{n-i\,n-i}^n(\{c\}_i^i) = 0 \qquad\qquad j = 0, .., n-1. \tag{I.29}$$

with $0^0 = 1$ and $L_{nn}^n(\{c\}_0^0) = L_{nn}^n$. The generalization of the solution then is

$$L_{n-i\,n-i}^n(\{c\}_i^i) = (-1)^i \begin{pmatrix} n \\ i \end{pmatrix} L_{nn}^n . \tag{I.30}$$

We can prove that this solves the equations (I.29) above by observing that they can be written as

$$\lim_{a \to 0} \left(\sum_{i=0}^{n} \left(a \frac{d}{da} \right)^j a^{n-j} L_{jj}^n (\{c\}_{n-i}^{n-i}) \right) = 0 \,.$$

(I.31)

Plugging in (I.30) we see that this becomes

$$\lim_{a \to 1} \left(a \frac{d}{da} \right)^j (-a+1)^n L_{nn}^n = 0 \,,$$

(I.32)

which is clearly satisfied. Using $\lim_{a \to 1} \left(a \frac{d}{da} \right)^n (-a+1)^n = (-1)^n n!$ one can also derive that the dependence on $\log^n \mu$ is

$$\log^n \mu \, L_{nn}^n \,.$$

(I.33)

This completes our alternative proof of the main result of [9].

I.3   The $O(N)$ nonlinear sigma model

The $O(N+1)/O(N)$ nonlinear sigma model has as Lagrangian

$$\mathcal{L}_{n\sigma} = \frac{F^2}{2} \partial_\mu \Phi^T \partial^\mu \Phi + F^2 \chi^T \Phi \,.$$

(I.34)

Φ is a real $N+1$ vector that transforms as the fundamental representation of $O(N+1)$ and satisfies the constraint $\Phi^T \Phi = 1$. The second term is the one that breaks the symmetry explicitly by setting

$$\chi^T = \left(M^2 \, 0 \ldots 0 \right) \,.$$

(I.35)

The vacuum is given by

$$\langle \Phi^T \rangle = (1 \, 0 \ldots 0) \,,$$

(I.36)

which breaks the $O(N+1)$ spontaneously to $O(N)$. There is both a spontaneous symmetry breaking triggered by the vacuum (I.36) and an explicit one given by $F^2 \chi^T \Phi$.

This Lagrangian corresponds to the lowest order Lagrangian of two-(quark-)flavour Chiral Perturbation Theory for $N = 3$ [2,20] and has been used to describe alternative Higgs sectors in several beyond the Standard Model scenarios.

As mentioned in the introduction, we make use of different parametrizations to check the validity of our results. We write Φ in terms of a real N-component [3] vector ϕ, which transforms linearly under the unbroken part

---

[3]We refer to these as a flavour components.

of the symmetry group, $O(N)$. We use here four different ways to do this parametrization

$$\Phi_1 = \begin{pmatrix} \sqrt{1 - \frac{\phi^T \phi}{F^2}} \\ \frac{\phi^1}{F} \\ \vdots \\ \frac{\phi^N}{F} \end{pmatrix} = \begin{pmatrix} \sqrt{1 - \frac{\phi^T \phi}{F^2}} \\ \frac{\phi}{F} \end{pmatrix}, \tag{I.37}$$

$$\Phi_2 = \frac{1}{\sqrt{1 + \frac{\phi^T \phi}{F^2}}} \begin{pmatrix} 1 \\ \frac{\phi}{F} \end{pmatrix}, \tag{I.38}$$

$$\Phi_3 = \begin{pmatrix} 1 - \frac{1}{2} \frac{\phi^T \phi}{F^2} \\ \sqrt{1 - \frac{1}{4} \frac{\phi^T \phi}{F^2}} \frac{\phi}{F} \end{pmatrix}, \tag{I.39}$$

$$\Phi_4 = \begin{pmatrix} \cos \sqrt{\frac{\phi^T \phi}{F^2}} \\ \sin \sqrt{\frac{\phi^T \phi}{F^2}} \frac{\phi}{\sqrt{\phi^T \phi}} \end{pmatrix}. \tag{I.40}$$

Φ_1 is the parametrization used in [2], Φ_2 the one originally introduced by Weinberg [20]. Φ_3 is such that the explicit symmetry breaking term in (I.34) only gives a mass term to the ϕ field but no vertices. Φ_4 is the parametrization one ends up with if using the general prescription of [21]. These are all examples of the parametrization that keeps the $O(N)$ symmetry manifest:

$$\Phi = \begin{pmatrix} \sqrt{1 - \frac{\phi^T \phi}{F^2} f^2 \left(\frac{\phi^T \phi}{F^2} \right)} \\ f \left(\frac{\phi^T \phi}{F^2} \right) \frac{\phi}{F} \end{pmatrix}. \tag{I.41}$$

Here $f(x)$ is any function with $f(0) = 1$.

One thing is worth mentioning. In this work we always calculate with the usual Feynman diagram techniques. In our calculation we split the N-vector field into an external (ϕ_E) and a loop (ξ) field, $\phi \rightarrow \phi_E + \xi$. The divergence structure we obtain is expressed in terms of ϕ_E and we then set $\phi_E \rightarrow \phi$ and use that as input for the next step. Splitting ϕ in this way, the symmetry is no longer manifest in each term. Since we are renormalizing these terms, it would be nice if they were obviously symmetric. We could have used the background field method, used e.g. in [2, 18], and split into a classical and a quantum field with well defined symmetry properties and then calculated the divergent part up to a given number of external legs. This way we would have been assured that our divergent Lagrangian can be rewritten into terms fully obeying the symmetry. Once that is done, we could then use the symmetric quantum field again for the next step. The problem is that the rewriting into

symmetric terms is not easy to implement. We have shown in Sec. I.2.2 that our method gives the correct answer too.

One additional way to check that our results are correct is to compare with the known results. For $N = 3$ our $O(N)$ corresponds to $SU(2) \times SU(2)/SU(2)$, and loop corrections to the pion mass up to two loops are fully known in this model [22, 23]. The leading terms at two-loop order were first obtained in [6]. They read

$$
\begin{aligned}
M_{phys}^2 &= M^2 \left(1 - \frac{1}{2} L_M + \frac{17}{8} L_M^2 + \cdots \right), \\
L_M &= \frac{M^2}{16\pi^2 F^2} \log \frac{\mu^2}{\mathcal{M}^2}.
\end{aligned}
\tag{I.42}
$$

where in numerical applications one usually chooses $\mathcal{M} = M$.

I.4   The large N approximation

The linear sigma model has been treated very much in the large N approximations. The literature can be traced back to [15] but the literature on the nonlinear sigma model is smaller. In addition, it is mainly restricted to the massless case while here we are interested in the massive case. [24] did include masses but only to first order. There are some subtleties involved in large N in effective theories because of the presence of the higher order Lagrangians, see e.g. [25]. We however keep our discussion on the level of the loop diagrams with the lowest order Lagrangian and stick to L_{nn}^n in the notation of Sect. I.2.3

We choose here the Lagrangian to be extensive in N. This means we have to choose $F^2 \propto N$. Looking at the Lagrangians in Sect. I.3 we easily see that vertices with $2n$ legs have a factor F^{2-2n} and are thus suppressed by N^{1-n}. Extra factors of N come from closed loops in the flavour index. It is sufficient to look at one-particle-irreducible (1PI) diagrams, the flavour indices for lines not inside a loop are determined by the external flavour indices.

We thus look at the one-particle-irreducible diagrams only and use methods similar to those used in [1] for proving the powercounting. A given diagram has N_L loops, N_{2n} vertices with $2n$ legs, N_I (internal) propagators and N_E external legs. These are related via

$$
\begin{aligned}
N_L &= N_I - \sum_n N_{2n} + 1, \\
2N_I + N_E &= \sum_n 2n N_{2n}.
\end{aligned}
\tag{I.43}
$$

We thus get

$$
N_L = \sum_n (n-1) N_{2n} - \frac{1}{2} N_E + 1.
\tag{I.44}
$$
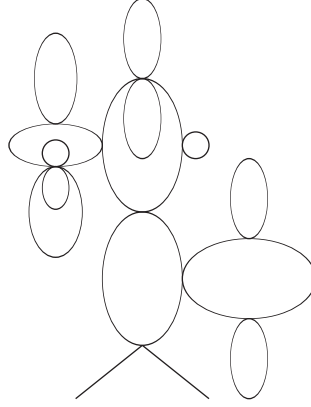
Figure I.1: A typical diagram that contributes at leading order in N. Note that vertices can have many different loops attached since the Lagrangians contain vertices with any number of fields. The flavour-loops coincide with the loops in momentum.

I

The tree level one-particle-irreducible diagram has one vertex with $2n = N_E$ and thus comes with a factor of $N^{1-N_E/2}$. A generic one-particle-irreducible loop diagram has thus a suppression factor

$$N^{-\Sigma_n (n-1)N_{2n}} = N^{-N_L - N_E/2 + 1},\qquad(\text{I}.45)$$

from the vertices. Extra factors of N come from the closed flavour loops where each closed flavour loop give a factor of N. (I.45) shows that for a diagram to be leading in N, there must be as many closed flavour loops as there are loops. Since the ϕ fields only carry one flavour index, this means that each loop must coincide with the flavour loop and there can be no lines shared between two loops. All diagrams that contribute to a given process at leading order in N are thus diagrams that only contain products of one-loop diagrams, these we call cactus diagrams after the looks of the "prickly pear" cactus. A typical example is shown in Fig. I.1.

How can we now resum all of these diagrams? The easiest way is to notice that they can be generated recursively. First we note that the inverse of the full propagator is given by the inverse of the lowest order propagator and the sum of all the one-particle-irreducible diagrams with two external legs. This leads to the equation graphically depicted in Fig. I.2. The difference with the usual gap equation in NJL-type theories as discussed in e.g. [16] is that we have an infinite number of terms here. This actually turns out to be manageable.

Let us look at the Lagrangians of Sect. I.3. They all contain at most two derivatives. The loops in Fig. I.2 are all tadpoles and thus produce no extra dependence on the external momentum p. All the dependence on p must come

$$(\;\rule[0.5ex]{1.5em}{2pt}\;)^{-1} = (\;\rule[0.5ex]{1.5em}{0.4pt}\;)^{-1} + \underset{\rule{2em}{0.4pt}}{\bigcirc} + \underset{\rule{2em}{0.4pt}}{\bigcirc\!\!\bigcirc} + \underset{\rule{2em}{0.4pt}}{\bigcirc\!\!\bigcirc\!\!\bigcirc} + \cdots$$

Figure I.2: The graphical representation of the equation that generates all the cactus diagrams for the propagator. A thick line indicates the full propagator, a thin line the inverse one.

from the derivatives present in the vertices. The full inverse propagator is thus of the form $Z_P p^2 - B_P$, where neither Z_P nor B_P depend on the momentum p. This is true for all parametrizations.

We now use the first parametrization. The vertices with derivatives are generated by

$$\frac{1}{2F^2} \frac{1}{1 - \frac{\phi^a \phi^a}{F^2}} \phi^b \partial_\mu \phi^b \phi^c \partial^\mu \phi^c \,, \tag{I.46}$$

where we have written $\phi^T \phi = \phi^a \phi^a$ to bring out the sum over flavour indices explicitly. Each loop must allow for a sum over the flavour indices to be leading in N. The derivatives must either both act on the external fields or both on the same loop to give a nonzero result[4]. When they act inside a loop, the fields $\partial_\mu \phi^b \partial^\mu \phi^c$ must be contracted to form the loop. This requires $b = c$ and the flavour in this loop is thus determined by the outer fields and cannot be separately summed over. Consequently, the diagram gives no leading N contribution.

If the derivatives hit the external legs, the indices in at least one loop are fixed by the external ones and again cannot be summed over. It follows that the contribution is not leading order in N.

In either case the loop diagrams generated by the kinetic term give no leading N correction, so $Z_P = 1$.

Thus we only need to look at the vertices coming from the mass term

$$\mathcal{L}_{\text{m}ass} = F^2 M^2 \sqrt{1 - \phi^a \phi^a / F^2} \equiv F^2 M^2 f(x) \equiv F^2 M^2 \sum_i a_i x^i \,, \tag{I.47}$$

with $x = \phi^a \phi^a / F^2$. Again, consider the a loop diagram. The external legs need to come from the same flavour index otherwise it will not be leading in $1/N$.

---

[4]This will not be true for more complicated processes but can be dealt with in that case as well [26].

For each term in (I.47) there are i ways to choose which x corresponds to the external legs

$$M^2 \phi_{ext}^a \phi_{ext}^a \sum_{i \geq 2} a_i i x^{i-1} = M^2 \phi_{ext}^a \phi_{ext}^a \left(\frac{df}{dx}(x) - a_1 \right) . \tag{I.48}$$

The sum in (I.48) starts from $i = 2$ since the $i = 0, 1$ terms are a constant and the tree level mass term respectively. Eq (I.47) then reads

$$-\frac{1}{2} M^2 \phi_{ext}^a \phi_{ext}^a \left(\frac{1}{\sqrt{1 - \frac{\phi^c \phi^c}{F^2}}} - 1 \right) . \tag{I.49}$$

The leading contribution comes from contracting the fields with the same flavour index. There is only one way to do this for each term. Each contraction corresponds to a tadpole in Fig. I.2. The full result can be written as

$$p^2 - B_P = p^2 - M^2 - M^2 \left(\frac{1}{\sqrt{1 + \frac{N}{F^2} A(B_P)}} - 1 \right) , \tag{I.50}$$

where $iA(B_P) = \int d^d p \, 1/(p^2 - B_P)$ is the relevant one-loop tadpole integral. The all-loop result at leading order in N is thus the solution of

$$M^2 = M_{phys}^2 \sqrt{1 + \frac{N}{F^2} A(M_{phys}^2)} . \tag{I.51}$$

Here B_P coincides with the physical mass squared, M_{phys}^2, since $Z_P = 1$.

The same result can be derived in the other parametrizations. If we take the third one, where the only vertices come from the term with derivatives, the same type of argument as above with derivatives and flavour indices shows that the only relevant vertex is

$$-\frac{1}{8F^2} \phi^a \phi^a \partial_\mu \phi^b \partial^\mu \phi^b . \tag{I.52}$$

So here the gap equation reduces to the first nontrivial term on the right-hand-side only. The structure of the inverse propagator is still $Z_P p^2 - B_P$ and the gap equation leads to two equations with $M_{phys}^2 = B_P / Z_P$

$$
\begin{aligned}
Z_P &= 1 + \frac{N}{4F^2 Z_P} A(M_{phys}^2),, \\
Z_P M_{phys}^2 &= M^2 - \frac{N}{4F^2 Z_P} M_{phys}^2 A(M_{phys}^2) .
\end{aligned}
\tag{I.53}
$$

Here we have expressed the integral containing an extra q^2 using (I.64) in terms of the one without. Solving leads to the solutions

$$
\begin{aligned}
Z_P &= \frac{1}{2}\left(1 + \frac{M^2}{M_{phys}^2}\right), \\
M^4 &= M_{phys}^4\left(1 + \frac{N}{F^2}A(M_{phys}^2)\right),
\end{aligned}
\tag{I.54}
$$

which agrees with the previous result (I.51).

The leading logarithm can be expressed by replacing $A(M_{phys}^2)$ by

$$
\overline{A}(M_{phys}^2) = \frac{M_{phys}^2}{16\pi^2}\log\frac{\mu^2}{M_{phys}^2}.
\tag{I.55}
$$

In terms of

$$
y = \frac{NM^2}{16\pi^2F^2}\log\frac{\mu^2}{M^2}
\tag{I.56}
$$

we can invert the result (I.51):

$$
\frac{M_{phys}^2}{M^2} = 1 - \frac{1}{2}y + \frac{5}{8}y^2 - y^3 + \frac{231}{128}y^4 - \frac{7}{2}y^5 + \frac{7293}{1024}y^6 - 15y^7 + \frac{1062347}{32768}y^8 + \cdots.
\tag{I.57}
$$

Note that (I.51) actually converges faster. Expanding the square root in

$$
z = \frac{NM_{phys}^2}{16\pi^2F^2}\log\frac{\mu^2}{M_{phys}^2}
\tag{I.58}
$$

we have

$$
\frac{M^2}{M_{phys}^2} = 1 + \frac{1}{2}z - \frac{1}{8}z^2 + \frac{1}{16}z^3 - \frac{5}{128}z^4 + \frac{7}{256}z^5 - \frac{21}{1024}z^6 + \frac{33}{2048}z^7 - \frac{429}{32768}z^8 + \cdots,
\tag{I.59}
$$

which has much smaller coefficients than (I.57).

I.5   The calculation

We determine the mass by finding the zero of the inverse propagator. We therefore must calculate all the one-loop diagrams that are needed to obtain the divergence of the inverse propagator to the order desired. At order $\hbar$ there is only one diagram, at $\hbar^2$ there are 2 and at order $\hbar^3$ there are 4. These are shown in Fig. I.3. We have not shown them but at order $\hbar^4$ there are 7 and at $\hbar^5$ there are 13 diagrams to be calculated.
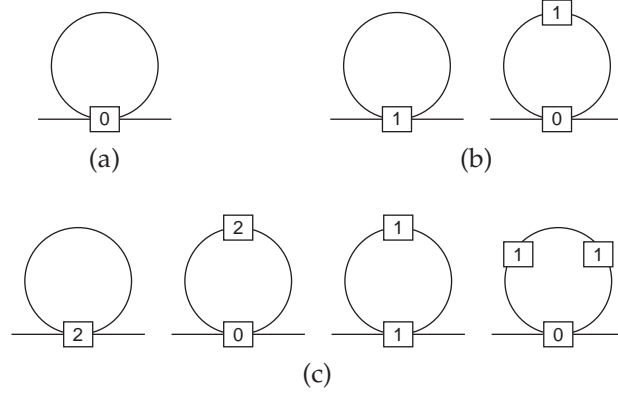
Figure I.3: The diagrams needed up to order 3 for the inverse propagator. Vertices of order $\hbar^i$ are indicated with $\boxed{\text{i}}$. (a) The diagram needed at order $\hbar$. (b) The 2 diagrams needed at order $\hbar^2$. (c) The 4 diagrams needed at order $\hbar^3$.
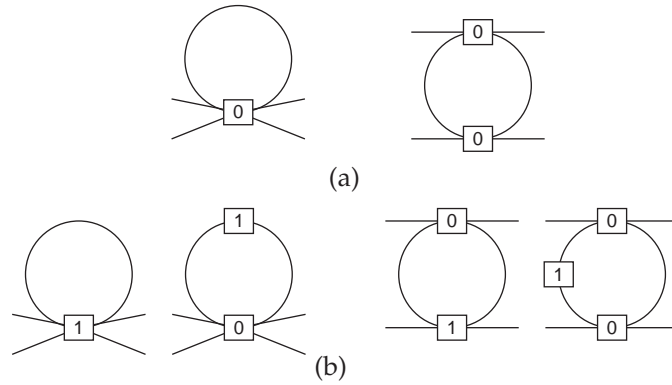
Figure I.4: The diagrams needed for the divergence of the 4-meson vector. (a) The 2 diagrams to order $\hbar$. (b) the 4 diagrams to order $\hbar^2$

To order $\hbar$ it is sufficient to know the lowest-order Lagrangian, but at order $\hbar^2$ we need to know the (divergent part of the) vertices coming from the Lagrangian of order $\hbar$ with two and four external legs. The diagram of Fig. I.3(a) gives the divergence of the vertex with two legs but we also need to calculate the divergence of the vertex with four legs. This requires the diagrams shown in Fig. I.4(a).

To order $\hbar^3$, we need still more vertices, we need the divergence of the two-leg vertex to order $\hbar^2$, these diagrams we already have but we also need
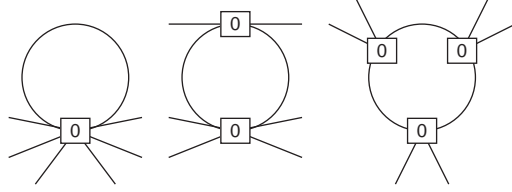
Figure I.5: The 3 diagrams needed for the divergence of the 6-meson vector to order $\hbar$.

the four-leg vertex to order $\hbar^2$ which can be calculated from the diagrams in Fig. I.4(b). Inspection of the vertices there shows we already have all we need but for the 6-leg vertex at order $\hbar$. To obtain that we also need to evaluate all diagrams shown in Fig. I.5. By now, the pattern should be clear, to get the mass at order $\hbar^n$ we need the 2 and four-meson vertex at order $\hbar^{n-1}$, the 2, 4 and 6-meson vertex at order $\hbar^{n-2}$ and so on. Similarly one can see that to get the mass at order $\hbar^n$, we need to calculate one-loop diagrams with up to n vertices. The extension to order $\hbar^5$ shows that we we need to calculate 18, 26, 33, 26 and 13 at orders $\hbar^1, \ldots, \hbar^5$ respectively.

We have organized this calculation by first expanding the lowest-order Lagrangian to the order needed, up to vertices with 12 mesons for this work. With these vertices we then calculate all 1PI diagrams with up to 10 external legs. The divergent part of all needed integrals can be calculated relatively easily using the technique described in App. I.7. At this stage, the dependence on external momenta is also put back as derivatives on the external legs and everything assembled to give the divergent part at order $\hbar$ for all the vertices with up to 10 legs using (I.22). So we have assembled everything we need to calculate the one-loop divergences to order $\hbar^2$. The 26 diagrams are evaluated and we obtain the divergences at order $\hbar^2$ using (I.26). The process is then repeated up to order $\hbar^5$. All of the above steps have been programmed in FORM. The CPU time needed increases rapidly with the order n one wishes to reach. The Lagrangians at higher orders tend to contain very many terms and constructing the diagrams with many external legs at higher orders is also extremely time consuming. The CPU time used on a typical PC for the mass-divergence to order $\hbar^n$ was approximately 0.1 seconds for $\hbar$, 0.3 seconds for $\hbar^2$ 11 seconds for $\hbar^3$, 700 seconds for $\hbar^4$ and 30000 seconds for $\hbar^5$. These running times were achieved after several optimizations in the choice of routing the external momenta through the Feynman diagrams.

We have performed the calculation for each of the four parametrizations shown in Sect. I.3. Since each parametrization distributes contributions rather differently over the different Feynman diagrams, this provides a strong check on the consistency of the final result.

i	a_i for $N=3$	a_i for general N
1	$-1/2$	$1 - 1/2\,N$
2	$17/8$	$7/4 - 7/4\,N + 5/8\,N^2$
3	$-103/24$	$37/12 - 113/24\,N + 15/4\,N^2 - N^3$
4	$24367/1152$	$839/144 - 1601/144\,N + 695/48\,N^2 - 135/16\,N^3 + 231/128\,N^4$
5	$-8821/144$	$33661/2400 - 1151407/43200\,N + 197587/4320\,N^2$ $-12709/300\,N^3 + 6271/320\,N^4 - 7/2\,N^5$

Table I.1: The coefficients a_i of the leading logarithm L_M^i up to $i = 5$ for the physical meson mass.

i	b_i for $N=3$	b_i for general N
1	$1/2$	$-1 + 1/2\,N$
2	$-13/8$	$1/4 - 1/4\,N - 1/8\,N^2$
3	$-19/48$	$2/3 - 11/12\,N + 1/16\,N^3$
4	$-5773/1152$	$-8/9 + 107/144\,N - 1/6\,N^2 - 1/16\,N^3 - 5/128\,N^4$
5	$-3343/768$	$-18383/7200 + 130807/43200\,N - 2771/2160\,N^2 - 527/1600\,N^3$ $+23/640\,N^4 + 7/256\,N^5$

I

Table I.2: The coefficients b_i of the leading logarithm $L_{M_{phys}}^i$ up to $i = 5$ for the lowest order meson mass in terms of the physical mass.

We can from these divergences then obtain the leading logarithm. This leads to the result for the physical mass

$$M_{phys}^2 = M^2 \left(1 + a_1 L_M + a_2 L_M^2 + a_3 L_M^3 + a_4 L_M^4 + a_5 L_M^5 + \cdots \right), \qquad (\text{I.60})$$

where L_M is defined in (I.42). The coefficients $a_1, \ldots, a_5$ are give in Tab. I.1 for $N = 3$ and general N. The result for $N = 3$ agrees with the known results for a_1 and a_2 given in (I.42) and the leading term in N at each order agrees with the expansion of the all-order result in the large N expansion (I.57). Note that the large N approximation is definitely not a good approximation to the $N = 3$ coefficients.

The result (I.60) can be inverted and we find again a better converging expansion.

$$M^2 = M_{phys}^2 \left(1 + b_1 L_{M_{phys}} + b_2 L_{M_{phys}}^2 + b_3 L_{M_{phys}}^3 + b_4 L_{M_{phys}}^4 + b_5 L_{M_{phys}}^5 + \cdots \right).$$
$$(\text{I.61})$$

The coefficients $b_1, \ldots, b_5$ are give in Tab. I.2 for $N = 3$ and general N. Just as

(a)   (b)
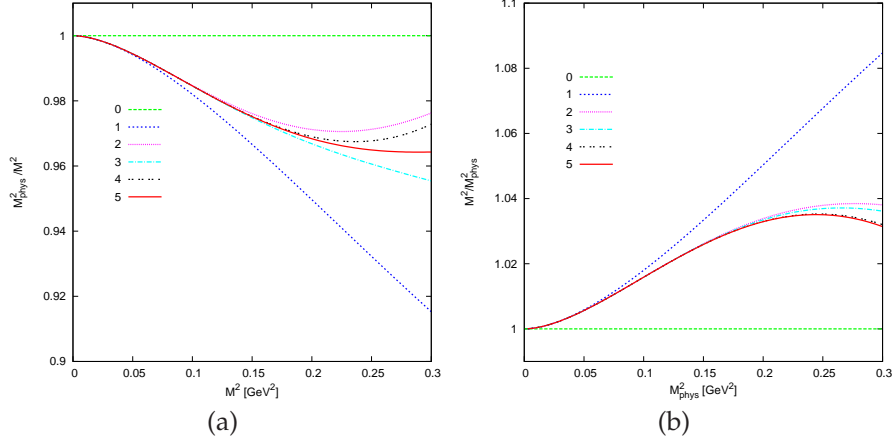
Figure I.6: The expansions of the leading logarithms order by order for $F = 0.090$ GeV, $\mu = 1$ GeV and $N = 3$. (a) M^2_{phys} in terms of M^2 Eq. (I.60) (b) M^2 in terms of M^2_{phys} Eq. (I.61).

the coefficients in (I.59) are much smaller than in (I.57) we see that the b_i are much smaller than the a_i.

In order to get a feeling of the size of these corrections and of the convergence of the series for the very relevant case $N = 3$ we have plotted them in Fig. I.6. On the left side we see the result (I.60) and on the right side the result (I.61) for a value of $F = 0.090$ GeV amd $\mu = 1$ GeV. Both clearly converge in the region shown and the inverse one clearly converges faster.

I.6   Conclusions and discussion

In this paper we have obtained three main results.

First we provided an alternative proof for the results of [9] for the leading divergence at any loop order. Our proof relies of course on the same physical principles as the one in [9] but is simpler algebraically.

Our second result is the large N expansion of the *massive* nonlinear $O(N)$ sigma model, we did not use the analog of the methods in [15] for the massless case but obtained a recursive equation to sum all the relevant cactus diagrams. This method is clearly extendable to other processes than the mass we considered here. The formula obtained for the mass in the large N limit (I.51) is remarkably simple. Its relevance for the real case $N = 3$ is not clear, since the large N result gives a rather poor approximation to the a_i coefficients when $N = 3$, as shown in Tab. I.1.

The third result is the actual calculation for general N of the leading logarithm for the meson mass to five-loop order. This result agrees with the known two-loop result for $N = 3$ and with the derived result for the leading term in N.

It is clear that the methods developed in this paper can be applied to other processes as well, both the large N method and the leading logarithms to higher loop orders for general N. Work is in progress for the decay constant, $\pi\pi$-scattering and the formfactors [26].

Acknowledgments

I

I.7   Integrals

We can get rather high powers of momenta in our the integrals. Let us first look at integrals without external momenta. These are of the form

$$I_{mn} = \frac{1}{i} \int \frac{d^d q}{(2\pi)^d} \frac{q_{\mu_1} \cdots q_{\mu_m}}{(q^2 - M^2)^n} \, . \tag{I.62}$$

This vanishes for m odd, and for even m we can use[5]

$$q_{\mu_1} \cdots q_{\mu_m} \quad \rightarrow \quad \frac{1}{2^{m/2} \left(\frac{n}{2} + 1\right)!} \left(q^2\right)^{m/2} G_{\mu_1 \dots \mu_m} ,$$

$$G_{\mu_1 \dots \mu_m} \quad = \quad g_{\mu_1 \mu_2} \cdots g_{\mu_{m-1} \mu_m} + g_{\mu_1 \mu_3} \cdots . \tag{I.63}$$

Where $g_{\mu\nu}$ is the metric tensor. The right hand side of the last term consists of all possible ways to put the Lorentz indices on the metric tensor $g_{\mu_i \mu_j}$ and is symmetric under all interchanges of the indices. After that we use recursively

$$\frac{q^2}{q^2 - M^2} = 1 + \frac{M^2}{q^2 - M^2} \tag{I.64}$$

---

[5]The formula is only valid for $d = 4$ which is sufficient for our purpose. We derived it using recursive methods but it is probably well known in the higher loop integral community.

to obtain terms either without propagators or without powers of q^2. Of the resulting integrals only two have a divergent part

$$
\begin{aligned}
\frac{1}{i} \int \frac{d^d q}{(2\pi)^d} \frac{1}{(q^2 - M^2)} &= \frac{1}{16\pi^2} \frac{M^2}{\epsilon} + \text{finite}, \\
\frac{1}{i} \int \frac{d^d q}{(2\pi)^d} \frac{1}{(q^2 - M^2)^2} &= \frac{1}{16\pi^2} \frac{1}{\epsilon} + \text{finite},
\end{aligned}
\tag{I.65}
$$

with $d = 4 - 2\epsilon$.

We need to do know the divergent parts of one-loop integrals with up to 5 propagators for this calculation. This we do by combining propagators using Feynman parameters and then shifting the momentum variable to obtain integrals of the type (I.62). The Feynman parameter integrals needed are always simple polynomial ones.

The above procedure can be programmed in FORM to work recursively.

I   References

[1] S. Weinberg, "Phenomenological Lagrangians," *Physica* **A96** (1979) 327.

[2] J. Gasser and H. Leutwyler, "Chiral Perturbation Theory to One Loop," *Ann. Phys.* **158** (1984) 142.

[3] J. Gasser and H. Leutwyler, "Chiral Perturbation Theory: Expansions in the Mass of the Strange Quark," *Nucl. Phys.* **B250** (1985) 465.

[4] J. Gasser and H. Leutwyler, "Low-Energy Theorems as Precision Tests of QCD," *Phys. Lett.* **B125** (1983) 325.

[5] L.-F. Li and H. Pagels, "Perturbation theory about a Goldstone symmetry," *Phys. Rev. Lett.* **26** (1971) 1204–1206.

[6] G. Colangelo, "Double chiral logs in the pi pi scattering amplitude," *Phys. Lett.* **B350** (1995) 85–91, `arXiv:hep-ph/9502285`.

[7] J. Bijnens, G. Colangelo, and G. Ecker, "Double chiral logs," *Phys. Lett.* **B441** (1998) 437–446, `arXiv:hep-ph/9808421`.

[8] J. Bijnens, "Chiral Perturbation Theory Beyond One Loop," *Prog. Part. Nucl. Phys.* **58** (2007) 521–586, `arXiv:hep-ph/0604043`.

[9] M. Buchler and G. Colangelo, "Renormalization group equations for effective field theories," *Eur. Phys. J.* **C32** (2003) 427–442, `arXiv:hep-ph/0309049`.

[10] M. Bissegger and A. Fuhrer, "Chiral logarithms to five loops," *Phys. Lett.* **B646** (2007) 72–79, `arXiv:hep-ph/0612096`.

[11] M. Bissegger and A. Fuhrer, "A renormalizable effective theory for leading logarithms in ChPT," *Eur. Phys. J.* **C51** (2007) 75–82, `arXiv:hep-ph/0701132`.

[12] N. Kivel, M. V. Polyakov, and A. Vladimirov, "Chiral Logarithms in the Massless Limit Tamed," *Phys. Rev. Lett.* **101** (2008) 262001, `arXiv:0809.3236 [hep-ph]`.

[13] N. A. Kivel, M. V. Polyakov, and A. A. Vladimirov, "Leading Chiral Logarithms for Pion Form Factors to Arbitrary Number of Loops," *JETP Lett.* **89** (2009) 529–534, `arXiv:0904.3008 [hep-ph]`.

[14] J. A. M. Vermaseren, "New features of FORM," `arXiv:math-ph/0010025`.

I

[15] S. R. Coleman, R. Jackiw, and H. D. Politzer, "Spontaneous Symmetry Breaking in the O(N) Model for Large N*," *Phys. Rev.* **D10** (1974) 2491.

[16] J. Bijnens, "Chiral Lagrangians and Nambu-Jona-Lasinio - like models," *Phys. Rept.* **265** (1996) 369–446, `arXiv:hep-ph/9502335`.

[17] J. Bijnens, G. Colangelo, and G. Ecker, "The mesonic chiral Lagrangian of order p**6," *JHEP* **02** (1999) 020, `arXiv:hep-ph/9902437`.

[18] J. Bijnens, G. Colangelo, and G. Ecker, "Renormalization of chiral perturbation theory to order p**6," *Annals Phys.* **280** (2000) 100–139, `arXiv:hep-ph/9907333`.

[19] I. Jack and H. Osborn, "Two loop background field calculations for arbitrary background fields," *Nucl. Phys.* **B207** (1982) 474.

[20] S. Weinberg, "Nonlinear realizations of chiral symmetry," *Phys. Rev.* **166** (1968) 1568–1577.

[21] S. R. Coleman, J. Wess, and B. Zumino, "Structure of phenomenological Lagrangians. 1," *Phys. Rev.* **177** (1969) 2239–2247.

[22] J. Bijnens, G. Colangelo, G. Ecker, J. Gasser, and M. E. Sainio, "Pion pion scattering at low energy," *Nucl. Phys.* **B508** (1997) 263–310, `arXiv:hep-ph/9707291`.

[23] U. Burgi, "Pion polarizabilities and charged pion pair production to two loops," *Nucl. Phys.* **B479** (1996) 392–426, `arXiv:hep-ph/9602429`.

[24] A. Dobado and J. Morales, "Pion mass effects in the large N limit of chi(PT)," *Phys. Rev.* **D52** (1995) 2878–2890, `arXiv:hep-ph/9407321`.

[25] S. Weinberg, "Effective field theories in the large N limit," *Phys. Rev.* **D56** (1997) 2303–2316, `arXiv:hep-th/9706042`.

[26] J. Bijnens and L. Carloni, "The Massive O(N) Non-linear Sigma Model at High Orders," *Nucl. Phys.* **B843** (2011) 55–83, `arXiv:1008.3499 [hep-ph]`.

II

The Massive $O(N)$ Non-linear Sigma Model at High Orders

Johan Bijnens and Lisa Carloni

Department of Astronomy and Theoretical Physics, Lund University
Sölvegatan 14A, SE–223 62 Lund, Sweden

II

We extend our earlier work on the massive $O(N)$ nonlinear sigma model to other observables. We derive expressions at leading order in the large N expansion at all orders in the loop expansion for the decay constant, vacuum expectation value, meson-meson scattering and the scalar and vector form factors. This is done using cactus diagram resummation using a generalized gap equation and other recursion relations. For general N we derive the expressions for the n-th loop order leading logarithms $(M^2/F^2 \log(\mu^2/M^2))^n$, up to five-loops for the decay constant and vacuum expectation value (VEV) and up to four-loops for meson-meson scattering, the scalar and vector form factors. We also quote our earlier result for the mass. The large N results do not give a good approximation for the case $N = 3$. We use our results to study the convergence of the perturbative series and compare with elastic unitarity.

II.1   Introduction

In a renormalizable field theory, given enough time and computer power, one may calculate an observable up to any order n in the perturbative expansion, study the convergence of the series and make a precision comparison with experimental results. In the absence of complete higher order calculations, a first estimate of the convergence of the perturbative series may come from the so-called leading logarithms (LL). These are terms of the form $\alpha^n \log^n \mu^2$, with μ the renormalization scale, which appear in the n-th order corrections of any observable's expression upon renormalization. The coefficients of these LL may be calculated using renormalization group methods.

In a non-renormalizable field theory the situation is more convoluted, since new terms appear in the Lagrangian at each order in the expansion. However, as Li and Pagels pointed out [1] to one-loop, the n-loop-order contributions will still contain a $c_n \log^n(\mu^2/M^2)$ term. Consider for example the expansion of the pion mass in the quark masses in Chiral Perturbation Theory [2]:

$$M_\pi^2 = M^2 \left[1 + \frac{M^2}{(4\pi F)^2} \left(-\frac{1}{2} \log \frac{M^2}{\mu^2} + \ell_3^r(\mu) \right) + \cdots \right] \tag{II.1}$$

where ℓ_3^r is a renormalized second order Lagrangian coupling and M and F are the lowest order Lagrangian parameters. Depending upon the μ^2/M^2 ratio, where the parameter M^2 is the lowest-order mass and μ is the renormalization scale, the term with the logarithm can be the largest part of the correction. In general the LL, now depending on a typical scale $\mathcal{M}$ of the process one looks at, may turn out to be a substantial fraction of the n-th-order correction. For many observables indeed the LL are the main contribution due to the enhancement of $\log(\mu^2/M^2)$ compared to the other contributions at the same order. This is true in particular for the $\pi\pi$ S-wave scattering length a_0^0 [2, 3] in Chiral Perturbation Theory (ChPT).

Many corrections of this type at one-loop have been calculated long ago, see the review [4] and references therein, mostly in the framework of Current Algebra, and in ChPT [2, 5, 6].

Weinberg pointed out in 1979 [5] that, because of renormalization group equations (RGE), the two-loop LL coefficient appearing in $\pi\pi$ scattering amplitude could be calculated using simple one-loop diagrams. This method was later used in [7] for two loop LL corrections to scattering lengths and slopes in $\pi\pi$ scattering and in [8] for the general three-flavour meson sector. Nowadays the extension to the full two-loop expressions for mesons is known for most observables [9].

Weinberg's renormalization argument was extended by Büchler and Colangelo [10] to all orders and to a generic non-renormalizable theory. They showed that the leading logarithms at any loop-order can be calculated using one-loop diagrams. They also showed that the coefficient of the leading

logarithm only depends upon the constants appearing in the lowest-order Lagrangian. In principle this coefficient at n-loop-order could have depended on all of the coupling constants in the Lagrangians $\mathcal{L}_m$ with $m < n$.

However, the problem remains that as n grows, the number of terms and counterterms in the Lagrangian grows very rapidly, and the renormalization group equations (RGE) become more involved. This renders the calculation of LL beyond the first few orders a Herculean task[1].

The alternative to performing these long calculations is to extract the LL series from a renormalizable theory in hopes that it will reproduce the LLs of the non-renormalizable theory. The authors of [12] applied this approach to the renormalizable linear sigma model and were able to resum the entire LL series by exploiting recursion relations. They however found recursive relations were not possible in the non-renormalizable non-linear sigma case [12].

In the massless case, a solution to managing the terms in the Lagrangian was found since the number of meson legs on the vertices one needs to consider remains limited [13]. This was used for meson-meson scattering [13] and the scalar and vector form factor [14] in the massless $O(N)$ model. This method works to arbitrarily high order and agrees with the known large N [15] results to all orders [13,14]. In the massless case, one may also use kinematic methods to extract the nonanalytic dependence on kinematic quantities. These have for instance been used to derive the form factors [16] up to five loop-order and to arbitrarily high order for both the form factors and the meson-meson scattering amplitude [17]. These methods essentially solve the leading logarithm problem in the massless case for the most useful observables.

In the massive case (which includes ChPT), however, tadpole diagrams no longer vanish and one needs to consider terms with an increasing numbers of meson legs. E.g. for the meson mass one needs to calculate one-loop diagrams with $2n$ meson legs in order to get the n-loop-order LL. In our earlier work [18] we showed that one does not need to explicitly construct the higher order Lagrangians in a symmetric form, nor does one need a minimal Lagrangian at each order. The LL series only requires order by order a complete enough Lagrangian to describe the observable at hand [18]. This means that one may let the algorithm itself generate all the necessary terms in the higher order Lagrangians.

We applied this method to obtain the leading logarithm to five-loop-order for the meson mass in the nonlinear $O(N)$-model. One set of results of this paper is to extend the calculation to the decay constant and vacuum expectation value also to five-loop-order. A similar amount of work allows to obtain the leading logarithms for meson-meson scattering and the scalar and vector form factors to four-loops and we present results for this as well. For

---

[1]See for example the two-loop leading logarithm in the non leptonic sector [11].

$N = 3$ the massive non linear $O(N)$ model is equivalent to two-flavour mesonic ChPT Lagrangian at lowest order in the sense that $O(4)/O(3)$ is isomorphic to $SU(2)_L \times SU(2)_R/SU(2)_V$. We have thus obtained the leading logarithms also for this physically interesting case to rather high loop-order.

In [18] we also extended the large N limit to the massive case and applied it for the meson mass. In this paper we extend those methods to many more observables and we find for all the cases considered simple expressions in terms of the physical quantities. However, as already observed in the massless case [13, 14] and for the mass [18], we again find that the large N result does not give a good approximation to the coefficient of the leading logarithm for general N and in particular not for $N = 3$.

We briefly summarize the methods for calculating leading logarithms of [10, 18] in Sect. II.2 and introduce the massive $O(N)$ nonlinear sigma model including external fields in Sect. II.3. Here we also define all the physical quantities we calculate. The next section discusses the large N-limit. We briefly recall the results of [18] and extend the method to the other observables. The leading logarithms for general N are discussed in Sect. II.5. There we also discuss the convergence of the various observables and compare some ways of expanding. The main results and conclusions are summarized in the last section.

One note about the cross-checks on our results. All calculations were performed using four different parametrizations for the fields. This means that for every parametrization the form of the Lagrangian and the couplings are different. These four different Lagrangians were fed into the same form FORM code [19]. The fact that the output for all observables came out the same regardless of the parametrization is a very good sanity check.

II.2   Counter terms and Leading Logarithms

In this section we present the results of [10] and [18]. We show how to calculate the LL coefficients and their connection to the counter terms used to renormalize the observable.

In order to calculate the matrix elements for the observables, consider the generating functional

$$W[j] = e^{iZ[j]}/\hbar = \int \mathcal{D}\phi_i e^{iS[\phi, j]/\hbar}. \tag{II.2}$$

where j is the classical source which allows one to extract all of the Green functions. The action S may be expanded around the classical action, $S = \sum_{n=0}^{\infty} \hbar^n S^{(n)}$. In practice one expands the Lagrangian into a sum of growing $\hbar$

order (bare) Lagrangians

$$\mathcal{L} = \sum_{n=0}^{\infty} \hbar^n \mathcal{L}^{(n)}. \tag{II.3}$$

The crucial difference between renormalizable and non-renormalizable theories is the number of terms appearing in each $\mathcal{L}^{(n)} = \sum_{i}^{N_n} c_i^{(n)} O_i^{(n)}$. In the former case the terms in all $\mathcal{L}^{(n)}$ are of the same form as in $\mathcal{L}^{(0)}$. In the later case, new terms appear at each order n. When calculating matrix elements beyond tree level, the loop corrections lead to divergences, which must be re-absorbed into a redefinition of the coupling constants. While for a renormalizable theory it suffices to reabsorb them into lowest order Lagrangian since they are all of the same form, in a non-renormalizable theory a divergence is absorbed by the higher order coupling constants. E.g. the divergence that appeared in the calculation of (II.1) was absorbed into ℓ_3. Alternatively, one may say that the renormalization consists in adding to the Lagrangian order by order operators $\mathcal{O}_i^{(n)}$ with diverging coefficients to cancel divergences, i.e. counterterms $c_{ik}^{(n)} \mathcal{O}_i^{(n)} / \epsilon^k$.

$$\mathcal{L}^{(n)} = \frac{1}{\mu^{\epsilon n}} \left[\mathcal{L}^{(n),\text{ren}} + \mathcal{L}^{(n),\text{div}} \right] = \frac{1}{\mu^{\epsilon n}} \left[c_{i0}^{(n)}(\mu) \mathcal{O}_i^{(n)} + \sum_{k=1}^{n} \frac{c_{ik}^{(n)} \mathcal{O}_i^{(n)}}{\epsilon^k} \right]. \tag{II.4}$$

where we have assumed one works in dimensional regularization[2], in which divergences appear as poles $1/\epsilon^k$, $\epsilon = 4 - d$. We have shown in [18] that set operators $\mathcal{O}_i^{(n)}$ need not be minimal or even complete for our purposes.

Consider an observable and the one particle irreducible (1PI) diagrams that may contribute at order n. That one only needs to consider 1PI diagrams was proven in [10]. Let L_ℓ^n be the n-th order contribution from ℓ loops. L_ℓ^n consists of a finite part and (possibly) several different poles

$$L_\ell^n = L_{\ell 0}^n + \sum_{k=1}^{l} \frac{L_{\ell k}^n}{\epsilon^k}. \tag{II.5}$$

In $L_{\ell k}^n / \epsilon^k$ we include only those divergences coming from the loop integration and not those coming from the diverging $c_{ik}^{(m)} \mathcal{O}_i$ vertices in the loops. Each loop may contain different $c_{ik}^{(m)} \mathcal{O}_i$ vertices. We indicate with $\{c\}_\ell^n$ the product $c_{i_1 k_1}^{(m_1)} c_{i_2 k_2}^{(m_2)} \cdots c_{i_r k_r}^{(m_r)}$ giving an n-th order, ℓ-loop contribution.

The recursive equations follow from the requirement that the divergences must cancel. The contribution at order $\hbar$ may be written as

$$\frac{1}{\epsilon} \left[\frac{1}{\mu^\epsilon} L_{00}^1 \left(\{c\}_1^1 \right) + L_{11}^1 \right] + \frac{1}{\mu^\epsilon} L_{00}^1 \left(\{c\}_0^1 \right) + L_{10}^1. \tag{II.6}$$

---

[2]The pre-factor $\frac{1}{\mu^{\epsilon n}}$ ensures that all Lagrangians have the same dimension d.

where $L^1_{11} = L^1_{11}\left(\{c\}^0_0\right)$. Expanding $\mu^{-\epsilon} = 1 - \epsilon \log \mu + \cdots$, one finds that to cancel the $1/\epsilon$ we need

$$L^1_{00}\left(\{c\}^1_1\right) = -L^1_{11}. \tag{II.7}$$

This determines all the needed $c^{(1)}_{i1}$ in terms of the lowest order parameters. From (II.6) we also get the explicit dependence on μ

$$-L^1_{00}\left(\{c\}^1_1\right)\log \mu = L^1_{11}\log \mu \tag{II.8}$$

where the equality follows from (II.7). To summarize, the counterterm $c^{(1)}_{11}$ is adjusted so that it cancels the divergence coming from the loop, L^1_{11}, this in turn determines the μ dependence and hence the coefficient of the LL. At second order the cancellation of the $1/\epsilon^2$ and $\log(\mu)/\epsilon$ pieces allow to obtain the leading divergence $c^{(2)}_{i2}$ from the one-loop part $L^2_{11}(\{c\}^1_1)$ and expanding μ^ϵ one finds that the coefficient of the LL $\log^2(\mu)$, is L^2_{22}. See [18] for a more detailed discussion.

These results may be generalized. At order n one may write

$$\frac{1}{\epsilon^n}\left[\frac{1}{\mu^{n\epsilon}}L^n_{00}\left(\{c\}^n_n\right) + \frac{1}{\mu^{(n-1)\epsilon}}L^n_{11}\left(\{c\}^{n-1}_{n-1}\right) + \cdots + \frac{1}{\mu^\epsilon}L^n_{n-1,n-1}\left(\{c\}^1_1\right) + L^n_{nn}\right]. \tag{II.9}$$

Requiring that the coefficients of $1/\epsilon^n, \log \mu/\epsilon^{n-1}, \log^2 \mu/\epsilon^{n-2}, \ldots$ cancel leads to a set of n equations, the solution of which is given by [18]

$$L^n_{n-i,n-i}\left(\{c\}^i_i\right) = (-1)^i \begin{pmatrix} n \\ i \end{pmatrix} L^n_{nn}. \tag{II.10}$$

In particular,

$$L^n_{11}\left(\{c\}^{n-1}_{n-1}\right) = (-1)^{n-1}n L^n_{nn} \tag{II.11}$$

and

$$L^n_{11}\left(\{c\}^{n-1}_{n-1}\right) = (-n)L^n_{00} \tag{II.12}$$

The coefficient of the leading logarithm is given by

$$L^n_{nn}\left(\log \mu\right)^n. \tag{II.13}$$

Eq. (II.11) is solved recursively. First one calculates the one loop counterterm. With this one, using (II.11), one may calculate L^2_{22}, the coefficient of the second order LL. This again fixes the $c^{(2)}_{i2}$ counterterm, which can be inserted back into Eq. (II.11), and so on. One only needs to insure that all the $c^{(n-1)}_{i,n-1}$ for all the $\mathcal{O}^{(n-1)}_i$ appearing in the calculation are determined.

II.3 Massive nonlinear $O(N+1)/O(N)$ sigma model

The $O(N+1)/O(N)$ nonlinear sigma model, including external sources[3], is described by the Lagrangian

$$\mathcal{L}_{n\sigma} = \frac{F^2}{2} D_\mu \Phi^T D^\mu \Phi + F^2 \chi^T \Phi, \qquad (\text{II}.14)$$

where Φ is a real $N+1$ vector, $\Phi^T = (\Phi^0 \ \Phi^1 \ \dots \ \Phi^N)$, which transforms as the fundamental representation of $O(N+1)$ and satisfies the constraint $\Phi^T \Phi = 1$. The covariant derivative is given by

$$\begin{aligned} D_\mu \Phi^0 &= \partial_\mu \Phi^0 + a_\mu^a \Phi^a, \\ D_\mu \Phi^a &= \partial_\mu \Phi^a + v^{ab} \Phi^b - a_\mu^a \Phi^0. \end{aligned} \qquad (\text{II}.15)$$

The vector sources satisfy $v_\mu^{ab} = -v_\mu^{ba}$ and correspond to the unbroken group generators while the axial a_μ^a sources correspond to the broken ones. Indices of the type $a, b, \dots$ run over $1, \dots, N$ in the remainder. The mass term $\chi^T \Phi$ contains the scalar, s^0, and pseudo-scalar, p^a external fields as well as the explicit symmetry breaking term M^2.

$$\chi^T = \left((2Bs^0 + M^2) \ p^1 \ \dots \ p^N \right). \qquad (\text{II}.16)$$

The term proportional to M^2 breaks the $O(N+1)$ symmetry explicitly to the $O(N)$, whereas the vacuum condensate

$$\langle \Phi^T \rangle = (1 \ 0 \ \dots \ 0), \qquad (\text{II}.17)$$

breaks it spontaneously to the same $O(N)$.

This particular model corresponds to lowest order two-flavour ChPT for $N = 3$ [2, 20]. It is also used as a model for a strongly interacting Higgs sectors in several beyond Standard models, see e.g. [21, 22].

---

[3]If one wishes to study a given current J^μ one adds an extra classical source field v_μ to the generating functional which couples to that current. Thus the generating functional becomes

$$W[j, v_\mu] = \int \mathcal{D}\phi e^{i \int (\mathcal{L} - j\phi - v_\mu J^\mu)} / \hbar.$$

The matrix elements involving J^μ can be obtained by functional derivation with respect to v_μ

$$J^\mu(x) = \left. \frac{\delta \log W}{\delta v_\mu(x)} \right|_{v_\mu = 0}.$$

The terminology for the external sources or fields is taken from two-flavour ChPT. The vector currents for $N = 3$ are given by $v^{ab} = \varepsilon^{cab}v^c$ with ε^{cba} the Levi-Civita tensor. The electromagnetic current at lowest order is associated to v^3. The external scalar source s^0 is instead associated to the QCD current $-\overline{u}u - \overline{d}d$ as in [2].

We write Φ in terms of a real N-component[4] vector ϕ, which transforms linearly under the unbroken part of the symmetry group, $O(N)$. In the calculations, for simplicity, we will refer to one particular parametrization, called Φ_1 below. We have, however, made use of four different parametrizations in order to check the validity of our results. These are

$$\Phi_1 = \begin{pmatrix} \sqrt{1 - \frac{\phi^T \phi}{F^2}} \\ \frac{\phi}{F} \end{pmatrix} \qquad \Phi_2 = \frac{1}{\sqrt{1 + \frac{\phi^T \phi}{F^2}}} \begin{pmatrix} 1 \\ \frac{\phi}{F} \end{pmatrix}$$

$$\Phi_3 = \begin{pmatrix} 1 - \frac{1}{2}\frac{\phi^T \phi}{F^2} \\ \sqrt{1 - \frac{1}{4}\frac{\phi^T \phi}{F^2}}\, \frac{\phi}{F} \end{pmatrix} \qquad \Phi_4 = \begin{pmatrix} \cos\sqrt{\frac{\phi^T \phi}{F^2}} \\ \sin\sqrt{\frac{\phi^T \phi}{F^2}}\, \frac{\phi}{\sqrt{\phi^T \phi}} \end{pmatrix}.$$

Φ_1 is the parametrization used in [2], Φ_2 a simple variation, Φ_3 is such that the explicit symmetry breaking term in (II.14) only gives a mass term to the ϕ field but no vertices. Φ_4 is the parametrization one ends up with if using the general prescription of [23].

The physical mass of the meson (squared), M_{phys}^2, we already calculated in [18]. The meson decay constant, F_{phys}, is defined by the matrix element of the axial current $j_{a,\mu}^b$

$$\langle 0|j_{a,\mu}^b|\phi^c(\mathbf{p})\rangle = iF_{\text{phys}}\mathbf{p}_\mu \delta^{bc}. \tag{II.18}$$

The lowest order is $F_{\text{phys}} = F$.

The vacuum expectation value (VEV) is defined by

$$V_{\text{phys}} = \langle -j_{s^0}^0 \rangle \overset{N=3}{=} \langle \overline{u}u + \overline{d}d \rangle. \tag{II.19}$$

In the second equation we have written out its meaning in terms of quarks. Its lowest order value is $V_{\text{phys}} \equiv V_0 = -2BF^2$.

The scalar form factor is defined as the matrix element of the scalar current between two mesons

$$\langle \phi^a(\mathbf{p}_f)| - j_{s^0}^0 |\phi^a(\mathbf{p}_i)\rangle = F_S[(\mathbf{p}_f - \mathbf{p}_i)^2]. \tag{II.20}$$

The value at zero momentum transfer can be derived from the meson mass via the Feynman-Hellmann theorem as

$$F_S(0) = 2B\frac{\partial M_{\text{phys}}^2}{\partial M^2}. \tag{II.21}$$

---

[4]We refer to these as a flavour components.

The vector form factor is defined similarly as

$$\langle \phi^a(\mathbf{p}_f)|j^{cd}_{V,\mu} - j^{dc}_{V,\mu}|\phi^b(\mathbf{p}_i)\rangle = \left(\delta^{ac}\delta^{db} - \delta^{ad}\delta^{bc}\right)i(\mathbf{p}_f + \mathbf{p}_i)^\mu F_V\left[(\mathbf{p}_f - \mathbf{p}_i)^2\right],\quad \text{(II.22)}$$

where we have exploited the antisymmetry of v^{ab}_μ. The vector currents j^c_V for the $N = 3$ are given by $j^{ab} = j^c_V \varepsilon^{cab}$ with ε^{cab} the Levi-Civita tensor. The electromagnetic current in this case to the lowest order is given by $j^3_{V,\mu} = (\bar{u}\gamma_\mu u - \bar{d}\gamma_\mu d)/2$. The singlet part does not appear to lowest order. The value of the vector form factor at $(\mathbf{p}_f - \mathbf{p}_i)^2 = 0$ is always 1 because of the conserved $O(N)$ symmetry.

In addition to the form factors we also define the radii and curvatures with $t = (\mathbf{p}_f - \mathbf{p}_i)^2$ and expanding around $t = 0$:

$$
\begin{aligned}
F_S(t) &= F_S(0)\left(1 + \frac{1}{6}\langle r^2\rangle_S t + c_S t^2 + \cdots\right). \\
F_V(t) &= 1 + \frac{1}{6}\langle r^2\rangle_V t + c_V t^2 + \cdots.
\end{aligned}
\quad \text{(II.23)}
$$

The final process we discuss is meson-meson scattering. The general amplitude is

$$
\begin{aligned}
\langle \phi^a(\mathbf{p}_a)\phi^b(\mathbf{p}_b)|\phi^c(\mathbf{p}_c)\phi^d(\mathbf{p}_d)\rangle &= \delta^{ab}\delta^{cd}A(s,t,u) + \delta^{ac}\delta^{bd}A(t,u,s) \\
&\quad + \delta^{ad}\delta^{bc}A(u,s,t),
\end{aligned}
\quad \text{(II.24)}
$$

with

$$s = (\mathbf{p}_a + \mathbf{p}_b)^2, \qquad t = (\mathbf{p}_a - \mathbf{p}_c)^2 \qquad u = (\mathbf{p}_a - \mathbf{p}_d)^2, \quad \text{(II.25)}$$

satisfying $s + t + u = 4M^2_{\text{phys}}$. $A(s,t,u)$ is symmetric in t and u. The proof of (II.24) for $N = 3$ is done using crossing and isospin symmetry [5], but may be generalized to the $O(N)$ symmetry case. There are three channels, the singlet, antisymmetric and symmetric combination, named $I = 0, 1$ and 2 (after isospin conservation). The amplitude in these three channels is given by

$$
\begin{aligned}
T^0(s,t) &= NA(s,t,u) + A(t,u,s) + A(u,s,t) \\
T^1(s,t) &= A(t,u,s) - A(u,s,t) \\
T^2(s,t) &= A(t,u,s) + A(u,s,t).
\end{aligned}
\quad \text{(II.26)}
$$

These amplitudes are projected onto the partial waves

$$T^I_\ell = \frac{1}{64\pi}\int_{-1}^{1} d(\cos\theta)P_\ell(\cos\theta)T^I(s,t), \quad \text{(II.27)}$$

with θ the scattering angle and P_ℓ the Legendre polynomials. Near threshold the partial waves can be expanded in terms of scattering lengths a^I_ℓ and slopes b^I_ℓ.

$$\Re\left[T^I_\ell\right] = q^{2\ell}\left(a^I_\ell + b^I_\ell q^2 + \cdots\right), \quad \text{(II.28)}$$

II

where $q^2 \equiv \frac{1}{4}\left(s - 4M_{\text{phys}}^2\right)$. The scattering lengths and slopes are normally given in units of powers of M_{phys}.

For all the quantities defined here, the $N = 3$ results with a complete $O(p^6)$ Lagrangian are known up to two loops, thus including the leading logarithms. This is an additional check on our calculation.

The results can be expressed in terms of the lowest order parameters, expanding in powers of

$$L = \frac{M^2}{16\pi^2 F^2} \log \frac{\mu^2}{M^2} \, , \tag{II.29}$$

or in terms of the physical mass and physical decay constant using

$$L_{\text{phys}} = \frac{M_{\text{phys}}^2}{16\pi^2 F_{\text{phys}}^2} \log \frac{\mu^2}{M_{\text{phys}}^2} \, . \tag{II.30}$$

In both cases we chose the mass scale in the logarithm to be the corresponding mass. In [18] we also used an expansion in

$$L_{M_{\text{phys}}} = \frac{M_{\text{phys}}^2}{16\pi^2 F^2} \log \frac{\mu^2}{M_{\text{phys}}^2} \, . \tag{II.31}$$

We use this hybrid form in this paper only for one figure.

II.4   Large N limit

When we consider the limit of large N we have to decide how the constants in the Lagrangian (II.14) depend on N. The first term can be made linear (extensive) in N by assuming $F^2 \propto N$ since $\Phi^T \Phi = 1$. The second term is then also linear in N if we set M^2 and B to be independent of N.

In the linear $O(N)$ model it is well known [15, 21] that the leading contribution in N comes from diagrams that contain only non-overlapping loops and in which each factor $1/N$ coming from a new interaction is canceled by the factor N introduced by summing over the N internal mesons in each bubble. In [18] we showed how this is also true in general for the non linear case which has vertices with any number of meson fields. The proof in [18] remains valid when vertices with external fields are included. The vertices with more mesons legs are suppressed by powers of $1/F$ as was the case for the purely mesonic vertices. The suppression factor compared to the lowest order of $1/F^{2L}$ with L the number of loops remains thus valid as well.

In Fig. II.1 we show such a typical diagram contributing to the meson self energy. All of these diagrams can be resummed by exploiting recursive methods.
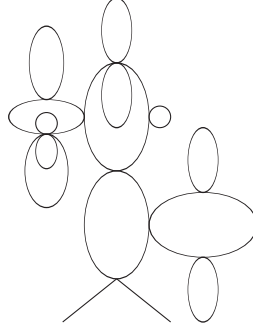
Figure II.1: A typical diagram which contributes at leading order in *N*. Note that vertices can have many different loops attached since the Lagrangians contain vertices with any number of fields. The flavour-loops coincide with momentum loops, i.e. the visible bubbles.

II

Figure II.2: The graphical representation of the equation that generates all the cactus diagrams for the propagator. A thick line indicates the full propagator, a thin line the lowest order one.

Consider for instance the inverse of the full propagator, it is given by the inverse of the lowest order propagator and the sum of all the 1PI diagrams with two external legs. By starting out with the lowest order propagator on the right hand side (rhs) and then reinserting the solution recursively we generate all cactus diagrams. In [18] we used this method to show that the full propagator in parametrization 1 in the large *N* limit is

$$i\Delta_{\text{full}}(\mathbf{q}^2) = \frac{i}{\mathbf{q}^2 - M_{\text{phys}}^2} \, . \tag{II.32}$$

Note that, as shown in [18] and below, in this parametrization in this limit there is no wavefunction renormalization. Let us note once more that in the following we derive the results in the first parametrization but the others can also be used and give the same results.

This method is similar to the gap equation used in e.g. NJL models [24]

Figure II.3: The graphical representation of the equation that generates all the one-particle-irreducible cactus diagrams for the decay constant. A thick line indicates the full propagator. The photon line indicates the insertion of the axial current a_μ^a.

but we have here an infinite number of terms on the right hand side. Similar resummations may be used for the other observables as shown below.

For completeness we quote the result for the physical mass [18], it is the solution of

$$M^2 = M_{\text{phys}}^2 \sqrt{1 + \frac{N}{F^2} \overline{A}(M_{\text{phys}}^2)}\,, \tag{II.33}$$

with

$$\overline{A}(M^2) = \frac{M^2}{16\pi^2} \log \frac{\mu^2}{M^2}\,. \tag{II.34}$$

Note that in non renormalizable field theories the large N limit also depends upon how $\mathcal{L}^{(n)}$ depend on N. The result (II.33) and those derived below assume that the finite part of any higher order coefficient vanishes, $c_{i0}^{(n>0)} = 0$, see [25] for a discussion. The formulas still give the leading logarithms even for non zero higher order coefficients as long as the Lagrangian remains at most linear in N.

II.4.1 Decay constant

From the Lagrangian (II.14) we can extract the vertices involving the axial current $j_a^{;\mu}$. These are given by $F^2(\partial^\mu \Phi^0 a_\mu^a \Phi^a - \partial^\mu \Phi^a a_\mu^a \Phi^0)$. In the first representation Φ_1, this leads to the couplings

$$a_\mu^a F \left[\phi^a \partial_\mu \sqrt{1 - \frac{\phi^T \phi}{F^2}} - \partial_\mu \phi^a \sqrt{1 - \frac{\phi^T \phi}{F^2}} \right]\,. \tag{II.35}$$

All 1PI cactus diagrams contributing to the matrix element in (II.18) can be generated by the diagrams with full propagators shown in Fig. II.3. Each of the tadpole loops in Fig. II.3 must contribute a factor of N, to be leading in N, thus it must be generated by the contraction of a $\phi^T \phi = \phi^b \phi^b$ pair, with a sum over the flavour index b. All other contractions only give subleading powers in N.

The first term in (II.35) then gives only terms with at least one loop integral that vanishes since it is odd in momentum.

We are thus left with the term

$$-F\partial_\mu\phi^a\mathcal{A}^\mu\sqrt{1-\frac{\phi^T\phi}{F^2}} \simeq -F\partial_\mu\phi^a\mathcal{A}^\mu\left[1-\frac{\phi^b\phi^b}{2F^2}+...\right].\tag{II.36}$$

When the ϕ^b are contracted, they give i^2 times the loop integral $A(M^2_{\text{phys}}) = (1/i)\int\frac{d^d p}{(2\pi)^d}/(p^2-M^2_{\text{phys}})$. Note that the mass in this expression is the physical mass and that the propagators in Fig. II.3 in the loops are the full propagators.

We now show that the wave function renormalization vanishes in parametrization 1. The part of the Lagrangian that can produce momentum dependence in the full propagator is given by

$$\mathcal{L}_{\text{kin}} = \frac{F^2}{2}\partial_\mu\Phi^T\partial^\mu\Phi = \frac{F^2}{2}\partial_\mu\sqrt{1-\frac{\phi^T\phi}{F^2}}\partial_\mu\sqrt{1-\frac{\phi^T\phi}{F^2}} + \frac{1}{2}\partial_\mu\phi^T\partial^\mu\phi.\tag{II.37}$$

The corrections to the canonical kinetic term come from the first term, which can be rewritten as

$$\begin{aligned}
\mathcal{L}_{\text{kin}}^{\text{corr}} &= \frac{1}{2F^2}\frac{(\phi^a\partial_\mu\phi^a)(\phi^b\partial^\mu\phi^b)}{1-\frac{\phi^T\phi}{F^2}} \\
&= \frac{1}{2F^2}(\phi^a\partial_\mu\phi^a)(\phi^b\partial^\mu\phi^b)(1+\frac{\phi^c\phi^c}{F^2}+\cdots).
\end{aligned}\tag{II.38}$$

In order to have a non-zero loop diagram the derivatives must either both act on internal legs or both on external legs. Either way, since the contracted legs must have the same flavour, $a \equiv b$, so there can be no sum over the flavour index and thus no leading in N correction. This means that in the large N approximation one has $Z = 1$ in this parametrization (this will not be true in general).

Putting the terms together, we find the physical decay constant to be related to the low energy constants F and M^2 by the simple relation

$$F_{\text{phys}} = F\sqrt{1+\frac{N}{F^2}A(M^2_{\text{phys}})}.\tag{II.39}$$

To get the LL series one should expand the square root, replace $A(M^2_{\text{phys}})$ by $\overline{A} = \frac{M^2_{\text{phys}}}{16\pi^2}\log\mu^2/M^2_{\text{phys}}$ and express the M^2_{phys} in terms of $L = \frac{M^2}{16\pi^2 F^2}\log\frac{\mu^2}{M^2}$.

To express this result in terms of the physical F_{phys} and M^2_{phys} instead, we can square (II.39) to obtain

$$1+\frac{N}{F^2}\overline{A}(M^2_{\text{phys}}) = \frac{1}{1-\frac{N}{F^2_{\text{phys}}}\overline{A}(M^2_{\text{phys}})},\tag{II.40}$$

II

Figure II.4: The equation for the vacuum expectation value V_{phys}. The open thin lined dots indicate an insertion of $-s^0$. A thick line indicates the full propagator.

which allows us to rewrite (II.33) and (II.39) as

$$
\begin{aligned}
M_{\text{phys}}^2 &= M^2 \sqrt{1 - \frac{N}{F_{\text{phys}}^2} \overline{A}(M_{\text{phys}}^2)}, \\[2mm]
F_{\text{phys}} &= \frac{F}{\sqrt{1 - \frac{N}{F_{\text{phys}}^2} \overline{A}(M_{\text{phys}}^2)}}.
\end{aligned}
\tag{II.41}
$$

II.4.2   Vacuum Expectation Value

In a similar fashion one can calculate the leading N vacuum expectation value series. Consider the second term in (II.14)

$$
F^2 \chi^T \Phi.
\tag{II.42}
$$

where $\chi^T = 2B_0(s^0 \;\; 0 \;\; \cdots \;\; 0)$. In the first representation this becomes

$$
2BF^2 \sqrt{1 - \frac{\phi^T \phi}{F^2}} = 2BF^2 \left(1 - \frac{1}{2} \frac{\phi^c \phi^c}{F^2} + \cdots \right).
\tag{II.43}
$$

In this case there is no need for wave function renormalization. In Fig. II.4 we show how the vacuum condensate is given by the sum of all the tadpole diagrams obtained by contracting the $\phi^c \phi^c$ fields in all possible ways. As explained for the decay constant, the leading in N contribution comes from the contractions of the same flavour index, i.e. $\phi^c \phi^c$. Each loop again implies the integral $A(M_{\text{phys}}^2)$. This leads to the following expressions for the vacuum expectation value in terms of the low energy constants F, M^2 and in terms of the physical F_{phys} and M_{phys}^2

$$
V_{\text{phys}} = V_0 \sqrt{1 + \frac{N}{F^2} \overline{A}(M_{\text{phys}}^2)},
\tag{II.44}
$$

or

$$
V_{\text{phys}} = \frac{V_0}{\sqrt{1 - \frac{N}{F_{\text{phys}}^2} \overline{A}(M_{\text{phys}}^2)}}.
\tag{II.45}
$$
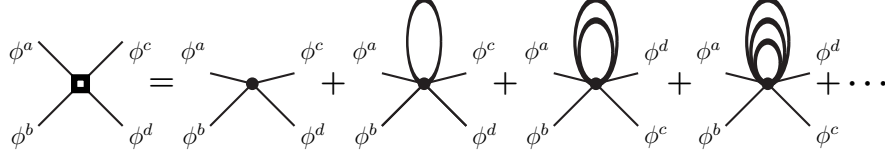
Figure II.5: The effective vertex for meson-meson scattering. The thick lines correspond to the full propagator produced by the graphs in Fig. II.2. The large dots are vertices from the Lagrangian (II.14).

II.4.3 $\pi\pi$-scattering amplitude

The meson-meson scattering amplitude defined in (II.24) in the leading N approximation is somewhat more involved. There is ample literature on the subject, see for example [15, 26] and more recently [13, 17], which deal with linear or nonlinear massless $O(N+1)/O(N)$ sigma models. In the massive case there is the additional complication that tadpoles do not vanish. As for the previous observables, in order to be leading in N, each momentum loop must correspond to a sum over the N flavours. We deal with all the generated cactus diagrams in three steps.

First, we consider all insertions on a meson line that do not carry away momentum and/or flavour. They can be dealt with simply by using the full propagator obtained earlier.

Next we deal with effective four-meson couplings, described by the left hand side (lhs) of the Eq. in Fig. II.5. These can be produced by resumming all the generalized tadpoles shown on the rhs in Fig. II.5, just as we did for M^2_{phys}, F_{phys} and for V_{phys}, see Figs. II.2, II.3 and II.4 respectively.

In the massive non-linear sigma model case, the effective four-ϕ couplings come from both the kinetic and the mass part of the Lagrangian. In the first representation these may be written as

$$\mathcal{L}^{(n\geq 4)\phi} = \frac{F^2}{2}\partial_\mu\sqrt{1-\frac{\phi^T\phi}{F^2}}\partial^\mu\sqrt{1-\frac{\phi^T\phi}{F^2}} + F^2M^2\sqrt{1-\frac{\phi^T\phi}{F^2}} - F^2M^2 + \frac{M^2}{2}\phi^T\phi.$$

(II.46)

Note that we have removed the kinetic terms that give the lowest order propagator. The first term may be expanded into

$$\mathcal{L}^{(n\geq 4)\phi}_{\text{kin}} = \frac{1}{2F^2}\frac{\partial_\mu\phi^a\phi^a\partial^\mu\phi^b\phi^b}{1-\frac{\phi^T\phi}{F^2}} = \frac{1}{2F^2}\left(\partial_\mu\phi^a\phi^a\partial^\mu\phi^b\phi^b\right)\sum_n\left(\frac{\phi^T\phi}{F^2}\right)^n.$$

(II.47)

The loops appearing on the rhs of the equation in Fig II.5 may be treated in

the leading N limit as before. The derivatives cannot both appear in the loops at leading order in N for the same reasons valid for wave function renormalization.

The $\mathcal{L}_{\text{kin}}^{(n\geq4)\phi}$ thus leads to an effective vertex

$$\frac{1}{2F^2}\frac{\partial_\mu\phi^a\phi^a\partial^\mu\phi^b\phi^b}{1+y} \tag{II.48}$$

where $y = \frac{N}{F^2}A(M_{\text{phys}}^2)$. The loop integral $A(M_{\text{phys}}^2)$ is again produced by the $\phi^T\phi = \phi^c\phi^c$ contractions.

$\mathcal{L}_{\text{mass}}^{(n\geq4)\phi}$ may be expanded with $\sqrt{1-\frac{\phi\phi}{F^2}} = \sum_{n=0}^{\infty}\begin{pmatrix} 1/2 \\ n \end{pmatrix}\left(-\frac{\phi^T\phi}{F^2}\right)^n$. As before, the loops must each come from one $\phi^T\phi$ pair, but now we have to take into account the number of ways in which the $\phi^T\phi$ pairs can be attached to the four external legs. For a term $(\phi^T\phi)^n$ there are $n(n-1)/2$ ways to select four outer fields and to contract the remaining $n-2$ pairs. If each contraction leads to a factor $-A(M_{\text{phys}}^2)$, then for each flavour the $(\phi^T\phi)^n$ term will contribute $(\phi^T\phi)^2/2\, n(n-1)[-A(M_{\text{phys}}^2)/F^2]^n$. The $\mathcal{L}_{\text{mass}}^{(n\geq4)\phi}$ will then contribute $(\phi^T\phi)^2/2\sum_{n=0}^{\infty}\begin{pmatrix} 1/2 \\ n \end{pmatrix}n(n-1)[-NA(M_{\text{phys}}^2)/F^2]^n$, which is the second derivative of $\sqrt{1-NA(M_{\text{phys}}^2)/F^2}$ with respect to $NA(M_{\text{phys}}^2)/F^2$.

The effective four meson vertex coming from the mass term is thus

$$-\frac{M^2}{8F^2}\frac{(\phi^T\phi)^2}{(1+y)^{(3/2)}}\,. \tag{II.49}$$

Using (II.33) and (II.39) one may write the total effective vertex which has the same form as the lowest order vertex but with physical quantities

$$\frac{1}{2F_{\text{phys}}^2}\phi^a\partial_\mu\phi^a\,\phi^b\partial^\mu\phi^b - \frac{M_{\text{phys}}^2}{8F_{\text{phys}}^2}\phi^a\phi^a\phi^b\phi^b\,. \tag{II.50}$$

This effective vertex corresponds to the first diagram in Fig. II.6 and leads to an amplitude $(p_a+p_b)\cdot(p_c+p_d) - M_{\text{phys}}^2$. Each of these vertices is the building block for the remaining diagrams in Fig. II.6.

We now concentrate on the $A(s,t,u)\delta^{ab}\delta^{cd}$ part of the amplitude defined in (II.24). The corrections to $(p_a+p_b)\cdot(p_c+p_d) - M_{\text{phys}}^2$ are generated by the fish-like diagrams given in Fig. II.6. This sum is very similar to the sum over bubbles used in the NJL model [24]. The structure of the vertex is such that for leading N it does not depend on the loop integral. Each flavour loop in
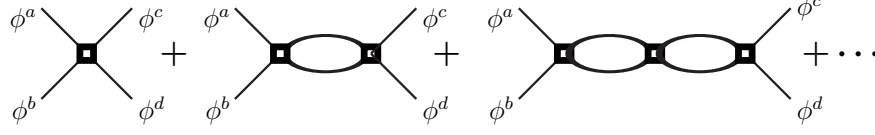
Figure II.6: The remaining diagrams for $A(s, t, u)$. The vertex is the one obtained from the effective vertex (II.50) with $\delta^{ab}\delta^{cd}$.

Fig. II.6 thus adds a factor

$$\frac{N(s - M^2_{\text{phys}})}{2F^2_{\text{phys}}} B\left(M^2_{\text{phys}}, M^2_{\text{phys}}, s\right) \tag{II.51}$$

with $s = (\mathbf{p}_a + \mathbf{p}_b)^2$ and B the standard two-propagator loop integral

$$B(m^2, m^2, \mathbf{p}^2) = \frac{1}{i} \int \frac{d^d \mathbf{q}}{(2\pi)^d} \frac{1}{(\mathbf{q}^2 - m^2)((\mathbf{q} - \mathbf{p})^2 - m^2)} . \tag{II.52}$$

The factor $1/2$ is from the symmetry factor in the loop. The sum of diagrams forms a geometric series which becomes

$$A(s, t, u) = \frac{s - M^2_{\text{phys}}}{F^2_{\text{phys}}} \frac{1}{1 - \frac{N}{2} \frac{s - M^2_{\text{phys}}}{F^2_{\text{phys}}} B\left(M^2_{\text{phys}}, M^2_{\text{phys}}, s\right)} . \tag{II.53}$$

This expression is in agreement[5] with both the results in (II.63) and what was found by [13] in the $M^2 \to 0$ limit.

An alternative way to resum the diagrams in Fig. II.6 is with a recursion relation, as depicted in Fig. II.7. Let's denote $A(s, t, u)$ by a thick double line and a wave function renormalized leg by a thick single line (remember that in the large N limit $Z = 1$). The lhs of the equation is then is result we sought after. On the rhs we have the renormalized effective 4ϕ vertex plus the $A(s, t, u)$ multiplied the renormalized fish diagram.

As for the mass case, solving the equation by first writing the lowest order expression on the rhs, and reinserting the solution into the equation and so on generates the whole set of diagrams in Fig. II.6.

---

[5]Compared with [26] we found an extra factor $1/2$ in front of the $B(M^2_{\text{phys}}, M^2_{\text{phys}}, s)$ function coming from the symmetry factor of the loop. Note that they only worked to first order in the mass.
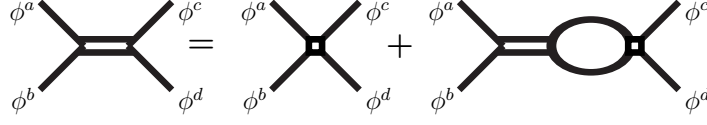
Figure II.7: The recursive equation which generates all the meson-meson scattering diagrams. The vertex is the effective vertex of (II.50). The double line is the full results for $A(s,t,u)$. The single thick line is the full meson propagator.
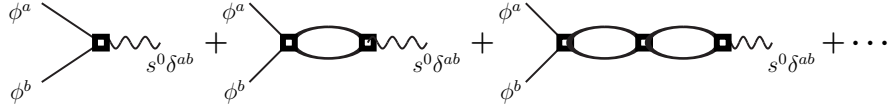
Figure II.8: The fish diagrams for the scalar form factor.

II.4.4   Vector and Scalar form factors

The vector and scalar form factors F_V and F_S in the large N limit are calculated in much the same manner. One constructs effective vertices and then sums the diagrams.

The result for the vector form factor is particularly simple. The vector form factor couplings come from $\mathcal{L}^{\text{kin}}$, in particular from $F^2(\Phi^T v_\mu \partial^\mu \Phi - \partial_\mu \Phi^T v^\mu \Phi)$. The effective vertex for the first parametrization $v_\mu^{ab}[\phi^a \partial^\mu \phi]$ is the same as the lowest order vertex and because of the antisymmetry in flavour indices of v_μ^{ab} there are also no diagrams similar to those of Fig. II.8. The full leading order in N result is thus

$$F_V(t) = 1. \tag{II.54}$$

The scalar current comes from $\mathcal{L}^{\text{kin}}$, which was discussed earlier for the VEV. The sum of all the tadpole diagrams leads to the effective vertex

$$-Bs^0 \frac{\phi^a \phi^a}{\sqrt{1+y}}. \tag{II.55}$$

In the scalar case however, one must also consider fish-like diagrams, see Fig. II.8. The arguments used for resumming these diagrams used for $\phi\phi$-scattering still apply.

The full result for the scalar form factor is thus

$$F_S(t) = \frac{F_S(0)}{1 - \frac{N}{2} \frac{t - M_{\text{phys}}^2}{F_{\text{phys}}^2} B\left(M_{\text{phys}}^2, M_{\text{phys}}^2, t\right)}, \tag{II.56}$$

with

$$F_S(0) = -\frac{V_{\text{phys}}}{F_{\text{phys}}^2}.$$ (II.57)

Here we have used the earlier results to write the expression in its simplest form.

II.5 Leading Logarithmic series for $O(N+1)/O(N)$

In this section we describe the calculation of the leading logarithms and quote results for various physical quantities. For a given observable O_{phys} we can write the leading logarithm expansion in many equivalent ways. The two we will use are of the form

$$O_{\text{phys}} = O_0 \left(1 + a_1 L + a_2 L^2 + \cdots \right),$$ (II.58)

with L defined in (II.29). We will also expand alternatively in the physical quantities

$$O_{\text{phys}} = O_0 \left(1 + c_1 L_{\text{phys}} + c_2 L_{\text{phys}}^2 + \cdots \right),$$ (II.59)

with L_{phys} defined in (II.30). In both cases we have chosen the mass scale in the logarithm to be the corresponding mass.

In [18] we described how to systematically take into account all the necessary diagrams for the renormalization of the ϕ mass up to five loops. At each order new diagrams are necessary. To renormalize the mass at one loop for instance, one must consider the $\mathcal{L}^0$ 4ϕ vertex and contract two of the legs. As the loop order grows, so does the number of outer legs one must consider and the number of possible one loop diagrams contributing. We give the related discussion here for the decay constant. The actual calculations were performed by using FORM [19] extensively.

II.5.1 Mass

The coefficients a_i of the logs L^i for the mass were calculated in [18] and are here reproduced for completeness in Tab. II.1. The coefficients in terms of fully physical quantities can be derived by using the results for the decay constant given below. They are given in Tab. II.2. The leading logarithm for the masses for $N = 3$ at two-loop was first calculated in [7] and later to full two-loop order in [27,28]. Our results agree with those.

In [18] we noticed that the expansion of M^2/M_{phys}^2 in $L_{M_{\text{phys}}}$ converged faster than the expansion of M_{phys}^2/M^2 in terms of L. This was true for both the

i	a_i for $N = 3$	a_i for general N
1	$-1/2$	$1 - 1/2\,N$
2	$17/8$	$7/4 - 7/4\,N + 5/8\,N^2$
3	$-103/24$	$37/12 - 113/24\,N + 15/4\,N^2 - N^3$
4	$24367/1152$	$839/144 - 1601/144\,N + 695/48\,N^2 - 135/16\,N^3$ $+231/128\,N^4$
5	$-8821/144$	$33661/2400 - 1151407/43200\,N + 197587/4320\,N^2$ $-12709/300\,N^3 + 6271/320\,N^4 - 7/2\,N^5$

Table II.1: The coefficients a_i of the leading logarithm L^i up to $i = 5$ for the physical meson mass [18].

i	c_i for $N = 3$	c_i for general N
1	$-1/2$	$1 - 1/2\,N$
2	$7/8$	$-1/4 + 3/4\,N - 1/8\,N^2$
3	$211/48$	$-5/12 + 7/24\,N + 5/8\,N^2 - 1/16\,N^3$
4	$21547/1152$	$347/144 - 587/144\,N + 47/24\,N^2 + 25/48\,N^3$ $-5/128\,N^4$
5	$179341/2304$	$-6073/1800 + 32351/2400\,N - 59933/4320\,N^2$ $+224279/43200\,N^3 + 761/1920\,N^4 - 7/256\,N^5$

Table II.2: The coefficients c_i of the leading logarithm L^i_{phys} up to $i = 5$ for the physical meson mass.

large N result and the general N case. From the large N result in (II.41) we would have naively expected to see a similar improvement in the expansion of M^2_{phys}/M^2 in terms of L_{phys}. Looking at the coefficients of Tab. II.2 one can see this is not the case. For completeness we also looked at the series of M^2/M^2_{phys} in terms of L_{phys}. The coefficients are of similar size as those in Tab. II.2.

We can now use these results to check the expansions and how fast they converge. In [18] the x-axis in Figs. 6(a) and (b) was unfortunately mislabeled. It should have been M [GeV] instead of M^2 [GeV^2]. We have therefore included a similar figure again. We chose $F = 0.090$ GeV and $\mu = 0.77$ GeV for the plots presented here in Fig. II.9. The expansion can also be done in the physical quantities and these we show as a function of M^2_{phys} with F_{phys} fixed at 0.093 GeV in Fig. II.10. Both cases have a similar convergence which is fairly slow for masses above about 300 MeV.
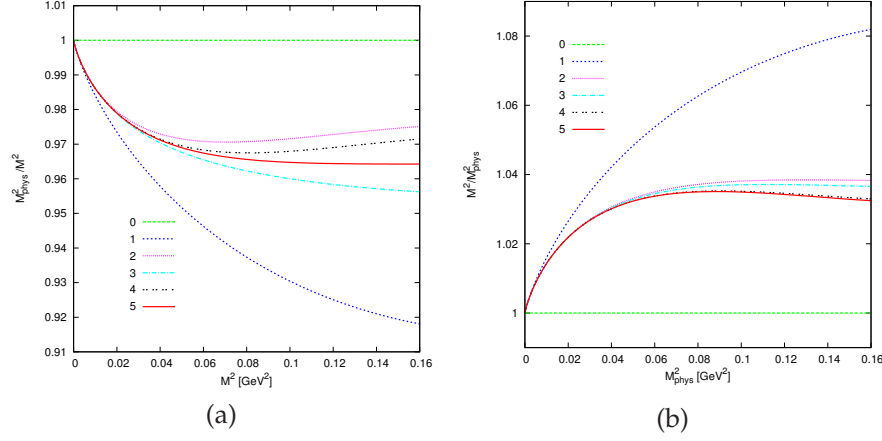
Figure II.9: The expansions of the leading logarithms order by order for $F = 0.090$ GeV, $\mu = 0.77$ GeV and $N = 3$. (a) M^2_{phys}/M^2, expansion in L. (b) M^2/M^2_{phys}, expansion in $L_{M_{\text{phys}}}$.
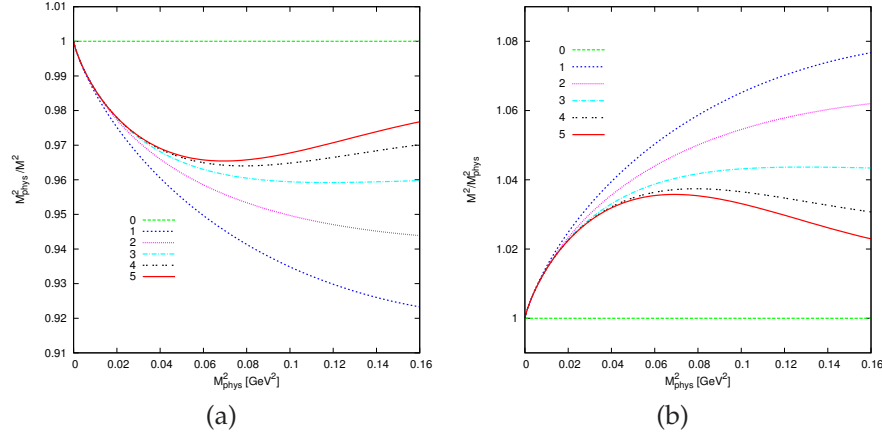
Figure II.10: The expansions of the leading logarithms order by order for $F_{\text{phys}} = 0.093$ GeV, $\mu = 0.77$ GeV and $N = 3$. (a) M^2_{phys}/M^2, expansion in L_{phys}. (b) M^2/M^2_{phys}, expansion in L_{phys}.

II.5.2   Decay constant

The decay constant F_{phys} is defined in (II.18). We thus need to evaluate a matrix-element with one external axial field and one incoming meson. The diagrams needed for the wave function renormalization were already evaluated
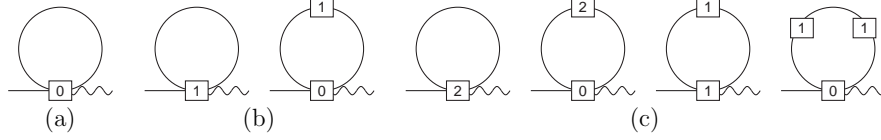
Figure II.11: The diagrams needed up to order 3 for the one particle irreducible diagrams with an external meson and an axial current. The wiggly line indicates the axial vector. Vertices of order $\hbar^i$ are indicated with $\boxed{i}$. (a) The diagram needed at order $\hbar$. (b) The 2 diagrams needed at order $\hbar^2$. (c) The 4 diagrams needed at order $\hbar^3$.
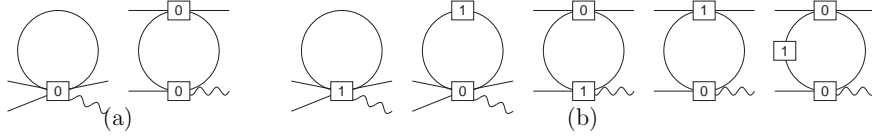
Figure II.12: The diagrams needed for the divergence of the 3-meson 1-axial-vector vertex. (a) The 2 diagrams to order $\hbar$. (b) the 5 diagrams to order $\hbar^2$

in the calculation for the mass [18] since we evaluated the inverse propagator there. What remains is thus the evaluation of all relevant 1PI diagrams with an external a_μ^a. At order $\hbar$ there is only one diagram, at $\hbar^2$ there are 2 and at order $\hbar^3$ there are 4. These are shown in Fig. II.11. We have not shown them but at order $\hbar^4$ there are 7 and at order $\hbar^5$ there are 13 diagrams to be calculated.

To order $\hbar$ it is sufficient to know the lowest-order Lagrangian, but at order $\hbar^2$ we need to know the (divergent part of the) vertices coming from the Lagrangian of order $\hbar$ with one and three external meson legs and one a_μ^a. The diagram of Fig. II.11(a) gives the divergence of the vertex with one meson and one axial vector leg but we also need to calculate the divergence of the vertex with three meson legs and one axial vector. This requires the diagrams shown in Fig. II.12(a).

To order $\hbar^3$, we need still more vertices, we need the divergence of the one meson one axial vector leg vertex to order $\hbar^2$. These diagrams we have already calculated, but we also need the four-leg vertex to order $\hbar^2$ which can be calculated from the diagrams in Fig. II.12(b). Inspection of the vertices there shows we already have all we need but for the five meson one axial vector leg vertex at order $\hbar$. To obtain that we also need to evaluate all diagrams shown in Fig. II.13. By now, the pattern should be clear, to get the mass at order $\hbar^n$ in [18] we needed the 2 and four-meson vertex at order $\hbar^{n-1}$, the 2, 4 and 6-meson vertex at order $\hbar^{n-2}$ and so on. Here we need for the decay constant
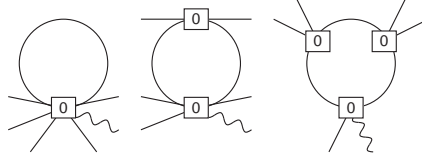
Figure II.13: The 3 diagrams needed for the divergence of the 6-meson vector to order $\hbar$.

to order $\hbar^n$ in addition the one meson one axial vector and three-meson–one-axial-vector vertex at order $\hbar^{n-1}$, the 1, 3 and 5-meson plus one axial vector vertex at order $\hbar^{n-2}$ and so on. Similarly one can see that to get the decay constant at order $\hbar^n$, we need to calculate one-loop diagrams with up to n vertices. The extension to order $\hbar^5$ shows that we we need to calculate the 18, 26, 33, 26 and 13 diagrams at orders $\hbar^1, \ldots, \hbar^5$ respectively for the mass/wave function renormalization and an additional 27, 45, 51, 33 and 13 diagrams at orders $\hbar^1, \ldots, \hbar^5$ for the 1PI diagrams with an axial-vector.

We have organized this calculation by first expanding the lowest-order Lagrangian to the order needed, up to vertices with 12 mesons or 11 mesons and one axial vertex. With these vertices we then calculate all 1PI diagrams with up to 10 external legs. The divergent part of all needed integrals can be calculated relatively easily using the technique described in App. I.7 of [18]. At this stage, the dependence on external momenta is also put back as derivatives on the external legs and everything assembled to give the divergent part at order $\hbar$ for all the vertices with up to 10 meson legs or nine mesons plus one axial-vector using (II.12). So we have assembled everything we need to calculate the one-loop divergences to order $\hbar^2$. The 26+45 diagrams are evaluated and we obtain the divergences at order $\hbar^2$ using (II.12). The process is then repeated up to order $\hbar^5$. All of the above steps have been programmed in FORM. The CPU time needed increases rapidly with the order n one wishes to reach. The Lagrangians at higher orders tend to contain very many terms and constructing the diagrams with many external legs at higher orders is also extremely time consuming. The CPU time used on a typical PC for the mass-divergence to order $\hbar^n$ was approximately 0.1 seconds for $\hbar$, 0.3 seconds for $\hbar^2$, 11 seconds for $\hbar^3$, 700 seconds for $\hbar^4$ and 30000 seconds for $\hbar^5$ plus a similar amount for the extra diagrams needed for the decay constant.

We now give the leading logarithms for the decay constant as a function of F and M^2 and of the physical F_{phys} and M^2_{phys}

$$F_{\text{phys}} \quad = \quad F\left(1 + a_1 L + a_2 L^2 + \cdots\right),$$

i	a_i for $N = 3$	a_i for general N
1	1	$-1/2 + 1/2\,N$
2	$-5/4$	$-1/2 + 7/8\,N - 3/8\,N^2$
3	$83/24$	$-7/24 + 21/16\,N - 73/48\,N^2 + 1/2\,N^3$
4	$-3013/288$	$47/576 + 1345/864\,N - 14077/3456\,N^2$ $+625/192\,N^3 - 105/128\,N^4$
5	$2060147/51840$	$-23087/64800 + 459413/172800\,N$ $-189875/20736\,N^2 + 546941/43200\,N^3$ $-1169/160\,N^4 + 3/2\,N^5$

Table II.3:　The coefficients a_i of the leading logarithm L^i for the decay constant F_{phys} in the case $N = 3$ and in the generic N case.

i	c_i for $N = 3$	c_i for general N
1	1	$-1/2 + 1/2\,N$
2	$5/4$	$1/2 - 7/8\,N + 3/8\,N^2$
3	$13/12$	$-1/24 + 13/16\,N - 13/12\,N^2 + 5/16\,N^3$
4	$-577/288$	$-913/576 + 2155/864\,N - 361/3456\,N^2 - 69/64\,N^3$ $+35/128\,N^4$
5	$-14137/810$	$535901/129600 - 2279287/172800\,N + 273721/20736\,N^2$ $-11559/3200\,N^3 - 997/1280\,N^4 + 63/256\,N^5$

Table II.4:　The coefficients c_i of the leading logarithm L^i_{phys} for the decay constant F_{phys} in the case $N = 3$ and in the generic N case.

$$F_{\text{phys}} \;\; = \;\; F\left(1 + c_1 L_{\text{phys}} + c_2 L^2_{\text{phys}} + \cdots\right). \qquad (\text{II}.60)$$

The first five a_i coefficients are listed in table II.3 for the generic N and for the interesting case $N = 3$. The equivalent results for the first five c_i are in table II.4. Note that once the expression of F_{phys} as a function of F is known one may express the remaining observables as a function of the physical M^2_{phys} and F_{phys}. This has already been used to calculate the c_i coefficients in tables II.2 and II.4 from the corresponding a_i.

We have plotted in Fig. II.14 the expansion in terms of the unrenormalized quantities and in terms of the physical quantities. In both cases we get a good convergence but it is excellent for the expansion in physical quantities.
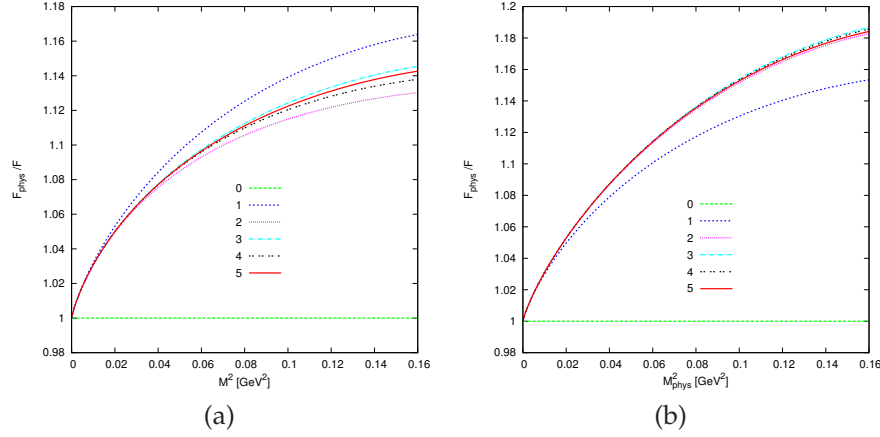
Figure II.14: The expansions of the leading logarithms order by order for $\mu = 0.77$ GeV and $N = 3$. (a) F_{phys}/F in terms of M^2, expansion in L with $F = 0.090$ GeV. (b) F_{phys}/F in terms of M^2_{phys}, expansion in L_{phys} with $F_{\text{phys}} = 0.093$ MeV fixed.

n	a_n for $N = 3$	a_n for general N
1	$3/2$	$+1/2\,N$
2	$-9/8$	$+3/4\,N - 3/8\,N^2$
3	$9/2$	$+3/2\,N - 3/2\,N^2 + 1/2\,N^3$
4	$-1285/128$	$+145/48\,N - 55/12\,N^2 + 105/32\,N^3 - 105/128\,N^4$
5	46	$+3007/480\,N - 1471/120\,N^2 + 557/40\,N^3$ $-1191/160\,N^4 + 3/2\,N^5$

II

Table II.5: The coefficients a_i of the leading logarithm L^i for the VEV V_{phys} in the case $N = 3$ and in the generic N case. Note that the coefficients in front of the first subleading N power are often large.

II.5.3 Vacuum expectation value

The expression for the leading logarithms of the vacuum expectation value V_{phys} follows from the definition (II.19). The diagrams needed and the principle of the calculation can be derived in the same way as we did for the decay constant in Sect. II.5.2. The first five coefficients a_i defined by

$$V_{\text{phys}} = -2BF^2 \left(1 + a_1 L + a_2 L^2 + \cdots \right),, \qquad (\text{II}.61)$$

are given in table II.5 for generic N and for the interesting case $N = 3$. The c_i for the leading logarithms in terms of physical quantities are given in table II.6.

n	c_n for $N = 3$	c_n for general N
1	$3/2$	$1/2\,N$
2	$21/8$	$-1/4\,N + 3/8\,N^2$
3	$75/16$	$1/4\,N - 1/2\,N^2 + 5/16\,N^3$
4	$1023/128$	$3/16\,N + 5/24\,N^2 - 59/96\,N^3 + 35/128\,N^4$
5	$2669/256$	$-4153/2880\,N + 12299/4320\,N^2 - 142/135\,N^3$
		$-167/320\,N^4 + 63/256\,N^5$

Table II.6: The coefficients c_i of the leading logarithm L^i_{phys} for the VEV V_{phys} in the case $N = 3$ and in the generic N case.
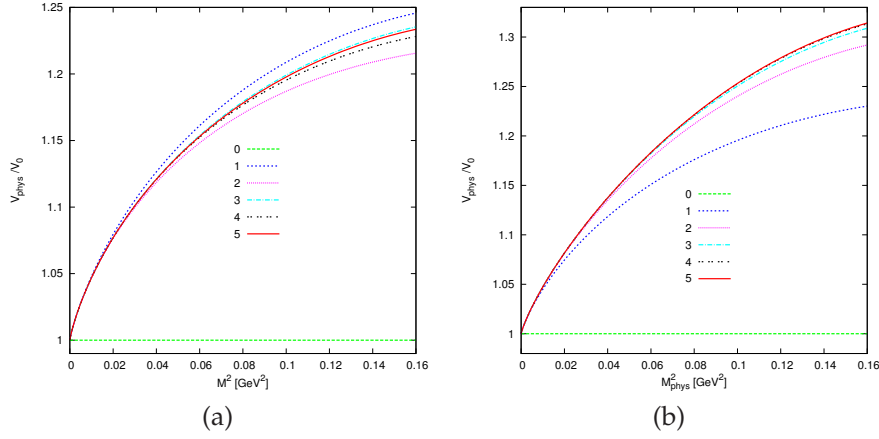
Figure II.15: The expansions of the leading logarithms order by order for $\mu = 0.77$ GeV and $N = 3$. (a) V_{phys}/V_0 in terms of M^2, expansion in L with $F = 0.090$ GeV. (b) V_{phys}/V_0 in terms of M^2_{phys}, expansion in L_{phys} with $F_{\text{phys}} = 0.093$ MeV fixed.

We have plotted in Fig. II.15 the expansion in terms of the unrenormalized quantities and in terms of the physical quantities. In both cases we get a good convergence but it is excellent for the expansion in physical quantities.

II.5.4 $\phi\phi$-scattering amplitude

Elastic $\pi\pi$-scattering is a the ideal interaction to test the convergence of the ChPT expansion since it only involves the $SU(2)_L \times SU(2)_R/SU(2)_V$ Goldstone bosons. It is also the simplest purely strong interaction process. This interaction has indeed been studied precisely for these reasons first by [29] at tree level and then by [2, 3] at one-loop level. One would expect the series to con-

verge rather rapidly, instead the authors of [3] found that some one-loop corrections were rather large. Specifically, as mentioned in the introduction, for the a_0^0 scattering length. On the other hand, the one-loop LL correction to a_1^1 arises only through F_π renormalization [7], which means that the chiral logs are not the main part of the one-loop correction. The issue of the convergence of the perturbative ChPT expansion for $\phi\phi$ scattering is delicate.

We have above obtained the all-order leading in large N result. From the calculations for the mass we have already obtained all the needed divergences to get the LL to four-loop order for meson scattering. The result can be written as expected in the form of (II.24). This is the first result where the choice of scale in the logarithm is not unique. We only quote here the expansion in terms of physical quantities and define

$$
\begin{aligned}
\tilde{s} &= \frac{s}{M_{\text{phys}}^2} \\
\Delta &= \frac{t-u}{M_{\text{phys}}^2} \\
L_{\mathcal{M}} &= \frac{M_{\text{phys}}^2}{16\pi^2 F_{\text{phys}}^2} \log\frac{\mu^2}{\mathcal{M}^2}\,.
\end{aligned}
\tag{II.62}
$$

II

with a generic scale $\mathcal{M}$. For scattering lengths an obvious choice is $\mathcal{M}=M_{\text{phys}}$ but in the massless case the choice is $\mathcal{M}^2=s$. Our result for general N is

$$
\begin{aligned}
\frac{F_{\text{phys}}^2}{M_{\text{phys}}^2}\,A(s,t,u) = \tilde{s} - 1 &+ L_{\mathcal{M}}\Big[(1/6\,\Delta^2 - \tilde{s}^2 + 1/2\,N\,\tilde{s}^2) + (11/3\,\tilde{s} - N\,\tilde{s}) \\
&+(-8/3 + 1/2\,N)\Big] + L_{\mathcal{M}}^2\Big[(5/96\,\tilde{s}\,\Delta^2 + 181/288\,\tilde{s}^3 + 5/96\,N\,\tilde{s}\,\Delta^2 \\
&-163/288\,N\,\tilde{s}^3 + 1/4\,N^2\,\tilde{s}^3) + (-5/12\,\Delta^2 - 91/36\,\tilde{s}^2 + 5/12\,N\,\Delta^2 \\
&+29/18\,N\,\tilde{s}^2 - 3/4\,N^2\,\tilde{s}^2) + (25/18\,\tilde{s} + 23/18\,N\,\tilde{s} + 3/4\,N^2\,\tilde{s}) + (4/3 \\
&-29/12\,N - 1/4\,N^2)\Big] + L_{\mathcal{M}}^3\Big[(361/17280\,\Delta^4 - 317/12960\,\tilde{s}^2\,\Delta^2 \\
&-21319/51840\,\tilde{s}^4 - 203/17280\,N\,\Delta^4 + 229/6480\,N\,\tilde{s}^2\,\Delta^2 \\
&+28081/51840\,N\,\tilde{s}^4 + 1/160\,N^2\,\Delta^4 + 11/1440\,N^2\,\tilde{s}^2\,\Delta^2 - 33/80\,N^2\,\tilde{s}^4 \\
&+1/8\,N^3\,\tilde{s}^4) + (-1901/25920\,\tilde{s}\,\Delta^2 + 51869/25920\,\tilde{s}^3 + 3073/25920\,N\,\tilde{s}\,\Delta^2 \\
&-49573/25920\,N\,\tilde{s}^3 + 41/288\,N^2\,\tilde{s}\,\Delta^2 + 8467/4320\,N^2\,\tilde{s}^3 - 1/2\,N^3\,\tilde{s}^3) \\
&+(1283/6480\,\Delta^2 - 907/720\,\tilde{s}^2 - 2503/2160\,N\,\Delta^2 - 7193/6480\,N\,\tilde{s}^2 \\
&+43/60\,N^2\,\Delta^2 - 3257/1080\,N^2\,\tilde{s}^2 + 3/4\,N^3\,\tilde{s}^2) + (-1189/1620\,\tilde{s} \\
&+2111/810\,N\,\tilde{s} + 607/108\,N^2\,\tilde{s} - 1/2\,N^3\,\tilde{s}) + (17/810 + 457/180\,N \\
&-22/5\,N^2 + 1/8\,N^3)\Big] + L_{\mathcal{M}}^4\Big[(1451/1244160\,\tilde{s}\,\Delta^4 + 6457/103680\,\tilde{s}^3\,\Delta^2
\end{aligned}
$$

$$+61781/248832\,\tilde{s}^5 + 143893/12441600\,N\,\tilde{s}\,\Delta^4 - 77957/2073600\,N\,\tilde{s}^3\,\Delta^2$$
$$-5387831/12441600\,N\,\tilde{s}^5 - 9089/1382400\,N^2\,\tilde{s}\,\Delta^4 + 5531/230400\,N^2\,\tilde{s}^3\,\Delta^2$$
$$+5592583/12441600\,N^2\,\tilde{s}^5 + 1/256\,N^3\,\tilde{s}\,\Delta^4 - 1/3840\,N^3\,\tilde{s}^3\,\Delta^2$$
$$-5267/21600\,N^3\,\tilde{s}^5 + 1/16\,N^4\,\tilde{s}^5) + (-6493/77760\,\Delta^4$$
$$+9023/103680\,\tilde{s}^2\,\Delta^2 - 684899/518400\,\tilde{s}^4 + 43523/345600\,N\,\Delta^4$$
$$-203777/1036800\,N\,\tilde{s}^2\,\Delta^2 + 20749/12150\,N\,\tilde{s}^4 - 19091/345600\,N^2\,\Delta^4$$
$$+146869/1036800\,N^2\,\tilde{s}^2\,\Delta^2 - 1840297/777600\,N^2\,\tilde{s}^4 + 7/320\,N^3\,\Delta^4$$
$$+143/5760\,N^3\,\tilde{s}^2\,\Delta^2 + 110897/86400\,N^3\,\tilde{s}^4 - 5/16\,N^4\,\tilde{s}^4)$$
$$+(-680609/1555200\,\tilde{s}\,\Delta^2 + 23719/103680\,\tilde{s}^3 - 331117/1555200\,N\,\tilde{s}\,\Delta^2$$
$$+2894959/1555200\,N\,\tilde{s}^3 + 16621/86400\,N^2\,\tilde{s}\,\Delta^2 + 2812631/777600\,N^2\,\tilde{s}^3$$
$$+77/288\,N^3\,\tilde{s}\,\Delta^2 - 153377/86400\,N^3\,\tilde{s}^3 + 5/8\,N^4\,\tilde{s}^3) + (39629/15552\,\Delta^2$$
$$+88013/129600\,\tilde{s}^2 - 186451/129600\,N\,\Delta^2 - 272671/77760\,N\,\tilde{s}^2$$
$$-9227/5400\,N^2\,\Delta^2 - 48067/6075\,N^2\,\tilde{s}^2 + 131/120\,N^3\,\Delta^2$$
$$+2017/3600\,N^3\,\tilde{s}^2 - 5/8\,N^4\,\tilde{s}^2) + (667007/48600\,\tilde{s}$$
$$-1109347/129600\,N\,\tilde{s} + 369719/43200\,N^2\,\tilde{s} + 2467/432\,N^3\,\tilde{s}$$
$$+5/16\,N^4\,\tilde{s}) + (-12349/864 + 102659/10800\,N + 36097/10800\,N^2$$
$$\left.-2887/480\,N^3 - 1/16\,N^4)\right] . \tag{II.63}$$

As for all other quantities we see large subleading in N corrections.

From the result (II.63) we can obtain the different amplitudes T^I defined in (II.26) and project on the partial waves using (II.27). The scattering lengths and slopes as defined in (II.28) can then obtained as well and we get the LL L^i_{phys} in terms of the physical M^2_{phys} and F_{phys}. We have LL contributions for all a^I_ℓ up to $\ell = 5$ and to the slopes up to $\ell = 4$. These we have all calculated for general N. We give the expansion in

$$d^I_{\ell,phys} = d^I_{\ell,tree}(1 + c_1 L^1_{\text{phys}} + c_2 L^2_{\text{phys}} + \cdots) \tag{II.64}$$

for the S-wave scattering lengths and slopes and only quote the phenomenologically relevant case of $N = 3$. As mentioned above a clear choice for the arbitrary scale in the logarithm is here the physical mass. The lowest order result and the expansion coefficients are given in table II.7. The one- and two-loop results agree with the earlier published ones [3, 7, 28][6]

We have plotted in Fig. II.16 the expansion in terms of the physical quantities of a^0_0 and a^2_0. There is an excellent convergence for mass up to 0.2 GeV but above 0.3 GeV it becomes rather slow for a^0_0. For a^2_0 it is somewhat better but also rather slow at the higher masses.

---

[6]The two-loop coefficients agree with those of [7] except for b^2_0. We have checked that using the full result from [28] and (3.13) in [7] reproduces our result.

d_ℓ^I	a_0^0	a_0^2	b_0^0	b_0^2
$d_{\ell,tree}^I$	$\dfrac{7M_{\text{phys}}^2}{32\pi F_{\text{phys}}^2}$	$\dfrac{-2M_{\text{phys}}^2}{32\pi F_{\text{phys}}^2}$	$\dfrac{8M_{\text{phys}}^2}{32\pi F_{\text{phys}}^2}$	$\dfrac{-4M_{\text{phys}}^2}{32\pi F_{\text{phys}}^2}$
c_1	$9/2$	$-3/2$	$26/3$	$-10/3$
c_2	$857/42$	$-31/6$	$1871/36$	$-169/36$
c_3	$153211/1512$	$-7103/216$	$2822/9$	$-352/9$
c_4	$41581/84$	$-7802/45$	$744463/43$	$-1309703/6480$

Table II.7:   The coefficients c_i of the leading logarithm series $d_{\ell,phys}^I = d_{\ell,tree}^I(1 + c_1 L_{\text{phys}}^1 + c_2 L_{\text{phys}}^2 + \cdots)$ for the $\mathcal{A}_{\pi\pi\to\pi\pi}$ for the scattering lengths, $d_\ell = a_0^0, a_0^2$, and for the slopes $d_\ell^I = b_0^0, b_0^2$ in the case $N = 3$. All in units of M_{phys}.
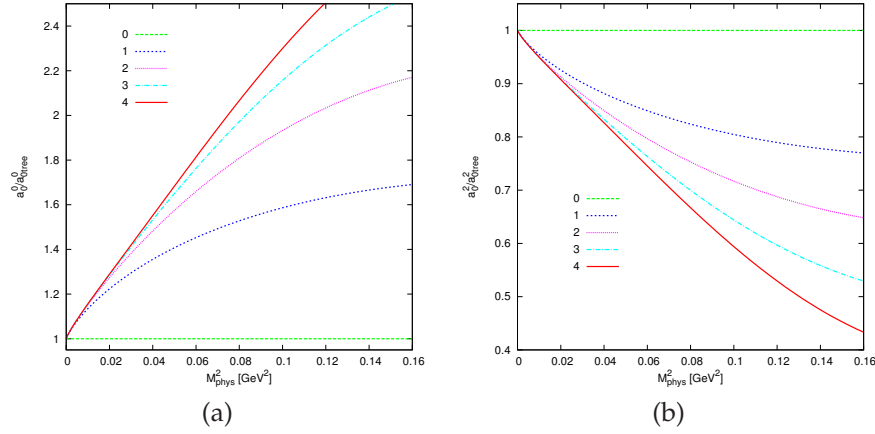
Figure II.16: The expansions of the leading logarithms order by order for $\mu = 0.77$ GeV and $N = 3$. (a) $a_0^0/a_{0\text{tree}}^0$ (b) $a_0^2/a_{0\text{tree}}^2$ in terms of M_{phys}^2, expansion in L_{phys} with $F_{\text{phys}} = 0.093$ MeV fixed.

In Fig. II.17 we plotted the expansion in terms of the physical quantities of the slopes b_0^0 and b_0^2. There is an excellent convergence for mass up to 0.25 GeV but above the convergence slower for b_0^0. b_0^2 converges better but also rather slow at the high mass end.

In the massless case we can obtain the coefficients at higher orders also with different methods [13, 17] and our result agrees with those. We can also use our result in this limit to test the often used elastic unitarity arguments.

(a)   (b)
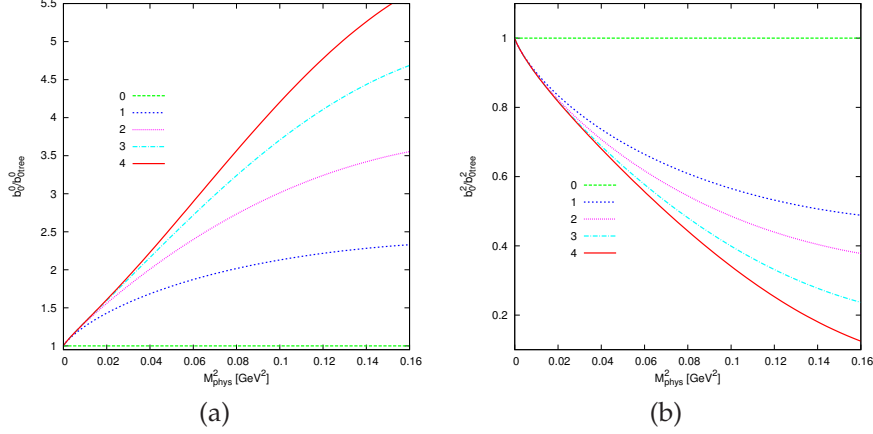
Figure II.17: The expansions of the leading logarithms order by order for $\mu = 0.77$ GeV and $N = 3$. (a) $b_0^0 / b_{0\text{tree}}^0$ (b) $b_0^2 / b_{0\text{tree}}^2$ in terms of M_{phys}^2, expansion in L_{phys} with $F_{\text{phys}} = 0.093$ MeV fixed.

The partial waves T_ℓ^I satisfy under the assumption of elastic unitarity

$$\Im \left[T_\ell^I \right] = \frac{\sqrt{s}}{2q} \left| T_\ell^I \right|^2 . \tag{II.65}$$

In the massless case the scale of the logarithm should be related to s and we know that this should come in the combination $l(\mu^2/s) = \ln|\mu^2/s| + i\pi\theta(s)$. The leading logarithm part can be written as

$$T_\ell^I = \sum_{n=0,\infty} e_n^I s^{n+1} l(\mu^2/s)^n . \tag{II.66}$$

In the chiral limit the interaction must vanish at $s = 0$. Inserting (II.66) in (II.65) and keeping only the leading logarithm part allows to determine all the higher coefficients in terms of the lowest order one.

$$e_n^I = \pi \left(\frac{e_0^I}{\pi} \right)^{n+1} . \tag{II.67}$$

Note that in the massless case there is really no regime where elastic unitarity (II.65) is valid. We are simply testing here how much of the leading logarithm in this case follows from the so-called righthand two-body cut. The result (II.67) can be written explicitly

$$T_\ell^I = \frac{e_0^I s}{1 - \frac{e_0^I s}{\pi} l(\mu^2/s)} . \tag{II.68}$$

	T_0^0		T_1^1		T_0^2	
e_ℓ^I	$\frac{1}{16\pi F_{\text{phys}}^2}$		$\frac{1}{32\pi F_{\text{phys}}^2}$		$\frac{-1}{32\pi F_{\text{phys}}^2}$	
	exact	elastic	exact	elastic	exact	elastic
f_1	25/18	1	0	1/2	$-10/9$	$-1/2$
f_2	25/18	1	5/4	1/4	35/36	1/4
f_3	18637/9720	1	$-901/3240$	1/8	$-50077/48600$	$-1/8$
f_4	540707/291600	1	207871/170100	1/16	134077/145800	1/16

Table II.8: The coefficients e_ℓ^I and f_i defined in (II.69) for the exact LL in the chiral limit and those derived using the assumption of elastic unitarity for the case $N = 3$ and T_0^0, T_1^1 and T_0^2.

In table II.8 we compare for $N = 3$ the exact coefficients derived from (II.63) with those from (II.68) for the expansion

$$T_\ell^I(s) = e_0^I s \left(1 + f_1 \frac{s}{16\pi^2 F_{\text{phys}}^2} l(\mu^2/s) + f_2 \left(\frac{s}{16\pi^2 F_{\text{phys}}^2} l(\mu^2/s) \right)^2 + \cdots \right). \quad \text{(II.69)}$$

It is clear from the table that the assumption of elastic unitarity does not give a good approximation to the LL in the chiral limit.

II

II.5.5 Form factors F_S and F_V

The vector and scalar form factors were defined in II.20 and II.22. The procedure to find the LL for this observable follow the same lines of the one for the decay constant, with the difference that in representation 1 the vertex between the meson fields and the vector current is simply given by

$$\mathcal{L}_{\text{int}} = (1/2)\, v_\mu^{ab} \left[\partial^\mu \phi_a \phi_b - \phi_a \partial_\mu \phi_b \right]. \quad \text{(II.70)}$$

For the wave function renormalization one may again use the results obtained for the mass calculation. As in the previous subsection we express here the results in terms of $\tilde{t} = t/M_{\text{phys}}^2$ and $L_{\mathcal{M}}$ with a scale $\mathcal{M}^2$ some combination of t and M_{phys}^2. The result for F_V to four-loop-order for the LL is:

$$F_V(t) = 1 + L_{\mathcal{M}} \left[1/6\,\tilde{t} \right] + L_{\mathcal{M}}^2 \left[\tilde{t}\,(-11/12 + 5/12\,N) + \tilde{t}^2\,(5/36 - 1/24\,N) \right]$$

$$+ L_{\mathcal{M}}^3 \left[\tilde{t}\,(+1387/648 - 845/324\,N + 7/9\,N^2) + \tilde{t}^2\,(-4007/6480 \right.$$

$$\left. + 3521/6480\,N - 29/180\,N^2) + \tilde{t}^3\,(+721/12960 - 47/1440\,N + 1/80\,N^2) \right]$$

n	$\langle r^2 \rangle_V$	c_V	$\langle r^2 \rangle_S$	c_S
c_1	1	—	6	—
c_2	2	$1/72$	$-29/3$	$43/36$
c_3	$853/108$	$-71/162$	$-581/54$	$-727/324$
c_4	$50513/1296$	$-25169/7776$	$-75301/648$	$4369/810$

Table II.9: The coefficients c_i of the expansion in L_{phys} in the expansion of the radii $\langle r^2 \rangle_{V,S}$ and the curvature $c_{V,S}$ in the $N = 3$ case.

$$+L_{\mathcal{M}}^4 \Big[\tilde{t} \left(-44249/15552 + 222085/31104\, N - 55063/10368\, N^2 \right.$$
$$+127/96\, N^3 \big) + \tilde{t}^2 \left(+349403/155520 - 15139/4860\, N + 86719/51840\, N^2 \right.$$
$$-199/480\, N^3 \big) + \tilde{t}^3 \left(-85141/155520 + 885319/1555200\, N \right.$$
$$-5303/19200\, N^2 + 21/320\, N^3 \big) + \tilde{t}^4 \left(+4429/103680 - 57451/1555200\, N \right.$$
$$+289/14400\, N^2 - 1/240\, N^3 \big) \Big]. \tag{II.71}$$

Note that $F_V(0) = 1$ as it should be. We can extract from this the expansion for the radius and curvature defined in (II.23). These are given in table II.9 in terms of the expansion in L_{phys} for the physical case $N = 3$. The general coefficients can be easily derived from (II.71). The dash indicates that this cannot appear to a given order for the LL. The result up to two-loop order agrees with the LL extracted from the full two-loop calculation [30]. We do not present numerical results for the vector form factor since these are dominated in the physical case $N = 3$ by the large higher order coefficient contributions, see e.g. [2, 30].

For the scalar form factor $F_S(t)$ defined in (II.20) we have already done the calculations we need to four-loop-order during the calculation for the VEV V_{phys} to five-loop-order. We write the result in the form

$$F_S(t) = F_S(0) f_S(t). \tag{II.72}$$

The value for $F_S(0)$ can be obtained from the calculation or via the Feynman-Hellman theorem in (II.21). The latter allows for the a_i coefficients for $F_S(0)$ expanded in terms of L to be derived easily from table II.1. We have checked that both methods agree. In table II.10 we quote the coefficients c_i of

$$F_S(0) = 2B \left(1 + c_1 L + c_2 L^2 + \cdots \right), \tag{II.73}$$

for the case $N = 3$ and general N.

	c_i for $N = 3$	c_i for general N
c_1	-1	$2 - N$
c_2	$31/8$	$5/4 - 1/4\,N + 3/8\,N^2$
c_3	$65/6$	$-5/3 + 41/12\,N + N^2 - 1/4\,N^3$
c_4	$76307/1152$	$655/144 - 901/144\,N + 341/48\,N^2 + 17/48\,N^3$ $+11/128\,N^4$

Table II.10: The coefficients c_i of the leading logarithm L_{phys}^i for the scalar form factor at zero momentum transfer $F_S(0)$ in the case $N = 3$ and in the generic N case.

We can now express $f_S(t)$ using the same notation as for $F_V(t)$.

$$
\begin{aligned}
f_S(t) = {} & 1 + L_{\mathcal{M}}\Big[\tilde{t}\,(-1/2 + 1/2\,N)\Big] + L_{\mathcal{M}}^2\Big[\tilde{t}\,(1/18 + 7/36\,N - 1/4\,N^2) \\
& + \tilde{t}^2\,(11/72 - 29/72\,N + 1/4\,N^2)\Big] + L_{\mathcal{M}}^3\Big[\tilde{t}\,(599/648 - 181/324\,N \\
& -53/108\,N^2 + 1/8\,N^3) + \tilde{t}^2\,(275/1296 - 427/648\,N + 301/432\,N^2 \\
& -1/4\,N^3) + \tilde{t}^3\,(-89/864 + 7/24\,N - 271/864\,N^2 + 1/8\,N^3)\Big] \\
& + L_{\mathcal{M}}^4\Big[\tilde{t}\,(-10981/3888 + 37373/7776\,N - 3733/2592\,N^2 - 23/48\,N^3 \\
& -1/16\,N^4) + \tilde{t}^2\,(-22859/28800 + 89951/48600\,N - 823067/777600\,N^2 \\
& -4021/21600\,N^3 + 3/16\,N^4) + \tilde{t}^3\,(-959/32400 + 82529/259200\,N \\
& -1421/2025\,N^2 + 51877/86400\,N^3 - 3/16\,N^4) + \tilde{t}^4\,(76459/1555200 \\
& -70997/388800\,N + 423961/1555200\,N^2 - 121/600\,N^3 + 1/16\,N^4)\Big].
\end{aligned}
$$
$$\tag{II.74}$$

From (II.74) we can derive the expression for the scalar radius and curvature defined in (II.23). The expansion coefficients c_i in terms of the physical logarithm L_{phys} are given in table II.9 for the physical case $N = 3$. The general case can be easily obtained from (II.74). The coefficients of the LL extracted from the full two-loop calculation of [30] agree.

In Fig. II.18 we plotted the expansion in terms of the physical quantities of the radius and curvature. There is an excellent convergence for masses up to 0.3 GeV but above the convergence is slower in both cases.

II.6 Conclusions

In this work we extended our previous work on the massive nonlinear $O(N + 1)/O(N)$ sigma model to many more observables. We calculated the

II
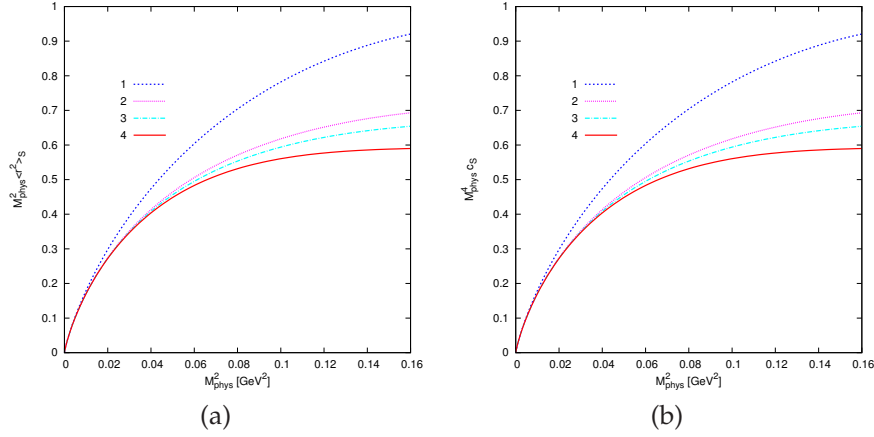
Figure II.18: The expansions of the leading logarithms order by order for $\mu = 0.77$ GeV and $N = 3$. (a) $M_{\mathrm{phys}}^2 \langle r^2 \rangle_S$ (b) $M_{\mathrm{phys}}^4 c_S$ in terms of M_{phys}^2, expansion in L_{phys} with $F_{\mathrm{phys}} = 0.093$ MeV fixed.

leading logarithmic corrections to the decay constant and the vacuum expectation value to five-loop-order and to the scalar and vector form factors and meson-meson scattering to four-loop order for generic N. We used these results to extract scattering lengths and slopes and have presented the physically most relevant cases for $N = 3$ of these. Results for all other cases have been obtained but would have added significantly to the length of the paper.

Our original hope had been to find a pattern behind the coefficients of the LL and to make an all order conjecture for the leading LL. We succeeded in deriving such an expression for the leading term in the large N limit but we found no general expression.

The large N approximation, as we already noted in [18], is a surprisingly poor approximation of the LL series for all of the observables we considered. For example, looking at the five-loop results, the first neglected term, the N^4 term, often has a large coefficient compared with the N^5 term. For this term to be negligible, i.e. a 10% correction of the leading term, N must be large, in some cases $N > 20$. This is understandable if one considers that the subleading $N^{i<n}$ terms in the coefficients come from non-cactus diagrams and different flavour routings of the cactus diagrams. Though each of these diagrams is suppressed by $1/N$ in the large N limit, the number of diagrams and the number of ways to route the flavour structure seem to produce large coefficients for the subleading in N terms.

We have also performed some numerical test of the convergence with parameter values of the range needed for two-flavour ChPT. For masses around

0.1 GeV the convergence for all quantities studied is excellent. It is reasonable for most quantities up to about 0.3 GeV as can be seen on the various plots but becomes unstable around 0.4 GeV for some of the quantities studied.

Acknowledgments

II

II   References

[1] L.-F. Li and H. Pagels, "Perturbation theory about a Goldstone symmetry," *Phys. Rev. Lett.* **26** (1971) 1204–1206.

[2] J. Gasser and H. Leutwyler, "Chiral Perturbation Theory to One Loop," *Ann. Phys.* **158** (1984) 142.

[3] J. Gasser and H. Leutwyler, "Low-Energy Theorems as Precision Tests of QCD," *Phys. Lett.* **B125** (1983) 325.

[4] H. Pagels, "Departures from Chiral Symmetry: A Review," *Phys. Rept.* **16** (1975) 219.

[5] S. Weinberg, "Phenomenological Lagrangians," *Physica* **A96** (1979) 327.

[6] J. Gasser and H. Leutwyler, "Chiral Perturbation Theory: Expansions in the Mass of the Strange Quark," *Nucl. Phys.* **B250** (1985) 465.

[7] G. Colangelo, "Double chiral logs in the pi pi scattering amplitude," *Phys. Lett.* **B350** (1995) 85–91, `arXiv:hep-ph/9502285`.

[8] J. Bijnens, G. Colangelo, and G. Ecker, "Double chiral logs," *Phys. Lett.* **B441** (1998) 437–446, `arXiv:hep-ph/9808421`.

[9] J. Bijnens, "Chiral Perturbation Theory Beyond One Loop," *Prog. Part. Nucl. Phys.* **58** (2007) 521–586, `arXiv:hep-ph/0604043`.

[10] M. Buchler and G. Colangelo, "Renormalization group equations for effective field theories," *Eur. Phys. J.* **C32** (2003) 427–442, `arXiv:hep-ph/0309049`.

[11] M. Buchler, "The leading two loop counterterm in the nonleptonic weak sector of CHPT," *Eur. Phys. J.* **C44** (2005) 111–126, `arXiv:hep-ph/0504180`.

[12] M. Bissegger and A. Fuhrer, "A renormalizable effective theory for leading logarithms in ChPT," *Eur. Phys. J.* **C51** (2007) 75–82, `arXiv:hep-ph/0701132`.

[13] N. Kivel, M. V. Polyakov, and A. Vladimirov, "Chiral Logarithms in the Massless Limit Tamed," *Phys. Rev. Lett.* **101** (2008) 262001, `arXiv:0809.3236 [hep-ph]`.

[14] N. A. Kivel, M. V. Polyakov, and A. A. Vladimirov, "Leading Chiral Logarithms for Pion Form Factors to Arbitrary Number of Loops," *JETP Lett.* **89** (2009) 529–534, `arXiv:0904.3008 [hep-ph]`.

[15] S. R. Coleman, R. Jackiw, and H. D. Politzer, "Spontaneous Symmetry Breaking in the O(N) Model for Large N*," *Phys. Rev.* **D10** (1974) 2491.

[16] M. Bissegger and A. Fuhrer, "Chiral logarithms to five loops," *Phys. Lett.* **B646** (2007) 72–79, `arXiv:hep-ph/0612096`.

[17] J. Koschinski, M. V. Polyakov, and A. A. Vladimirov, "Leading Infrared Logarithms from Unitarity, Analyticity and Crossing," *Phys. Rev.* **D82** (2010) 014014, `arXiv:1004.2197 [hep-ph]`.

[18] J. Bijnens and L. Carloni, "Leading Logarithms in the Massive O(N) Nonlinear Sigma Model," *Nucl. Phys.* **B827** (2010) 237–255, `arXiv:0909.5086 [hep-ph]`.

[19] J. A. M. Vermaseren, "New features of FORM," `arXiv:math-ph/0010025`.

[20] S. Weinberg, "Nonlinear realizations of chiral symmetry," *Phys. Rev.* **166** (1968) 1568–1577.

[21] M. B. Einhorn, "Speculations on a Strongly Interacting Higgs Sector," *Nucl. Phys.* **B246** (1984) 75.

[22] F. Sannino, "Dynamical Stabilization of the Fermi Scale: Phase Diagram of Strongly Coupled Theories for (Minimal) Walking Technicolor and Unparticles," `arXiv:0804.0182 [hep-ph]`.

[23] S. R. Coleman, J. Wess, and B. Zumino, "Structure of phenomenological Lagrangians. 1," *Phys. Rev.* **177** (1969) 2239–2247.

[24] J. Bijnens, "Chiral Lagrangians and Nambu-Jona-Lasinio - like models," *Phys. Rept.* **265** (1996) 369–446, `arXiv:hep-ph/9502335`.

[25] S. Weinberg, "Effective field theories in the large N limit," *Phys. Rev.* **D56** (1997) 2303–2316, `arXiv:hep-th/9706042`.

[26] A. Dobado and J. R. Pelaez, "On the large N(f) limit of chiral perturbation theory," *Phys. Lett.* **B286** (1992) 136–146.

[27] U. Burgi, "Pion polarizabilities and charged pion pair production to two loops," *Nucl. Phys.* **B479** (1996) 392–426, `arXiv:hep-ph/9602429`.

[28] J. Bijnens, G. Colangelo, G. Ecker, J. Gasser, and M. E. Sainio, "Pion pion scattering at low energy," *Nucl. Phys.* **B508** (1997) 263–310, `arXiv:hep-ph/9707291`.

[29] S. Weinberg, "Pion scattering lengths," *Phys. Rev. Lett.* **17** (1966) 616–621.

II

[30] J. Bijnens, G. Colangelo, and P. Talavera, "The vector and scalar form factors of the pion to two loops," *JHEP* **05** (1998) 014, arXiv:hep-ph/9805389.

III

Visible Effects of Invisible Hidden Valley Radiation

Lisa Carloni and Torbjörn Sjöstrand

Department of Theoretical Physics, Lund University,
Sölvegatan 14A, SE–223 62 Lund, Sweden

Assuming there is a new gauge group in a Hidden Valley, and a new type of radiation, can we observe it through its effect on the kinematic distributions of recoiling visible particles? Specifically, what are the collider signatures of radiation in a hidden sector? We address these questions using a generic $SU(N)$-like Hidden Valley model that we implement in PYTHIA. We find that in both the e^+e^- and the LHC cases the kinematic distributions of the visible particles can be significantly affected by the valley radiation. Without a proper understanding of such effects, inferred masses of "communicators" and of invisible particles can be substantially off.

III

III.1 Introduction

One common feature in New Physics models is the conservation (or near conservation) of a new quantum number. Often it is associated with a parity symmetry, like R-parity in supersymmetric models or T-parity in Little Higgs ones. Such conserved parity-like symmetries serve two basic model-building purposes: firstly, they forbid odd-parity tree level corrections to electroweak precision observables, and secondly, they make the lowest lying odd-parity state stable, thus providing a possible dark matter candidate. The new charge may alternatively come from a continuous symmetry, a global symmetry or a new gauge symmetry, for example, and still fulfill the same purposes.

Regardless of the specific model realization, we can imagine that a new conserved quantum number is discovered at LHC.

In this article, we wish to take some first steps towards addressing a general phenomenological question: *if a new apparently conserved charge should be discovered, is it possible to determine experimentally whether it arises from a discrete, a global or a gauge symmetry? Specifically, is it possible to determine whether it is the source of a new field?*

In principle, a continuous symmetry has additive quantum number conservation whereas a discrete one has multiplicative conservation. To distinguish between gauge and global symmetries one could look for Gauge bosons, for Goldstone bosons and in general at the particle spectrum. The new sector however may be "hidden". That is, the carriers of the new symmetry, for the two basic reasons mentioned above, could lie entirely within the new sector and be neutral under (or have very weak) SM interactions. Indeed, a new unbroken symmetry would have to be invisible or else it would have already been found. Thus any radiation or other dynamic phenomena associated with it would be invisible to SM matter.

If the charge did radiate in the new sector, would we be still be able to observe indirectly the effects of the hidden radiation? How would the kinematic distributions of the visible particles be affected? Could we extract information from these kinematic distributions about the dynamics within the hidden sector? Could one distinguish Abelian from non-Abelian gauge groups, study the different particle (or unparticle) contents or measure the strength of the couplings? This could lead to a better understanding of the higher-energy dynamics, the ultraviolet completion of the theory, the symmetries involved, and possibly even the mechanism by which they are broken. The ideal terrain to begin to explore these effects is Hidden Valley models [1]. We extend this name to the class of models satisfying the following criteria. First, there must be a *new light hidden sector* (the valley), decoupled from the visible SM one, that has not yet been discovered because of some barrier. This can be an energy barrier or of another nature, e.g. symmetry-forbidding tree-level cou-

plings. Second, the decoupling of the new hidden valley sector from the visible SM one must happen at relatively low energies, around the TeV scale, in such a way that the cross sections for Standard visible particles disappearing into the hidden sector (and vice versa) are small enough to evade the current experimental limits, and yet large enough to be observable at LHC. These experimental limits are of course model dependent, as we will discuss in sections III.2 and III.4.

Typically, the valley particles "v-particles" are charged under a valley group G_v and neutral under the SM group G_{SM}, and the SM particles are neutral under G_v. In order to have interactions between the two sectors there has to be a "communicator" which couples to both SM and valley particles. A common choice is to have a coupling via a Z' or via loops of heavy particles carrying both G_{SM} and G_v charges.

Examples of Hidden Valleys can be found in many models, such as String Theory [2], Twin Higgs models [3], folded SUSY [4,5], and Unparticle models [6,7].

Hidden Valley scenarios can naturally provide candidates for Dark Matter and can easily fit cosmological constraints. Just to give an example, in [1] the v-interactions ensure that all particles efficiently decay to the lightest mesons. These mesons are allowed to annihilate to neutral π_v^0s, which can then tunnel back into the SM. So long as the lifetime of the π_v^0 is $\tau \ll 1$ sec, the number of πs left will decay exponentially before big-bang nucleosynthesis.

The reason why these scenarios are ideal to study the effects of radiation is the large disparity in the masses of the communicators and the v-particles. Typically, the communicator has a mass around the decoupling scale, say the TeV scale, while the v-particle mass may be as low as 1–10 GeV. If both the communicator and the v-particle are charged under a new gauge G_v, they will radiate gauge bosons, and the larger their mass ratio the larger the amount of phase space available for the radiation, both in the normal and in the hidden sector. Thus if any effect at all are to be observable, it would be in this kind of scenario.

We have devised a Hidden Valley toy model to tackle the issue, and have implemented it in the PYTHIA 8 Monte Carlo event generator [8]. The implementation allows for different valley flavour contents, particle masses, gauge groups and v-gauge couplings. In this way one may accommodate a range of different Hidden Valley scenarios.

MC event generators offer flexible approaches to model radiation and parton shower evolution in great detail. One new central feature in the PYTHIA 8 implementation is the "competition" mechanism between the hidden and the SM radiation, which is implemented as an "interleaved" shower, wherein different kinds of emissions, SM and hidden, can alternate if viewed in terms of a common shower evolution scale. As a consequence, subsequent emissions

III

in the visible sector, of gluons or photons, will then tend to have a lower energy than they would have had, had the hidden radiation not been there. This is the key mechanism whereby we gain access to the information about the radiation in the hidden sector.

The intention of this article is not a full-fledged experimental analysis of how a new sector should be discovered and explored, neither with respect to potential background processes nor to detector-specific capabilities — since our implementation is publicly available, we safely leave it to the experimental community to assess. What we want to ascertain here is if *there are observable signals of hidden valley radiation at all*, at the simple parton and hadron levels.

It is not trivial to decide which visible particle kinematic distributions one should study to reveal valley radiation effects and to discriminate between different models. For instance, at an e^+e^- collider the rise of the communicator pair-production cross section near threshold could allow to determine its spin, and thereafter the absolute size of the cross section could suggest the presence of new "colour" factors — recall that the pair-production of particles in the fundamental representation of a new $SU(N)$ group gives a factor N in the cross section. Such measurements would not directly probe the hidden sector, however: they would not reveal whether a new group is gauged, or what is the coupling strength in it. For a hadron collider, like the LHC, the uncertainty in the event-by-event subcollision energy $\sqrt{\hat{s}}$ undermines analyses solely based upon the value of cross-section. The best strategy is thus to complement cross-section with invariant mass measurements and the study of other boost-invariant quantities (for a recent review see the proceedings [9]).

This is the reason why we choose to study MT2 [10] distributions, which give relations between communicator and v-particle mass. These observables are specifically designed to be boost-invariant and to deal with BSM models in which more than one particle escapes detection, such as in our toy model. But we also study "hidden observables", like the invariant mass distribution of a hidden particle together with its associated hidden radiation.

The effects of the hidden radiation on these distributions and how much one may observe depends on the details of the scenario considered, of course, but also depend heavily upon the collider type considered, on its center of mass energy, and on its integrated luminosity $\mathcal{L}$. We consider two different LHC scenarios, one for the early data (the first 18 to 24 months at 7 TeV with an expected integrated luminosity $\mathcal{L} = 1$ fb^{-1}) and one for later data ($\sqrt{s} = 14$ TeV and integrated luminosity $\mathcal{L} = 100$ fb^{-1}). The conclusions in the two cases will be quite different. For e^+e^- collisions we will mainly refer to an ILC at 800 GeV, though we mention CLIC production cross sections at 3 TeV.

III.2   Hidden Valley scenarios

As mentioned in the introduction a Hidden Valley is a light hidden sector, consisting of particles which, depending on the model, might have masses as low as 10 GeV. The detailed spectrum of the v-particles and their dynamics within the hidden valley depends upon the valley gauge group G_v, the spin and number of particles present in the theory, and the representation they belong to.

The effects of the hidden sector on the visible particle spectra will depend upon the way the hidden sector communicates with the SM, whether it is via a Higgs, multiple Higgses, a Z', heavy sterile neutrinos or via loop of heavy particles charged under both SM and valley gauge interactions.

We would like to give a panoramic view of the different Hidden Valley scenarios without going into details and to underline those features that may be simulated with the new tools.

The simplest possibility is a QCD-like scenario, with a strong coupling constant, which may run like the QCD coupling does, with QCD-like hadronization generating valley pions, v-ηs, v-Ks, v-nucleons etc. The Standard Model $SU(3)_c \times SU(2) \times U(1)$ sector could couple ultra-weakly with the hidden $SU(N)$ sector via a neutral Z'. This scenario was investigated by Strassler and Zurek with tools analogous to the ones used to simulate QCD [1]. It displays some rather startling features. For instance, a v-π could have a displaced decay in the muon spectrometer in the ATLAS detector, resulting in a large number of charged hadrons traversing the spectrometer, or it could decay in the hadronic calorimeter producing a jet with no energy deposited in the electromagnetic calorimeter and no associated tracks in the inner detector. Experimental studies for these scenarios are currently under way, by the D0, CDF, LHCb, ATLAS and CMS collaborations.

Typical hidden valley-like signatures appear also in Unparticle models with mass gaps [7]. These models display a conformal dynamic above the mass gap, and a hidden valley behaviour when the conformal symmetry is broken. Regardless of the dynamics above the mass gap, whether it is strongly coupled or weakly coupled, the signatures are similar to the ones mentioned in the previous scenario (displaced vertices and missing energy signals). This is because only the lower energy states, light stable hidden hadrons can decay back into Standard Model particles. The higher energy states, be they narrow resonances or a continuum of resonances, decay rapidly to these lower light stable hadrons. As for the previous scenario, a parton shower is a key tool to study these models, not so much to determine the phenomenology qualitatively, but because it the only element of the hidden dynamics which is sensitive to the higher-energy conformal (or next-to-conformal) dynamics. The conformal dynamics will be reflected in the parton shower evolution, which

III

can be rather different from the regular QCD one, especially in theories with a strong dynamics above the mass gap.

There are of course many other Hidden-Valley related models, such as Quirky models [11], just to give an example, in which the parton shower evolution does not play the key role it does in the previous cases. Typically their phenomenology is better captured in terms of string dynamics and string fragmentation.

In this paper we do not address the issue of string fragmentation or hadronization. Our main focus is on the parton shower, as this best captures the nature of the hidden radiation.

The model we built to investigate the existence of a this new radiation exploits but a few features common in many hidden valley scenarios: the presence of a new unbroken hidden gauge group, of a heavy communicator, charged under both SM and hidden sector gauge group and decaying into a visible and an invisible light particle, charged only under the new gauge group. These characteristics fit many Hidden Valley models, we however make an additional assumption, which is that the production cross sections[1] should be large enough for the effects of the hidden radiation to be discernable. This model was then implemented in the PYTHIA event generator. Notice however, that the shower mechanism we implemented is rather different from the ones mentioned above, as we will discuss in the next section.

III.3   Monte Carlo Tools in PYTHIA 8

In order to allow detailed studies of a set of scenarios, the models have been implemented in the PYTHIA event generator, and will be publicly available from version 8.140 onwards.

III.3.1   Particle content

For simplicity we assume that the HV contains either an Abelian $U(1)$ or a non-Abelian $SU(N_c)$ gauge group, with spin 1 gauge bosons. The former group could be unbroken or broken, while the latter always is assumed unbroken. Casimir constants could be generalized to encompass other gauge groups, should the need arise, but for now we do not see that need. The gauge bosons are called γ_v and g_v, respectively.

A particle content has been introduced to mirror the Standard Model flavour structure. These particles, collectively called F_v, are charged under both the SM and the HV symmetry groups. Each new particle couples flavour-diagonally to a corresponding SM state, and has the same SM charge and

---

[1]We will discuss the production cross sections in section III.4.

name	partner	code	name	partner	code
D_v	d	4900001	E_v	e	4900011
U_v	u	4900002	ν_{Ev}	ν_e	4900012
S_v	s	4900003	MU_v	μ	4900013
C_v	c	4900004	ν_{MUv}	ν_μ	4900014
B_v	b	4900005	TAU_v	τ	4900015
T_v	t	4900006	ν_{TAUv}	ν_τ	4900016
g_v		4900021			
γ_v		4900022			
q_v		4900101			

Table III.1: The allowed particle content in the HV scenarios, with their SM partners, where relevant. The code is an integer identifier, in the spirit of the PDG codes, but is not part of the current Amsler:2008zzb standard.

colour, but in addition is in the fundamental representation of the HV colour, see Table III.1. Their masses and widths can be set individually. It would also be possible to expand the decay tables to allow for flavour mixing.

These particles can decay to the corresponding SM particle, plus an invisible, massive HV particle q_v, that then also has to be in the fundamental representation of the HV colour: $F_v \to f q_v$. The notation is intended to make contact with SM equivalents, but obviously it cannot be pushed too far. For instance, not both F_v and q_v can be fermions. We allow the F_v to have either of spin 0, 1/2 and 1. Currently the choice of q_v spin is not important but, for the record, it is assumed to be spin 1/2 if the F_v is a boson and either of spin 0 and 1 if F_v is a fermion.

III

III.3.2 Production processes

The HV particles have to be pair-produced. The production processes we have implemented are the QCD ones, $gg \to Q_v \overline{Q}_v$ and $q\overline{q} \to Q_v \overline{Q}_v$, for the coloured subset Q_v of F_v states, and the electroweak $f\overline{f} \to \gamma^*/Z^0 \to F_v \overline{F}_v$ for all states. All of them would contribute at a hadron collider, but for a lepton one only the latter would be relevant. Each process can be switched on individually, e.g. if one would like to simulate a scenario with only the first F_v generation.

Note that pair production cross sections contain a factor of N_c, with $N_c = 1$ for an $U(1)$ group, for the pair production of new particles in the fundamental representation of the HV gauge group, in addition to the ordinary colour factor for Q_v. Other things equal, this could be used to determine N_c from data, as already discussed. For the case of a spin 1 F_v it is possible to include an anomalous magnetic dipole moment, $\kappa \neq 1$.

The spin structure of the $F_v \to f q_v$ decay is currently not specified, so the

decay is isotropic. Also the Yukawa couplings in decays are not set as such, but are implicit in the choice of widths for the F_v states.

The kinematics of the decay is strongly influenced by the q_v mass. This mass is almost unconstrained, and can therefore range from close to zero to close to the F_v masses. We will assume it is not heavier than them, however, so that we do not have to consider the phenomenology of stable F_v particles.

III.3.3   Parton showers

Both the F_v and the q_v can radiate, owing to their charge under the new gauge group, i.e. $F_v \rightarrow F_v \gamma_v$ and $q_v \rightarrow q_v \gamma_v$ for a $U(1)$ group, and $F_v \rightarrow F_v g_v$ and $q_v \rightarrow q_v g_v$ for a $SU(N_c)$ one. In the latter case also non-Abelian branchings $g_v \rightarrow g_v g_v$ are allowed. Currently both γ_v and g_v are assumed massless, but a broken $U(1)$ with a massive γ_v is foreseen.

These showers form an integrated part of the standard final-state showering machinery. Specifically, HV radiation is interleaved with SM radiation in a common sequence of decreasing $p_\perp$. That is, at the stage before the F_v's decay, they may radiate g, γ and γ_v/g_v, in any order. For the i'th emission, the $p_\perp$ evolution starts from the maximum scale given by the previous emission. The overall starting scale $p_{\perp 0}$ is set by the scale of the hard process. Thus the probability to pick a given $p_\perp$ takes the form

$$
\frac{\mathrm{d}\mathcal{P}}{\mathrm{d}p_\perp} = \Big(\frac{\mathrm{d}\mathcal{P}_{\mathrm{QCD}}}{\mathrm{d}p_\perp} \quad + \quad \frac{\mathrm{d}\mathcal{P}_{\mathrm{QED}}}{\mathrm{d}p_\perp} + \frac{\mathrm{d}\mathcal{P}_{\mathrm{HV}}}{\mathrm{d}p_\perp} \Big) \times
$$
$$
\exp\Big(\quad - \quad \int_{p_\perp}^{p_{\perp i-1}} \Big(\frac{\mathrm{d}\mathcal{P}_{\mathrm{QCD}}}{\mathrm{d}p'_\perp} + \frac{\mathrm{d}\mathcal{P}_{\mathrm{QED}}}{\mathrm{d}p'_\perp} + \frac{\mathrm{d}\mathcal{P}_{\mathrm{HV}}}{\mathrm{d}p'_\perp} \Big) \mathrm{d}p'_\perp \Big) \quad \text{(III.1)}
$$

where the exponential corresponds to the Sudakov form factor. Implicitly one must also sum over all partons that can radiate.

To be more precise, radiation is based on a dipole picture, where it is a pair of partons that collectively radiates a new parton. The dipole assignment is worked out in the limit of infinitely many (HV or ordinary) colours, so that only planar colour flows need be considered. Technically the total radiation of the dipole is split into two ends, where one end acts as radiator and the other as recoiler. The recoiler ensures that total energy and momentum is conserved during the emission, with partons on the mass shell before and after the emission. In general the dipoles will be different for QCD, QED and HV.

To take an example, consider $q\bar{q} \rightarrow Q_v \overline{Q}_v$, which proceeds via an intermediate s-channel gluon. Since this gluon carries no QED or HV charge it follows that the $Q_v \overline{Q}_v$ pair forms a dipole with respect to these two emission kinds. The gluon *does* carry QCD octet charge, however, so $Q_v \overline{Q}_v$ do *not* form a QCD dipole. Instead each of them is attached to another parton, either the beam

remnant that carries the corresponding anticolour or some other parton emitted as part of the initial-state shower. This means that QCD radiation can change the invariant mass of the $Q_v\overline{Q}_v$ system, while QED and HV radiation could not. When a γ or γ_v is emitted the dipole assignments are not modified, since these bosons do not carry away any charge. A g or g_v would, and so a new dipole would be formed. For QCD the dipole between Q_v and one beam remnant, say, would be split into one between the Q_v and the g, and one further from the g to the remnant. For HV the $Q_v\overline{Q}_v$ dipole would be spit into two, Q_vg_v and $g_v\overline{Q}_v$. As the shower evolves, the three different kinds of dipoles will diverge further.

Note that, in the full event-generation machinery, the final-state radiation considered here is also interleaved in $p_\perp$ with the initial-state showers and with multiple parton-parton interactions.

There is made a clean separation between radiation in the production stage of the $F_v\overline{F}_v$ pair and in their respective decay. Strictly speaking this would only be valid when the F_v width is small, but that is the case that interests us here. In the decay $F_v \to fq_v$ the QCD and QED charges go with the f and the HV one with q_v. For all three interactions the dipole is formed between the f and the q_v, so that radiation preserves the F_v system mass, but in each case only the relevant dipole end is allowed to radiate the kind of gauge bosons that go with its charge. (Strictly speaking dipoles are stretched between the f or q_v and the "hole" left behind by the decaying F_v. The situation is closely analogous to $t \to bW^+$ decays.)

The HV shower only contains two parameters. The main one is the coupling strength α_v, i.e. the equivalent of α_s. This coupling is taken to be a constant, i.e. no running is included.

From a practical point of view it is doubtful that such a running could be pinned down anyway, and from a theory point of view it means we do not have to specify the full flavour structure of the hidden sector. The second parameter is the lower cutoff scale for shower evolution, by default chosen the same as for the QCD shower, $p_{\perp\mathrm{min}} = 0.4$ GeV.

The HV showers are not matched onto higher-order matrix elements for the emissions of hard γ_v/g_v in the production process, and so contain an element of uncertainty in that region. For the decay process the matching to first-order matrix elements has been worked out for all the colour and spin combinations that occur in the MSSM [12], and is recycled for the HV scenarios, with spin 1 replaced by 0 for non-existing (in MSSM) combinations. This means that the full phase space is filled with (approximately) the correct rate. Some further approximations exists, e.g. in the handling of mass effects in the soft region. The chosen behaviour has been influenced by our experience with QCD, however, and so should provide a good first estimate. More than that we do not aim for in this study.

III

III.4   The model: SM and $SU(3)_v$ radiation

To be specific, in the following we explore two similar Hidden Valley exper-
imental scenarios. In the first, the communicator E_v is a spin 1/2 particle
charged under both the SM $SU(2) \times U(1)$ and the valley gauge group $SU(3)_v$.
We assume it has the same SM charges an electron would have, so it may
be pair-produced in e^+e^- collisions, via $Z/\gamma^\star$. Under the unbroken $SU(3)_v$,
it transforms like a **3**, so it radiates both γs and massless hidden valley glu-
ons g_vs. After the parton shower, the E_v eventually decays into a visible SM
electron e and an invisible spin 0 valley "quark" q_v. This q_v belongs to the
fundamental representation of $SU(3)_v$ and is not charged under the SM gauge
group, so it only radiates g_vs. See Fig.III.1.

   The key feature is interleaved radiation, already introduced above. In the
current context it works as follows. Once the E_v has been produced it may
radiate a SM γ, say. This radiation will subtract energy from the E_v and the
following emission, be it another SM photon or a valley gluon, will have less
phase space to radiate into. In an analogous way, assuming a valley g_v is
emitted next, it subtracts energy from E_v and affects the following emissions
which, again, could be either visible or invisible.
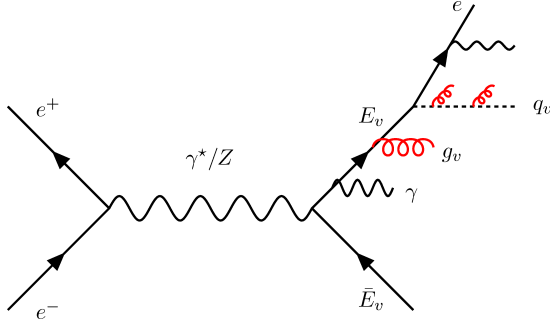
Figure III.1: An $E_v\bar{E}_v$ pair is produced via $Z/\gamma^\star$. Since E_v is charged under both
$SU(2) \times U(1)$ and $SU(3)_v$, it radiates both γs and g_vs. It eventually decays into e
and q_v. These then each radiate into their respective sector. Notice that q_v here refers
to a spin 0 particle.

   In the second scenario the communicator between SM sector and Hidden
Valley sector is a quark-like, spin 1/2 object Q_v, belonging to the $(\mathbf{3}, \mathbf{3})$ rep-
resentation of the gauge group $SU(3)_c \times SU(3)_v$. The Q_vs are pair produced
(mostly) via strong interactions (gluon-gluon or $q\bar{q}$ fusion). We choose the
scenario in which only one vector-like Q_v is produced, the D_v. This D_v emits
massless valley gluons (since the $SU(3)_v$ is assumed to be unbroken) and these
may in turn radiate more g_vs. During the shower evolution, *both* types of glu-

	ILC	CLIC		LHC	LHC
	(800 GeV)	(3 TeV)		(7 TeV)	(14 TeV)
$M_{E_v} = 300$ GeV	398 fb	44 fb	$M_{D_v} = 300$ GeV	$1.39 \cdot 10^4$ fb	$1.04 \cdot 10^5$ fb
$M_{E_v} = 500$ GeV	-	41 fb	$M_{D_v} = 500$ GeV	654 fb	$7.27 \cdot 10^3$ fb
$M_{E_v} = 1$ TeV	-	32 fb	$M_{D_v} = 1$ TeV	3.21 fb	124 fb

Table III.2: The order of magnitude of the total production cross sections, in fb, at ILC (via $Z/\gamma^\star$), LHC (via $q\bar{q}$ or gg fusion) with $\sqrt{s} = 7$ TeV and 14 TeV, for various values of the communicator mass. The spin of the communicator is assumed to be 1/2.

ons are radiated until finally each D_v decays into a visible SM d quark and an invisible spin 0 valley q_v. The decays are flavour diagonal, $D_v \rightarrow d + q_v$.
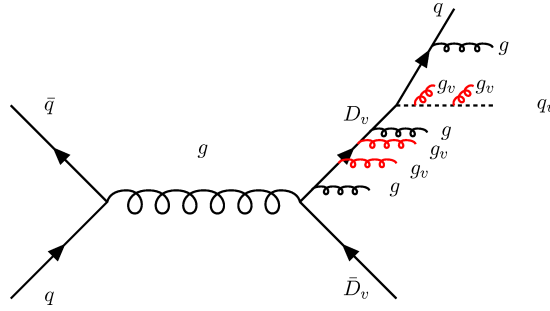
Figure III.2: Pair production of hidden valley D_vs. Each D_v can radiate gs and g_vs, and eventually decays $D_v \rightarrow q_v d$. The visible d then can radiate further gs and the invisible q_v further g_vs.

The SM quark d transforms as a $(\mathbf{3}, \mathbf{1})$ under $SU(3)_c \times SU(3)_v$, so it radiates only SM gluons, while the valley q_v belongs to the $(\mathbf{1}, \mathbf{3})$ representation of $SU(3)_c \times SU(3)_v$, so not having any SM color charge, it radiates only g_vs, see figure III.2.

In both scenarios there are just three parameters left to vary: the size of the valley coupling constant α_v, the masses of the communicator particles M_{E_v} or M_{D_v} and the mass of the valley scalar M_{q_v}.

Below, in Table III.2, we list the total production cross sections at different colliders: e^+e^- with $\sqrt{s} = 800$ GeV or $\sqrt{s} = 3$ TeV, and LHC with $\sqrt{s} = 7$ TeV or $\sqrt{s} = 14$ TeV for some typical M_{E_v}, M_{D_v} mass values.

We also show the spin dependence of the $E_v \bar{E}_v$ production cross section at e^+e^- colliders for the three cases: F_v spin 0 and q_v spin 1/2, F_v spin 1/2 and q_v spin 0 or 1, and F_v spin 1 and q_v spin 1/2, Fig. III.3.

The higher the spin, the larger the cross section. Indeed, the curve corre-
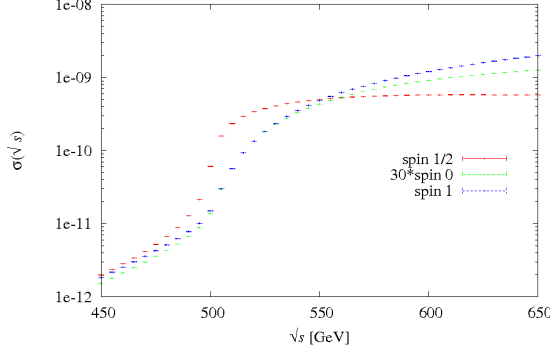
Figure III.3: The spin dependence of the $E_v\bar{E}_v$ production cross section at e^+e^- colliders for E_v spin 1/2, 0 and 1. $M_{E_v} = 250$ GeV, the mass spread $\Gamma_{E_v} = 2$ GeV, $M_{q_v} = 50$ GeV. The spin 0 curve has been scaled by a factor 30.

sponding to E_v spin 0 has been scaled by a factor 30 to emphasize the similarity in shape with the spin 1 curve. Note that the processes proceed through the s-channel exchange of a spin 1 γ^*/Z^*. Thus the production of a spin 1/2 pair has only a threshold factor β from phase space, where β is the velocity of the produced pair in the γ^*/Z^* decay vertex, while the other two have an (approximate) additional factor β^2 from helicity considerations. The results have again been obtained with a $SU(3)_v$ group, and are directly proportional to the N_c chosen. Since we would not expect gauge groups with N_c above (some multiple of) 30, the conclusion would be that a threshold scan of the cross section could be used to determine both the E_v spin and the number of hidden colours, as well as the E_v mass, of course. A caveat would be that we have here only considered the E_v gauge production mechanism, not the possibility of a significant $t-$channel Yukawa contribution. The reason for not including this production channel is that it would imply a large decay width for the E_v, which would give additional large and model dependent effects to the cross section around threshold (see below).

The experimental constraints on these two types of setup are similar to the ones for New Charged Leptons and Leptoquark production[2]. For the New Charged Leptons the PDG [13] gives the lower bound $m_{L^\pm} > 100.8$ GeV. For scalar and vector Leptoquark states we use the direct limits coming from leptoquark pair production and subsequent $LQ \rightarrow \nu q$ decay searches [14]. For the all generation search $m_{LQ} > 136$ GeV in the scalar case and $m_{LQ} > 200$ GeV in the vector case, where one assumes the branching ratio $B(\nu q) = 1$. Bounds on

---

[2]We do not make use of the limits coming from the D0 or CDF $\tilde{q} \rightarrow j + \not{E}_T$ searches, because these depend upon the chosen mSUGRA scenario.
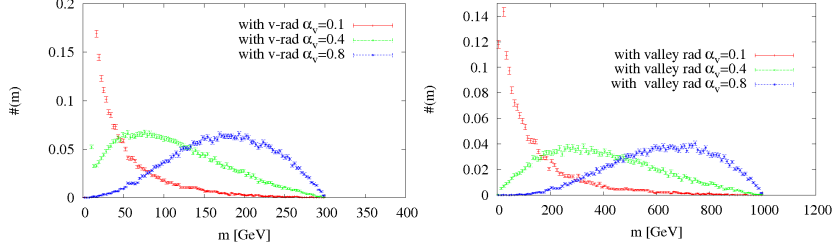
Figure III.4: Left: the effective invariant mass distribution for the q_v at LHC for $\alpha_v = 0.1, 0.4, 0.8$. $M_{D_v} = 300$ GeV, nominal q_v mass $M_{q_v} = 10$ GeV and $\sqrt{s} = 7$ TeV. Right: the effective invariant mass distribution for the q_v at LHC for $\alpha_v = 0.1, 0.4, 0.8$. $M_{D_v} = 1$ TeV, nominal q_v mass $M_{q_v} = 10$ GeV and $\sqrt{s} = 14$ TeV. Notice how the mean value of the distribution shifts from the bare mass $m_{q_v} = 10$ GeV towards $m_{q_v}^{\max} = m_{D_v}$ GeV as the coupling constant grows.

the leptoquark mass for the third generation decaying into νb are more stringent [15], $m_{LQ} > 229$ GeV.

We view these boundaries as simply indicative of the mass range we should contemplate and chose masses that are well beyond these boundaries. Our studies are in any case not critically dependent on them.

We assumed the communicators to be massive, M_{E_v} in the range [250,300] GeV for the ILC case, M_{D_v} in the range [300, 500] GeV for the LHC 7 TeV run, and [0.5,1] TeV for the 14 TeV run. The hidden scalar is taken to be light, M_{q_v} as light as 10 GeV. The α_v parameter is allowed to vary over a wide range, and results shown for interesting values.

Depending on the size of these parameters, the effects of the radiation on the lepton or quark kinematic distributions can be significant, as we will show in the next two sections. But whether these effects will be observable strongly depends on the statistics at hand. We assume an integrated luminosity $L = 200$ fb^{-1} for the ILC, 1 fb^{-1} for the 7 TeV LHC run and 100 fb^{-1} for the 14 TeV one.

The hidden radiation affects the visible particle kinematics through two mechanisms. The first one, interleaved radiation from the E_v or D_v, we already discussed. The second is radiation off the q_v after E_v/D_v decay. This causes the invariant mass for the system made out of q_v and the radiated g_vs to be larger than the on-shell q_v mass. This invariant mass can be viewed as the off-shell mass with which the q_v is produced at the decay vertex. In Fig. III.4 one may see the effects of the valley radiation on the off-shell mass, for the $D_v \rightarrow d + q_v$ case. As the hidden valley coupling α_v increases, the q_v radiates more and more into the hidden sector, and the mean value of the distribution shifts from M_{q_v} towards M_{D_v}. At the same time more and more energy is subtracted from the visible recoiling particle, in this case the *d* and its system of emitted gluons.

The effect is more obvious when the mass difference $M_{D_v} - M_{q_v}$ is large, since more phase space is available for the radiation.

The size of the deviations induced by these two combined mechanisms is very much dependent on the collider, as we already stressed above. In the next two sections we will discuss the various cases separately.

III.5 Effects of $SU(3)_c$ radiation at e^+e^- colliders

We begin by studying the $e^+e^- \to \gamma^*/Z \to \bar{E}_v E_v$, scenario, which allows for many simplifications compared to the quark case, and therefore offers a convenient warmup. For the ILC with $\sqrt{s} = 800$ GeV and an assumed integrated luminosity of $L = 200$ fb^{-1} per year an $M_{E_v} = 300$ GeV translates into about 80000 $\bar{E}_v E_v$ pairs.

III.5.1 Collisions in the center-of-mass frame

To illustrate the principles, as a very first step we will neglect bremsstrahlung and beamstrahlung. We then only need to consider two types of interactions, electromagnetic and valley $SU(3)_v$ radiation in the final state, with coupling constants α and α_v. No fragmentation or hadronization need to be taken into account.

Since the center of mass (CM) of the collision is at rest, there is a clean relationship between the mass of the hidden valley q_v, M_{q_v}, and that of the communicator M_{E_v}. In the absence of radiation (hidden or standard), this can be inferred from the distribution of the energy of the emitted electrons, in particular from the upper endpoint of this distribution, describing the electron maximum energy. This is obtained when the electron is emitted in the same direction as the E_v is moving in, with the q_v in the opposite direction. One may use this maximization condition to derive the relationship between M_{q_v} and M_{E_v}.

In the rest frame of the E_v, neglecting the electron mass,

$$
\begin{aligned}
P_{E_v} &= (M_{E_v}, 0, 0, 0) \,, \\
P_{q_v} &= \left(\frac{M_{E_v}^2 + M_{q_v}^2}{2M_{E_v}}, 0, 0, -\frac{M_{E_v}^2 - M_{q_v}^2}{2M_{E_v}^2} \right) \,, \\
P_e &= (\frac{M_{E_v}^2 - M_{q_v}^2}{2M_{E_v}}, 0, 0, \frac{M_{E_v}^2 - M_{q_v}^2}{2M_{E_v}}) \,.
\end{aligned}
\tag{III.2}
$$

Assuming the boost to the CM rest frame is at an angle θ with respect to the e

direction in the E_v rest frame, the electron energy will be given by

$$E'_e = \gamma(E_e + \beta|\mathbf{p}_e|\cos\theta) = \frac{\sqrt{s}}{4}\left(1 - \frac{M^2_{q_v}}{M^2_{E_v}}\right)\left(1 + \sqrt{1 - \frac{4M^2_{E_v}}{s}}\cos\theta\right), \quad \text{(III.3)}$$

where $\cos\theta = \pm 1$ gives the upper and lower edge of the energy spectrum. If the decay is assumed isotropic, $\mathrm{d}\mathcal{P}/\mathrm{d}\cos\theta = $ constant, the electron energy spectrum is flat between the limits.

So if one can measure the maximum and minimum energy E'_e, one may solve for M_{E_v} and M_{q_v}. Fig. III.5 shows the energy distribution E_e of the electrons produced with and without hidden radiation. In the latter case the spectrum is shifted to lower values, as the hidden sector takes a bigger fraction of the available energy, by radiation off both the E_v and the q_v. The endpoints remain the same, as there is always a fraction of events where radiation is negligible. As we have assumed a modest width of 1 GeV for the E_v there is a tiny tail beyond the expected edge. (We could cope with a wide range of widths, but have picked values in the GeV range, so that the possibility of a Breit-Wigner-shaped mass broadening is not overlooked, while still maintaining a credible simulation in terms of resonance diagrams only.) The key point to observe, however, is how the upper "shoulder" is softened by the hidden radiation. Thereby a precision measurement of this region would offer a direct check on the amount of hidden radiation. At the lower end, QED cascades such as $e^- \rightarrow e^-\gamma \rightarrow e^-e^+e^-$ contribute to the spectrum, but are easily eliminated if only the highest-energy lepton is considered, Fig. III.6, or at least only the highest two. We should clarify that the electron energy studied in this section includes photons emitted near the electron direction, since we here include a Durham "jet" algorithm that clusters photons within a 3 GeV $p_T \sin\theta/2$ distance of the electron.

Whether and how well one would actually be able to observe these endpoints will be very model and detector dependant. Regardless of the background or detector sensitivity, we expect that the endpoints of the distribution will have low statistics, given that they correspond to extreme kinematical configurations. Most likely, one will need to rely on data points in the shoulder region to fit the curve and extrapolate the endpoint $E'_{e,\mathrm{max}}$. These shoulder data points would be the ones most affected by the radiation, so the mass M_{E_v} and M_{q_v} inferred from them would be significantly different when hidden radiation is included. On the one hand, the curve corresponding to having valley radiation is always softer than the one without, so some mean of the threshold region will give too low an endpoint. On the other hand, if one only tries e.g. a linear fit, the shape of the fall-off in the threshold region would suggest too high an endpoint. A readiness to include a parametric shape for the endpoint region, that takes into account a tuneable radiation contribution, will help ensure a better extraction of the relevant mass parameters.
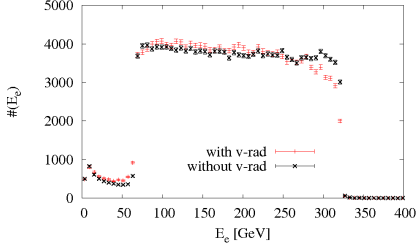
III

Figure III.5: the energy distribution of the visible electrons. Looking at the upper shoulder of the distribution, the upper (black) and lower (red) curves give the prediction for $E_v \rightarrow e^- q_v$ when hidden valley radiation is not or is take into account; in both cases electromagnetic radiation is included. Center of mass energy $\sqrt{s} = 800$ GeV, $M_{E_v} = 300$ GeV, $M_{q_v} = 50$ GeV and $\alpha_v = 0.05$. Number of events per 6 GeV bins, luminosity $L = 200$ fb^{-1}. The error is purely statistical.
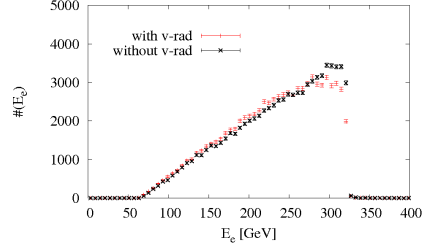
Figure III.6: The energy distribution of the most energetic electron in each event, under the same conditions.

Notice that the curve corresponding to having valley radiation always lies below the one without, implying that the value of $E'_{e,\max}$ with the radiation would always be higher than the one without. This is a reflection of the two mechanisms we mentioned in the previous section: first, the the valley gluons g_v subtract energy from the E_v, ultimately subtracting it from the es, and second, when they are emitted by the q_v, they change its effective mass, $M_{q_v}^{\text{eff}} > M_{q_v}$, as one may see in Fig. III.4, again subtracting energy from the decay e.

Would it be possible to describe the curves with hidden radiation using a model without it, but with different mass parameters M_{E_v} and M_{q_v}? Fig. III.7 shows the effects of changing the invisible particle mass M_{q_v} in model with and without radiation. The "fingerprint" of the v-radiation is clear: a softening in the shoulder of the distribution which leaves the endpoints fixed. A simple change in the mass parameters of the model without hidden radiation (in this case M_{q_v}) changes the endpoints and leaves the sharp drop of the shoulder unchanged.

Notice how so long as the mass difference $M_{E_v} - M_{q_v} > 40$ GeV one may always distinguish between any two curves with and without radiation. This of course α_v dependent.

In Fig. III.8 instead one can see the α_v dependence of the energy distribu-
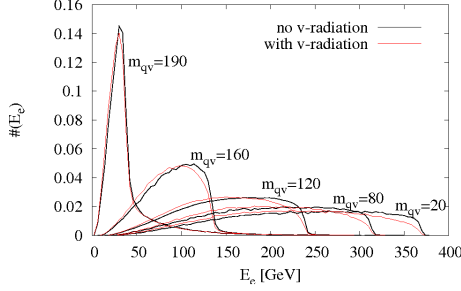
Figure III.7: We compare the energy distributions of the most energetic electron emitted in each event, in the case $\sqrt{s} = 800$ GeV. The communicator mass is fixed at $M_{E_v} = 200$ GeV, while M_{q_v} is allowed to vary between 20 and 190 GeV. The valley gauge coupling is fixed at $\alpha_v = 0.1$ in order to isolate the mass dependence. Each endpoint corresponds to two curves, the lower one being the one with and the top one the one without hidden valley radiation.
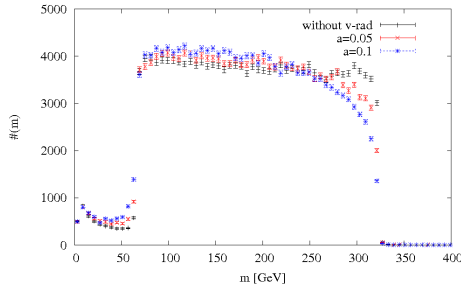
Figure III.8: α_v dependence of the energy of the visible electrons. The (black) squared-off curve corresponds to the model with no valley radiation, the uppermost if one looks at the shoulder. Below it are the curves corresponding to valley coupling constant $\alpha_v = 0.05$ and $\alpha_v = 0.1$. Number of electrons per 6 GeV bin, $\sqrt{s} = 800$ GeV, $M_{E_v} = 300$ GeV and $M_{q_v} = 50$ GeV.

III

tion for the visible electrons in each event. Notice how even for a coupling as low as $\alpha_v = 0.05$ the effects of the v-radiation on the shoulder region are already sizeable.

There are some parameter regions (e.g. when the E_v-to-q_v mass splitting is small) where the shape of the distribution of the hardest leptons is no longer conclusive in distinguishing between a model with and one without valley radiation. In this case one may consider other observables which have an "orthogonal" dependence on the valley parameters. We studied η, linearized sphericity S and the number of emitted leptons, for example. There is no

unique strategy in this case, one must perform a case by case study of the different observables in the different parameter regions to determine which one displays the largest separation between the model with and the model without radiation. As a general rule, we found that three observables were normally sufficient to distinguish the two.

III.5.2   Collisions not in the center-of-mass frame: MT2

We now consider the effect of initial-state radiation (ISR). This causes unobservable radiation, mainly along the beamline, but also some transverse kicks. Beamstrahlung is highly machine-dependent and thus not included, but is purely longitudinal. The methods we will introduce to handle bremsstrahlung also automatically handle beamstrahlung with little or no degradation of performance, so from now on we will not address the latter specifically.

For our theoretical studies, in order to avoid the clustering of ISR γ radiation with the leptons coming from the hard interaction, we apply a cut on the $\eta > 5$. The symmetry of the system now being cylindrical, we also changed the clustering algorithm to the cylindrical fastjet [16].

The major consequence of ISR is that the collision now no longer happens in the CM rest frame, with the information connected to the p_z, the momentum along the beampipe, no longer available. In this case it is convenient to introduce a new variable called Cambridge MT2, see [10].

The MT2 variable was invented precisely to treat events in which the new particles are pair-produced and then each decay into one particle that is directly observable and another particle whose existence may only be inferred from from missing *transverse* momenta.

This observable is somewhat inspired by the transverse mass m_T used at hadron colliders to measure the mass of the W boson in the decay $W \rightarrow e\nu$. The neutrino escapes detection, its only trace in the detector being missing momentum. In this case one can construct the variable

$$m_T^2 = 2(E_T^e \, \slashed{E}_T^N - \mathbf{p}_T^e \cdot \mathbf{p}_T^N). \tag{III.4}$$

Here E_T is defined as $E_T = \sqrt{m^2 + \mathbf{p}_T^2}$, although in this particular case the electron and neutrino masses can be neglected, of course. The m_T^2 variable has the property that

$$m_T^2 \leq m_W^2 \tag{III.5}$$

If there is enough statistics to ensure that the kinematic configuration corresponding to the maximum is hit, this gives a measurement of (a lower bound on) the W mass. Analogously, one may build a variable called MT2, with the property that its upper bound describes the mass of the communicators, i.e. the particles that were pair-produced.
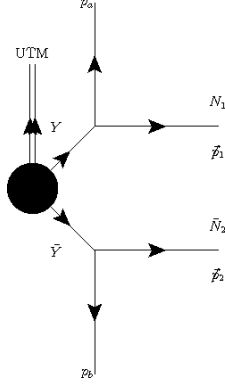
Figure III.9: The MT2 diagram for the shortest, simplest decay chain . Two communicator particles are pair-produced and each decay into a visible (a or b) and an invisible (N_1 and N_2) particle. Upstream transverse momentum (before the decay) is also possible, but it must be known. Longitudinal momentum information is not available.
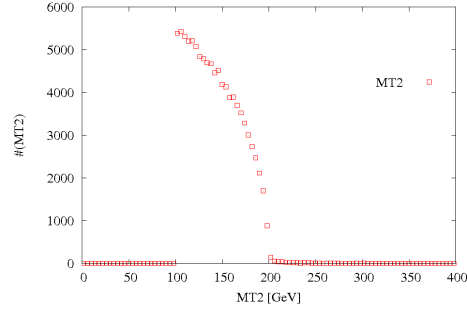
Figure III.10: An example of the MT2 method applied to the communicator mass M_{E_v}. Histogram of the MT2 values obtained for a communicator mass $M_{E_v} = 200$ GeV and M_{q_v} and an invisible particle mass $M_{q_v} = 100$ GeV. The small tail in the distribution is due to the $\Gamma = 1$ GeV spread in the mass distribution (more about his in the following).

Now consider the process described in Fig. III.9. Two particles Y are pair-produced, then each of them decays into a visible particle (a or b in the figure) and one that escapes detection, called $N_{1,2}$. One cannot use the transverse momentum in this case since there are two particles escaping detection, both contributing to the missing transverse momentum $p\!\!\!/_T$. The observable MT2 is defined as

$$\text{MT2} \equiv \min_{p\!\!\!/_{T1}+p\!\!\!/_{T2}=p\!\!\!/_T} \left[\max \left\{ m_T^2(\mathbf{p}_{Ta}, p\!\!\!/_{T1}), m_T^2(\mathbf{p}_{Tb}, p\!\!\!/_{T2}) \right\} \right]. \tag{III.6}$$

where $p\!\!\!/_{T1,T2}$ are all the possible 2-momenta taken away by the Ns, such that their sum gives the observed missing momenta, $p\!\!\!/_{T1} + p\!\!\!/_{T2} = p\!\!\!/_T$.

MT2 coincides with the mass of the communicator Y, i.e. MT2 has a maximum, when for both communicator decays the visible and the invisible particles are produced at the same rapidity and

$$\left(\frac{\mathbf{p_a}}{E_a} - \frac{\mathbf{p_1}}{E_1} \right) \propto \left(\frac{\mathbf{p_b}}{E_b} - \frac{\mathbf{p_2}}{E_2} \right). \tag{III.7}$$

For the studies in this article we used a particularly simple version of the MT2 algorithm [17], the source code of which can be downloaded from

http://daneel.phyics.uc.davis.edu/ Cheng:2008hk/mt2-1.01a/test.
A more sophisticated algorithm is described in [18]. The simpler method is
based on the use of "kinematic constraints" [17, 19–21]

$$
\begin{aligned}
\mathbf{p}_1^2 = \mathbf{p}_2^2 &= \mu_N^2 \\
(\mathbf{p}_1 + \mathbf{p}_a)^2 &= (\mathbf{p}_2 + \mathbf{p}_b)^2 = \mu_Y^2 \\
p_1^x + p_2^x &= \not{p}^x \\
p_1^y + p_2^y &= \not{p}^y
\end{aligned}
\tag{III.8}
$$

In the case of two invisible and at least two visible particles as in Fig. III.9
the two methods actually coincide [17].

The inputs of the MT2 method are m_N, m_a, m_b, $\mathbf{p}_T^a$, $\mathbf{p}_T^b$ and $\not{p}_T$. Notice
that m_a and m_b may change quite substantially from event to event, since they
each correspond to the invariant masses of the clustered visible particles (in
this case the lepton and the photons) of each branch. The output of the MT2
method is one single MT2 value per event. Fig. III.10 illustrates a typical use
of the MT2 variable. If one histograms the MT2 values over a large number of
events, the upper edge of this distribution gives a lower limit on the commu-
nicator mass M_Y.

Whether the event rate in the upper-edge kinematic region defined in
eq. (III.7) is large enough to be able to extract the endpoint MT2$^{\max}$ = M_Y,
for a given luminosity, depends of course on the interactions. Even more than
for the energy variable in the previous section, it is not unlikely that MT2$^{\max}$
might have to be extrapolated from points in the shoulder region.

There are many other methods to determine mass relations between the the
new particles, [21, 22], just to cite some. Some of these are very closely related
to MT2, such as [23]. Some of these require cascade decay chains, or make
assumptions about the new particles involved in the decay chain being on
shell, or require high luminosity. Where this information is actually available,
one should of course make use of it, [24, 25].

The assumptions in this study, though, are that each of the identical decay
chains consists of a single two-body decay and that the integrated luminos-
ity, at least for the LHC at 7 TeV study, might be rather low (1 fb^{-1}). These
effectively preclude the use of many of the above methods.

In Fig. III.11 one may see the effect of the valley radiation on the MT2
distribution for different α_v values and communicator mass parameters. The
interesting region is again represented by the "shoulder" of the distribution.
Notice how the amount of invisible radiation, and thus the effect on MT2$^{\max}$,
increases with $M_{E_v} - M_{q_v}$, analogously to what happens in the energy distri-
butions. The size of these effects may be compared with the effects coming
from ISR, in Fig. III.12.

The MT2 distribution might present a tail, due to the Breit-Wigner spread
Γ that we allow for, see Fig. III.13. As one may see, all the MT2 data points
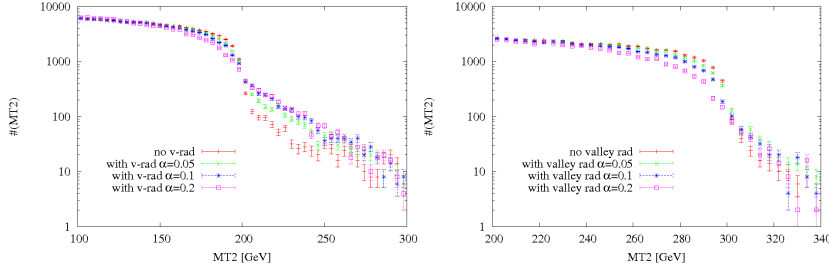
Figure III.11: The effect of valley radiation on the variable MT2 for different $\alpha_v = 0.05, 0.1, 0.2$ values (close-up on the shoulder region) at CLIC. The distributions were obtained assuming a luminosity $L = 1\,\text{fb}^{-1}$, $\sqrt{s} = 1$ TeV and $M_{q_v} = 50$ GeV. Left: the effect for a hypothetical $M_{E_v} = 200$ GeV. Right: the effect of valley radiation on MT2 for a hypothetical $M_{E_v} = 300$ GeV.
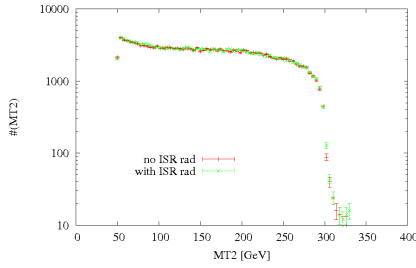
Figure III.12: The effects of initial-state radiation on the MT2 distribution and on the value of the M_{E_v} mass one infers. Number of events per 4 GeV bin, for an e^+e^- collider with $\sqrt{s} = 1$ TeV, $L = 1\,\text{fb}^{-1}$, $M_{E_v} = 300$ GeV, $\Gamma_{E_v} = 2$ GeV, $M_{q_v} = 50$ GeV. All other effects have been switched off.

III

which lie above $\text{MT2}^{\text{max}} = M_{E_v} = 300$ GeV correspond to E_vs which actually have a larger mass than the nominal M_{E_v}.

As we already stated above, m_N, the mass of the invisible particle, is an input parameter. MT2^{max} only gives one single relation between M_Y and m_N. Depending upon the decay chain topology and the presence or not of upstream transverse momentum (UTM, in the following, may come from ISR or from previous decays), there are different strategies to determine both masses simultaneously: the MT2 "kink" method [23], the invariant mass endpoint [26–29] or the constrained kinematic method [24], the polynomial intersection method [25], and $\mathbf{p}_T$ reconstruction [30–32], just to cite some possibilities. Most methods, however [24, 26–29], [25], require longer decay chains (at least two two-body decays) or a special topology, such as 4 on-shell intermediate
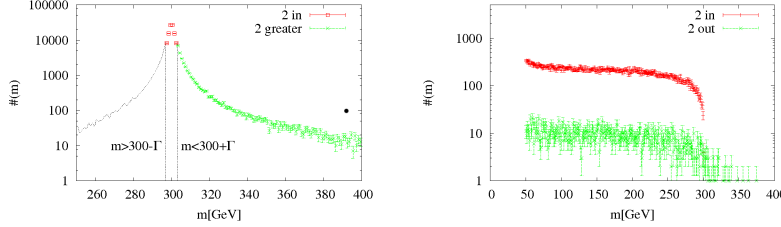
Figure III.13: Left: the (right side of the) Breit-Wigner mass distribution of the communicator E_v with an $M_0 = M_{E_v} = 300$ GeV and a width $\Gamma_{E_v} = 3$ GeV. Right: MT2 distribution for the same points. The upper (red) points correspond to considering only E_vs having masses within the $|m_{E_v} - M_{E_v}| < \Gamma_{E_v}$ GeV interval. The lower points (green) describe the MT2 points corresponding to both E_vs having a mass greater than $M_{E_v} + \Gamma_{E_v}$. All other effects have been switched off. Number of events per 1 GeV bin, $\sqrt{s} = 800$ GeV, $M_{q_v} = 50$ GeV, integrated luminosity $L = 200$ fb^{-1}. The error is purely statistical.

resonances [24] or 5 or more on-shell intermediate resonances [25].

If each decay chain consists of a single two-body decay, where the visible one may or may not be a composite of visible particles, as described in Fig. III.9, one may use the MT2 "kink method" [23] to fix the value of m_N, i.e. exploit the fact that MT2$^{\mathrm{max}}$ as a function of the invisible particle trial mass μ_N has a "kink" for $\mu_N = m_N$. The authors of [33] point out that in order to have a substantial change in the gradient $\frac{dMT2^{\mathrm{max}}}{d\mu_N}|_{\nu_N=m_N}$, there must be substantial event-by-event changes, though. This can be triggered by substantial $O(M_Y)$ differences in the ν_N, caused by the visible system being a collection of two or more particles, or by a large UTM. Otherwise the kinematics is so constrained that the gradients for $\mu_N < m_N$ and $\mu_N > m_N$ have to be the same, and no kink is possible.

If a sizable UTM $\mathbf{p_T}$ is present, one may use the MT2$\perp$ method [34]. This method uses the fact that $N(\mu_N)$, the number of times the $MT2(\mu_N, \mathbf{p}_T)$ is larger than $MT2(\mu_N, 0)$, has a minimum for $\mu_N = m_N$. The advantage of using this method rather that MT2kink is that $MT2(\mu_N, 0)$ may be calculated analytically and measured using the *whole* data sample, regardless the $\mathbf{p_T}$. This may be shown by using the fact that $MT2(\mu_N, 0)$ corresponds to MT2$^{\mathrm{max}} \perp (\mu_N)$,

$$\mathrm{MT2}^{\mathrm{max}}_{T\perp} = \min_{\not{p}_\perp = p_{1T\perp} + p_{2T\perp}} \left[\max \left\{ \mathrm{M}^2_{1T\perp}, \mathrm{M}^2_{2T\perp} \right\} \right], \tag{III.9}$$

the one-dimensional analogue of MT2, where

$$\begin{aligned} \mathrm{M}^2_{iT\parallel} &= m_i^2 + \mu_N^2 + 2(E_{iT\parallel}E^N_{iT\parallel} - p_{iT\parallel} \cdot p^N_{iT\parallel}) \\ M^2_{iT\perp} &= m_i^2 + \mu_N^2 + 2(E_{iT\perp}E^N_{iT\perp} - p_{iT\perp} \cdot p^N_{iT\perp}), \end{aligned}$$

and where $\perp$ and $\parallel$ refer to the projections of the $\mathbf{p_T}$ along the direction of the UTM.

We will not discuss further the different methods to extract the two new particle masses, but refer the interested reader to the proceedings from the TeV 2009 [9] conference and to the review [33]. We however wish to make a few remarks about the impact that valley radiation might have on these observables. Consider the MT2$\perp$ case, for example.

In the presence of valley radiation one needs to consider two sources of deviations. Firstly, the tails coming from the interleaved radiation mechanism, see the MT2 distributions in Fig. III.11. Secondly, as discussed in the previous section, in the presence of valley radiation, we expect the mean value of the invisible particle q_v invariant mass to shift from its Breit-Wigner central value $\langle M_{q_v}^{\text{eff}} \rangle = \mu_N$ towards the communicator mass M_{E_v} (or M_{D_v}) value. We will show in subsection III.6.2 that the MT2 distribution one obtains may be significantly affected, see Fig. III.4 for th LHC case. The MT2$_{T\perp}^{\text{max}}(\mu_N)$ should be similarly affected. The number of events having $\tilde{M}_Y(\mu_N, \mathbf{P}_T) > \tilde{M}_Y(\mu_N, 0)$ would then change accordingly, as would the minimum point $\mu_N = M_N$.

We will return on the issue of the the trial mass and the radiation in subsection III.6.2. In the following, unless otherwise specified, the analysis will always assume $\mu_N = m_N$.

III.6   Effects of $SU(3)_v$ radiation at LHC

At LHC the D_v communicators are (mostly) pair-produced by gg or $q\bar{q}$ fusion and decay flavour diagonally into a SM d quark and a valley q_v. For our study we assume the D_vs to be spin $1/2$ particles, and the q_vs to be scalars. As earlier this choice affects the production cross section, but now both s- and t-channel exchange are involved, which complicates the pattern. Each D_v radiates both SM gs and valley g_vs. These in turn may radiate further gs and g_vs, respectively. Once the D_v has decayed, the q radiates gluons, while the q_v radiates g_vs. The amount of hidden radiation emitted depends upon the valley coupling constant α_v and on the mass ratio M_{q_v}/M_{D_v}, see Fig. III.4. At the LHC the communicator mass reach will be larger than for the ILC, so typically there will be more phase space available for the radiation. Both the valley gluons radiated by the D_v and those radiated by the q_v have an impact on the visible particle distributions. The lighter the particle, the lower the cut-off scale for the radiation however, so it will be the q_v that radiates the most, as before.

When compared with the CLIC case, the LHC scenario presents several complications. Firstly one needs to convolute the production cross section with parton distribution functions. Thus the hard interaction — the production of the D_v pair — no longer happens in or close to the center-of-mass rest frame. In this case it is crucial to consider longitudinally boost invariant ob-

III

servables such as MT2. Secondly, both initial- and final-state QCD radiation are more intense than the QED one is for the ILC case, resulting in a considerably larger upstream transverse momentum and an increased misassignment of radiation. Thirdly, there is an underlying-event activity that gives rise both to a generic low-$p_\perp$ background and to occasional further hard partons that may be confused with the ones related to the valley process. Fourthly, the partons hadronize into more-or-less well-defined hadronic jets, the reconstruction of which introduces further smearing of the relevant kinematic distributions. And finally, the set of possible background processes is much more varied and challenging to suppress. In our study we will take into account the first four points, but leave the last one to the experimental community, where already a large number of background-suppression techniques have been developed for various scenarios.

III.6.1   LHC with 7 TeV

The LHC will initially be running at of $\sqrt{s} = 7$ TeV and it is expected to deliver 1 fb^{-1} of data in 2010–2011. Under these conditions we need to consider much lower masses M_{D_v} for the communicator than for the ultimate energy and luminosity case, in order to have large enough production cross sections, see Table III.2.

Based on the above discussions, we choose to study the MT2 distribution, and specifically its dependence on the v-radiation and on the α_v value. In Fig. III.14 we have plotted the α_v dependence for three different mass values $M_{D_v} = 300, 400$ and 500 GeV. The larger the mass difference $M_{D_v} - M_{q_v}$ the more phase space is available for the radiation. The smaller the M_{q_v}, the lower the cut-off on the momenta, so the larger the amount of soft radiation. Given the low statistics, the (purely statistical) error bars on the endpoints are rather large, and even in the shoulder of the distribution it is hard to distinguish the curve with an $\alpha_v = 0.1$ from the curve with no radiation for the 300 GeV mass. In the intermediate case $M_{D_v} = 400$ GeV, we need to have a rather strong $\alpha_v = 0.2$ coupling before the two curves can be separated.

In Fig. III.15 we show the MT2 dependence on the invisible q_v mass M_{q_v}, where the trial mass μ_{q_v} is assumed to coincide with M_{q_v}. Whether we look at the curves with a valley radiation (valley coupling $\alpha_v = 0.1$, left plot in Fig. III.15) or at the curves without hidden radiation (right plot in Fig. III.15), the data points corresponding to $M_{q_v} = 10, 50$ GeV are hardly distinguishable. The independence of the MT2 on the M_{q_v} value appears to be a characteristic which the radiation leaves unchanged.

One could argue that the fact that MT2 is hardly dependent on the M_{q_v} is due to the mass ratio M_{D_v}/M_{q_v} being fairly large compared to the difference between the two M_{q_v} values we considered. Would this argument still hold
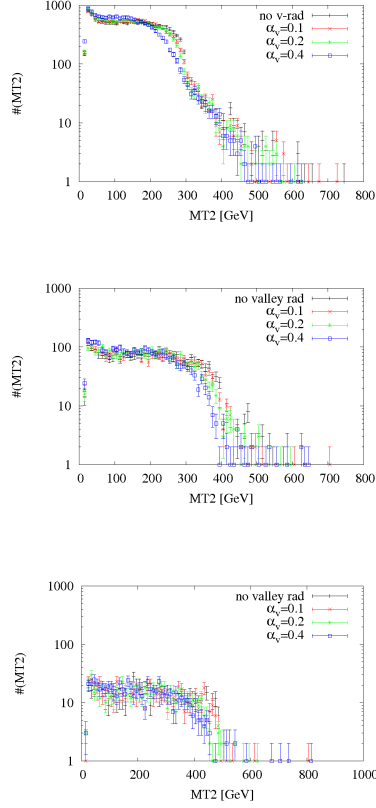
Figure III.14: The dependence of the MT2 distribution on the α_v value for $M_{D_v} = 300, 400, 500$ GeV and $M_{q_v} = 10$ GeV. The black curve corresponds to having no valley radiation. The red, green and blue curve correspond to $\alpha_v = 0.1, 0.2, 0.4$ respectively. For the first 2 years LHC is assumed to run $\sqrt{s} = 7$ TeV and to yield an integrated luminosity of 1 fb^{-1}. The y axis corresponds to the number of events per 10 GeV mass bin, for this integrated luminosity of 1 fb^{-1}.

true when the v-radiation is larger?

For larger values of the α_v one should consider the fact that the MT2 input parameter M_{q_v} corresponds to the mass of the q_v as seen by the visible particles. The visible particle momenta, i.e. the momenta of the d and the g radiated by it, which enter MT2, actually correspond to the invariant mass $M_{q_v}^{\text{eff}}$ rather than the nominal mass value M_{q_v}.

In Fig. III.4 we show this invariant mass distribution and how this changes as a function of the coupling constant α_v. As α_v grows q_v emits more and more
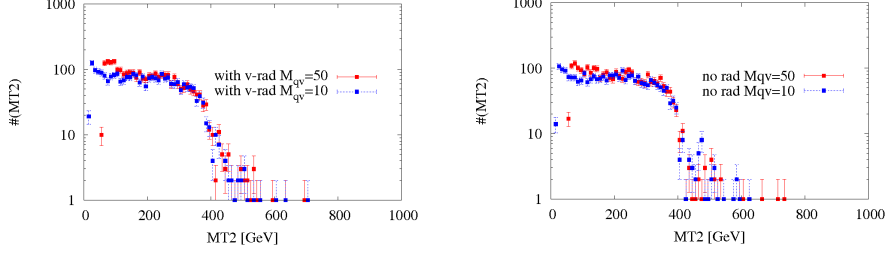
Figure III.15: Left: the M_{q_v} dependence of the MT2 when the valley radiation has $\alpha_v = 0.1$. The blue curve corresponds to $M_{q_v} = 10$ GeV and the red one to $M_{q_v} = 50$ GeV. Right: The same M_{q_v} dependence of the MT2 in the case of no valley radiation. $M_{D_v} = 400$ GeV, $\sqrt{s} = 7$ TeV and $L = 1$ fb^{-1}.

valley gluons g_v. The invariant mass of the $q_v + g_v$s system then grows, i.e the mean effective mass of the q_v as seen from the SM q shifts from the bare $M_{q_v} = 10$ GeV towards $M_{q_v}^{\max} = M_{D_v}$. The energy which is left for the d quark then gets smaller as the $\langle M_{q_v}^{\text{eff}} \rangle \to M_{D_v}$ as shown by

$$E_d = \frac{M_{D_v}^2 - M_{q_v}^2}{2M_{D_v}}, \tag{III.10}$$

where for simplicity we have put the $m_d = 0$.
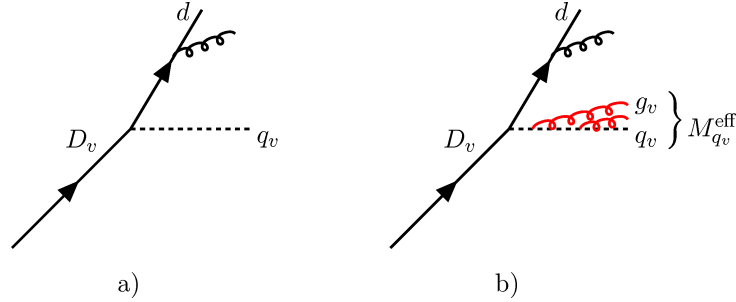
Figure III.16: Left: model a) decay $D_v \to dq_v$ with no v-radiation, M_{q_v} has a fixed value; right: model b) decay $D_v \to dq_v$ with v-radiation, the system $q_v + g_v$s has an invariant mass distribution.

Were this distribution a very narrow peak around $\langle M_{q_v}^{a,\text{eff}} \rangle$, there would be no difference between the two cases in Fig. III.16 so long as $\langle M_{q_v}^{a,\text{eff}} \rangle = M_{q_v}^b$, i.e. between a fixed $M_{q_v}^b$ value and an invariant mass distribution. One could speculate that so long as the mean value of the invariant mass $\langle M_{q_v}^{\text{eff}} \rangle \ll M_{D_v}$

the MT2 would basically remain unaffected.

Imagine though having a v-radiation large enough to shift the $\langle M_{q_v}^{\text{eff}} \rangle$ substantially, $M_{q_v}^{\text{eff}} \to M_{D_v}$, e.g. $\alpha = 0.4$. One would naïvely think that replacing the M_{q_v} with $\langle M_{q_v}^{\text{eff}} \rangle$ would give a better description of the case with radiation. However Fig. III.4 shows that for $\alpha_v > 0.1$ the invariant mass distribution would also have a large spread around this central value. We will show in the next section that this spread causes further complications. It is precisely the spread in the distribution which constitutes the difference between case a) and case b), and it is this spread which is ultimately responsible for the different behaviour of the MT2 in the two cases.

III.6.2   LHC with 14 TeV

If we now assume that LHC will collect 100 fb^{-1} of data at center of mass energy $\sqrt{s}$ =14 TeV, then one may consider larger communicator masses, $O(1\text{TeV})$, and still deal with a sufficient number of events, see Table III.2. If the q_v remains light, the mass ratio M_{D_v}/M_{q_v} can be considerable and consequently the phase space available for radiation can be large. We expect the effects of the radiation to be significant.

In Fig. III.17 we show the dependence of the MT2 distribution on the hidden valley coupling constant α_v, assuming we know the mass of the invisible particle so $\mu_{q_v} = M_{q_v}$. In this case we are describing the strong coupling regime $\alpha_v = 0.1, 0.4, 0.8$.

III
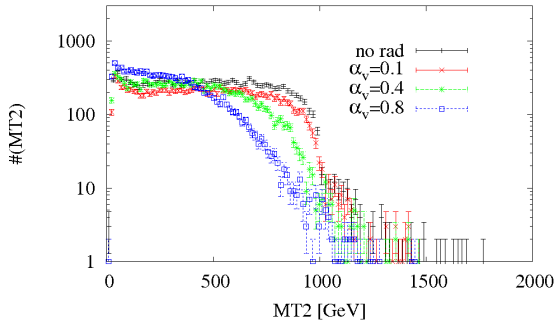
Figure III.17: MT2 distribution function for the communicator masses $M_{D_v} = 1$ TeV when there is valley radiation $\alpha_v = 0.1$ (red), 0.4 (green), 0.8 (blue) and when there is not (black curve). $\sqrt{s} = 14$ TeV, $M_{q_v} = 10$ GeV. Number of events per 15 GeV bin.

Notice how in this case one can actually separate (at least before any background or detector simulation is taken into account) the curve with $\alpha_v = 0.1$ and the one without the radiation.

In the above study the assumption is that events are generated with a bare mass M_{q_v} and analyzed with the same (or almost the same) trial mass $\mu_{q_v} = M_{q_v}$. From the discussion in subsection III.5.2, we could conclude that it is not very likely that we would know the mass of the q_v with high precision when valley radiation is present.

In a hidden valley scenario the mass of the q_v is assumed to be much lighter than the D_v mass, so we do not expect the MT2 to be very sensitive to q_v mass differences of the order $\Delta M_{q_v} \ll M_{D_v}$. Indeed, the authors of [23] and [33] show that the MT2$^{\mathrm{max}}$ mass dependence on the trial mass μ_{q_v} is rather weak so long as $\mu_{q_v} < M_{q_v}$, whereas MT2$^{\mathrm{max}}$ grows much more rapidly when $\mu_{q_v} > M_{q_v}$. The $\mu_{q_v} < M_{q_v}$ case is exactly what one observes in Fig. **??**.

Let us however make the conservative assumption that we only know the order of magnitude of the M_{q_v}. Imagine trying to distinguish between the two models we described in Fig. III.16, a) the model with no radiation and b) the model with the radiation, when $\langle M_{q_v}^{b,\mathrm{eff}} \rangle = M_{q_v}^b$. To be more concrete, assume a) has a fixed value mass $M_{q_v}^a = 395$ GeV and b) has an invisible particle mass $M_{q_v}^b = 10$ GeV and $\alpha_v = 0.28$. We choose the value $\alpha_v = 0.28$ so that $\langle M_{q_v}^{b,\mathrm{eff}} \rangle = M_{q_v}^a$.

In Fig. **??**, left side, we see the MT2 distribution for model a) for the case $M_{D_v} = 1$ TeV. As one may observe, this is a function of the trial mass μ_{q_v}, the best profile being the one with $\mu_{q_v} = M_{q_v}^a$. For $\mu_{q_v} \ll M_{q_v}^a$, even for substantial changes in μ_{q_v} the MT2$^{\mathrm{max}}$ does not change much. This essentially confirms what was reported by [23, 33].

On the right side of Fig. **??** one may see the same distributions for the model with radiation. Contrary to what one would expect from the naïve arguments given in the previous subsection, we see that choosing $\mu_{q_v} \sim \langle M_{q_v}^{b,\mathrm{eff}} \rangle$ does not give the best description of the system. The MT2 curve overshoots the M_{D_v} value by a good 10%. As anticipated in the previous subsection, this is due to the invariant mass distribution spread. Looking at Fig. III.19, one may see that the invariant mass distribution has a wide spread, so event by event there could be large variations in the $M_{q_v}^{b,\mathrm{eff}}$. If one chooses a $\mu_{q_v} \ll \langle M_{q_v}^{b,\mathrm{eff}} \rangle$ to analyze the set of events, for example the $\mu_{q_v} = 1$ GeV chosen in Figure **??**, most of the events will have a "real" q_v mass, the invariant mass $M_{q_v}^{b,\mathrm{eff}}$, larger than the trial mass μ_{q_v}. Since MT2$^{\mathrm{max}}(\mu_{q_v}) <$ MT2$^{\mathrm{max}}(M_{q_v}^{b,\mathrm{eff}})$ when $\mu_{q_v} < \langle M_{q_v}^{b,\mathrm{eff}} \rangle$, these points do not contribute to increase the MT2$^{\mathrm{max}}$ value much, and the distribution will resemble rather closely the one obtains for $M_{q_v}^b = 10$ GeV, apart from the softening in the shoulder. This is precisely what happens in the $\mu_{q_v} = 1,100$ GeV curves in Fig. **??**.

When one takes a $\mu_{q_v} \sim \langle M_{q_v}^{b,\mathrm{eff}} \rangle$ instead, e.g. $\mu_{q_v} = 350$ GeV (which according to the naïve arguments of the last subsection should have been the best of the three μ_{q_v} choices), more and more events have a "real" invisible
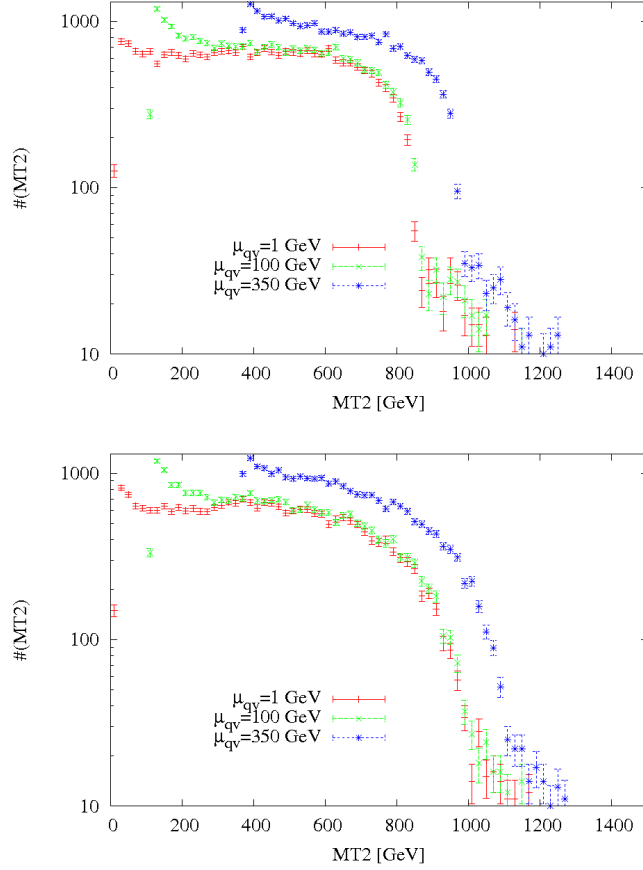
Figure III.18: Left: model a) comparison between different $\mu_{q_v} = 1, 100, 350$ GeV for $M_{q_v} = 395$ GeV. Right: model b) comparison between different μ_{q_v} for $M_{q_v} = 10$ GeV, $\alpha_v = 0.28$, $\langle M_{q_v}^{\text{eff}} \rangle = 395$ GeV. In both models $M_{D_v} = 1$ TeV, $\sqrt{s} = 14$ TeV and the luminosity is assumed to be $L = 100$ fb^{-1}, 20 GeV bins.

particle mass $M_{q_v}^{b,\text{eff}} < \mu_{q_v}$. In Fig. III.19 these are the points to the left of the $\mu_{q_v} = 350$ GeV line. These events will, if there is enough statistics, give MT2$^{\text{max}}(\mu_{q_v}) >$MT2$^{\text{max}}(M_{q_v}^{b,\text{eff}})$, the real M_{D_v} value. This is what happens to the curve for $\mu_{q_v} = 350$ GeV.

To prove this point, we separately plot the MT2 distributions for the events with $M_{q_v}^{b,\text{eff}} < \mu_{q_v}$ and the ones with $M_{q_v}^{b,\text{eff}} > \mu_{q_v}$. As Fig. III.20 shows, for the
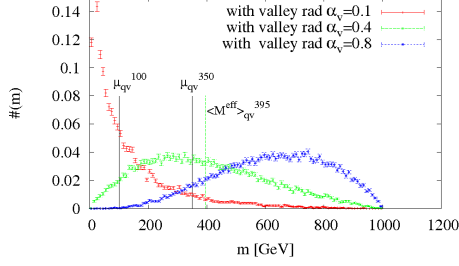
Figure III.19: The invariant mass distribution for the q_v and the trial masses we considered, $\mu_{q_v} = 1, 100, 350$ GeV.
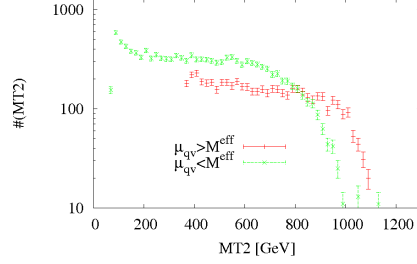
Figure III.20: MT2 distribution when both q_v invariant masses $M_{q_v}^{b,\text{eff}} < \mu_{q_v}$ (upper) and when both are $M_{q_v}^{b,\text{eff}} > \mu_{q_v}$ (bottom), when $M_{q_v}^{b} = 10$ GeV, $\alpha_v = 0.28$ and $\mu_{q_v} = 350$ GeV.

former set $\text{MT2}^{\max} \geq M_{D_v}$.
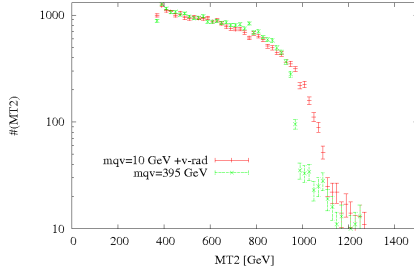
Figure III.21: Comparison between model a) $M_{q_v} = 395$ GeV and b) $M_{q_v}^{b} = 10$ GeV, $\alpha_v = 0.28$, $\langle M_{q_v}^{b,\text{eff}} \rangle = 395$ GeV for $\mu_{q_v} = 350$ GeV. In both models $M_{D_v} = 1$ TeV, $\sqrt{s} = 14$ TeV and the luminosity is assumed to be $L = 100$ fb^{-1}, 20 GeV bins. Notice that in this case the curve with the radiation is the lower one.

This said, we may return to the issue of distinguishing between the two models a) and b). As one may see in Figure III.21, the two curves corresponding to the two models have very different shapes, the one with no radiation being the sharper one. Notice however that now the curve with radiation lies above the one without. This is not in contradiction with what we have shown in the previous sections.

Summarizing, in the not-so-strong coupling regime $\alpha_v \sim 0.1$, when the in-

variant mass distribution is strongly peaked in M_{q_v}, one may[3] distinguish two models with the same values for M_{D_v} and M_{q_v}, one with v-radiation and one without. The curve corresponding to the no hidden radiation model will have a steeper drop in the shoulder region.

For larger couplings, $\alpha_v > 0.2$, one should note that two MT2 distributions with the same endpoints may correspond to different M_{D_v} values in the two cases, depending on whether the majority of the events have an invariant mass which is greater or smaller than the trial mass. A very conservative approach to solving this problem could simply be to assume $\mu_{q_v} = 0$ GeV or in any case $\mu_{q_v} \ll \langle M_{q_v}^{\text{eff}} \rangle$.

III.7   Conclusions

We have here addressed the issue of detecting and identifying hidden radiation through its influence on SM parton showers, and in general through its impact on visible particle kinematic distributions. We have done so in the context of Hidden Valley models, which we find are well suited to display the effects, but the specific models studied should be viewed only as representatives of a broad range of possible models with new symmetries. Thus, while we focus on the phenomenology of a fairly generic toy model, we also provide tools in PYTHIA 8 to simulate the effects of hidden radiation in various other hidden valley scenarios, e.g. different gauge groups, particle contents, and gauge and decay couplings. The novel feature in these tools is the interleaved SM and valley parton shower, i.e. the competition between visible and hidden radiation.

Our preliminary study of the phenomenology of the toy model at e^+e^- and at LHC colliders shows the following.

At an 800 GeV ILC collider we could expect to observe hidden radiation for valley gauge couplings as small as $\alpha_v \geq 0.05$, so long as the mass of the communicator is smaller than 300 GeV and $M_{q_v} \ll M_{E_v}$.

For the LHC phenomenology we need to distinguish between the first two year running with $\sqrt{s} = 7$ TeV and $L = 1$ fb^{-1} and later years with full design energy $\sqrt{s} = 14$ TeV and $L = 100$ fb^{-1}. Whether one could observe hidden radiation or not depends strongly on the communicator mass, which determines the amount of statistics. The main signal of the hidden radiation — at least in our studies — is the softening of the shoulder of the MT2 distribution. In the lower-energy case, for communicator masses around 500 GeV or higher, the statistics is so poor that one cannot expect to distinguish even a very strong coupling $\alpha_v = 0.4$. For two models with and without hidden radiation, with equal M_{D_v} masses in the [300, 400] GeV range and equal $M_{q_v} \leq 50$ GeV, one

---

[3] At least before background and detector analysis.

would need a valley coupling of the order $\alpha_v \geq 0.2$ or larger to induce large enough effects on the MT2 distribution to distinguish between the two. In the higher-energy case, for order TeV communicator masses and M_{q_v} smaller than 100 GeV, the MT2 distributions show sizable changes already for $\alpha_v = 0.1$.

We have also studied how the MT2 distribution depends upon the M_{q_v}, the invariant mass $M_{q_v}^{\text{eff}}$, and the trial mass μ_v. In the case of a Hidden Valley scenario, M_{q_v} is always assumed to be $M_{q_v} \ll M_{D_v}$. Taking a trial mass $\mu_{q_v} \ll M_{D_v}$ as an input parameter for the MT2 is thus a natural choice. When the q_v mass is larger though, e.g. $M_{q_v} \sim M_{D_v}$, the issue of the trial mass μ_{q_v} is no longer so trivial. The $M_{q_v}^{\text{eff}}$ can be a broad distribution when radiation is present. Especially in the strong interaction case, $\alpha_v \geq 0.2$, $\langle M^{\text{eff}} \rangle$ is strongly shifted towards M_{D_v}. This means that when one chooses a trial mass $\mu_{q_v} \sim \langle M^{\text{eff}} \rangle$, roughly half of the events will have $\mu_{q_v} > M^{\text{eff}}$, causing the MT2$^{\text{max}}$ to overshoot the real value. In this case the new masses thus have to be extracted from a combined fit, in which both masses and couplings enter as unknowns.

Further studies of the background and detector simulations should follow, both for the kind of scenarios we have explored here and for other possible ones. This preliminary study, however, shows unequivocally that parton showers are a key tool in determining the presence of new hidden gauge groups and in the exploration of the hidden sector gauge group dynamics.

Acknowledgments

III   References

[1] M. J. Strassler and K. M. Zurek, "Echoes of a hidden valley at hadron colliders," *Phys. Lett.* **B651** (2007) 374–379, `arXiv:hep-ph/0604261`.

[2] R. Blumenhagen, M. Cvetic, P. Langacker, and G. Shiu, "Toward realistic intersecting D-brane models," *Ann. Rev. Nucl. Part. Sci.* **55** (2005) 71–139, `arXiv:hep-th/0502005`.

[3] Z. Chacko, H.-S. Goh, and R. Harnik, "The twin Higgs: Natural electroweak breaking from mirror symmetry," *Phys. Rev. Lett.* **96** (2006) 231802, `arXiv:hep-ph/0506256`.

[4] M. J. Strassler, "Possible effects of a hidden valley on supersymmetric phenomenology," `arXiv:hep-ph/0607160`.

[5] K. M. Zurek, "Multi-Component Dark Matter," *Phys. Rev.* **D79** (2009) 115002, `arXiv:0811.4429 [hep-ph]`.

[6] H. Georgi, "Unparticle Physics," *Phys. Rev. Lett.* **98** (2007) 221601, `arXiv:hep-ph/0703260`.

[7] M. J. Strassler, "Why Unparticle Models with Mass Gaps are Examples of Hidden Valleys," `arXiv:0801.0629 [hep-ph]`.

[8] T. Sjostrand, S. Mrenna, and P. Z. Skands, "A Brief Introduction to PYTHIA 8.1," *Comput. Phys. Commun.* **178** (2008) 852–867, `arXiv:0710.3820 [hep-ph]`.

[9] G. Brooijmans *et al.*, "New Physics at the LHC. A Les Houches Report: Physics at TeV Colliders 2009 - New Physics Working Group," `arXiv:1005.1229 [hep-ph]`.

[10] C. G. Lester and D. J. Summers, "Measuring masses of semiinvisibly decaying particles pair produced at hadron colliders," *Phys. Lett.* **B463** (1999) 99–103, `arXiv:hep-ph/9906349`.

[11] J. Kang and M. A. Luty, "Macroscopic Strings and 'Quirks' at Colliders," *JHEP* **11** (2009) 065, `arXiv:0805.4642 [hep-ph]`.

[12] E. Norrbin and T. Sjöstrand, "QCD radiation off heavy particles," *Nucl. Phys.* **B603** (2001) 297–342, `hep-ph/0010012`.

[13] **Particle Data Group** Collaboration, C. Amsler *et al.*, "Review of particle physics," *Phys. Lett.* **B667** (2008) 1.

III

[14] **D0** Collaboration, V. M. Abazov *et al.*, "Search for scalar leptoquarks in the acoplanar jet topology in $p\bar{p}$ collisions at $\sqrt{s}$ = 1.96- TeV," *Phys. Lett.* **B640** (2006) 230–237, `arXiv:hep-ex/0607009`.

[15] **D0** Collaboration, V. M. Abazov *et al.*, "Search for third-generation leptoquarks in $p\bar{p}$ collisions at $\sqrt{s}$ = 1.96-TeV," *Phys. Rev. Lett.* **99** (2007) 061801, `arXiv:0705.0812 [hep-ex]`.

[16] M. Cacciari and G. P. Salam, "Dispelling the N^3 myth for the k_t jet-finder," *Phys. Lett.* **B641** (2006) 57–61, `arXiv:hep-ph/0512210`.

[17] H.-C. Cheng and Z. Han, "Minimal Kinematic Constraints and MT2," *JHEP* **12** (2008) 063, `arXiv:0810.5178 [hep-ph]`.

[18] C. Lester, "The Oxbridge MT2 / Stransverse Mass Library." Http://www.hep.phy.cam.ac.uk/ lester/mt2/index.html.

[19] H. Bachacou, I. Hinchliffe, and F. E. Paige, "Measurements of masses in SUGRA models at CERN LHC," *Phys. Rev.* **D62** (2000) 015009, `arXiv:hep-ph/9907518`.

[20] B. C. Allanach, C. G. Lester, M. A. Parker, and B. R. Webber, "Measuring sparticle masses in non-universal string inspired models at the LHC," *JHEP* **09** (2000) 004, `arXiv:hep-ph/0007009`.

[21] I. Hinchliffe, F. E. Paige, M. D. Shapiro, J. Soderqvist, and W. Yao, "Precision SUSY measurements at CERN LHC," *Phys. Rev.* **D55** (1997) 5520–5540, `arXiv:hep-ph/9610544`.

[22] D. R. Tovey, "Measuring the SUSY mass scale at the LHC," *Phys. Lett.* **B498** (2001) 1–10, `arXiv:hep-ph/0006276`.

[23] W. S. Cho, K. Choi, Y. G. Kim, and C. B. Park, "Gluino Stransverse Mass," *Phys. Rev. Lett.* **100** (2008) 171801, `arXiv:0709.0288 [hep-ph]`.

[24] H.-C. Cheng, J. F. Gunion, Z. Han, G. Marandella, and B. McElrath, "Mass Determination in SUSY-like Events with Missing Energy," *JHEP* **12** (2007) 076, `arXiv:0707.0030 [hep-ph]`.

[25] H.-C. Cheng, D. Engelhardt, J. F. Gunion, Z. Han, and B. McElrath, "Accurate Mass Determinations in Decay Chains with Missing Energy," *Phys. Rev. Lett.* **100** (2008) 252001, `arXiv:0802.4290 [hep-ph]`.

[26] B. K. Gjelsten, D. J. Miller, 2, and P. Osland, "Measurement of SUSY masses via cascade decays for SPS 1a," *JHEP* **12** (2004) 003, `arXiv:hep-ph/0410303`.

[27] D. Costanzo and D. R. Tovey, "Supersymmetric particle mass measurement with invariant mass correlations," *JHEP* **04** (2009) 084, `arXiv:0902.2331 [hep-ph]`.

[28] M. Burns, K. T. Matchev, and M. Park, "Using kinematic boundary lines for particle mass measurements and disambiguation in SUSY-like events with missing energy," *JHEP* **05** (2009) 094, `arXiv:0903.4371 [hep-ph]`.

[29] K. T. Matchev, F. Moortgat, L. Pape, and M. Park, "Precise reconstruction of sparticle masses without ambiguities," *JHEP* **08** (2009) 104, `arXiv:0906.2417 [hep-ph]`.

[30] K. Kawagoe, M. M. Nojiri, and G. Polesello, "A new SUSY mass reconstruction method at the CERN LHC," *Phys. Rev.* **D71** (2005) 035008, `arXiv:hep-ph/0410160`.

[31] M. M. Nojiri, G. Polesello, and D. R. Tovey, "A hybrid method for determining SUSY particle masses at the LHC with fully identified cascade decays," *JHEP* **05** (2008) 014, `arXiv:0712.2718 [hep-ph]`.

[32] B. Webber, "Mass determination in sequential particle decay chains," *JHEP* **09** (2009) 124, `arXiv:0907.5307 [hep-ph]`.

[33] A. J. Barr and C. G. Lester, "A Review of the Mass Measurement Techniques proposed for the Large Hadron Collider," *2010 J. Phys.* **G** (3001), `arXiv:1004.2732 [hep-ph]`.

[34] P. Konar, K. Kong, K. T. Matchev, and M. Park, "Superpartner Mass Measurement Technique using 1D Orthogonal Decompositions of the Cambridge Transverse Mass Variable M_{T2}," *Phys. Rev. Lett.* **105** (2010) 051802, `arXiv:0910.3679 [hep-ph]`.

III

IV

Discerning Secluded Sector gauge structures

Lisa Carloni, Johan Rathsman and Torbjörn Sjöstrand

Theoretical High Energy Physics,
Department of Astronomy and Theoretical Physics, Lund University,
Sölvegatan 14A, SE 223-62 Lund, Sweden

New fundamental particles, charged under new gauge groups and only weakly coupled to the standard sector, could exist at fairly low energy scales. In this article we study a selection of such models, where the secluded group either contains a softly broken $U(1)$ or an unbroken $SU(N)$. In the Abelian case new γ_v gauge bosons can be radiated off and decay back into visible particles. In the non-Abelian case there will not only be a cascade in the hidden sector, but also hadronization into new π_v and ρ_v mesons that can decay back. This framework is developed to be applicable both for e^+e^- and pp collisions, but for these first studies we concentrate on the former process type. For each Abelian and non-Abelian group we study three different scenarios for the communication between the standard sector and the secluded one. We illustrate how to distinguish the various characteristics of the models and especially study to what extent the underlying gauge structure can be determined experimentally.

IV

IV.1   Introduction

There are basically two ways in which one can envision new physics beyond the standard model that can be searched for at future colliders. One possibility is to have theories with new heavy particles coupling to the standard model with either the ordinary gauge couplings, as in supersymmetry, or with couplings of a similar magnitude. This implies heavy particle masses, in order to avoid collider constraints. The other possibility, which we want to explore in this paper, is that new light particles are ultra-weakly coupled to the standard model particles, because they are not charged under the standard model gauge groups. Instead they couple to the ordinary matter through some heavy state which carries both SM charges and charges of a new unknown gauge group, also carried by the light states.

There have been several suggestions for theories with this type of secluded sectors (sometimes also called hidden valleys or dark sectors), proposing non-conventional new physics with unexpected and unexplored signals could show up at current colliders such as the Large Hadron Collider (LHC) or a future linear electron-positron collider.

One example is the so-called hidden valley scenarios by Strassler and collaborators [1–7], where the SM gauge group is extended by a new unspecified gauge group G. In the original paper [1] this group is a $U(1)' \times SU(N)$. The new matter sector consists of $v-$particles (where v stands for "valley"), which are charged under the new gauge group and neutral under the standard one. The two sectors communicate via higher dimensional operators, induced either by heavy particle loops or by a Z' which can couple to both sectors.

An interesting feature of models with secluded sectors is that they naturally give rise to dark matter candidates. Likewise, some of the recently proposed dark matter models may present hidden sector features. Specific dark matter models developed in the last few years such as [8–12] suggest the existence of a GeV scale mass dark photon or scalar that is introduced to enhance the dark matter annihilation cross section, in order to fit the data from PAMELA [13,14] and originally ATIC [15], although the latter data have later been superseded by more precise measurements from FERMI [16]. Here we will mainly be interested in models with dark photons originating from a softly broken $U(1)$, which couple to standard model particles through so called kinetic mixing with the ordinary photon [17] through heavy particle loops in a similar way to the hidden valley scenarios.

The hidden valley-like theories and the dark matter models mentioned above share two features: the enlarging of the standard model symmetries to include a new gauge group G and the presence of new light particle sectors that are solely charged under this new gauge group. If the new light particles can decay into standard model particles, their existence could be inferred from
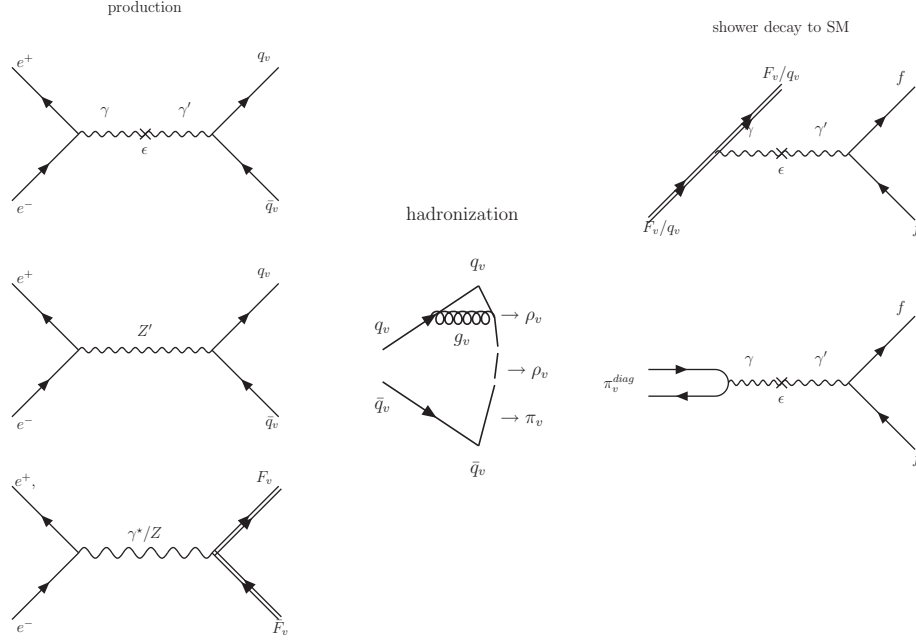
Figure IV.1: The different mechanisms for production, hadronization and decay that we consider as explained in the text.

their effect on standard model particle phenomenology. In [18] we studied the effects of the new gauge group radiation, specifically the kinematic effects of $SU(3)'$ radiation from fermions charged under both the SM and the new gauge group on the kinematic distributions of visible particles. In this paper we address the issue of discerning between different gauge structures. Specifically, we want to outline the differences between signatures arising from a secluded sector broken $U(1)'$ gauge group with a light γ_v and those arising from a confining $SU(N)$. In both cases we assume there is a mechanism for the secluded particles to decay back into the SM.

In order to distinguish which features of a given model are linked to the gauge group structure and which to the other details of the model, we consider different production processes and different mechanisms for the decay back into the SM. The various possibilities are summarized in Fig. IV.1. For the production we consider three mechanisms. In the first case the portal to the hidden sector is through kinetic mixing between the SM photon and a light $U(1)$ gauge boson. In the second case we have production via a Z'. In the kinetic mixing of γ-γ_v, the γ_v is assumed to have a mass around 1-10 GeV and

the mixing ϵ is assumed to be $\epsilon \sim 10^{-3}$, while in the Z' case, the mass of the Z' would be around 1-6 TeV [1]. The third case is where the production happens via SM gauge bosons as in [18]. In this case the particles are assumed to have both SM charges and secluded sector ones. To distinguish them we will call them F_v in the following, to separate them from particles that are only charged under the secluded gauge group, which we call q_v. We will also assume that the F_v particles will decay into a standard model particle f and a secluded sector particle q_v, *i.e.* $F_v \to f q_v$.

If the particles of the secluded sector are charged under a non-Abelian $SU(N)$ or a softly broken Abelian $\not{U}(1)$ with a light γ_v, there will also be additional radiation of gauge bosons. In the former case, the v-gluons will be connected to the q_vs (produced directly or via the F_vs) and form a confined system which will then hadronize.

Depending on the nature of the secluded hadrons thus produced, they may then decay back into standard model particles through kinetic mixing or a heavy Z'. In both cases this decay can be very slow, so much so as to generate displaced vertices and other exotic signatures as for example discussed in [2]. In the case of γ_v radiation instead, the gauge bosons may decay directly back into the SM through kinetic mixing γ_v-γ, while the q_vs will not be able to decay back into the SM since they carry the secluded gauge charge.

Thus, in both the non-Abelian and Abelian cases, we can have models where some of the particles produced will decay back into SM particles and some of them will be invisible. The questions we want to address is thus how the production of visible particles depends on the secluded gauge structure and whether it is possible to tell a non-Abelian and Abelian gauge group apart also when other features of the models are very similar.

The paper is structured as follows. Section IV.2 gives a short overview of the general model considerations that underlie our studies, with particular emphasis on the production mechanisms that are relevant in various scenarios, and some comments on the decay mechanisms that lead to signals in visible distributions. In section IV.3 we provide a more in-depth overview of the new physics aspects that we have implemented in PYTHIA 8: the particle content, the parton showers, notably for the broken $U(1)$ case, the hadronization in the secluded sector, and the decay back to the visible one. In Section IV.4 we proceed to describe the phenomenology of the various scenarios, in the context of an e^+e^- linear collider. While less interesting than a corresponding LHC phenomenology, it allows us to better highlight the relevant features of the model as such. In section IV.5 we further study distributions that could offer a discrimination between an Abelian and a non-Abelian scenario for the secluded sector. In Section IV.6 we summarize our findings, and give an outlook. Finally in Appendix IV.6 we provide information how the simulation of a wide range of scenarios can be set-up.

IV.2   Overview of hidden sector scenarios

As already mentioned in the introduction there are many different types of models that can display hidden sectors and the common feature is that they communicate with the standard model through some heavy states. This communication can occur in many different ways and we will distinguish three different types in the following: via kinetic mixing, via a heavy Z', and via heavy fermions that carry SM charges.

The common feature of the models we consider is that the SM group $SU(3)_C \times SU(2)_L \times U(1)_Y$ is augmented by a new gauge group G. For each scenario we will consider two cases - one *Abelian* where G contains a softly broken $\cancel{U}(1)$ with a light gauge boson γ_v and one *non-Abelian* where G contains an unbroken $SU(N)$ factor mediated by a then massless g_v.

The particle content consists of q_v particles and/or F_v particles. With q_v particles we indicate fermions or scalars (with spin = 1/2, 0, 1) charged solely under the new gauge group. With F_v we indicate particles (spin $s = 0, 1/2, 1$) which may couple to both secluded sector and standard model sector. Though in principle one could choose any spin assignment among the ones above, we have chosen to analyze the case in which F_v and q_v are fermions, except in the case when the q_vs are produced from a F_v decay when we assume them to be scalars. In addition, in all the scenarios we consider both F_v and q_v belong to the fundamental representation of the group G. Finally, the G sector charges are constrained by anomaly cancellation. For an example see [1].

IV.2.1   Kinetic mixing scenarios

As already alluded to, one way of producing the secluded sector particles is through kinetic mixing. In the scenarios we wish to investigate, the SM U(1) (effectively the photon) mixes kinetically with a new GeV mass γ_v and produces a pair of secluded sector particles, see Fig. IV.1. This mechanism is mostly relevant in the case when the secluded sector contains new fermions which are charged only under the new gauge group G. In addition we will in this scenario only consider those cases when the SM particles are not charged under the new U(1). Communication between the SM and secluded sectors then only comes from kinetic mixing between the standard model U(1) gauge boson and the new gauge boson, as described by

$$\mathcal{L}_{\text{kin}} = -\frac{1}{4}\epsilon_1 \left(F_1^{\mu\nu} \right)^2 - \frac{1}{2}\epsilon F_1^{\mu\nu} F_{2,\mu\nu} - \frac{1}{4}\epsilon_2 \left(F_2^{\mu\nu} \right)^2. \tag{IV.1}$$

In the case of two $U(1)$ gauge symmetries ($U(1)_1 \times U(1)_2$), the non-vanishing mixing ϵ arises naturally as one integrates out loops of heavy fermions coupling to both the associated gauge bosons [17] so long as there is a mass splitting among them. The relation between the size of the mixing and the mass

IV

splitting is given by

$$\epsilon = \frac{e_1 e_2}{16\pi^2} \ln \left(\frac{M_{12}^{(1)}}{M_{12}^{(2)}} \right), \qquad (\text{IV}.2)$$

where e_1 and e_2 are the gauge couplings of the fermions in the loop to the two $U(1)$ gauge bosons, A_1 and the new A_2 respectively, and $M_{12}^{(1)}$ and $M_{12}^{(2)}$ are their masses. In general, the $U(1)_1$ and the $U(1)_2$ will not be orthogonal. One may however chose the $U(1)_1$ generator so that the fermions that are only charged under $U(1)_1$ do not have any charge shift, while those that couple to $U(1)_2$ do [17].

For the case of non-Abelian groups, $G_1 \times G_2 \times G_3$, a mixing can come from the spontaneous breaking of the group down to $H \times U(1)_1 \times U(1)_2$. Also in this case the $U(1)_1$ and the $U(1)_2$ will not be orthogonal, as long as the three couplings associated to the unbroken symmetries are different.

The kinetic mixing mechanism has been used in model that want to describe various recent cosmic ray measurements in terms of dark matter models. The most important signal here is the positron excess observed by PAMELA [14]. At the same time, any model wanting to explain this excess also has to explain the absence of an anti-proton excess observed by PAMELA [13] and finally the measurements of the total electron and positron flux observed by the Fermi LAT collaboration [16]. The models are set up so that the dark matter particles will annihilate into a dark photon or scalar which couples to SM particles through kinetic mixing. The mass of the dark matter particle is then determined by the scale at which the positron excess is observed, to be of order 0.1–1 TeV.

In addition, the large positron excess observed also means that there must be some enhancement mechanism of the dark matter annihilation cross section. One way to do this is to invoke Sommerfeld enhancement[1] by introducing a light dark photon or scalar. The mass of the dark photon (or scalar) in these models is typically in the GeV range, which means that decays into $\bar{p}$ and π^0 are kinematically suppressed relative to the lepton decays and thus also explain the non-observation of any anti-proton excess by PAMELA [13].

A recent example of models that fits all these data is given by [19], but there are still large uncertainties due to cosmological assumptions such as the dark matter distribution and propagation of cosmic particles.

The dark gauge group G_{dark} is largely unspecified in these types of models except that it must contain a U(1) factor in order for the kinetic mixing with the SM photon. This means that there could also be additional Abelian or non-Abelian factors in G_{dark}. In the following we will consider the cases when G_{dark} contains an additional $U(1)$, which is spontaneously broken giving a massive

---

[1]Resummation of t-channel exchanges of a new light particle.

Z', or an additional $SU(N)$ factor giving a confining force for the secluded sector particles.

The phenomenology and constraints on these types of models at low energy e^+e^- colliders such as Belle, BaBar, DAΦNE, KLOE and CLEO have been studied by [20–23].

IV.2.2 Z' **mediated scenarios**

The second type of scenarios we want to consider are those that are similar to the original hidden valley scenario [1] with a massive Z' coupling to both SM fermions and secluded sector ones. Thus, the processes we are interested in are when SM fermions annihilate into the secluded sector Z' which in turn gives a pair of secluded particles, as depicted in Fig. IV.1.

In these types of models it is typically assumed that the Z' acquires a mass by spontaneous symmetry breaking of a $U(1)$ symmetry by a $\langle \phi \rangle$ whereas the origin of the secluded sector $\slashed{U}(1)$ is not discussed.

The secluded sector particles that the Z' would decay to could be either charged solely under the valley gauge group G or charged under G and (parts of) the SM $SU(3)_C \times SU(2)_L \times U(1)_Y$. In the latter case, the particles would on the one hand have to be very massive (several hundreds of GeV) due to experimental constraints and on the other hand they would be more effectively produced through their SM couplings. Thus we will not consider this possibility more here. In contrast the particles charged solely under the secluded gauge group could be light with a mass in the $1 - 50$ GeV range, thanks to the reduced coupling through the heavy Z'.

As a consequence of the heavy mass of the Z', the s-channel pair production cross section will be peaked at $\sqrt{\hat{s}} \sim m_{Z'}$ and be suppressed at an e^+e^- collider unless $\sqrt{s} \sim M_{Z'}$. At a hadron collider the production of the Z' would be dominantly on-shell if the overall center of mass energy is large enough and there is enough support from the parton density functions.

In the original hidden valley model the secluded sector group also contains a confining $SU(N)$. Thus the produced secluded sector particles would have to hadronize into hadrons which are neutral under this $SU(N)$. Another possibility is that there is instead an additional $\slashed{U}(1)$ which would instead give radiation of γ_vs.

Finally it should be noted that also in this case there is kinetic mixing between the Z and the Z', which primarily is important for setting limits on the mass and couplings of the Z' from LEP as discussed in [1].

IV

IV.2.3   SM gauge boson mediated scenarios

The final type of scenario that we consider are ones where the "communicator" is charged under both the SM and new interactions. This scenario and its implementation into PYTHIA 8 has been described in [18] so here we only briefly recapitulate the main features.

In this model the new heavy communicator particle F_v would be pair produced with SM strength, which means that it would have to be quite heavy in order to not have been already seen at colliders. Another consequence is that the communicator would decay into a SM and pure hidden sector particle, dubbed q_v, so that quantum numbers are conserved. In the simple case in which neither q_vs nor v-gauge bosons leak back into the SM, as in the scenario in [18], this entails a missing energy signal.

Also in this case, the secluded sector group can be either Abelian or non-Abelian. In both cases we will assume that the produced γ_vs or hadrons can decay back to SM particles through kinetic mixing via loops of the F_v particles or via a Z'.

IV.2.4   Decays back to the SM

First of all we mention again the case of secluded particles which are charged both under the SM and secluded gauge groups, F_v, which we assume decay according to $F_v \rightarrow f q_v$. All other particles produced by either of the mechanisms described above may decay back to SM particles as long as they do not carry any charge under the secluded gauge group. Essentially these decays will be through kinetic mixing with SM gauge bosons or through a heavy Z' as detailed below.

In the Abelian case, with a light secluded sector γ_v, the q_vs will be stable, but the γ_vs that are radiated in connection with the primary hard process will decay back to SM particles, $\gamma_v \rightarrow f\bar{f}$. The strength of the kinetic mixing ϵ, together with the available phase space, determines the decay width $\Gamma_{\gamma_v \rightarrow f\bar{f}}$. Since the γ_v is light, it will mainly mix with the standard model photon and thus the branching ratios for different channels will depend on the electric charge of the produced SM particles. In essence this means that the decays will be similar to a off-shell photon, γ^* with the virtuality given by m_{γ_v}. We also note that if the kinetic mixing is small, the life-time could be so large as to give displaced vertices.

In the non-Abelian case the secluded sector hadrons may also decay back into the SM via kinetic mixing of the γ_v with the SM photon or via a heavy Z'. In this case the phenomenology will depend on the number of light flavours N_{flav} in the secluded sector. In the following we will assume that $N_{\text{flav}} \geq 2$ and only consider the case when the fundamental particles are fermions as in [1] although similar arguments can be made also in the case of scalar constituents.

Thus, the bound states will be the secluded sector version of mesons, baryons and possibly also glueballs. For the decays back to SM particles, it is the meson states that are of primary interest and therefore we concentrate on them here.

With N_{flav} light flavours, there will be of the order N_{flav}^2 mesons with a given spin out of which approximately N_{flav} are flavour neutral and can decay back into the SM via kinetic mixing or a Z'. The SM decay products will depend on the spin of the secluded meson. For a spin zero meson, helicity suppression leads to dominance by the heaviest SM particle available whereas for a spin 1 meson it will depend on the couplings to the particle mediating the decay, *i.e.* either to the photon in the case of kinetic mixing or to the Z'.

The phenomenology will thus depend on the relative production of spin-0 and spin-1 mesons and their masses. If the confinement scale Λ_v in the secluded sector is large compared to masses of the lightest secluded sector fermions the situation will be similar to QCD. In other words there will be a light spin-0 π_v with mass much smaller than the spin-1 ρ_v. Thus all ρ_v will decay to pairs of π_vs and the SM particles produced will be the heaviest one available.

If Λ_v is of the order of the masses of the lightest secluded sector fermions then the mass splitting between the spin-0 and spin-1 mesons will be small and thus the spin-1 meson will be metastable and instead decay back into the SM, again via either kinetic mixing or a Z', but in this case, there not being any helicity suppression, the decay will be similar to that of an off-shell photon. Thus in this case there will also be an abundance of leptons produced along with hadrons.

If all constituent masses are much larger than the confinement scale, the lowest lying $SU(N)$ neutral states would be glueballs as discussed in [7]. We do not discuss their phenomenology here. We will also not consider so called quirks [24] which are charged both under the SM $SU(3)_C$ and a secluded $SU(N)$ with the confinement scale Λ being much smaller than the F_v masses.

Finally we note that similarly to the Abelian case some of the secluded sector hadrons could be metastable and decay back into the detectors with displaced vertices.

IV.3   Physics in the secluded sector

For the studies in this article we have developed a framework to simulate the physics of a secluded sector. It contains a flexible setup that can be used to study different production mechanisms, perturbative shower evolution scenarios, non-perturbative hadronization sequences and decays back into the visible sector. Parts of the framework were already in use for our previous study [18] but significant new capabilities have been added. These are available starting with PYTHIA 8.150. The physics content will be described in the

following, while technical details on how to set up a variety of scenarios is outlined in Appendix A. The studies presented in this article only give a glimpse of the possibilities.

IV.3.1 Particles and their properties

The key aspect of a scenario is that of the valley gauge group G, which we allow to be either $U(1)$ or $SU(N)$. The gauge bosons of these groups are named γ_v and g_v, respectively. The former can be broken or unbroken, i.e. γ_v can have a mass, while the latter is always unbroken so that g_v remains massless.

The rest of the particles, i.e. the "matter" content, fall into two main categories: those charged under both the SM and the v sector, and those that are pure v-sector particles.

For the doubly charged ones, dubbed F_v, 12 particles are introduced to mirror the Standard Model flavour structure, see Tab. IV.2 in the appendix. Each F_v particles couples flavour-diagonally to the corresponding SM particle. In addition to its SM charges, it is also put in the fundamental representation of G. For $U(1)$ the charge is taken to be unity, while for $SU(N)$ the "charge" is $C_F = (N^2 - 1)/(2N)$ while pair production cross sections obtain a factor of N enhancement. Although the name suggests that the F_v are fermions, they can be spin 0, 1/2 or 1 particles. If the F_v particles have spin 1 then their production cross section depends also on the presence or not of an anomalous magnetic dipole moment.

The valley secluded sector further contains a purely G interacting sector. At the parton level this consists of q_vs, belonging to the fundamental representation of G. The name is introduced to reflect the similarities with the quark in QCD. The q_v particle is stable and invisible to SM interactions. Its spin, 0 or 1/2, is adapted to the choice of spin made for F_v, in case the scenario allows for $F_v \to f q_v$ decay, where f is a SM particle. The spin structure of the $F_v \to f q_v$ decay is currently not specified, so the decay is isotropic.

In the $G = U(1)$ scenarios only one q_v is assumed to exist. F_v decays, if allowed kinematically, are flavour diagonal, $F_v^i \to f^i q_v$, with a common (Yukawa) coupling strength. Given that both the F_vs and the q_vs have a unit of $U(1)$ charge, they can radiate γ_v gauge bosons. If $U(1)$ is unbroken the γ_v is massless and stable. For a broken symmetry, $G = \cancel{U}(1)$, the γ_v can decay back to a SM fermion pair through the mechanisms discussed in the previous Section IV.2. For kinetic mixing or decay via a Z', branching ratios by default are assumed to be proportional to the respective fermion coupling to the photon, whenever the production channel is allowed by kinematics. The γ_v decay can be either prompt or displaced.

If instead $G = SU(N)$, the massless g_v gauge bosons are self-interacting, such that the parton shower will also have to allow for $g_v \to g_v g_v$ splittings,

with no equivalence in the $U(1)$ case. The self-interactions also lead to confinement, like in QCD. In Section IV.3.3 below we will explain how the resulting picture can be described in terms of "strings" stretched from a q_v end via a number of intermediate g_vs to a $\bar{q}_v$ end. The string can break, by the production of new $q_v\bar{q}_v$ pairs, to produce a set of v-mesons formed by the q_v of one break and the $\bar{q}_v$ from an adjacent one. To first approximation these v-mesons would be stable, and so the whole v-hadronization process would be invisible. One would not even have the kind of indirect recoil effects that the v-shower can give. If kinetic mixing or decay via a Z' is assumed, it would again be possible to let the v-mesons decay back to a SM fermion pair.

With only one q_v species there would only be one kind of v-mesons, and so the choice would be between two extremes: either all the energy deposited in the hidden sector decays back to be visible, or none of it. The more interesting scenarios — e.g. in terms of offering a bigger challenge to sort out what is going on — are the ones where only part of the v-mesons can decay back. Therefore a variable number N_{flav} of separate q_v flavours are assumed to exist (at most 8 in the current implementation). This gives N_{flav}^2 different possible v-meson flavour combinations, out of which only N_{flav} are flavour-diagonal and thus able to decay back into the SM sector. It would be possible to assign individual masses to the q_vs and v-mesons, but for now we assume one common q_v "constituent" mass and one common v-meson mass, twice as large as the former.

By analogy with QCD two separate spin states are assumed, denoted π_v and ρ_v. For now mass splitting is taken to be small, such that $\rho_v \to \pi_v\pi_v$ is kinematically forbidden, as is the case in QCD for the s and heavier quarks. The decay of the flavour-diagonal mesons is different in the two cases: by helicity (non)conservation the π_v couplings to a pair of SM fermions f provides an extra factor m_f^2, an addition to the squared charge and phase space factors factors present for the ρ_v mesons.

In the confining $SU(N)$ case also a v-glueball is introduced. It is only rarely used, to handle cases where the invariant mass of the invisible-sector fragmenting system is too large to produce one single on-shell v-meson and too small to give two of them. Then it is assumed that an excited v-meson state is produced, that can de-excite by the emission of these invisible and stable g_vg_v bound states.

In summary, by default the v-particles with no SM couplings are not visible. Their presence can only be deduced by the observation of missing (transverse) momentum in the event as a whole. On top of this we allow two different mechanisms by which activity can leak back from the hidden sector. The first is the $F_v \to fq_v$ decay and showers from the F_v and q_v, in the scenario in which F_v has both SM charges and G charges, as discussed in our previous article [18]. The second is the decay of SM gauge bosons produced through mixing by the

IV

G group gauge bosons in the kinetic mixing case, either the massive γ_v for $\cancel{U}(1)$ or the diagonal v-mesons for $SU(N)$.

IV.3.2 Valley parton showers

Parton showers (PS) offer a convenient approximation to higher-order matrix elements, which by the use of Sudakov form factors contain a resummation of virtual corrections to match the real emissions [25]. For the current studies, the PYTHIA $p_\perp$-ordered parton showers [26] are extended to the secluded sector, and the approach used to take into account massive radiating particles [27] must, for the $\cancel{U}(1)$ scenario, be extended to the case where also the radiated gauge boson is massive. This section gives a summary of the showering framework, with emphasis on aspects new to this study (relative to [18]).

In the most general case, final-state QCD, QED and valley radiation are interleaved in one common sequence of decreasing emission $p_\perp$ scales. That is, emissions of a SM g/γ or a hidden γ_v/g_v can alternate in the evolution of a F_v. Of course any of the related charges can be zero in a specific process, in which case the following expressions simplify accordingly. For the i'th emission, the $p_\perp$ evolution starts from the maximum scale given by the previous emission, with an overall starting scale $p_{\perp 0}$ set by the scale of the hard process, or of the decay in which the radiating particle was produced. Thus the probability to pick a given $p_\perp$ takes the form

$$\frac{\mathrm{d}\mathcal{P}}{\mathrm{d}p_\perp} = \left(\frac{\mathrm{d}\mathcal{P}_{\mathrm{QCD}}}{\mathrm{d}p_\perp} \quad + \quad \frac{\mathrm{d}\mathcal{P}_{\mathrm{QED}}}{\mathrm{d}p_\perp} + \frac{\mathrm{d}\mathcal{P}_{\mathrm{secl}}}{\mathrm{d}p_\perp} \right) \times$$
$$\exp \left(\quad - \quad \int_{p_\perp}^{p_{\perp i-1}} \left(\frac{\mathrm{d}\mathcal{P}_{\mathrm{QCD}}}{\mathrm{d}p'_\perp} + \frac{\mathrm{d}\mathcal{P}_{\mathrm{QED}}}{\mathrm{d}p'_\perp} + \frac{\mathrm{d}\mathcal{P}_{\mathrm{secl}}}{\mathrm{d}p'_\perp} \right) \mathrm{d}p'_\perp \right) \quad \text{(IV.3)}$$

where the exponential corresponds to the Sudakov form factor. Implicitly one must also sum over all partons that can radiate.

To be more precise, radiation is based on a dipole picture, where it is a pair of partons that collectively radiates a new parton. The dipole assignment is worked out in the limit of infinitely many (hidden or ordinary) colours, so that only planar colour flows need be considered.

Technically the total radiation of the dipole is split into two ends, where one end acts as radiator and the other as recoiler. The recoiler ensures that total energy and momentum is conserved during the emission, with partons on the mass shell before and after the emission. Each radiation kind defines its set of dipoles. To take an example, consider $q\overline{q} \to F_v \overline{F}_v$, which proceeds via an intermediate s-channel gluon. Since this gluon carries no QED or hidden charge it follows that the $F_v \overline{F}_v$ pair forms a dipole with respect to these two emission kinds. The gluon *does* carry QCD octet charge, however, so $F_v \overline{F}_v$ do *not* form a QCD dipole. Instead each of them is attached to another parton,

either the beam remnant that carries the corresponding anticolour or some other parton emitted as part of the initial-state shower. This means that QCD radiation can change the invariant mass of the $F_v \overline{F}_v$ system, while QED and hidden radiation could not. When a γ or γ_v is emitted the dipole assignments are not modified, since these bosons do not carry away any charge. A g or g_v would, and so a new dipole would be formed. For QCD the dipole between F_v and one beam remnant, say, would be split into one between the F_v and the g, and one further from the g to the remnant. For the secluded sector the $F_v \overline{F}_v$ dipole would be split into two, $F_v g_v$ and $g_v \overline{F}_v$. As the shower evolves, the three different kinds of dipoles will diverge further.

Note that, in the full event-generation machinery, the final-state radiation considered here is also interleaved in $p_\perp$ with the initial-state showers and with multiple parton-parton interactions [28].

If the F_v fermion is allowed to decay into a SM and a hidden particle, one must also consider the hidden radiation from the hidden particle.

There is a clean separation between radiation in the production stage of the $F_v \overline{F}_v$ pair and in their respective decay. Strictly speaking this would only be valid when the F_v width is small, but that is the case that interests us here.

In the decay $F_v \rightarrow f q_v$ the QCD and QED charges go with the f and the valley one with q_v. For all three interactions the dipole is formed between the f and the q_v, so that radiation preserves the F_v system mass, but in each case only the relevant dipole end is allowed to radiate the kind of gauge bosons that goes with its charge. (Strictly speaking dipoles are stretched between the f or q_v and the "hole" left behind by the decaying F_v. The situation is closely analogous to $t \rightarrow bW^+$ decays.)

The number of parameters of the hidden shower depends upon the scenario. In the case of the interleaved shower, there are only two, the most important on being one the coupling strength α_v, i.e. the equivalent of α_s. This coupling is taken to be a constant, i.e. no running is included.

From a practical point of view it is doubtful that such a running could be pinned down anyway, and from a theory point of view it means we do not have to specify the full flavour structure of the hidden sector. The second parameter is the lower cutoff scale for shower evolution, by default chosen the same as for the QCD shower, $p_{\perp\text{min}} = 0.4$ GeV.

Shower kinematics with massive hidden photons

Showers are expected to reproduce the soft and collinear behaviour of (leading-order) matrix elements (MEs), but there is no guarantee how trustworthy they are for hard wide-angle emissions. Therefore various correction techniques have been developed [25]. The technique we will use here is to generate trial emissions according to the PS, but then use the weights ratio ME/PS to accept emissions, i.e. PS times ME/PS equals ME. For this re-weighting

IV

recipe to work, obviously the ME weight has to be below the PS one, but the difference should not be too big or else the efficiency will suffer. It should also be noted that the ME/PS ratio is evaluated without including the Sudakov form factor of the shower, while the shower evolution itself does build up the Sudakov. By the veto algorithm it then follows that the ME expression is exponentiated to provide the kernel of the Sudakov [29], a technique nowadays used as a key ingredient of the POWHEG approach [30]. The choice of shower evolution variable lives on in the integration range of the Sudakov, but for the rest the PS expressions disappear in the final answer.

In the past, this approach has only been developed for the emission of a massless gluon, however, and we now need to generalize that to an arbitrary combination of masses. A technical task is to recast the ME and PS expressions to use the same phase space variables, such that the ratio is well-defined.

We follow the existing approach of mapping the PS variables onto the ME ones. Below we therefore introduce the ME three-body phase space, subsequently how the PS variables populate this phase space, and finally how the presence of two shower histories can be taken into account.

Consider a dipole of invariant mass m_0, consisting of two endpoint partons 1 and 2, with nominal masses m_1 and m_2. Assume that a shower emission occurs from the parton-1 dipole end, generating a new particle 3 with mass m_3. This implies that there was an intermediate off-shell state 13 with mass m_{13}. That is, the kinematics to describe is $p_0 \rightarrow p_{13} + p_2 \rightarrow p_1 + p_3 + p_2$. Averaging over the angular orientation of events, the MEs can be written in terms of the $x_i = 2p_i p_0 / m_0^2$ and the $r_i = m_i^2 / m_0^2$ variables, where the x_i reduce to energy fractions in the dipole rest frame, with normalization $x_1 + x_2 + x_3 = 2$. This means there are only two free independent variables, traditionally x_1 and x_2.

The PS is instead described in terms of the $p_{\perp\text{evol}}^2$ and z variables. In the soft and collinear emission limit these are well defined, but away from these limits different possibilities could be contemplated. Our choice is such that

$$m_{13}^2 = m_1^2 + \frac{p_{\perp\text{evol}}^2}{z(1-z)} \,, \tag{IV.4}$$

or

$$p_{\perp\text{evol}}^2 = z(1-z)(m_{13}^2 - m_1^2) \,. \tag{IV.5}$$

By standard two-body kinematics for $p_0 \rightarrow p_{13} + p_2$ it follows that

$$x_2 = \frac{m_0^2 + m_2^2 - m_{13}^2}{m_0^2} = 1 + r_2 - r_{13} \,, \tag{IV.6}$$

and thus $x_1 + x_3 = 2 - x_2 = 1 + r_{13} - r_2$. If $m_1 = m_3 = 0$ one would further require that $z = x_1/(x_1 + x_3)$. Taken together, this is enough to specify the three four-vectors p_2, $p_1^{(0)}$ and $p_3^{(0)}$, up to three angles. These are chosen at

follows: in the p_0 rest frame parton 2 is assumed to keep its direction of motion when $m_1 \to m_{13}$, while 1 and 3 are selected to have an flat distribution in the azimuthal angle around the 13 direction, which is parallel with the 1 direction before the emission.

The kinematics for the case with massive partons 1 and 3 can then be constructed from the massless four-vectors as

$$p_1 = (1 - k_1)p_1^{(0)} + k_3 p_3^{(0)} \tag{IV.7}$$

$$p_3 = (1 - k_3)p_3^{(0)} + k_1 p_1^{(0)} \tag{IV.8}$$

$$k_{1,3} = \frac{m_{13}^2 - \lambda_{13} \pm (m_3^3 - m_1^2)}{2m_{13}^2} \tag{IV.9}$$

$$\lambda_{13} = \sqrt{(m_{13}^2 - m_1^2 - m_3^2)^2 - 4m_1^2 m_3^2} \tag{IV.10}$$

The physics content is that the directions of partons 1 and 3 in the p_{13} rest frame are retained, while their three-momenta are scaled down by a common factor sufficient to put the two partons on their mass shells. Since m_{13} is not changed by the operation it is necessary that $m_{13} > m_1 + m_3$ for the rescaling to work.

The rescalings imply that

$$\frac{x_1}{x_1 + x_3} = \frac{x_1}{2 - x_2} = (1 - k_1)z + k_3(1 - z) = (1 - k_1 - k_3)z + k_3 , \tag{IV.11}$$

and thus

$$z = \frac{1}{1 - k_1 - k_3}\left(\frac{x_1}{2 - x_2} - k_3\right) . \tag{IV.12}$$

Now we need to find the Jacobian to translate the shower emission rate from the $(p_{\perp\text{evol}}^2, z)$ space to the (x_1, x_2) one. Note that $m_{13}^2 = m_0^2(1 - x_2) + m_2^2$ is independent of x_1, and thus so are k_1 and k_3. Therefore only the "diagonal" terms $\partial p_{\perp\text{evol}}^2 / \partial x_2$ and $\partial z / \partial x_1$ are needed.

The shower emission rate itself is

$$\frac{\mathrm{d}p_{\perp\text{evol}}^2}{p_{\perp\text{evol}}^2} \frac{2\,\mathrm{d}z}{1 - z} . \tag{IV.13}$$

Here an overall coupling factor $C_F \, \alpha_v / 2\pi$ is omitted for simplicity. Also the Sudakov form factor is omitted, as already motivated. The z-dependent part may seem unfamiliar, but is an upper approximation to the more familiar $q \to qg$ splitting kernel $(1 + z^2)/(1 - z)$, where the difference between the two is absorbed into the ME/PS weighting.

IV

Put together, the shower emission rate translates into

$$
\frac{\mathrm{d}p^2_{\perp\mathrm{evol}}}{p^2_{\perp\mathrm{evol}}} \;=\; \frac{\mathrm{d}(m^2_{13} - m^2_1)}{m^2_{13} - m^2_1} = \frac{\mathrm{d}x_2}{1 - x_2 + r_2 - r_1} \; , \tag{IV.14}
$$

$$
\frac{2\,\mathrm{d}z}{1-z} \;=\; \frac{2\,\mathrm{d}x_1}{(1 - k_1 - k_3)(2 - x_2)} \frac{1}{1 - \frac{1}{1-k_1-k_3}\left(\frac{x_1}{2-x_2} - k_3\right)}
$$

$$
\;=\; \frac{2\,\mathrm{d}x_1}{x_3 - k_1(x_1 + x_3)} \; . \tag{IV.15}
$$

When $m_3 \to 0$, and hence $k_1 \to 0$, this simplifies to the familiar expression [27]

$$
W_{PS,1} = \frac{\mathrm{d}p^2_{\perp\mathrm{evol}}}{p^2_{\perp\mathrm{evol}}} \frac{2\,\mathrm{d}z}{1-z} = \frac{2\,\mathrm{d}x_1\,\mathrm{d}x_2}{(1 - x_2 + r_2 - r_1)x_3}. \tag{IV.16}
$$

If only parton 1 can radiate, as in $F_v \to q_v + f \to q_v + \gamma_v + f$, we are done. The fact that the MEs also contain a contribution from γ_v emission off the F_v does not change the picture, since that does not introduce any new singularities, and empirically the PS expression provides a valid upper limit.

For the radiation $F_v\overline{F}_v \to F_v\overline{F}_v\gamma_v$ the sum of the two possible shower emissions are needed to match to the full MEs. Alternatively, and more conveniently, the ME expression can be split into two parts, each to be compared with only one shower history. This split is done in proportion to the respective propagator, i.e. assumed emission off parton i is proportional to $1/(m^2_{i3} - m^2_i)$. The relative probability for parton 1 to radiate thus is

$$
P_1 = \frac{m^2_{23} - m^2_2}{(m^2_{13} - m^2_1) + (m^2_{23} - m^2_2)} = \frac{1 - x_1 + r_1 - r_2}{x_3} \; , \tag{IV.17}
$$

so that the ME weight to be associated with this dipole end is

$$
W_{ME.1} = P_1 \frac{1}{\sigma_0} \frac{\mathrm{d}\sigma}{\mathrm{d}x_1\,\mathrm{d}x_2} \,\mathrm{d}x_1\,\mathrm{d}x_2 \; . \tag{IV.18}
$$

Thus we arrive at the ME/PS correction factor

$$
R_1 = \frac{W_{ME,1}}{W_{PS,1}} \;=\; \frac{(1 - x_1 + r_1 - r_2)(1 - x_2 + r_2 - r_1)}{2} \frac{1}{\sigma_0} \frac{\mathrm{d}\sigma}{\mathrm{d}x_1\,\mathrm{d}x_2}
$$

$$
\times \; \frac{x_3 - k_1(x_1 + x_3)}{x_3} \; . \tag{IV.19}
$$

All the explicit dependence on m_3 is located in k_1 in the last term, but obviously implicitly the whole kinematics setup is affected by the value of m_3.

The matrix elements for the radiation off $F_v\overline{F}_v$ are calculated with them as stable final-state particles. This means that, to preserve gauge invariance, they

must be assigned the same mass. On the other hand, since they are supposed to decay, we allow them to have a Breit-Wigner mass distribution. To resolve this discrepancy, the real kinematics with two different masses is shifted to a fictitious one where F_v and $\overline{F}_v$ have the same mass, and it is this fictitious one that is used in the three-parton matrix-element evaluation. As a guiding principle, the F_v and $\overline{F}_v$ three-momenta are kept unchanged in the $F_v\overline{F}_v$ rest frame, and only energy is shuffled so as to equalize the masses. Denoting the average mass $\overline{m}$, the conservation of three-momentum implies that

$$\sqrt{\frac{m_{12}^2}{4} - \overline{m}^2} = \sqrt{\frac{(m_{12}^2 - m_1^2 - m_2^2)^2 - 4m_1^2 m_2^2}{4m_{12}^2}} \; , \tag{IV.20}$$

which gives

$$\overline{m}^2 = \frac{m_1^2 + m_2^2}{2} - \frac{(m_1^2 - m_2^2)^2}{4m_{12}^2} \; . \tag{IV.21}$$

As above, the modified four-vectors $\overline{p}_1$ and $\overline{p}_2$ can be written as linear combinations of the original ones, with the constraints $\overline{p}_1^2 = \overline{p}_2^2 = \overline{m}^2$ giving the solution

$$\overline{p}_1 \;\; = \;\; p_1 + \frac{m_2^2 - m_1^2}{2m_{12}^2}(p_1 + p_2) \; , \tag{IV.22}$$

$$\overline{p}_2 \;\; = \;\; p_2 - \frac{m_2^2 - m_1^2}{2m_{12}^2}(p_1 + p_2) \; . \tag{IV.23}$$

This translates into identical relationships for the modified matrix-element variables $\overline{x}_1$ and $\overline{x}_2$ in terms of the original x_1 and x_2 ones.

Matrix element for radiation in production

The implementation of the $U(1)$ has required the calculation of matrix element corrections $|M|^2_{f\bar{f}\to F_v\overline{F}_v\gamma_v}$ for the pair production process $f\bar{f} \to F_v\overline{F}_v\gamma_v$ described in Fig. **??**. This has required the generalization of the matrix element corrections in [27] to the case of a massive photon:

$$|M|^2_{f\bar{f}\to F_v\overline{F}_v} \;\; = \;\; (1 - 4r_1)^{3/2} \; , \tag{IV.24}$$

$$\frac{|M|^2_{f\bar{f}\to F_v\overline{F}_v\gamma_v}}{|M|^2_{f\bar{f}\to F_v\overline{F}_v}} \;\; = \;\; (r_3 + 2r_1)(-1 + 4r_1)\left(\frac{1}{(1-x_1)^2} + \frac{1}{(1-x_2)^2}\right)$$

$$+ \;\; \frac{-1 + 8r_1 - x_2}{1 - x_1} + \frac{-1 + 8r_1 - x_1}{1 - x_2}$$

$$+ \;\; \frac{2(1 - 6r_1 + 8r_1^2 + 4r_3r_1)}{(1 - x_1)(1 - x_2)} + 2 \; . \tag{IV.25}$$
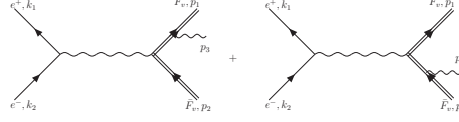
IV

Figure IV.2: The Feynman diagrams for the production.

Here $r_1 = r_2 = \overline{m}^2/m_0^2$ and $r_3 = m_{\gamma_v}^2/m_0^2$. (Expressions for $r_1 \neq r_2$ have also been obtained but, by the preceding trick, are not needed.) Coupling constants have been omitted, as discussed before for the shower. Furthermore, to simplify calculations, the process is taken to proceed via the exchange of a scalar particle instead of a spin 1 gauge boson. The $|M|^2_{f\bar{f} \to F_v \bar{F}_v \gamma_v}$ spin information, relevant for decay angular distributions, will be lost this way. Effects are known to be minor for the ME correction ratio [27]. As an illustration, the above expression reduces to $(x_1^2 + x_2^2)/((1-x_1)(1-x_2)) + 2$ for $r_1 = r_2 = r_3 = 0$, where the first term is the familiar expression for $e^+e^- \to \gamma^*/Z^* \to q\bar{q}$, and the second finite term comes in addition for a spin 0 exchanged particle.

Matrix element for radiation in decay
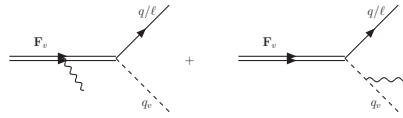
Figure IV.3: The Feynman diagrams for the $F_v \to qv \ q/\ell$ decay.

The matrix elements corresponding to $F_v \to q_v f \gamma_v$ are

$$|M|^2_{F_v \to q_v f} = (1 - r_1 + r_2 + 2q_2)\sqrt{(1 - r_1 - r_2)^2 - 4r_1 r_2} \qquad \text{(IV.26)}$$

$$\frac{|M|^2_{F_v \to q_v f \gamma_v}}{|M|^2_{F_v \to q_v f}} = \frac{(r_3/2 + 2r_1^2 + r_2 r_3/2 + q_2 r_3 - 2r_1 - r_1 r_3/2 - 2r_1 r_2 - 4r_1 q_2)}{(1 + r_2 - r_1 - x_2)^2}$$

$$+ \frac{(-2 + 2r_2^2 + 2r_1^2 + 2r_2r_3 - 4q_2 + 2q_2r_3 + 4q_2r_2 - 4r_1r_2 - 4r_1q_2)}{(1 + r_2 - r_1 - x_2)(r_3 - x_3)}$$

$$+ \frac{(-2 - r_3/2 - 2r_2 - 4q_2 + 2r_1)}{(1 + r_2 - r_1 - x_2)}$$

$$+ \frac{(-2 - r_3 - 2r_2 - r_2r_3 - 4q_2 - 2q_2r_3 + 2r_1 + r_1r_3)}{(r_3 - x_3)^2}$$

$$+ \frac{(-1 - r_3 - r_2 - 4q_2 + r_1 - x_2)}{(r_3 - x_3)} + 1 . \tag{IV.27}$$

where $r_1 = m_{\bar{q}_v}^2/m_F^2$, $r_2 = m_f^2/m_F^2$, $r_3 = m_{\gamma_v}^2/m_F^2$ and $q_2 = m_f/m_F = \sqrt{r_2}$. The calculation has been done for the specific choice of F_v and f being fermions, and q_v a scalar, but again the result should be representative also for other spin choices.

IV.3.3 Hidden sector hadronization

If the G group is the unbroken $SU(N)$, the gauge boson g_v is massless and the partons are confined. The picture therefore is closely similar to that of QCD, and we will use exactly the same framework to describe hadronization physics as in QCD: the Lund string model [31].

For the hidden sector, the model is most easily illustrated for the production of a back-to-back $q_v\bar{q}_v$ pair, with the perturbative emission of additional g_vs neglected for now. In that case, as the partons move apart, the physical picture is that of a v-colour flux tube being stretched between the q_v and the $\bar{q}_v$. If the tube is assumed to be uniform along its length, this automatically leads to a confinement picture with a linearly rising potential, $V(r) = \kappa r$.

In order to obtain a Lorentz covariant and causal description of the energy flow due to this linear confinement, the most straightforward approach is to use the dynamics of the massless relativistic string with no transverse degrees of freedom. The mathematical, one-dimensional string can be thought of as parameterizing the position of the axis of a cylindrically symmetric flux tube.

Now consider the simple $q_v\bar{q}_v$ two-parton event further. As the q_v and $\bar{q}_v$ move apart from the creation vertex, the potential energy stored in the string increases, and the string may break by the production of a new $q_v'\bar{q}_v'$ pair, so that the system splits into two colour singlet systems $q_v\bar{q}_v'$ and $q_v'\bar{q}_v$. If the invariant mass of either of these systems is large enough, further breaks may occur, and so on until only v-mesons remain. A system with n primary v-mesons thus requires $n - 1$ breaks $q_{v,i}\bar{q}_{v,i}$ to produce a chain of v-mesons $q_v\bar{q}_{v,1}$, $q_{v,1}\bar{q}_{v,2}$, $q_{v,2}\bar{q}_{v,3}$, $\ldots$, $q_{v,n-1}\bar{q}_v$ stretching from the q_v end to the $\bar{q}_v$ one.

The flavour of each $q_{v,i}\bar{q}_{v,i}$ is supposed to be a random choice among the N_{flav} different flavours. Since all are taken to have the same mass, for now, they are also produced at the same rate. This thus also goes for the N_{flav}^2 different

IV

v-meson flavour combinations. If the q_v are fermions then both pseudoscalar and vector v-mesons can be produced, π_v and ρ_v. Again disregarding possible effects of a mass splitting, simple spin counting predicts a relative production rate $\pi_v : \rho_v = 1 : 3$.

The possibility of higher excited states is disregarded, as is known to offer a good approximation for the QCD case. Also v-baryon production is left out, which is a 10% effect in QCD. For a generic $SU(N)$ group a v-baryon needs to consist of N v-quarks. This should lead to exceedingly tiny rates for $N > 3$, while $N = 2$ could offer a more robust v-baryon production rate.

The space–time picture of the string motion can be mapped onto a corresponding energy–momentum picture by noting that the constant string tension implies that the v-quarks lose a constant amount of energy per distance traveled. The different breaks are space-like separated, but two adjacent breaks are constrained by the fact that the string piece created by them has to be on the mass shell for the v-meson being produced. The space-like separation implies that the fragmentation process can be traced in any order, e.g. from one of the endpoints inwards, while the constraint implies that there is only one kinematical degree of freedom for each new v-meson. Typically it is chosen to be z, the light-cone momentum fraction that the new v-meson takes from whatever is left in the system after previously produced v-meson have been subtracted off.

By symmetry arguments one arrives at the Lund-Bowler shape of the z probability distribution [32]

$$f(z) \propto \frac{1}{z^{1+bm_{q_v}^2}} (1-z)^a \exp\left(-\frac{bm_{m_v}^2}{z}\right) , \qquad \text{(IV.28)}$$

where $m_{m_v} \approx 2m_{q_v}$ is the mass of the produced v-meson. The equation contains two free parameters, a and b. Roughly speaking, these regulate the average rapidity spacing of the v-mesons, and the size of the fluctuations around this average. While a is dimensionless, b is not, which means that it becomes necessary to adjust b as m_{q_v} is changed. For instance, assume that the q_v mass is related to the strong-interaction scale Λ_v. Then, if Λ_v, m_{q_v}, m_{m_v} and the collision energy are scaled up by a common factor, we would want to retain the same rapidity distribution of produced v-mesons. This is achieved by rewriting $bm_{m_v}^2 = (bm_{q_v}^2)(m_{m_v}^2/m_{q_v}^2) = b'(m_{m_v}^2/m_{q_v}^2)$, where now b' can be assumed constant.

In additional to fluctuations in the longitudinal fragmentation, it is assumed that each new $q_v'\bar{q}_v'$ pair produced when the string breaks also carries an opposite and compensating transverse momentum component. The $p_\perp$ of the $q_{v,i-1}\bar{q}_{v,i}$ meson is then given by the vector sum of its two constituent $p_\perp$ values. The pair $p_\perp$ naturally arises in a tunneling production process, which also leads to a Gaussian $p_\perp$ distribution. The width σ of this Gaussian again should

scale like Λ_v, so we rewrite as $\sigma = (\sigma/m_{q_v})m_{q_v} = \sigma' m_{q_v}$. When the v-mesons are allowed to acquire a $p_\perp$ it should be noted that the $m^2_{m_v}$ in eq. (IV.28) must be replaced by $m^2_{\perp m_v} = m^2_{m_v} + p^2_\perp$.

In lack of further knowledge, it is convenient to assign b' and σ' values by analogy with standard QCD. To be more specific, we have in mind something like the s quark, with a bare mass of the same order as Λ. For heavy quarks, like c and b in QCD, tunneling is suppressed, and the framework would have to be further modified. To assess uncertainties in a scenario, it would make sense to vary b' and σ' values over some range, say a factor of two in either direction.

So far, the emission of g_vs has been neglected. When it is included, more complicated string topologies can arise. Like in QCD, the complexity is reduced by using the planar or large-N_C limit [33]. In it a v-gluon is assigned an incoherent sum of a (v-)colour charge and a different anticolour one. In a branching $q_v \rightarrow q_v g_v$ the initial q_v colour is taken away by the g_v and a new colour-anticolour pair is stretched between the final q_v and g_v. Similarly $g_v \rightarrow g_v g_v$ is associated with the creation of a new colour. That way partons nearby in the shower evolution also come to be colour-connected. This leads to a picture of a single string, consisting of several separate string pieces, stretching from one q_v end to the g_v it shares one colour with, on to the next colour-related g_v, and so on until the $\bar{q}_v$ string end is reached. Several separate string pieces could have formed, had perturbative branchings $g_v \rightarrow q_v\bar{q}_v$ been included, but, as in QCD, $g_v \rightarrow q_v\bar{q}_v$ should be rare both in relation to the more singular $g_v \rightarrow g_v g_v$ and in absolute terms.

The motion of a string with several gluon kinks can be quite complicated, but it is possible to extend the fragmentation framework of a single straight string also to the more complex topologies [34]. Basically the string will break up along its length by the production of new $q'_v\bar{q}'_v$ pairs, with two adjacent breaks correlated in such a way that the v-meson produced between them is on the mass shell. Sometimes the two breaks will be on either side of a g_v string corner.

One of the key virtues of the string fragmentation approach is that it is collinear and infrared safe. That is, the emission of a gluon disturbs the overall string motion and fragmentation vanishingly little in the small-angle/energy limit. Therefore the choice of lower cut-off scale for parton showers is not crucial: letting the shower evolve to smaller and smaller scales just adds smaller and smaller wrinkles on the string, which still maintains the same overall shape.

The complete v-string fragmentation scenario contains a set of further technical details that are not described here. The key point, however, is that essentially all of the concepts of normal string fragmentation framework can be taken over unchanged. The one new aspect is what to do when the invariant

IV

mass of the hidden-valley system is too large to produce one single on-shell v-meson and too small to give two of them. As already explained, then the emission of v-glueballs is used to balance energy-momentum.

IV.3.4   Decays back into the SM sector

Disregarding the trivial direct decay $F_v \to f q_v$, the main decay modes back into the SM are through γ_v kinetic mixing or Z' decay. For $G = \mathcal{U}(1)$ the γ_v therefore can decay to SM particles with the same branching ratios as a photon of corresponding mass, i.e. $\propto e_f^2 N_c$, with $N_c = 1$ for leptons. For $G = SU(N)$ only the flavour-diagonal mesons can decay, either with a γ_v or a Z'. (The former would imply that $G = SU(N) \times U(1)$, which would require some further extensions relative to the scenarios studied here.) A ρ_v meson, with spin 1, could have the same branching ratios as above, or slightly modified depending on the Z' couplings. A π_v meson, with spin 0, would acquire an extra helicity factor m_f^2 that would favor the heaviest fermions kinematically allowed. Should the π_v be scalar rather than pseudoscalar there would also be a further threshold suppression, in addition to the phase space one.

The decay back into the standard model would be accompanied by normal QED and QCD radiation, where relevant. Quarks and gluons would further hadronize, as described by the normal Lund string model. That model is not carefully set up to handle different exclusive states if the γ_v or ρ_v / π_v mass is very low, of the order 1 or 2 GeV, but should be good enough as a starting point. For studies that zoom in on one specific mass, more carefully constructed decay tables could be used instead.

IV.4   Analysis of the different scenarios

The tools described above allow us to simulate several different setups. We concentrate on the phenomenology of the six scenarios listed in Table IV.1. Three different production mechanisms are involved: s-channel pair production via kinetic mixing with the light γ_v (KM$_{\gamma_v}$), s-channel pair production mediated by a Z' (M$_{Z'}$) and s-channel pair production via SM gauge bosons (SM) and the F_v particles. For each of these production mechanisms an Abelian setup and a non-Abelian one are considered, labeled by A and NA respectively. Note that the Abelian/non-Abelian group we refer to in the following analyses correspond to the G gauge group, not to the production mechanisms. In the Abelian case $G = \mathcal{U}(1)$, while in the non-Abelian case $G = SU(3)$.

The phenomenology of the six scenarios is a function of the pair production cross section, which will in general depend upon the specific model realization of each setup. In particular, for the KM scenarios, the cross section will

	production	radiation	hadronization	decay to SM
AM$_{Z'}$	$e^+e^- \to Z' \to q_v\bar{q}_v$	$q_v \to q_v\gamma_v$	—	$\gamma_v \to$ SM
NAM$_{Z'}$	$e^+e^- \to Z' \to q_v\bar{q}_v$	$q_v \to q_v g_v,\, g_v \to g_v g_v$	$q_v\bar{q}_v \sim \pi_v/\rho_v$	$\pi_v/\rho_v \to$ SM
KMA$_{\gamma_v}$	$e^+e^- \to \gamma_v \to q_v\bar{q}_v$	$q_v \to q_v\gamma_v$	—	$\gamma_v \to$ SM
KMNA$_{\gamma_v}$	$e^+e^- \to \gamma_v \to q_v\bar{q}_v$	$q_v \to q_v g_v,\, g_v \to g_v g_v$	$q_v\bar{q}_v \sim \pi_v/\rho_v$	$\pi_v/\rho_v \to$ SM
SMA	$e^+e^- \to \gamma^* \to E_v\bar{E}_v$	$q_v \to q_v\gamma_v$	—	$\gamma_v \to$ SM
SMNA	$e^+e^- \to \gamma^* \to E_v\bar{E}_v$	$q_v \to q_v g_v,\, g_v \to g_v g_v$	$q_v\bar{q}_v \sim \pi_v/\rho_v$	$\pi_v/\rho_v \to$ SM

Table IV.1: The six scenarios studied.

depend upon the size of the kinetic mixing parameter ϵ, while for the Z' mediate ones on the mass of the Z' and on its couplings to the SM particles and to the v-quarks. The analysis is performed on per-event distributions, so as to factor out this model dependence. Assuming the same number of events are produced, the phenomenology of the setups will depend upon a different number of parameters. For the KMA$_{\gamma_v}$ and the AM$_{Z'}$ one must fix the q_v masses, the γ_v mass and the $U(1)$ coupling constant α_v, while for the SMA production one must also fix the F_v masses. In the corresponding KMNA$_{\gamma_v}$, AM$_{Z'}$ and SMNA one must fix the meson masses, but these will be connected to the q_v masses chosen, and furthermore the g_v remains massless. We select a scenario in which $m_{q_v} \sim \Lambda$, so that $m_{\pi_v} \sim m_{\rho_v}$. This in turn ensures (as already described in section IV.2.4) that meson decay into SM lepton is not supressed. For simplicity, in the following analysis we assume only one mass for all v-quark flavours, and only one common π_v/ρ_v mass $m_{\pi_v/\rho_v} = 2m_{q_v}$. One additional simplification in the following analysis, is that for the SM cases we assume the pair production of one single E_v belonging to the standard model doublet with no consideration for anomaly cancellation issues. In the non-Abelian case we have assumed simple proportions $1 : 3$ for $\pi_v : \rho_v$ production from fragmentation, which comes from spin counting when the q_v has spin $1/2$. The branching ratios of the decays to standard model particles are fixed by the kinetic mixing mechanism.

IV

We concentrate on the phenomenology of the six setups at an e^+e^- collider with center-of-mass (CM) energy of 800 GeV. A similar study for pp colliders like the LHC is also possible, and obviously more relevant in the near future, but makes it less transparent to compare and understand the properties of the models. Bremsstrahlung corrections have been included, and we shall see that these can give a non-negligible effect, whereas the machine-specific beamstrahlung has not. All of the figures in this section are based on a Monte Carlo statistics of 10000 events.

As a consequence of the e^+e^- collider choice, the events have a spherical symmetry rather than a cylindrical one, i.e. are described in terms of particle energy and (θ, ϕ) variables rather than in terms of E_T and (η, ϕ). The jet
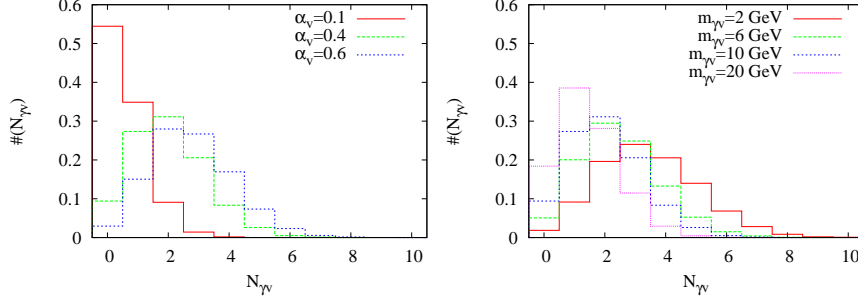
Figure IV.4: $AM_{Z'}$: the number of γ_v gauge bosons emitted per event. On the left we highlight the α_v dependence, while on the right the m_{γ_v} dependence. On the left side $m_{q_v} = 50$ GeV, $m_{\gamma_v} = 10$ GeV and $\alpha_v = 0.1, 0.4, 0.6$, while on the right side $m_{\gamma_v} = 2, 6, 10, 20$ GeV and the coupling is fixed at $\alpha_v = 0.4$.

clustering algorithms are thus determined by the spherical topology and we primarily use the PYTHIA built-in `ClusterJet` Jade algorithm [35, 36]. The Jade algorithm is geared towards clustering objects nearby in mass, and so for clustering a variable number of fixed-mass $\gamma_v/\pi_v/\rho_v$ systems it is more relevant than clustering e.g. in transverse momenta or angles.

IV.4.1 Basic distributions

The phenomenology of the six different setups is discussed in detail in dedicated subsections. We here would like to discuss the general features of the secluded sector signals and to introduce the observables we focus on.

One of the benefits of a Monte Carlo simulation is that one may look behind the scene, to study also the distributions of the invisible secluded sector particles. These can then be compared with the SM particle distributions to determine which features are governed by the the secluded sector dynamics, and which come from the decays to the SM. In this spirit, Fig. IV.4 shows the number of γ_v gauge bosons emitted per event in the $AM_{Z'}$ case. On the left we highlight the α_v dependence, on the right the m_{γ_v} dependence. Not unexpectedly, the number of γ_v increases almost linearly with α_v, up to saturation effects from energy–momentum conservation.

Compare this distribution with the corresponding non-Abelian $AM_{Z'}$ case in Fig. IV.5 for the flavour diagonal π_v/ρ_v. Again the number of g_v grows with α_v [2], but the number of v-mesons does not primarily reflect this α_v dependence.

---

[2]Note that, in this case, the emission rate $q_v \to q_v g_v$ is proportional to $C_F \alpha_v$, with $C_F = (N^2 - 1)/(2N)$, and $g_v \to g_v g_v$ to $N\alpha_v$.
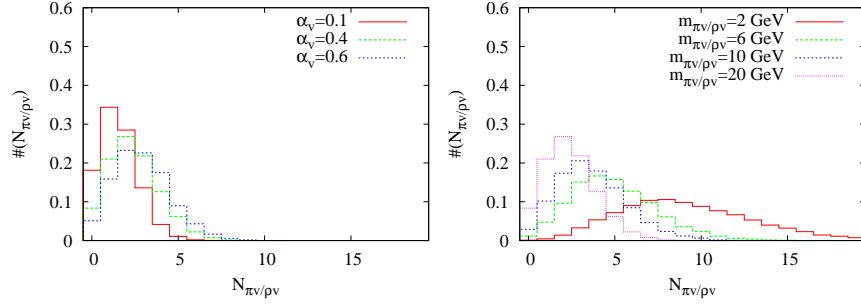
Figure IV.5: $NAM_{Z'}$: the number of flavour diagonal π_v/ρ_v mesons emitted per event. On the left we emphasize the α_v dependence, while on the right the m_{π_v/ρ_v} dependence. On the left the meson mass is fixed at $m_{\pi_v/\rho_v} = 10$ GeV and the coupling varies among $\alpha_v = 0.1, 0.4, 0.6$, while on the right side $m_{\pi_v/\rho_v} = 2, 6, 10, 20$ GeV (which in turn implies $m_{q_v} = 1, 3, 5, 10$ GeV), the coupling is fixed at $\alpha_v = 0.4$ and the number of flavours is $N_{\text{flav}} = 4$.

Instead the number of v-mesons produced by string fragmentation rather reflects the masses of the v-quarks (and thereby of the mesons) and the fragmentation parameters, see Fig. IV.5 right plot. Specifically, even with α_v set to zero for the perturbative evolution, there would still be non-perturbative production of v-mesons from the single string piece stretched directly from the q_v to the $\bar{q}_v$. With α_v nonzero the string is stretched via a number of intermediate g_v gluons that form transverse kinks along the string, and this gives a larger multiplicity during the hadronization.

Comparing the number of γ_v in Fig. IV.4 with the corresponding distributions in the other Abelian setups, KMA_{γ_v} and SMA, in Fig. IV.12 and Fig. IV.14 respectively, the two KMA_{γ_v} and $\text{AM}_{Z'}$ setups produce similar distributions, while the SMA produces much fewer γ_v. The SMA difference is due to the more complicated kinematics, where the electrons from the $E_v \rightarrow eq_v$ decays take away a large fraction of energy and momentum that then cannot be used for γ_v emissions.

The average charged multiplicity of an event, Fig. IV.6, will be directly proportional to the number of $\gamma_v/\pi_v/\rho_v$ produced. The trends from above are thus reproduced, that the non-Abelian multiplicity varies only mildly with α_v, while the variation is more pronounced in the Abelian case. The constant of proportionality depends on the $\gamma_v/\pi_v/\rho_v$ mass, with more massive states obviously producing more charged particles per state. This offsets the corresponding reduction in production rate of more massive $\gamma_v/\pi_v/\rho_v$, other conditions being the same. Similarly the number of jets should be proportional to the number of $\gamma_v/\pi_v/\rho_v$ emitted, see further Sec. IV.4.2.
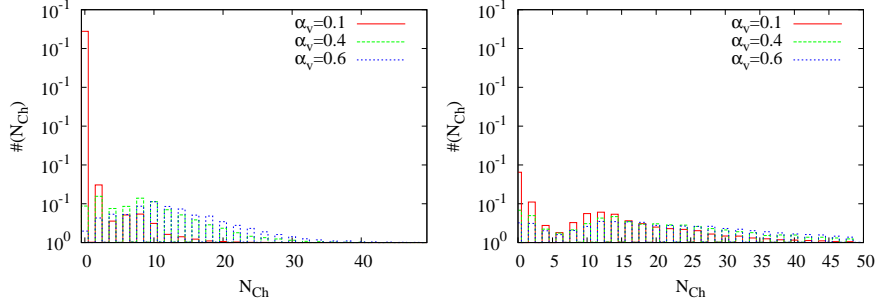
IV

Figure IV.6: $AM_{Z'}$, $NAM_{Z'}$: α_v dependence of the overall number of charged particles emitted per event in the Abelian (left) and non-Abelian (right) case. For the Abelian cases $m_{q_v} = 50$ GeV and $m_{\gamma_v} = 10$ GeV, for the non-Abelian cases $m_{q_v} = 5$ GeV, $m_{\pi_v/\rho_v} = 10$ GeV.

Without an understanding of the $\gamma_v/\pi_v/\rho_v$ mass spectra, the mix of effects would make an α_v determination nontrivial, especially in the non-Abelian case. Even with a mass fixed, e.g. by a peak in the lepton pair mass spectrum, other model parameters will enter the game. One such parameter is the number N_{flav} of q_v flavours. Since only $1/N_{\text{flav}}$ of the π_v/ρ_v would decay back into the SM the visible energy is reduced accordingly. With all q_v having the same mass, the relation $\langle E_{\text{visible}} \rangle / E_{\text{cm}} = 1/N_{\text{flav}}$ works fine to determine N_{flav}, but deviations should be expected for a more sophisticated mass spectrum . Furthermore the $\pi_v : \rho_v$ mix, with different branching ratios for the two, needs to be considered. If the π_v fraction is large, the number of heavy leptons and hadrons produced may increase substantially, see [1].

In Fig. IV.7 we show the energy spectra of the hidden sector γ_v and ρ_v/π_v. Note the difference between the $NAM_{Z'}$ setup and the $KMNA\gamma_v$ one. This is due to the difference in the amount of initial-state radiation in the two cases, as discussed in Sec. IV.4.3 and shown in Fig. IV.11.

The energy and momenta of the v-sector particles not decaying back into the SM is the prime source of the missing $p_\perp$ distributions, [3] see Fig. IV.8. In each of the six setups there is only one source of missing energy. In the Abelian ones it is the q_vs that escape detection, while in the non-Abelian ones it is the stable non-diagonal v-mesons. For KMA_{γ_v} the falling Abelian $\not{p}_\perp$ spectra are easily understood from the bremsstrahlung nature of the γ_v emissions. The spike at $\not{p}_\perp = 0$ comes from events without any emissions at all, where all the energy is carried away by the invisible q_vs, and would hardly be selected by a detector trigger. (ISR photons might be used as a trigger in this case,

---

[3]with some extra effects from neutrinos e.g. in b, c and τ decays, included in the plots but here not considered on their own.
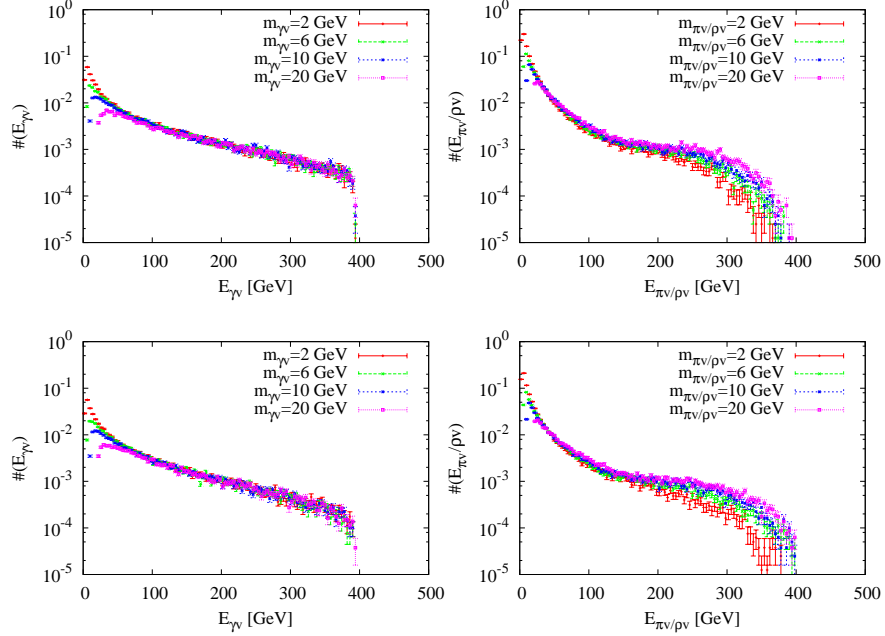
Figure IV.7: $M_{Z'}$ vs KM_{γ_v}: the energy spectrum of the γ_v and diagonal π_v/ρ_v emitted per event. On top: left side shows the energy distribution for $AM_{Z'}$, the right side shows the corresponding one for $NAM_{Z'}$. Bottom: left side shows the energy distribution for KMA_{γ_v}, right side shows $KMNA_{\gamma_v}$. For the abelian cases $mq_v = 50$ GeV, for the non abelian cases $m_{q_v} = m_{\gamma_v}/2$. In all four cases $\alpha_v = 0.4$.

but with irreducible backgrounds e.g. from $Z^0 \rightarrow \nu\bar{\nu}$ it is not likely.). In the KMNA case the momentum of non-diagonal v-mesons does not leak back, this again allows a falling slope and a spike at $\not{p}_\perp = 0$, for events in which equal amount of energy in the non-diagonal mesons radiated from either side of the $q_v\bar{q}_v$ system. For the SMA and SMNA scenarios, on the other hand, the starting point is the pT imbalance that comes from the e^+ and e^- from the E_v and $\bar{E}_v$ decays, which have no reason to balance each other. So even without γ_v emission, or diagonal π_v/ρ_v, there will will be a $p_\perp$ imbalance.

In the SMNA case, though the spectrum is shifted towards lower missing $\not{p}_\perp = 0$ because on average a higher number of mesons are radiated, so it is less likely to have an event with the two leptons back-to-back. There could also be $\not{p}_\perp = 0$ cases in which all the mesons are flavour diagonal and all the energy-momenta decays back into the SM, but these events are very rare.

In the Abelian case, the missing $p_\perp$ distribution is directly connected to the
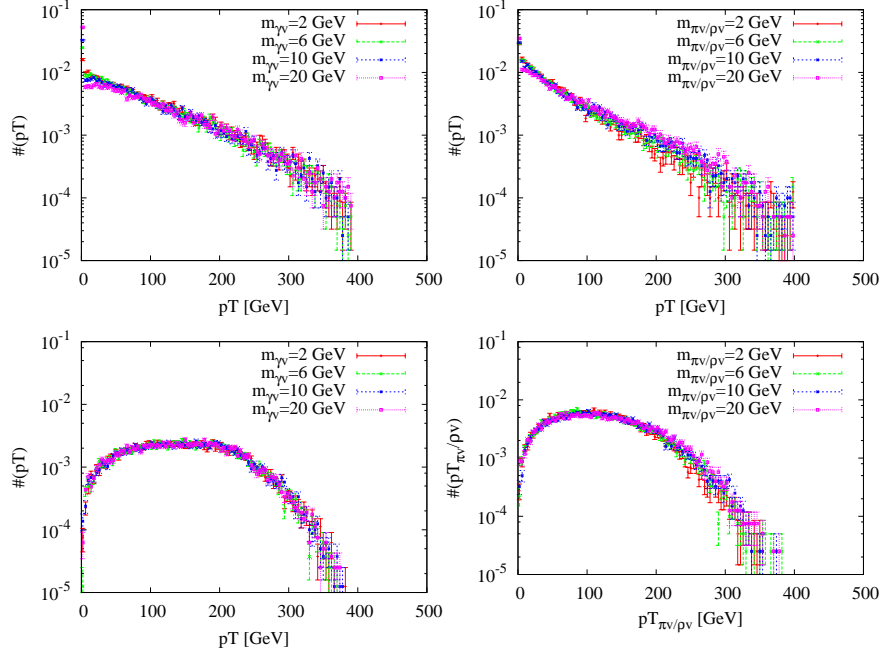
IV

Figure IV.8: KMA_{γ_v}, $KMNA_{\gamma_v}$, SMA, $SMNA$: the $\not{p}_\perp$ spectrum in each event. For the Abelian cases (left) the $\not{p}_\perp$ is due to the q_v escaping detection. For the non-Abelian cases (right) it is due to the v-flavoured mesons not decaying into SM particles. In the Abelian cases $m_{q_v} = 50$ GeV, while in the non-Abelian cases (right) $m_{q_v} = 1, 3, 5, 10$. For all plots $\alpha_v = 0.4$.

mass parameter values m_{q_v} and, in the SMA case, to the m_{E_v}. The value of m_{q_v} in the KM/Z' mediated cases may be extracted from the kinematic limit given by the "shoulder" of the distribution. In the SM-mediated case, where two different fermion mass scales are involved, one can extract a relationship for the relative size of the two from lepton energy distributions such as the one in Fig. IV.16, see [18] for details. The distribution that directly pinpoints the mass of the particle decaying back into the SM, though, is the invariant mass of the lepton pairs produced, and that of the hadronic jets. We will discuss these distributions in the sections dedicated to each scenario.

IV.4.2 $AM_{Z'}$ and $NAM_{Z'}$

In discussing the phenomenology of the different scenarios we will describe the v-sector particle distributions first, then the visible particle distributions
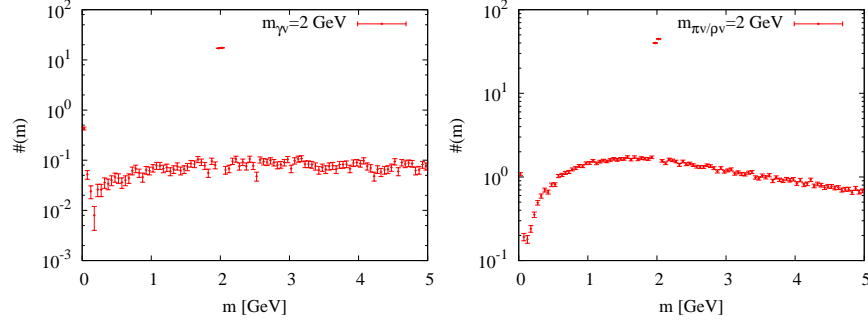
Figure IV.9: $AM_{Z'}$ and $NAM_{Z'}$. The distribution of the invariant mass of the lepton pairs. Note the peak at 2 GeV, in both cases corresponding to the mass to be reconstructed $m_{\gamma_v} = m_{\rho_v/\pi_v}$. On the left, in the Abelian case, $m_{q_v} = 50$ GeV, while on the right, in the non-Abelian case, $m_{q_v} = 1$ GeV. The coupling is fixed at $\alpha_v = 0.4$.

followed by the jet distributions.

The number of particles of γ_v photons emitted in the $AM_{Z'}$ and $NAM_{Z'}$ scenarios was described in Fig. IV.4 and Fig. IV.5 in the previous section. The difference between the Abelian and non-Abelian dependence on the α_v and $m_{\gamma_v/\pi_v/\rho_v}$ parameters has already been highlighted in the same Sec. IV.4.1, as well as the $\gamma_v/\pi_v/\rho_v$ energy distributions, the charged multiplicity and the $\not{p}_\perp$ spectrum. The difference between KMA_{γ_v} and SMA was also discussed.

The difference between the Abelian and non-Abelian $\not{p}_\perp$ distribution in Fig. IV.8 is more subtle. In the Abelian case an event has maximum $p_\perp$ inbalance when one of the $q_v/\bar{q}_v$ produced emits a collinear γ_v which takes most of the q_v ($\bar{q}_v$) momentum while the other v-quark has no emission and goes undetected. The more γ_v are emitted, the less likely it is that the undetected $\bar{q}_v$ will have maximal energy. This remains true for all the m_{γ_v} contemplated (except in the low-$p_\perp$ region). In the non-Abelian case, to have large $p_\perp$ inbalance the event must produce few energetic mesons back-to-back and have the mostly flavoured mesons at one end and mostly flavour neutral mesons at the other end. When the meson mass is lower, there is a higher probability of the string producing a large number of mesons and the likelihood of having large $\not{p}_\perp$ falls rapidly. When the meson masses are higher and fewer π_v/ρ_v are produced the high $\not{p}_\perp$ distribution falls off less rapidly.

The $\gamma_v/\pi_v/\rho_v$ mass can be extracted from the lepton pair invariant mass, where it shows up as a well-defined spike, Fig. IV.9. (The additional spike near zero mass is mainly related to Dalitz decay $\pi^0 \to e^+e^-\gamma$.) Once the mass is known, the remaining hadrons and photons may be clustered using the Jade algorithm, with $m_{\gamma_v/\pi_v/\rho_v}$ as the joining scale. The corresponding number of jets and invariant mass distribution for the hadronic jets is given in Fig. IV.10.
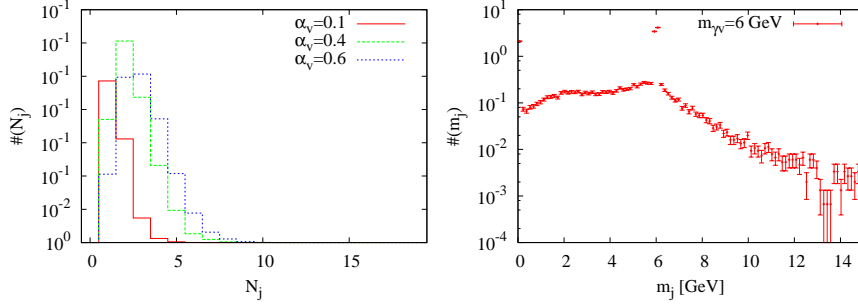
IV

Figure IV.10: $AM_{Z'}$: the number of jets per event and the distribution of the invariant mass of the jets. In both plots the q_v mass is $m_{q_v} = 50$ GeV. The left side shows the α_v dependence for $m_{\gamma_v} = 10$ GeV, while the right side shows the jet invariant mass distribution for $\alpha_v = 0.4$ and $m_{\gamma_v} = 6$ GeV. The jet reconstruction algorithm is Jade, with m_{cut} corresponding to the γ_v mass. Note the peak at 6 GeV.

The jet invariant mass distribution clearly shows the peaks connected to the invariant mass of the γ_v. The background comes from several sources. The spike at zero mass is mainly related to ISR photons; although we assume no detection within 50 mrad of the beam directions, some isolated photons do show up above this angle and form jets on their own. When kinematically possible, τ decays and c and b decays will also occur. These contain neutrino products that reduce the visible mass, thus contributing to a continuum below the mass peak. Finally, misidentifications among partly overlapping systems leads to tails on both sides of the peak.

An efficient clustering algorithm should maintain the ratio between the average number of γ_v particles produced and the number of jets found, as is confirmed by comparing the plots on left side of Figs. IV.4 and IV.10. In this particular exercise we have relied on the extraction of the relevant mass scale from the lepton pair invariant mass distribution. This should be guaranteed by the presence of leptons in all six scenarios. Specifically, if the only way to decay back into the SM is via kinetic mixing, the $\gamma_v \to SM$ branching ratios are fixed by the off-shell γ^* branching ratios. In the non-Abelian case the absence of a spin 1 v-meson would reduce the rate of e^+e^- and $\mu^+\mu^-$ pairs by helicity suppression. However, also in such scenarios, a simple trial-and-error approach with a range of jet clustering scales would suffice to reveal a convincing jet mass peak.

More information about the event and the model parameters can be extracted from the angular distributions in Sec. IV.4.5.
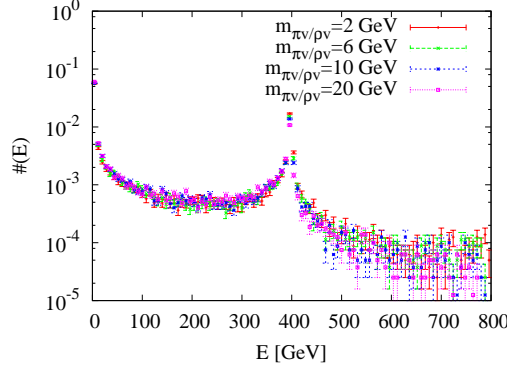
Figure IV.11: *KMNA$_{\gamma_v}$*: The total energy radiated in ISR photons. Note the spike around 400 GeV: a large fraction of the events will have a reduced $\hat{s}$ due IS photon emission. The q_v mass is fixed by $m_{q_v} = m_{\pi/\rho_v}/2$.

IV.4.3 KMA$_{\gamma_v}$ and KMNA$_{\gamma_v}$

The Z' mediated and γ_v mediated setups are effectively very similar, once the difference in coupling constants is factored out. The phenomenology can appear rather different, however, because of the initial state radiation from the electron/positron beams. To view this, recall that the photon bremsstrahlung spectrum is spiked at small energy fractions, $\propto dz_\gamma/z_\gamma$, and that therefore the electron-inside-electron PDF roughly goes like $dz_e/(1-z_e)$, with $z_e = 1 - z_\gamma$. In the case of a γ or light γ_v propagator, behaving like $1/\hat{s} = 1/(z_e s)$, this combines to give a $dz_e/(z_e(1-z_e)) = dz_\gamma/((1-z_\gamma)z_\gamma)$ spectrum. The complete description includes the emission of multiple photons off both incoming beams, but the key features above described are readily visible in Fig. IV.11. Specifically, the spike at $E_{\text{ISR}} = 400$ GeV corresponds to the emission of an energetic photon on one side only, while the non-negligible tail above that requires hard emissions on both sides.

Note that while the number of v-particles produced are similar for KMA$_{\gamma_v}$ and AM$_{Z'}$ in the Abelian case, Fig. IV.4 vs. Fig. IV.12, they are different in the non-Abelian case, Fig. IV.5 vs. Fig. IV.13. Specifically, the higher average multiplicity in the non-Abelian case leads to a double spike in the distribution, a normal one from events with little ISR and an extra low-multiplicity one from events with much ISR.

IV.4.4 SMA and SMNA

The number of v-particles produced in the standard model mediated scenarios is shown in Fig. IV.14, and the energy of the γ_v photons and of the v-mesons
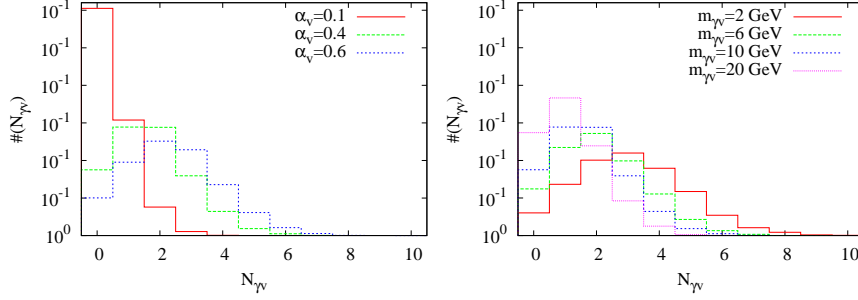
IV

Figure IV.12: KMA_{γ_v}: the number of γ_v gauge bosons emitted per event. On the left we emphasize the α_v dependence, while on the right the m_{γ_v} dependence. In both plots the q_v mass is $m_{q_v} = 10$ GeV. On the left side $m_{\gamma_v} = 10$ GeV and $\alpha_v = 0.1, 0.4, 0.6$, while on the right side $m_{\gamma_v} = 2, 6, 10, 20$ GeV and the coupling is fixed at $\alpha_v = 0.4$.
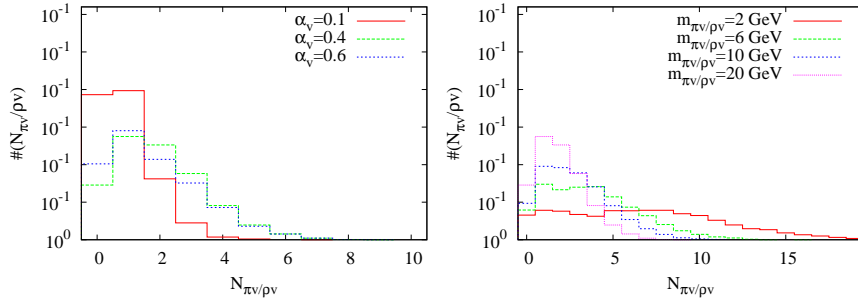

Figure IV.13: $KMNA_{\gamma_v}$: the number of flavour diagonal π_v/ρ_v gauge bosons emitted per event. On the left we emphasize the α_v dependence, while on the right the m_{π_v/ρ_v} dependence. On the left side $m_{\pi_v/\rho_v} = 10$ GeV and $\alpha_v = 0.1, 0.4, 0.6$, while on the right side $m_{\pi_v/\rho_v} = 2, 6, 10, 20$ GeV and the coupling is fixed at $\alpha_v = 0.4$.

in Fig. IV.15. The kinetic boundary $E^{\max}$ is different in the two cases, owing to the choice of $m_{q_v} = 50$ GeV in the Abelian case. This reduces the energy available for γ_v emissions. The $\not{p}_\perp$ distribution was shown in Fig. IV.8 and has already been discussed.

The most important distribution to pinpoint the masses of the model is the lepton energy spectrum, Fig. IV.16. In this case leptons may come from both the kinetic mixing decays of the γ_v and from the decays of the E_v into eq_v. The energy spectra are very different in the two cases. The leptons coming from the E_v decays tend be highly energetic, while the rest are less so. A reasonable first approximation is to associate the highest energy electron and positron
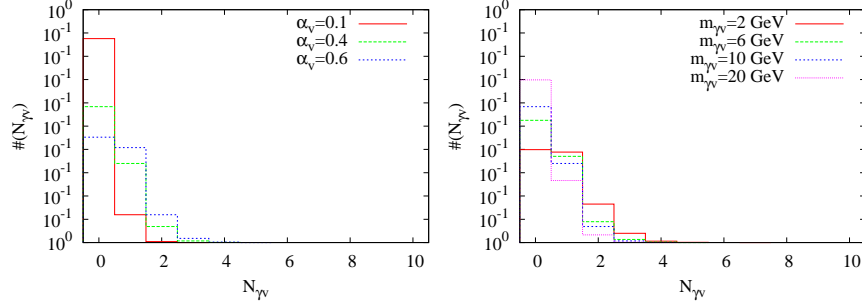
Figure IV.14: *SMA*: the number of γ_v gauge bosons emitted per event. On the left we emphasize the α_v dependence, while on the right the m_{γ_v} dependence. In both plots $m_{E_v} = 250$ GeV and $m_{q_v} = 50$ GeV. On the left side $m_{\gamma_v} = 10$ GeV and $\alpha_v = 0.1, 0.4, 0.6$, while on the right side $m_{\gamma_v} = 2, 6, 10, 20$ GeV and the coupling is fixed at $\alpha_v = 0.4$.
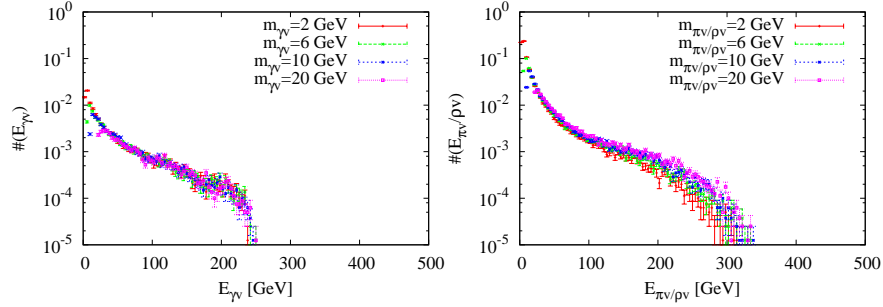

Figure IV.15: *SMA* vs *SMNA*: the energy spectra of the γ_v and of the diagonal π_v/ρ_v emitted per event. The left side shows the energy distribution for SMA $m_{E_v} = 250$, GeV $m_{q_v} = 50$ GeV, the right side shows the corresponding distribution for SMNA (in this case $m_{q_v} = 1, 3, 5, 10$ GeV corresponds to half of the π_v/ρ_v mass.).

IV

with the two E_v decays, and the rest with the $\gamma_v/\pi_v/\rho_v$ ones. The curve in Fig. IV.16 represents the sum of the steeply falling spectrum associated to the leptons coming from γ_v decay, and a flat spectrum associated to the leptons from $E_v \rightarrow eq_v$ decay. The upper and lower shoulders of the former energy distributions then give a relationship between the E_v and the q_v masses [18].

IV.4.5 Angular distributions and event shapes

The distribution of the production cross-section as a function of the angle between the jets and the beam axis has a characteristic dependence on the spin
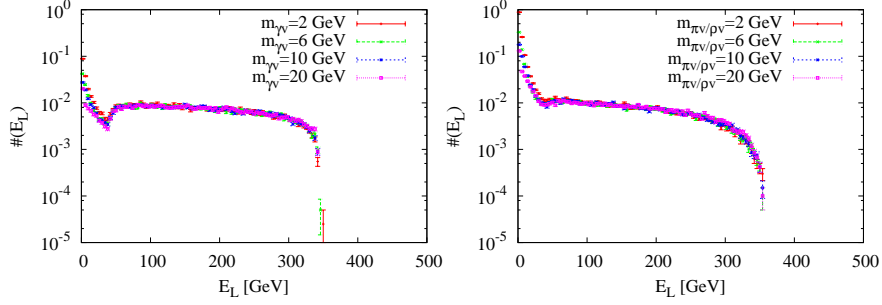
Figure IV.16: *SMA* vs *SMNA*: the lepton energy spectra in the Abelian (left) case and in the non-Abelian (right) case. In the Abelian case GeV $m_{q_v} = 50$ GeV, while in the non-Abelian case $m_{q_v} = 1, 3, 5, 10$ GeV. In both cases $m_{E_v} = 250$ GeV.
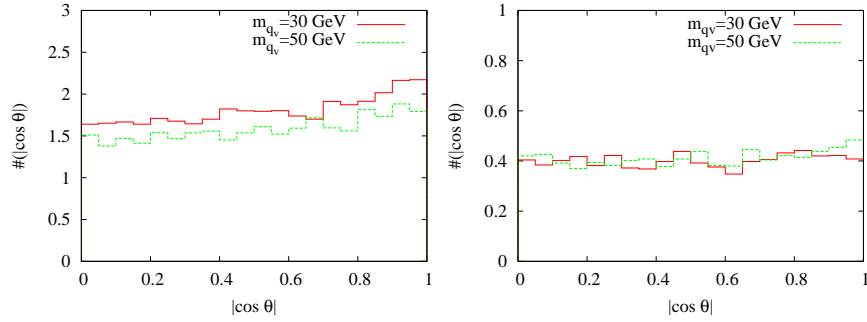

Figure IV.17: *AM$_{Z'}$* and *SMA*: the distribution of $\cos\theta_i$, where θ_i is the angle between the ith jet and the beam axis, for $m_{q_v} = 30$ GeV and for $m_{q_v} = 50$ GeV. A lower cut on the invariant mass $m_j > m_{\gamma_v/\pi_v/\rho_v}/2$ was applied in this case. In both cases $m_{\gamma_v} = 10$ GeV and the v-coupling is fixed to $\alpha_v = 0.4$, $m_{q_v} = 10$ GeV.

of the pair-produced particles. This fact may be used to identify the q_v spin.

In Fig. IV.17 one may observe the $\cos\theta_i$ distribution, where θ_i is the polar angle between the ith jet and the beam axis, for $m_{\gamma_v} = 10$ GeV. Only jets with a reconstructed mass $m_j > m_{\gamma_v}/2$ are shown, since lower-mass jets are strongly contaminated by ISR photons above the $\theta_{\text{cut}} = 50$ mrad cut. The production cross-section for $e^+e^- \to q_v\bar{q}_v$, with q_v a massless spin 1/2 fermion, is proportional to $1 + \cos^2\theta$. In the AM$_{Z'}$ case one must allow for corrections due to the θ_{cut}, to the q_v being massive and to the γ_v radiation; typically this leads to a somewhat flatter distribution. In the SMA case the isotropic decays $E_v \to eq_v$ flattens whatever original $e^+e^- \to E_v\bar{E}_v$ distribution, unless the eq_v decay products are highly boosted. In our case a small ISR contamination is still visible
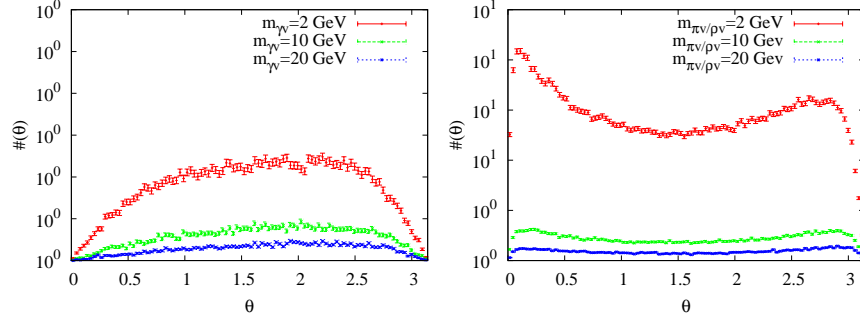
Figure IV.18: AM'_Z and NAM'_Z: the distribution of θ_{ij}, the angle between the γ_vs in the Abelian case (left), or the angle between the diagonal mesons in the non-Abelian case (right). The distributions are shown as functions of the mass $m_{\gamma_v} = m_{\pi_v/\rho_v}$. The coupling constant is $\alpha_v = 0.4$ in both cases. Note that the number of γ_v and diagonal π_v/ρ_v is different in the two cases.

close to $\cos\theta = 1$, but otherwise the distribution is flat.

The distribution of opening angles in pairs of v-particles, θ_{ij}, should give some insight whether the secluded sector G is an Abelian or a confining non-Abelian group. In an Abelian event the $q_v\bar{q}_v$ quarks define a dipole emission axis. To first approximation the v-gammas are emitted independently, i.e. with a flat distribution in the ϕ angle around the dipole axis, and uniformly in rapidity along this axis. In the non-Abelian case the emissions occur along a chain of dipoles, that is reconfigured by each new emission, since the g_vs carry v-colour charge. This implies a different underlying correlation structure, but it is unclear what happens with this correlation on the way through the v-hadronization process and the decays back into the standard sector, and how best to search for it.

In Fig. IV.18 we show the θ_{ij} distribution of v-particle pairs, for the Abelian $AM_{Z'}$ and non-Abelian $NAM_{Z'}$ cases. Note how the θ_{ij} 0 and θ_{ij} π angles are preferred in non-Abelian case. The comparison is somewhat misleading, however, in the sense that we compare scenarios with the same $m_{\gamma_v} = m_{\pi_v/\rho_v}$ and the same α_v, but with different numbers of v-particles per event (see Fig. IV.4) and different v-particle energy distributions. In Sec. IV.5 we will discuss further these distributions under more similar conditions.

In Fig. IV.19 we show the reconstructed jet-jet $\cos\theta_{ij}$ distributions corresponding to the v-particle distributions in Fig. IV.18. Note how the relative difference between the Abelian and non-Abelian scenarios is maintained.

In order to characterize the shape of the events one may also use thrust and (the linearized version of) sphericity [37–39]. These indicate whether an event is more pencil-like, $T=1$ and $S = 0$, or more spherical, $T = 1/2$ and $S = 1$.
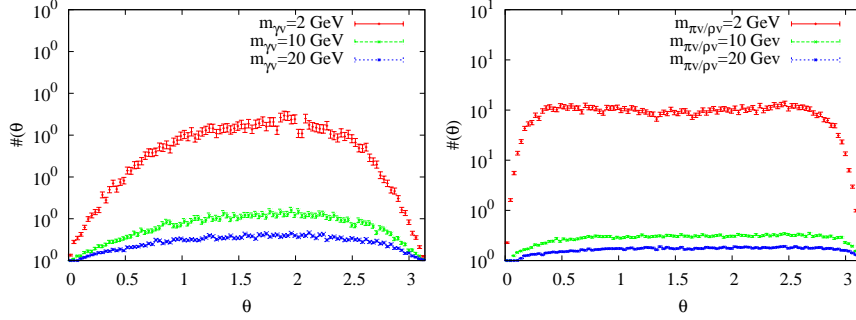
IV

Figure IV.19: AM'_Z and NAM'_Z: the distribution of θ_{ij}, the angle between the jets in the Abelian case (left) and in the non-Abelian case (right). The distributions are shown as functions of the mass $m_{\gamma_v} = m_{\pi_v/\rho_v}$. The v-coupling is fixed to $\alpha_v = 0.4$.

Sphericity and thrust are primarily intended for events analyzed in their own rest frame, while the visible systems we study have a net momentum that is compensated by the stable secluded-section particles, plus ISR photons going down the beam pipe and neutrinos. Since we are interested in the properties of the visible system itself, not in its net motion, the analysis is performed in the rest frame of this visible system. In addition, for the SMA scenarios, a further distortion occurs by the kinematics of the $E_v \to eq_v$ decays, and by the presence of the resulting $e^{\pm}$ in the final state. To this end, the highest-energy electron and positron are excluded from the definition of the visible system.

In Fig. IV.20 we show the thrust distributions in the six scenarios, and in Fig. IV.21 the sphericity distributions. As one may have predicted, the events become less pencil-like as the coupling α_v grows. In addition the SM mediated events are less likely to be pencil-like than the KM or Z' mediated ones.

IV.5   Analysis: comparing $\not{U}(1)$ and $SU(N)$

In this section we begin to address the issue of discriminating between Abelian and non-Abelian scenarios in cases in which smoking-gun discriminating signals are absent. To this end we consider the most challenging scenario, in which γ_v and π_v, ρ_v have the same mass, and the same average number of v-particles leak back into the SM sector, carrying the same average amount of energy. We also consider the same production mechanism, to reduce model dependence and to isolate the effects of the hidden sector dynamics.

So how could the Abelian and non-Abelian scenarios come to have so similar properties? First off, of course, $m_{\gamma_v} = m_{\pi_v} = m_{\rho_v}$ needs to be assumed.
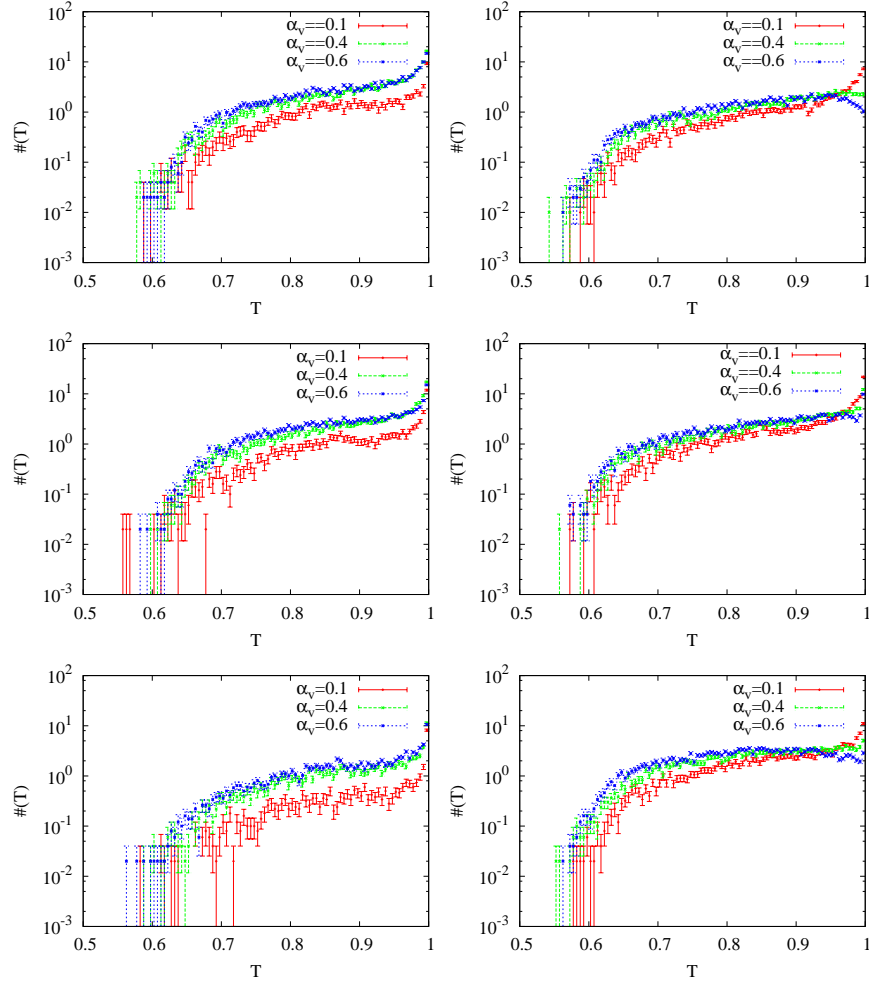
Figure IV.20: The plots show the thrust distribution for the six scenarios as a function of the α_v. These correspond to, from top to bottom, $M_{Z'}$, $KM\gamma_v$ and SM production. The plots on the left show the Abelian case while the plot on the right show the non-Abelian cases. For all Abelian plots, the parameters are set to $m_{q_v} = 50$ GeV and $m_{\gamma_v} = 10$ GeV. For the SMA case $m_{E_v} = 250$ GeV is set as well. For the non-Abelian cases, the mass of the mesons is fixed to $m_{\pi_v/\rho_v} = m_{\gamma_v}$

Thereafter the value of N_{flav} in the non-Abelian model specifies that exactly an average fraction $1/N_{\text{flav}}$ of the full energy leaks back into the visible sector. In the Abelian model, for a given m_{q_v}, α_v is the only free parameter that could be
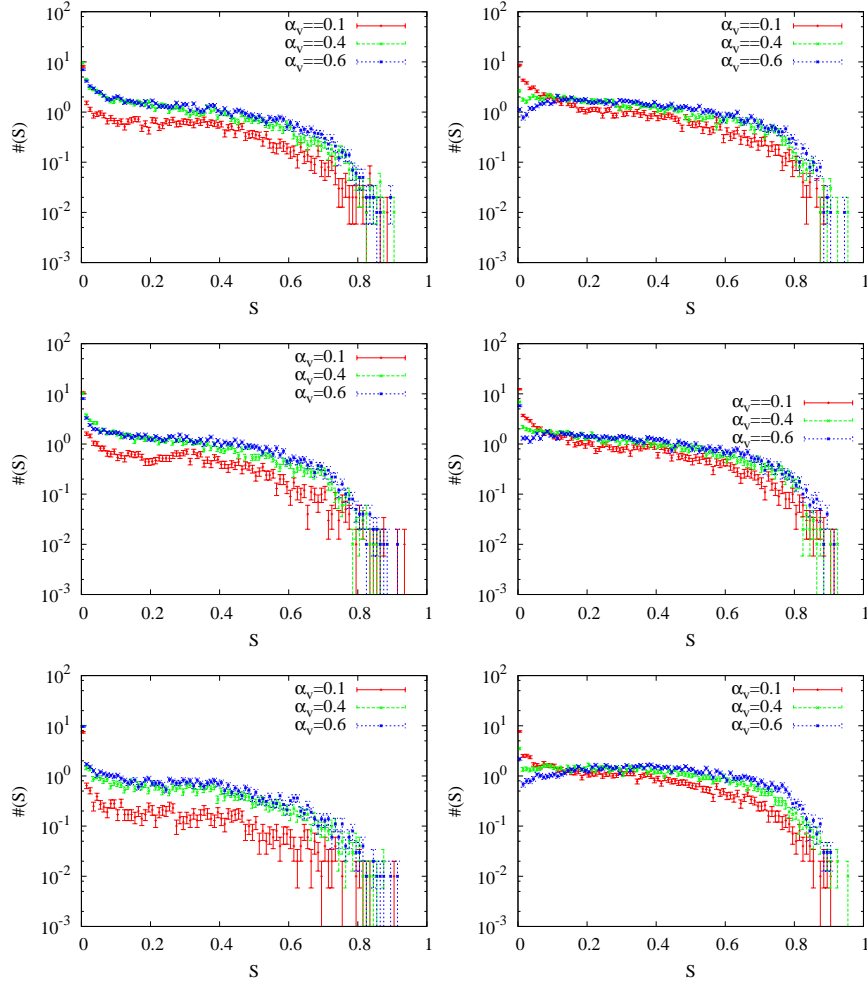
Figure IV.21: The plots show the (linearized) sphericity distribution for the six scenarios as a function of the α_v. These correspond to, from top to bottom, KM$_{Z'}$, KMγ_v and SM production. The plots on the left show the Abelian case while the plot on the right show the non-Abelian cases. For all Abelian plots, the parameters are set to $m_{q_v} = 50$ GeV and $m_{\gamma_v} = 10$ GeV. For the SMA case $m_{E_v} = 250$ GeV is set as well. For the non-Abelian cases, the mass of the mesons is fixed to $m_{\gamma_v/\pi_v/\rho_v} = 10$ GeV.

fixed to give that average energy. For this parameter set, the number and energy spectrum of γ_vs are predicted entirely by the perturbative cascade. These distributions now need to be roughly reproduced by the non-Abelian model,

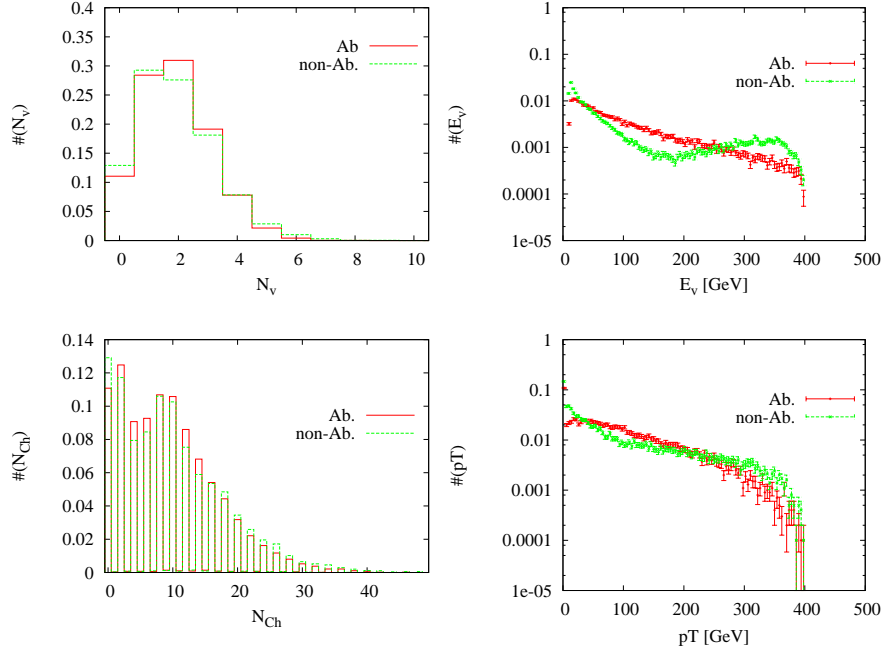Figure IV.22: The plots show the comparison between the Abelian and the non-Abelian setups: the number of γ_vs (Abelian) or diagonal π_vs/ρ_vs (non-Abelian) (top left), the v-particle energy distribution (top right), the number of SM charged particles produced, and the missing $p_\perp$. The scenarios are chosen to yield similar distributions.

which first of all means the same average number of v-particles decaying back into the SM. While $m_{q_v} = m_{\pi_v}/2$ is fixed in this case, there is freedom in the choices of α_v and non-perturbative fragmentation parameters. Recall that the number of v-particles will not vanish in the $\alpha_v \to 0$ limit for the non-Abelian model, unlike the Abelian one. Actually it turns out to be slightly difficult to reduce the non-Abelian multiplicity down to the level set by the Abelian scenario. With an α_v comparable to that of a QCD cascade at a corresponding energy/mass ratio, the longitudinal fragmentation function needs to be made harder by decreasing a and increasing b' relative to the QCD values.

Using such a strategy, a matching pair of scenarios have been constructed, an AM$'_Z$ model with $m_{q_v} = 20$ GeV, $m_{\gamma_v} = 10$ GeV and $\alpha_v = 0.3$, and a NAM$'_Z$ with $m_{q_v} = 5$ GeV, $m_{\pi_v/\rho_v} = 10$ GeV, $N_{\text{flav}} = 4$, $\alpha_v = 0.15$, $a = 0.12$ and $b' = 2$. This gives fair agreement, as can be seen in Fig. IV.22.

We can now compare the angular distributions in the two cases. In Fig. IV.23 (left) one may observe how in the non-Abelian case the θ_{ij} distri-
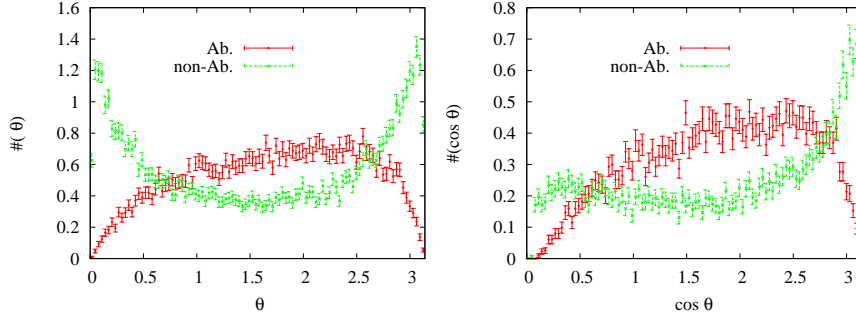
IV

Figure IV.23: The plots show the comparison between the Abelian and the non Abelian setups. On the left is the $\cos\theta_{ij}$ between the v-particles which can decay back into the SM. On the right is the corresponding $\cos\theta_{ij}$ between the jets in the detector.

bution of the angle between the visible v-particles is much more peaked near 0 and π than in the Abelian one. The plot on the right shows how this characteristic is maintained in jet distributions.

We have repeated the study for some different model parameters and found similar results. In the second comparison the AM$'_Z$ model has $m_{q_v} = 50$ GeV, $m_{\gamma_v} = 10$ GeV and $\alpha_v = 0.43$, while NAM$'_Z$ has $m_{q_v} = 5$ GeV, $m_{\pi_v/rho_v} = 10$ GeV, $N_{\text{flav}} = 4$, $\alpha_v = 0.18$, $a = 0.2$ and $b' = 2$.

It is tempting to ascribe the observed differences to different radiation/hadronization patterns in the two scenarios, ultimately deriving from the different dipole emission topologies already discussed. One attractive possibility is that the relative lack of peaking at $\cos\theta_{ij} = \pm 1$ for the Abelian scenario is a consequence of the dead cone effect, i.e. the suppression of emissions parallel to a massive radiating particle. A back-to-back $q_v\bar{q}_v$ pair undergoing non-Abelian hadronization would have no corresponding suppression for v-hadron formation along this axis. However, considering of the flexibility that exists in the tuning of non-perturbative hadronization parameters, and the differences observed in the v-particle energy spectrum, we will not now be as bold as to exclude the possibility of a closer match. If such a match required straining the non-perturbative model to behave rather differently from QCD extrapolations, however, then such tunes would not be particularly credible.

IV.6 Summary and Outlook

In this article we have compared six different scenarios of a generic secluded-sector character. These are either kinetic mixing with a light γ_v, or Z', or new F_v particles, and in each case either with a broken $U(1)$ or an unbroken $SU(N)$.

The F_v particles are charged both under the Standard Model groups and the new secluded-sector groups, and so are guaranteed a significant production rate, whenever kinematically possible, whereas the rate via γ_v or Z' depends on a number of parameters such as the γ/γ_v mixing parameters or the Z' coupling structure and mass. In this article we have completely disregarded such rate issues and instead studied the properties of the different models on an event-by-event basis.

In order to do so, we have developed a new flexible framework that implements hadronization in the hidden sector. Similar modeling in the past have relied on simple rescaling of QCD, whereas here we set up hidden-sector string fragmentation as a completely separate framework, though sharing the same underlying space–time structure of the hadronization process. We have also expanded on our previous work with parton showers in the hidden sector, possibly interleaved with radiation in the visible sector, by allowing for the emission of massive γ_vs, when the $U(1)$ group is broken. In order to obtain the correct behaviour, both in the soft/collinear limits and for hard emissions, the shower is matched to first-order matrix elements we have calculated for the massive γ_v cases. Much of the framework presented here could be applied also to other related scenarios, although there are limits. For instance, implicitly it has been assumed that the q_v masses are not too dissimilar from the confinement scale Λ of the new $SU(N)$ group — hadronization would look rather different in the limit $m_{q_v} \gg \Lambda$.

In the scenarios where F_vs are produced and promptly decay like $F_v \to f q_v$, the presence of the fermions f in the final state is a distinguishing factor, and the f energy spectrum can be used to extract information on mass scales in the secluded sector. At first glance, the production mediated by a γ_v or a Z' would seem to be more similar. The different location of the propagator mass peaks leads to quite significant patterns of initial-state photon radiation, however, that would be easily observed.

The challenge, thus, is to distinguish an Abelian and a non-Abelian scenario interactions in the secluded sector. In certain cases that would be straightforward, e.g. if there is only one q_v species, so that all energy decays back into the standard sector in the non-Abelian models. It is possible to fix parameters in the non-Abelian cases so that only some fraction decays, so that the level of activity matches Abelian α_v one.

Our first investigations here point to differences showing up in event properties related to the overall structure of the energy and particle flow. More elaborate tunings possibly might bring the models closer together, but one would hope that data still would favour "what comes naturally" in either of the models.

There are also more handles than the ones we have used. We have shown that not only lepton pairs but also jets are amenable to mass peak identifica-

IV

tion, which would allow to divide events into several subsystems and analyze their relative location, e.g. searching for coherence effects. Should lifetimes be long enough to induce displaced vertices, not only would that be a spectacular signal, but it would also be a boon to such analysis efforts.

The most obvious next step would be to study these models for consequences at the LHC. The task can be split into three parts: cross sections, triggers and model-specific event properties. The cross sections are so intimately related to the choice of masses and couplings that it will be impossible to exclude the possibility of a secluded sector, only to separate excluded and not-excluded regions of parameter space, in close analogy with SUSY. The obvious trigger would be $\not{p}_\perp$, but we have seen that this would not work for non-Abelian scenarios with one q_v flavour. It would then need to be supplemented by the presence of (multiple) lepton pairs of some fixed invariant mass and, if we are lucky, displaced vertices. The final step would be to understand whether the more busy environment in hadronic events would still allow to distinguish Abelian and non-Abelian models — the separation between the three production scenarios we have considered here should still be straightforward. Chances are that this will bring us full circle to the cross sections issue, since more sophisticated analyses will require a decent event rate to start out from.

Acknowledgements

IV.A   Scenario selection and setup

We here present some information relevant to get going with secluded-sector event generation in PYTHIA 8. Basic knowledge of the program is assumed [40].

The v-particle content is summarized in Tab. IV.2. Needless to say, not all of them would be relevant for each specific scenario. Internally further copies of q_v may be used, up to code 4900108, but these do not appear in the event record. Properties of the particles can be set to modify the scenarios, notably mass (m0); only the g_v must remain massless. If $F_v \to f q_v$ is allowed, masses must be chosen so that the decay is kinematically possible. The π_v and ρ_v masses should be set at around twice the q_v one. For unstable particles

name	name	identity	comment
D_v	Dv	4900001	partner to the d quark
U_v	Uv	4900002	partner to the u quark
S_v	Sv	4900003	partner to the s quark
C_v	Cv	4900004	partner to the c quark
B_v	Bv	4900005	partner to the b quark
T_v	Tv	4900006	partner to the t quark
E_v	Ev	4900011	partner to the e lepton
ν_{E_v}	nuEv	4900012	partner to the ν_e neutrino
M_v	MUv	4900013	partner to the μ lepton
ν_{M_v}	nuMUv	4900014	partner to the ν_μ neutrino
T_v	TAUv	4900015	partner to the τ lepton
ν_{T_v}	nuTAUv	4900016	partner to the ν_τ neutrino
g_v	gv	4900021	the v-gluon in an $SU(N)$ scenario
γ_v	gammav	4900022	the v-photon in a $U(1)$ scenario
Z', Z_v	Zv	4900023	massive gauge boson linking SM- and v-sectors
q_v	qv	4900101	matter particles purely in v-sector
π_v^{diag}	pivDiag	4900111	flavour-diagonal spin 0 v-meson
ρ_v^{diag}	rhovDiag	4900113	flavour-diagonal spin 1 v-meson
π_v^{up}	pivUp	4900211	flavour-nondiagonal spin 0 v-meson
ρ_v^{up}	rhovUp	4900213	flavour-nondiagonal spin 1 v-meson
	ggv	4900991	glueball made of v-gluons

Table IV.2: The allowed new particles in valley scenarios. Names are gives as used in this text and as in PYTHIA 8 event listings. The identity code is an integer identifier, in the spirit of the PDG codes, but is not part of the current PDG standard [41].

the width (`mWidth`) and allowed mass range (`mMin` and `mMax`) can be set. To generate displaced vertices the $c\tau$ value must be set (`tau0`). Spin choices are described later.

Several particles by default are set stable, so it is necessary to switch on their decay (`mayDecay`). For γ_v, π_v^{diag} and ρ_v^{diag} no decay channels are on by default, since that set depends so strongly on the mass scale selected. The simple way, of switching on everything (`onMode = on`) works in principle, but e.g. a 10 GeV γ_v would then be above the $b\bar{b}$ threshold but below the $B\bar{B}$ one, and so generate a trail of (harmless) error messages. Also the branching ratios of the decay channels may need to be adjusted, based on the scenario. The Z_v ones are mainly place-fillers, to give one example.

The list of processes is shown in Tab. IV.3. It would be possible to switch on all of them with `HiddenValley:all = on`, but normally that would imply a mix of different scenarios that does not appear plausible. Many processes should also be viewed in the context of the other choices made.

Finally, the list of relevant model parameters is shown in Tab. IV.4. On top

IV

code	flag	process
4901	`HiddenValley:gg2DvDvbar`	$gg \to D_v \bar{D}_v$
4902	`HiddenValley:gg2UvUvbar`	$gg \to U_v \bar{U}_v$
4903	`HiddenValley:gg2SvSvbar`	$gg \to S_v \bar{S}_v$
4904	`HiddenValley:gg2CvCvbar`	$gg \to C_v \bar{C}_v$
4905	`HiddenValley:gg2BvBvbar`	$gg \to B_v \bar{B}_v$
4906	`HiddenValley:gg2TvTvbar`	$gg \to T_v \bar{T}_v$
4911	`HiddenValley:qqbar2DvDvbar`	$q\bar{q} \to g^* \to D_v \bar{D}_v$
4912	`HiddenValley:qqbar2UvUvbar`	$q\bar{q} \to g^* \to U_v \bar{U}_v$
4913	`HiddenValley:qqbar2SvSvbar`	$q\bar{q} \to g^* \to S_v \bar{S}_v$
4914	`HiddenValley:qqbar2CvCvbar`	$q\bar{q} \to g^* \to C_v \bar{C}_v$
4915	`HiddenValley:qqbar2BvBvbar`	$q\bar{q} \to g^* \to B_v \bar{B}_v$
4916	`HiddenValley:qqbar2TvTvbar`	$q\bar{q} \to g^* \to T_v \bar{T}_v$
4921	`HiddenValley:ffbar2DvDvbar`	$f\bar{f} \to \gamma^* \to D_v \bar{D}_v$
4922	`HiddenValley:ffbar2UvUvbar`	$f\bar{f} \to \gamma^* \to U_v \bar{U}_v$
4923	`HiddenValley:ffbar2SvSvbar`	$f\bar{f} \to \gamma^* \to S_v \bar{S}_v$
4924	`HiddenValley:ffbar2CvCvbar`	$f\bar{f} \to \gamma^* \to C_v \bar{C}_v$
4925	`HiddenValley:ffbar2BvBvbar`	$f\bar{f} \to \gamma^* \to B_v \bar{B}_v$
4926	`HiddenValley:ffbar2TvTvbar`	$f\bar{f} \to \gamma^* \to T_v \bar{T}_v$
4931	`HiddenValley:ffbar2EvEvbar`	$f\bar{f} \to \gamma^* \to E_v \bar{E}_v$
4932	`HiddenValley:ffbar2nuEvnuEvbar`	$f\bar{f} \to \gamma^* \to \nu_{E_v} \bar{\nu}_{E_v}$
4933	`HiddenValley:ffbar2MUvMUvbar`	$f\bar{f} \to \gamma^* \to M_v \bar{M}_v$
4934	`HiddenValley:ffbar2nuMUvnuMUvbar`	$f\bar{f} \to \gamma^* \to \nu_{M_v} \bar{\nu}_{M_v}$
4935	`HiddenValley:ffbar2TAUvTAUvbar`	$f\bar{f} \to \gamma^* \to T_v \bar{T}_v$
4936	`HiddenValley:ffbar2nuTAUvnuTAUvbar`	$f\bar{f} \to \gamma^* \to \nu_{T_v} \bar{\nu}_{T_v}$
4941	`HiddenValley:ffbar2Zv`	$f\bar{f} \to Z_v^*(\to q_v \bar{q}_v)$

Table IV.3: Allowed processes that can be switched on individually.

is the choice between a $U(1)$ and an $SU(N)$ scenario. The F_v and q_v spins must be selected in a coordinated fashion, to be consistent with $F_v \to f q_v$ decays. The choice of F_v spin directly affects the process (differential) cross sections. If F_v has spin 1 also the choice of an anomalous magnetic moment would have an influence.

The kinetic mixing switch allows to reuse the γ^*-mediated processes in a completely different context than originally foreseen, in which the F_v have no Standard Model coupling but are produced by $\gamma - \gamma_v$ mixing. Actually this redefines the F_v to be equivalent with what we normally call q_v. Thus a process like $f\bar{f} \to \gamma^* \to E_v \bar{E}_v$ becomes $f\bar{f} \to \gamma^* \to \gamma_v^* \to q_v \bar{q}_v$. To complete this transformation you need to set the E_v stable (`mayDecay = false`), uncharged (`chargeType = 0`) and invisible (`isVisible = false`).

The shower parameters should be self-explanatory. The lower cutoff scale

parameter	def.	meaning
Scenario		
`HiddenValley:Ngauge`	3	1 for $U(1)$, N for $SU(N)$
`HiddenValley:spinFv`	1	0, 1 or 2 for F_v spin 0, 1/2 and 1
`HiddenValley:spinqv`	0	q_v spin 0 or 1 when $s_{F_v} = 1/2$
`HiddenValley:kappa`	1.	F_v anomalous magnetic dipole moment
`HiddenValley:doKinMix`	off	allow kinetic mixing
`HiddenValley:kinMix`	1.	strength of kinetic mixing, if on
Showers in secluded sector		
`HiddenValley:FSR`	off	allow final-state radiation
`HiddenValley:alphaFSR`	0.1	constant coupling strength
`HiddenValley:pTminFSR`	0.4	lower cutoff of shower evolution
Hadronization in secluded sector		
`HiddenValley:fragment`	off	allow hadronization
`HiddenValley:nFlav`	1	N_{flav}, number of distinct q_v species
`HiddenValley:probVector`	0.75	fraction of spin-1 v-mesons
`HiddenValley:aLund`	0.3	a parameter in eq. (IV.29)
`HiddenValley:bmqv2`	0.8	$b' = bm_{q_v}^2$ parameter in eq. (IV.29)
`HiddenValley:rFactqv`	1.0	r parameter in eq. (IV.29)
`HiddenValley:sigmamqv`	0.5	σ', such that $\sigma = \sigma' m_{q_v}$

Table IV.4: The parameters that can be set to select the model to study, with default values and some expanations.

can be raised in proportion to the characteristic mass scales, but ought to be no more than $m_{q_v}/2$, say. A lower cutoff means longer execution time without any significant change of event properties.

The hadronization parameters have also been discussed before, except for r, which is providing slightly more flexibility to the Lund–Bowler fragmetation function than in eq. (IV.28)

$$f(z) \propto \frac{1}{z^{1+rb'}} (1-z)^a \exp\left(-\frac{b' m_{m_v}^2}{z\, m_{m_q}^2}\right) . \qquad (\text{IV.29})$$

where r could be set anywhere between 0 and 1. The dimensionless σ' parameter is normalized so that the q_v of each new pair produced in the hadronization has a $\langle p_\perp^2 \rangle = (\sigma' m_{q_v})^2$.

Behind the scenes, the `HiddenValleyFragmentation` class can reuse most of the standard `StringFragmentation` and `MiniStringFragmentation` machineries. Specifically, already for the Standard Model hadronization, the selection of flavour, z and $p_\perp$ is relegated to three "helper" classes. The three new classes `HVStringFlav`, `HVStringZ` and `HVStringPT` derive from their respective SM equivalent, and cleanly replace these three aspects while keeping

IV

the rest of the handling of complex string topologies. Specifically, it would be straightforward to expand towards a richer flavour structure in the secluded sector. Note, however, that it is important to select v-quark "constituent" masses that reasonably match the intended v-meson mass spectrum, since such relations are assumed in parts of the code. Furthermore, with new q_v defined with separate particle data, one must disable the few lines in `HiddenValleyFragmentation::init(...)` that now duplicate the one q_v into several identical copies.

IV   References

[1] M. J. Strassler and K. M. Zurek, "Echoes of a hidden valley at hadron colliders," *Phys. Lett.* **B651** (2007) 374–379, `arXiv:hep-ph/0604261`.

[2] M. J. Strassler and K. M. Zurek, "Discovering the Higgs through highly-displaced vertices," *Phys. Lett.* **B661** (2008) 263–267, `arXiv:hep-ph/0605193`.

[3] M. J. Strassler, "Possible effects of a hidden valley on supersymmetric phenomenology," `arXiv:hep-ph/0607160`.

[4] T. Han, Z. Si, K. M. Zurek, and M. J. Strassler, "Phenomenology of Hidden Valleys at Hadron Colliders," *JHEP* **07** (2008) 008, `arXiv:0712.2041 [hep-ph]`.

[5] M. J. Strassler, "Why Unparticle Models with Mass Gaps are Examples of Hidden Valleys," `arXiv:0801.0629 [hep-ph]`.

[6] M. J. Strassler, "On the Phenomenology of Hidden Valleys with Heavy Flavor," `arXiv:0806.2385 [hep-ph]`.

[7] J. E. Juknevich, D. Melnikov, and M. J. Strassler, "A Pure-Glue Hidden Valley I. States and Decays," *JHEP* **07** (2009) 055, `arXiv:0903.0883 [hep-ph]`.

[8] N. Arkani-Hamed, D. P. Finkbeiner, T. R. Slatyer, and N. Weiner, "A Theory of Dark Matter," *Phys. Rev.* **D79** (2009) 015014, `arXiv:0810.0713 [hep-ph]`.

[9] K. M. Zurek, "Multi-Component Dark Matter," *Phys. Rev.* **D79** (2009) 115002, `arXiv:0811.4429 [hep-ph]`.

[10] M. Baumgart, C. Cheung, J. T. Ruderman, L.-T. Wang, and I. Yavin, "Non-Abelian Dark Sectors and Their Collider Signatures," *JHEP* **04** (2009) 014, `arXiv:0901.0283 [hep-ph]`.

[11] C. Cheung, J. T. Ruderman, L.-T. Wang, and I. Yavin, "Kinetic Mixing as the Origin of Light Dark Scales," *Phys. Rev.* **D80** (2009) 035008, `arXiv:0902.3246 [hep-ph]`.

[12] D. E. Morrissey, D. Poland, and K. M. Zurek, "Abelian Hidden Sectors at a GeV," *JHEP* **07** (2009) 050, `arXiv:0904.2567 [hep-ph]`.

[13] O. Adriani *et al.*, "A new measurement of the antiproton-to-proton flux ratio up to 100 GeV in the cosmic radiation," *Phys. Rev. Lett.* **102** (2009) 051101, `arXiv:0810.4994 [astro-ph]`.

IV

[14] **PAMELA** Collaboration, O. Adriani *et al.*, "An anomalous positron abundance in cosmic rays with energies 1.5-100 GeV," *Nature* **458** (2009) 607–609, `arXiv:0810.4995 [astro-ph]`.

[15] J. Chang *et al.*, "An excess of cosmic ray electrons at energies of 300-800 GeV," *Nature* **456** (2008) 362–365.

[16] **The Fermi LAT** Collaboration, A. A. Abdo *et al.*, "Measurement of the Cosmic Ray e+ plus e- spectrum from 20 GeV to 1 TeV with the Fermi Large Area Telescope," *Phys. Rev. Lett.* **102** (2009) 181101, `arXiv:0905.0025 [astro-ph.HE]`.

[17] B. Holdom, "Two U(1)'s and Epsilon Charge Shifts," *Phys. Lett.* **B166** (1986) 196.

[18] L. Carloni and T. Sjostrand, "Visible Effects of Invisible Hidden Valley Radiation," *JHEP* **09** (2010) 105, `arXiv:1006.2911 [hep-ph]`.

[19] L. Bergstrom, J. Edsjo, and G. Zaharijas, "Dark matter interpretation of recent electron and positron data," *Phys. Rev. Lett.* **103** (2009) 031103, `arXiv:0905.0333 [astro-ph.HE]`.

[20] B. McElrath, "Invisible quarkonium decays as a sensitive probe of dark matter," *Phys. Rev.* **D72** (2005) 103508, `arXiv:hep-ph/0506151`.

[21] B. Batell, M. Pospelov, and A. Ritz, "Probing a Secluded U(1) at B-factories," *Phys. Rev.* **D79** (2009) 115008, `arXiv:0903.0363 [hep-ph]`.

[22] R. Essig, P. Schuster, and N. Toro, "Probing Dark Forces and Light Hidden Sectors at Low-Energy e+e- Colliders," *Phys. Rev.* **D80** (2009) 015003, `arXiv:0903.3941 [hep-ph]`.

[23] M. Reece and L.-T. Wang, "Searching for the light dark gauge boson in GeV-scale experiments," *JHEP* **07** (2009) 051, `arXiv:0904.1743 [hep-ph]`.

[24] J. Kang and M. A. Luty, "Macroscopic Strings and 'Quirks' at Colliders," *JHEP* **11** (2009) 065, `arXiv:0805.4642 [hep-ph]`.

[25] A. Buckley *et al.*, "General-purpose event generators for LHC physics," `arXiv:1101.2599 [hep-ph]`.

[26] T. Sjostrand and P. Z. Skands, "Transverse-momentum-ordered showers and interleaved multiple interactions," *Eur. Phys. J.* **C39** (2005) 129–154, `arXiv:hep-ph/0408302`.

[27] E. Norrbin and T. Sjöstrand, "QCD radiation off heavy particles," *Nucl. Phys.* **B603** (2001) 297–342, `hep-ph/0010012`.

[28] R. Corke and T. Sjostrand, "Interleaved Parton Showers and Tuning Prospects," `arXiv:1011.1759 [hep-ph]`.

[29] M. Bengtsson and T. Sjostrand, "Coherent Parton Showers Versus Matrix Elements: Implications of PETRA - PEP Data," *Phys. Lett.* **B185** (1987) 435.

[30] S. Frixione, P. Nason, and C. Oleari, "Matching NLO QCD computations with Parton Shower simulations: the POWHEG method," *JHEP* **11** (2007) 070, `arXiv:0709.2092 [hep-ph]`.

[31] B. Andersson, G. Gustafson, G. Ingelman, and T. Sjostrand, "Parton fragmentation and string dyanmics," *Phys. Rept.* **97** (1983) 31.

[32] M. G. Bowler, "e+ e- Production of Heavy Quarks in the String Model," *Zeit. Phys.* **C11** (1981) 169.

[33] G. 't Hooft, "A planar diagram theory for strong interactions," *Nucl. Phys.* **B72** (1974) 461.

[34] T. Sjostrand, "Jet fragmentation of nearby partons," *Nucl. Phys.* **B248** (1984) 469.

[35] **JADE** Collaboration, W. Bartel *et al.*, "A measurement of the tottal cross section and a stidy of inclusive muon production for the process e+ e- to hadrons in the energy range between 39.79-GeV and 46.78- GeV," *Phys. Lett.* **B160** (1985) 337.

[36] **JADE** Collaboration, W. Bartel *et al.*, "Experimental Studies on Multi-Jet Production in e+ e- Annihilation at PETRA Energies," *Z. Phys.* **C33** (1986) 23. See also S. Bethke, Habilitation thesis, LBL 50-208 (1987).

[37] R. K. Ellis, W. J. Stirling, and B. R. Webber, *QCD and Collider Physics*, vol. 8. Cambridge University Press, 1996.

[38] S. Brandt, C. Peyrou, R. Sosnowski, and A. Wroblewski, "The Principal axis of jets. An Attempt to analyze high- energy collisions as two-body processes," *Phys. Lett.* **12** (1964) 57–61.

[39] J. D. Bjorken and S. J. Brodsky, "Statistical Model for electron-Positron Annihilation Into Hadrons," *Phys. Rev.* **D1** (1970) 1416–1420.

[40] T. Sjostrand, S. Mrenna, and P. Z. Skands, "A Brief Introduction to PYTHIA 8.1," *Comput. Phys. Commun.* **178** (2008) 852–867, `arXiv:0710.3820 [hep-ph]`.

[41] **Particle Data Group** Collaboration, K. Nakamura *et al.*, "Review of particle physics," *J. Phys.* **G37** (2010) 075021.

IV